Scholars' Mine

Doctoral Dissertations

Student Theses and Dissertations

Summer 2017

Design and performance of cost-effective ultra-high performance concrete for prefabricated elements

Weina Meng

Recommended Citation

DESIGN AND PERFORMANCE OF COST-EFFECTIVE ULTRA-HIGH

PERFORMANCE CONCRETE FOR PREFABRICATED ELEMENTS

by

WEINA MENG

A DISSERTATION

Presented to the Faculty of the Graduate School of the

MISSOURI UNIVERSITY OF SCIENCE AND TECHNOLOGY

In Partial Fulfillment of the Requirements for the Degree

DOCTOR OF PHILOSOPHY

in

CIVIL ENGINEERING

2017

Approved by

Dr. Kamal Henri Khayat, Advisor
Dr. John Joseph Myers
Dr. Grace (Guirong) Yan
Dr. Aditya Kumar
Dr. K.Chandrashekhara

ABSTRACT

This study presented in this thesis aims to: (1) develop a mixture design methodology for cost-effective ultra-high-performance concrete (UHPC) incorporating high volume of supplementary cementitious materials and conventional concrete and masonry sands; (2) developed UHPC with adapted rheology incorporating lightweight sand, hybrid fibers, and nanomaterials with improved properties; (3) design prefabricated UHPC panels with fiber-reinforced polymers (FRP) for enhanced flexural properties of stay-in-place panels made with optimized UHPC; and (4) explore potential applications of such UHPC elements. The proposed design methodology produced UHPC mixtures with 28-days compressive strengths higher than 125 and 168 MPa under standard water curing and 1-d steam curing at 90 ℃. To further improve the properties, internal curing using pre-saturated lightweight sand, rheology control of the suspending mortar before steel fibers addition, and reinforcement of hybrid fibers and carbon nanomaterials, were employed. The outcome indicated: (a) the optimum replacement ratio of lightweight sand to river sand in the UHPC was 25% to increase mechanical properties and reduce shrinkage; (b) at steel fiber content of 2%, the optimal plastic viscosity of the suspending mortar was 53 ± 3 Pa·s to secure favorable fiber distribution and enhance flexural properties of the UHPC; (c) through use of hybrid steel fibers, the flexural strength, tensile strength, and autogenous shrinkage of UHPC can increase by up to 20%, 25%, and reduced by 40%, respectively; (d) adding nanomaterials at a volume fraction of 0.3% increased the tensile strength and energy absorption capacity of the UHPC by 55% and 185%, respectively. In the end, novel applications of the developed reinforced and non-reinforced UHPC-FRP systems were explored for various applications.

ACKNOWLEDGEMENTS

There are surely much better ways to thank those I love the most, those with whom I sincerely share all the sadness and happiness, and who were always there for me. I wish to express special and sincere gratitude to my parents Mrs. Xianqing Liang and Mr. Jinhua Meng for their selfless love, my parents-in-law Mrs Guofang Zhang and Mr. Jianshe Bao for their unconditional support and care. My deepest gratitude I need to express to Yi Bao, my beloved husband for his love and all the beautiful moments we shared together.

TABLE OF CONTENTS

LIST OF FIGURES

xix

1. INTRODUCTION

1.1. BACKGROUND, PROBLEM, AND JUSTIFICATION

Deterioration of civil infrastructure has drawn worldwide concerns, due to the large amount of annual outlay for repair and rehabilitation as well as the profound detrimental impacts on the society and the environment (Jonkers et al. 2010). Therefore, sustainable construction materials have been attracting intensive research interests, such as concrete with reduced embodied energy and carbon footprint and enhanced durability. The ecological targets include minimization of exploitation of non-renewable resources, regeneration of renewable resources, and the reduction of building waste and residues. Efficient use of raw materials for the production of building materials and concepts of recycling waste are necessary to meet the needs of future generations. Furthermore, the development of innovative materials and methods aiming at extending the life-time of infrastructure is mandatory. With superior durability, ultra-high performance concrete (UHPC) is particularly interesting in infrastructure applications where the service life is a key factor.

However, several challenges have prevented UHPC from being applied widely. These challenges include, but are not limited to: 1) extremely high initial materials cost; 2) high autogenous shrinkage (high risk of cracking); 3) demanding curing, and 4) relatively low tensile/flexural strength and ductility compared with widely used that of engineered cementitious composite.

1.2. LITERATURE REVIEW

The following sections offered a general overview of the UHPC technology:

1.2.1. Overview of UHPC. The concept of UHPC was first introduced by De Larrard and Sedran (1994).

The ACI 239 developed the following definition, pending approval: "Ultra-High Performance Concrete (UHPC) is a cementitious, concrete materials that has a minimum specified compressive strength of 150 MPa with specified durability, tensile ductility and toughness requirements; fibers are generally included to achieve specified requirements" (ACI 239 2012). With appropriate combination of cementitious materials, adequate sand gradation, and incorporation of fiber reinforcement, high-range water reducer (HRWR),

and curing regimes, UHPC can be produced to deliver high flowability (self-consolidating), mechanical properties, and durability (De Larrard and Sedran 1994; Richard and Cheyrezy 1995). Typical behavior of UHPC in a uniaxial state of stress in comparison with other concrete is shown in Figure 1.1. UHPC is distinguished between other fiber-reinforced concrete (FRC) as a material exhibiting strain hardening in tension.
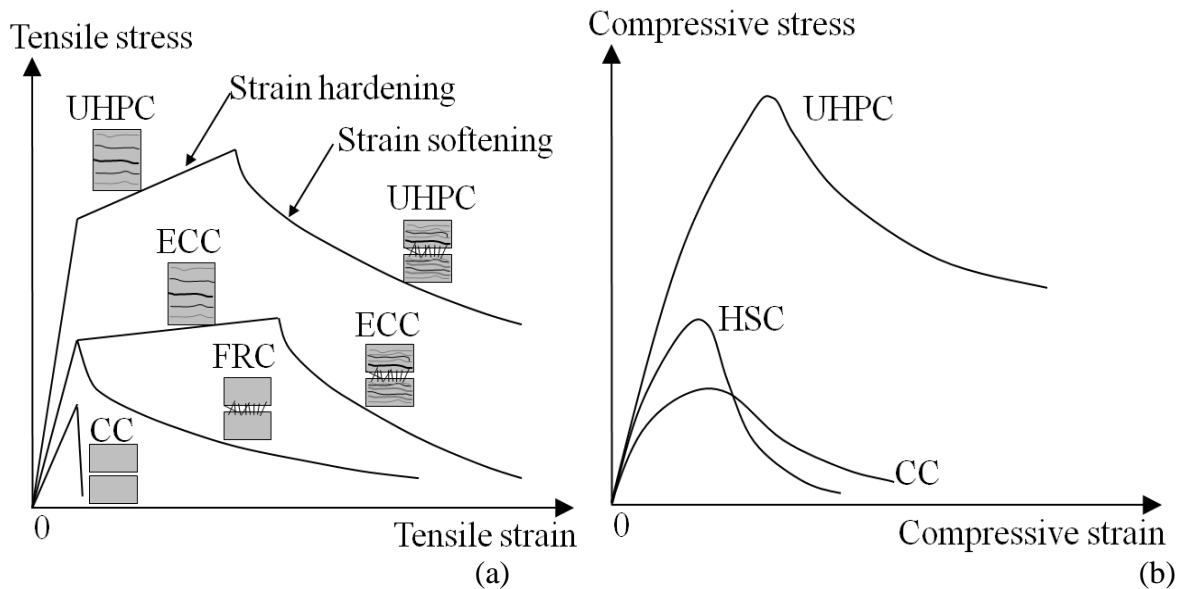
Figure 1.1. Typical response of UHPC in uniaxial stress state compare with conventional concrete (CC), high-performance concrete (HPC), fiber-reinforced concrete (FRC), and engineered cementitious composites (ECC): (a) uniaxial tension, (b) uniaxial compression.

By utilizing the UHPC material's unique combination of improved properties, infrastructure construction and performance can be accelerated, improved, and advanced. Benefits include: simplified construction techniques, speed of construction, improved durability, reduced maintenance, reduced out-of-service duration, reduced element size and complexity, extended serviceability life, and improved resiliency (ACI 239 C 2016; Ghoeim et al. 2010). In North America, UHPC has been gaining interests in construction of highway and bridges in forms of precast girders (Perry and Seibert 2008), full-depth deck panels (Asleti et al. 2011), in-fill deck joints/connections (Perry and Weiss 2009), and thin prefabricated panels for wall elements (Seibert et al. 2012).

1.2.2. Basic Information on UHPC Mix Design. To design and develop very high strength and durability of UHPC, according to recent research, first of all, the composite porosity should be minimized. The maximum packing density should be provided by determination of suitable particle size distribution of granular components. The water-to-binder ratio (w/b) should be reduced by incorporating with high-range water reducer (HRWR). If possible, vacuum process or pressure could be applied to UHPC before setting. Secondly, heat treatment and pozzolans (i.e. silica fume, fly ash, and slag) are normally employed to modify the microstructure of concrete matrix. Heat treatment can provide more energy for cementitious materials to hydrate and result in denser microstructure, and thus, increase the properties of UHPC. Thirdly, the physical homogeneity of materials should be guaranteed. These can be secure by using high mixing energy mixer and incorporating some fine aggregate, for instance, quartz sand.

1.2.2.1 Minimization of porosity. One of the primary factors in the UHPC porosity reduction is obtaining the maximum possible packing density of the particles. For example, Yu et al. (2014) adapted the modified Andreasen and Andersen model as a targeted function for the optimization of particles gradation (including cementitious materials and sand), as shown in Equation 1.1 (Funk and Dinger 1994):

$$P(D) = \frac{D^q - D_{min}^q}{D_{max}^q - D_{min}^q}$$

Equation 1.1

where P(D) represents the weight percentage of sand passing the sieve with size D, D_{max} is the maximum particle size (μm), D_{min} is the minimum particle size (μm), and q is the distribution modulus which is related to the sand particle size. For fine particles, q can be set at 0.23 (q < 0.25). The granular components proportions were adjusted until the best fit is achieved between the composed gradation curve and the targeted curve, using an optimization algorithm based on the least square method. When the discrepancy between the targeted curve and the composed gradation is minimized, the components proportioning can be considered as optimum.

The second important factor influencing the reduction of porosity is the decrease in w/b. This is possible due to application of new generation HRWR or superplasticizer,

which enables significant reduction in mixing water amount. The average value of w/b can be reduced even lower than 0.2. Such a small amount of water can be completely used up during cement hydration. This limits the possibility of formation of capillary pores due to excess unreacted water.

The third way of reducing the porosity is minimize the air in the UHPC mixture. Richard and Cheyrezy (1995) reported that applied pressure before setting can significantly reduce the porosity and allow the removal of excess water. In addition, air detraining mixture can be also used to reduce the air in concrete (Meng and Khayat 2017a). Dils et al. (2015) applied vacuum mixing to reduce the air in UHPC less than 1%.

1.2.2.2 Modification of the matrix microstructure. The modification of matrix microstructure is generally done by proper curing regime. In most reported studies, heat curing is normally used. The steam curing at 90 ℃ is applied to accelerate the processes of cement hydration and enhances the pozzolanic activity of pozzolans (Graybeal 2006). Elevated temperatures causes increase in SiO_2 solubility, regardless of its form (amorphous or crystalline). This can increase the quantity of C-S-H phase, which can lead to reduction of the porosity (Richard and Cheyrezy 1995). Another type of heat treatment is called autoclave process, which is conducted at 250 ℃. Under this condition, other than the changes taking place at 90 ℃, the crystalline forms of hydrated calcium silicates appears (Zdeb and Śliwiński 2009). These crystalline phases result in greater mechanical properties due to lower porosity compared with the amorphous phase (Richard and Cheyrezy 1995; Zdeb and Śliwiński 2009).

However, the heat curing method is energy consuming and impractical for bulk applications by the concrete profession. In addition, it is well established that the temperature above 70 °C can cause delayed ettringite formation as a disruptive process during service life of the concrete (Tayler et al. 2001). The expansion occurs typically after 1 to 4 months under laboratory conditions but in field concretes it can be much later. Thus, some researchers have attempted to achieve compressive strengths greater than 150 MPa without heat curing (Habel et al. 2006; Monai and Schnabl 2008; Wille et al. 2012). It is understood that an increase in the spread value achievable by changing the type of material within its class, and/or by changing the materials proportions indicates an improved particle packing while the amount of water is kept constant (Wille et al. 2011).

Therefore the amount of water and thus the w/b ratio can be reduced while maintaining workability. This leads to an increase in dense microstructure and high mechanical properties. Note that simply reducing the w/b ratio while not having a higher packing density leads to a decrease in workability and an increase in the amount of entrapped air, and thus, no enhancement in microstructure (Wille et al. 2011). However, researches on hydration and pozzolanic reaction of UHPC showed that the average C-S-H chain length was short and the pozzolanic activity were weak when the curing temperature was 20 ℃ (Zhang et al. 2008). If the curing ages was reasonably prolonged, the compressive strength could also reach to 150 MPa (Zhang et al. 2008).

In addition, the supplementary cementitious material (SCM), such as silica fume, fly ash, rise husk ash, and slag, is believed to modify the hydration and microstructure development of UHPC (Zhang et al. 1996; Juenger and Siddique 2015). Because of the pozzolanic reaction, the concrete with SCM has lower $Ca(OH)_2$ content than the mixture with SCM (Zhang et al. 1996). The incorporation of the SCM in concrete reduces its porosity and the $Ca(OH)_2$ amount in the interfacial zone; the width of the interfacial zone between the aggregate and the cement paste was also reduced compared with the composite without SCM (Juenger and Siddique 2015).

1.2.2.3 Increasing the homogeneity of the material. To increase the homogeneity of the material, the reduced maximum grain size is normally used, such as quartz sand (MSA ≤ 600 μm) (Graybeal 2010; Bonneau et al. 2000).

This results in obtaining high homogeneity of the composite, which is directly reflected in the actual distribution of stress in the transition zone between paste and aggregate under loading.

Recently, researchers attempted to use conventional concrete sand (MSA ≥ 2mm) was used to replace quartz sand and reduce the initial unit cost. Yang et al. (2009) used two types of local natural sand to replace finely ground quartz sand. Experimental results indicated that the use of natural sand led to reduction in compressive strength and fracture energy of about 15% lower than those of UHPC made with quartz sand. Under this circumstance, high mixing energy (mixing speed) should be applied to secure the homogeneity of materials (Dils et al. 2015).

1.2.3. Constituent Materials of UHPC. Obtaining the adequate composition of the UHPC should consider not only the determination of the relative proportions between the components characterized by different sizes of grains, but also appropriate selection of materials with proper physical and chemical properties.

1.2.3.1 Cementitious materials. The cementitious materials of UHPC should be carefully selected. Failed to appropriate selection may lead to mitigation in properties.

1.2.3.1.1 <u>Cement.</u> Cement is the basic ingredient of UHPC, which accounts for around 30% of concrete volume. As it is known, Portland cement consists of finely ground clinker and gypsum. The main compositions of clinker include C3S, C2S, C3A and C4AF. C-S-H gel, a hydration product of C2S and C3S, is the main contributor to the strength of concrete. It has been observed in a research that a combined C2S + C3S composition greater than 65% in cement is preferred for developing UHPC (Wille et al. 2011).

As another most important phase, C3A was reported significantly reducing the effectiveness of HRWR (Zdeb and Śliwiński 2009). The hydration product of C3A does not contribute to the strength of concrete, but it can bind HRWR and result in less HRWR available to improve the workability. The content of C3A and gypsum in cement has significant influence on the properties of concrete, especially workability. It was suggested that, the C3A content of cement should be less than 8% for production of UHPC (Cherezy et al. 1995).

Alkali content is another factor in cement that should be considered for the selection of cement. It was reported in literature that the increase in the alkali in the liquid accelerated the hydration of C3A by depressing the Ca^{2+} released from gypsum (Jawed and Skanlny 1978). In addition, the increase of alkali content reduced the later age compressive strength of concrete. It could increase the porosity of the microstructure and result in generation of low strength alkali-containing C-S-H gel (Suzuki et al. 1986). An increase in the alkali content of cement also increases the potential of the alkali-silicate-reaction (ASR) in concrete (Multon et al. 2008). It was documented that the alkali content should be limited into 0.9% Na2Oeq to limit the ASR expansion.

For the design of UHPC mixtures, the choice of cement is a crucial step. The suggestion by Aïtcin (2000) is that the cement used should be cement not rich in C3S and

C3A. Low shrinkage cements may also be preferred since the high cement content of UHPC can make it more susceptible to high shrinkage. According to (Wille et al. 2012) cement with a $d_{50} \approx 10$ μm is recommended for UHPC. However, concrete made with this cement can be more prone to early-age cracking due to their increased heat of hydration and significantly increased autogenous strains and stresses that can develop when self-desiccation occurs.

      1.2.3.1.2 <u>Silica fume.</u> The binder used for UHPC is normally multi-componential, containing a large amount of pozzolanic additives, such as silica fume.

      Silica fume, also known as microsilica (MS) or condensed silica fume is a by-product of the production of silicon metal or ferrosilicon alloys. Silica fume is composed of very small, glassy silica particles which are perfectly spherical. There are four mechanisms of silica fume to enhance the properties of UHPC. First, its small grain size can fill the empty spaces between the much larger grains of cement and aggregate, so that the packing density of the dry ingredient can be maximized. Secondly, the perfect sphericity of the basic particles can enhance the lubrication of the mixture. Thirdly, due to pozzonlanic reaction, the silica fume can react with $Ca(OH)_2$ to form dense C-S-H. Finally, apart from the quantitative reduction of Portlandite in mixture, the nucleation abilities of silica fume can promote the precipitation of hydration product. It is also observed that the addition of silica fume can modify the interfacial transition zone between aggregate and paste by hindrance of precipitation of large and oriented Portlandite crystals on the surface of aggregate (Scrivener et al. 2004). Furthermore, the use of silica fume can change the average C/S ratio in C-S-H phase from about 1.7 to 1.2, which is beneficial with limiting the progress of corrosion, especially in the presence of alkaline ions (Matte and Moranville 1998). Research has shown that low carbon content silica fume is preferred to achieve good workability (Wille and Boisvert-Cotulio 2013). In most publication, the silica fume is a required component of UHPC. However, 25% silica fume, by volume is routinely added in UHPC. The high amount of silica fume may have adverse effect on workability and the cost-effectiveness of UHPC. The optimum amount is still in desired to be investigated.

      1.2.3.1.3 <u>Fly ash.</u> Fly ash is readily available from waste products of the coal power industry (Schmidt et al. 2003). It has the lubricating effect, helping make UHPC

mixes self-compacting. It is reported that the electro static repulsion and ball bearing effect of fly ash can improve workability of fresh concrete. The loss on ignition value of fly ash has significant effect on the workability of concrete by influencing the tendency of absorbing HRWR (Dhir et al. 1988). The pozzolanic reaction of fly ash is relatively slow, and the addition of fly ash can retard the hydration of cement (He et al. 1984). This is because that the FA surface acts like a calcium-sink. The calcium in solution is absorbed by fly ash, as AFt phases preferentially forms on the surface of fly ash (Wei et al. 1985). This depresses the Ca^{2+} concentration in solution during the first 6 h of hydration, and the formation of a Ca-rich surface layer on the clinker minerals is also postponed (Wei et al. 1985). Therefore, the $Ca(OH)_2$ and C–S–H nucleation and crystallization are delayed and the cement hydration is simultaneously retarded (Wei et al. 1985). Nevertheless, the pozzolanic reaction of fly ash can be further proceeding and the mechanical properties of concrete at later ages can be further enhanced (Berry et al. 1990). At later ages, denser impermeable concrete microstructure is formed which exhibits higher compressive strength and better durability (Dhir et al. 1988). The underlying mechanisms were considered as dilution effect, pozzolanic reactivity which resulted in the depletion of calcium hydroxide, alkali binding ability (reduce ASR) (Diamond 1981), and reduced permeability as a result of more supplemental C–S–H gel produced from the pozzolanic reaction. Moreover, fly ash was also found to significantly reduce the autogenous shrinkage of concrete (Lee et al. 2003).The use of fly ash can be beneficial from workability and economic consideration in UHPC.

1.2.3.1.4 GGBS. As a supplementary cementitious materials, the ground granulated blast-furnace (GGBS) was also reported used in UHPC to improve its properties and cost-effectiveness (Babu and Kumar 2000; Yu et al. 2015). GGBS is a glassy material from by-product of blast furnace iron-making (Regourd et al. 1983). It mainly contains calcium silicoaluminate with high reactivity characteristics (Babu and Kumar 2000). Its pozzolanic reaction can be activated by several methods, but the hydration product is always C–S–H. In most cases, GGBS reacts very fast at very early age. This can enhance the mechanical properties of mortar or concrete at early age (Wu et al. 1983). In blended cements, GGBS is chemically activated by $Ca(OH)_2$ and gypsum (Thomaasin et al. 1977). It can significantly decrease the content of $Ca(OH)_2$ crystals in

the aggregate–mortar ITZ. Moreover, it reduces the mean size of $Ca(OH)_2$ crystals, which make the microstructure of ITZ more dense (Gao et al. 2005). Due to these effects, high strength becomes possible for concrete with an optimum amount of GGBS replacing a part of Portland cement. It is also reported that the weak zone at the coarse aggregate–mortar interface almost vanishes in concrete in which 40% cement is replaced by GGBS with a specific surface area of 425 m^2/kg (Gao et al. 2005). The weak zone completely vanishes when GGBS with a specific surface area of 600 m^2/kg replaces 20% of the cement (Gao et al. 2005). Replacing cement with high volume of GGBS can be used to effectively enhance the properties of UHPC.

      1.2.3.2 HRWR. Besides the cementitious materials, a compatible HRWR is also an important for UHPC. To minimize the retardation of the cement hydration, a HRWR or polycarboxylate ether (PCE) with long side chains is preferable (Zingg et al. 2009). On top a longer side chain will have a lower affinity for intercalation and thus the formation of organomineral phases which counteract the dispersion ability of the HRWR (Plank et al. 2006). A higher strength of electrostatic and better steric stabilization is obtained by HRWR with a moderate side chain density (Flatt and Houst 2001, Zingg et al. 2009). With that, the cement particles can be more effectively dispersed. For the same side chain density and side chain length a shorter backbone length gives the most effective polymer (Plank et al. 2006). However, Flatt and Houst (2001) pointed out that the effectiveness of different HRWR should be compared at full surface coverage of the cement particles with the different superplasticizers. In case cement produces hydrates rather fast, for example, the UHPC, the addition time of the HRWR and the length of the side chains play an important role. The addition time is also very important with regard to the formation of organomineral phases, especially in case of linear polyelectrolyte polymers were used (Flatt and Houst 2001).

      1.2.3.3 Sand. Sand plays the role of confining the cement matrix to add strength and replacing binder to reduce the cost of concrete. A variety of quartz sand is usually used for UHPC, which is chemically active under steam curing conditions. Experiments by Ma and Schneider (2002) showed that up to 30 percent of the volume of cementitious materials can be replaced by crushed quartz with no reduction in compressive strength. Besides reducing the cement requirement, crushed quartz also improves the flowability of

a UHPC mixture. However, under room temperature curing, the use of quartz sand is not economical, since the benefit of it could not be utilized. Moreover, the high cost of quartz sand is the disadvantage that restricts the wider usage of UHPC.

To alleviate both the environmental and economic impact of UHPC, the conventional concrete sand was used as an economic replacement for quartz sand (Yang et al. 2009). To produce concrete with high compressive strength, the preferred sand is expected to have strong texture and limited chemical reactivity. Siliceous aggregate is one of the examples of strong and chemically stable aggregate. Chemically stable aggregate presents reduced chance of chemically deleterious reaction in UHPC, such as ASR. UHPC usually does not contain sand with MSA greater than 1 mm. However, studies have found some advantages in using coarser sand. Wille and Boisvert-Cotulio (2013) reported that concrete matrix with coarse sand demanded less water to achieve comparable spread values in comparison with matrix with only fine sand. Another study showed that the autogenous shrinkage could be significantly reduced by including sand with an aggregate size ranging from 2 to 5 mm compared with UHPC with quartz sand (Ma et al. 2004). It is always important to find out the optimal sand content of concrete for specific application. Note that the sand-to-cementitious material ratio (s/cm) ranging from 1 to 1.4 has been found to be the optimal range of UHPC (Wille and Boisvert-Cotulio 2013; Li 2016).

1.2.3.4 Reinforcing fibers. Fibers are added to cementitious materials to improve the characteristics in the hardening or the hardened state. To optimize the performance of a single fiber, fibers need to be homogeneously distributed; clustering of fibers has to be counteracted.

The mixture composition of fiber-reinforced concrete often is a compromise between the requirements on the fresh and the hardened states. The shape of the fibers differs from that of the aggregates; due to the long elongated shape and/or a higher surface area, the workability of concrete is affected. Stiff fibers, such as steel fibers, can change the structure of the granular skeleton, while flexile fibers, such as synthetic fibers, can fill the space between them. Stiff fibers push apart particles that are relatively large compared with the fiber length, the porosity of the granular skeleton increases. The practical fiber content is limited: a sudden decrease of workability occurs at a certain

fiber content, which depends on the mixture composition and the applied fiber type. The fiber aspect ratio (L_f/d_f) as well as the fiber volume should be optimized to enhance mechanical properties and workability (Swamy and Mangat 1974).

Steel fibers are normally incorporating in UHPC. Current UHPC are classified into two groups according to the type of steel fiber used in UHPC matrices. In the first group, high strength smooth steel fibers with diameter less than 0.2 mm and fiber length less than 13 mm, are applied in UHPC matrices (Wille et al. 2011; Chanvillard and Rigaud 2003). The use of the micro straight steel fiber normally required relatively high amount (i.e. $V_f \geq 26\%$) to secure the strain hardening behavior. The large amount of fiber significantly increases the cost of UHPC. For example, 4% of fiber can be more expensive than the matrix material. Thus, from a cost perspective, the fiber volume contents should be minimized for practical application of UHPC. In the second group, relatively small amount of deformed steel fibers (i.e. hooked-end and twisted fibers) with less than 2% was reinforced in a UHPC matrix to produce the strain hardening behavior accompanied with multiple micro-cracks (Wille and Naaman 2011). In this group, the deformed steel fibers are with length and diameter greater than 30 mm and 0.3 mm, respectively. The higher equivalent bond strength of deformed fiber compared with straight fibers is favorable for strain hardening with multiple micro-cracks (Kim et al. 2007 and 2010). It was reported that UHPC using 2% hooked fibers produced a high post-cracking strength ($\approx$15 MPa) and a high strain capacity ($\approx$0.5%) (Wille et al. 2014). However, there is a limit in the amount of deformed steel fibers that can be mixed since the higher aspect ratio and longer length of deformed steel fibers causes a serious reduction in workability.

The approach selected in this research is to blend macro- and micro-fibers in a UHPC matrix to enhance both the post cracking strength (tensile strength) and strain capacity (ductility) of UHPC by using a small amount of fibers without reduction in workability. In blending macro- and micro-fibers, it is expected that macro-fibers are more effective in increasing ductility while micro-fibers are effective in enhancing tensile strength and other mechanical properties.

1.2.3.5 Typical composition of UHPC. As stated previously, UHPC formulations often consist of a combination of Portland cement, fine sand, cementitious

materials, HRWR, fibers, and water. Depend on the specific application, different combinations of these materials can be used. Some commercially available products are listed in Table 1.1. As can be seen in Table 1.1, high volume of binder content, silica fume, and silica sand are normally used in UHPC. To produce a more cost-effective UHPC, other types of economical SCMs, such as fly ash and GGBS, and conventional concrete sand are investigated in this study, which is presented in the later sections.

Table 1.1 Typical compositions of UHPCs.

Type	Materials	kg/m^3
UHPC type 1 (Graybeal 2006)	Portland cement	712
	Fine sand	1020
	Silica fume	231
	Ground quartz	211
	HRWR	30.7
	Accelerator	30.0
	Steel fibers	156
	Water	109
UHPC type 2 (Rossi et al. 2005)	Portland cement	1050
	Sand	514
	Silica fume	268
	HRWR	44
	Steel fibers	858
	Water	180

Type	Materials	Proportioning ratio, by mass
UHPC type 3 (Wille et al. 2011)	Portland cement	1.0
	Fine sand	0.92
	Silica fume	0.25
	Glass powder	0.25
	HRWR	0.0108
	Steel fibers	0.22 to 0.31
	Water	0.18 to 0.20
UHPC type 4 (Williams et al. 2009)	Portland cement	1.0
	Sand	0.967
	Silica fume	0.389
	Silica flour	0.277
	HRWR	0.0171
	Steel fibers	0.31
	Water	0.208

1.2.4. Characteristics of UHPC. The general properties of a typical UHPC is presented below:

1.2.4.1 Fresh and physical properties. UHPC is kind of a self-consolidating concrete, as it is mainly used in the construction with complicated formwork and dense reinforcement. To ensure a certain flowability of UHPC is one of the most important tasks for the development of UHPC. Similar as the self-consolidating concrete, the test of the flowability of UHPC is to allow it to spread freely on a steady leveled platform using

a mini-slump cone, instead of being dropped on a flow table for 25 times. It is recommended by Wille et al. (2011) that, the mini-slump flow spread value of UHPC is preferable greater or equals than 280 mm to release most of the air in the concrete. The segregation and bleeding are not likely problems to UHPC without fibers, since it has a sticky consistency even with a high flow, and the difference in density of paste and aggregate is small. However, when steel fibers are presented, the segregation may become an issue as the specific gravity of steel is much higher than that of cementitious mortar. To design UHPC, the rheological properties of it should be carefully considered. The optimal rheological properties could be determined to guarantee high flowability and uniform dispersion of steel fibers in UHPC (Nehdi et al. 1998).

Setting time is also important for applications where the UHPC is expected to achieve required strength with a relatively short time. However, UHPC normally have much longer initial and final setting time than that of conventional concrete due to the use of high amount of HRWR. The initial setting time for UHPC is ranging from 70 minutes to 15 hours, and the corresponding final setting time is in between 5 to 20 hours for different UHPC formulations (Graybeal 2011). The use of accelerators is one of the solutions to counter severely delayed setting. Other methods include elevated temperature curing which has been proved that the both the initial and final set are significantly reduced by higher curing temperature (Graybeal 2006).

1.2.4.2 Mechanical properties. One of the most significant assets of UHPC is the improvement in compressive strength. This improvement in compressive strength has far exceeded the results achieved with conventional concrete and can allow for the possibility of UHPC to be more competitive in markets that have been typically dominated by steel construction. The significant improvements in compressive strength are complimented by the fact that UHPC also exhibits tensile strength that has not been demonstrated in conventional concrete. This tensile strength allows the material to support both pre-cracking and post-cracking loads without experiencing a brittle failure. UHPC can develop tensile strength ranging from 5-15 MPa with various curing regimes (Spasojevic 2008). These tensile strength values are achieved as a result of the interaction of the steel fibers on the microscopic level and their ability to sustain load after the onset of cracking. In addition to the improvements in tensile strength, UHPC can also achieve

flexural strengths ranging from 25-40 MPa (Spasojevic 2008). This combination of the tensile and flexural strength makes UHPC a ductile material, capable of supporting significant loads beyond cracking, which would be the ideal materials for enhanced durability required structures.

Moreover, the UHPC can have a modulus of elasticity ranging from 50 to 60 GPa with an ultimate compressive strength between 150 to 180 MPa at 28 d (Spasojevic 2008). The development of modulus of elasticity of UHPC had a good correlation with the development of compressive strength of UHPC (Graybeal 2006). For comparison, the mechanical properties of conventional concrete, high performance concrete, and UHPC are listed in Table 1.2.

Table 1.2 Mechanical properties of conventional concrete, high performance concrete, and UHPC. (Spasojevic 2008)

Parameter	Conventional concrete (35 MPa)	High performance concrete (100 MPa)	UHPC (150 MPa)
Density (kg/m^3)	20002800	20002800	23002700
Compressive strength (MPa)	≤ 60	60100	≥ 150
Tensile strength (MPa)	≤ 3	≤ 5	≥ 8
Modulus of elasticity (GPa)	30	45	5060
Fracture energy (J/m^2)	30200	≤ 150	10000

1.2.4.3 Shrinkage. The shrinkage behavior of UHPC includes drying shrinkage and autogenous shrinkage which are resulted from different mechanisms.

Drying shrinkage is caused by loss of moisture from the UHPC. Autogenous shrinkage consists of chemical shrinkage due to cement hydration and self-desiccation due to loss of moisture. After mixing, chemical shrinkage proceeds uninhibited until the largest particles in the UHPC mix have no global degrees of freedom. The solid skeleton that forms restrains chemical shrinkage, causing air voids in the matrix (Habel et al. 2006). As a result, the relative humidity in the pores of the concrete decreases rapidly in a process called self-desiccation. The self-desiccation leads to increased capillary tension in the pores of the UHPC, and the capillary tension drives the shrinkage of the matrix. When the relative humidity drops to approximately 70%, its time rate of change slows dramatically. This nearly constant relative humidity corresponds with a near stop in autogenous shrinkage of UHPC. Early age shrinkage values can be very high of UHPC, Cheyrezy and Behloul (2001) indicated linear shrinkage strain while UHPC is still in the

liquid phase could be as high as 2120 μm/m. The shrinkage occurring between initial set and final set is estimated as high as 760 μm/m, while the shrinkage at 90 d is about 1400 μm/m (Cheyrezy and Behloul 2001). Loukili et al. (1999) reported the autogenous shrinkage of UHPC approximately 875 μm/m at 40 d and 890 μm/m at the age of 90 d. Graybeal (2006) reported a total shrinkage of UPHC without heat curing at 40 d as 790 μm/m. The use of SCMs is shown to significantly reduce the autogenous shrinkage of UHPC under ambient temperature (Ghafari et al. 2016). Fibers are also reported to act as a local restraint for shrinkage. Habel et al. (2006) and Cheyrezy and Behloul (2001) also suggest that including 2% fibers in UHPC can reduce shrinkage up to 10 to 20% compared with UHPC without fibers.

1.2.4.4 Durability. Apart from being far stronger than conventional concrete, UHPC also has exceptional durability.

The durability of UHPC is related to decreased porosity and improved material homogeneity. Due to the very low porosity of UHPC, the transport of water and solutions, transporting harmful materials as chlorides, takes place in capillary pores of UHPC is very limited. It results in a highly improved resistance to the penetration of chlorides, frost and freezing attack. UHPC's excellent resistance to freeze-thaw cycles also develops from the dense matrix and very low w/b, making it ideal for virtually any climate condition. More information of durability comparison of conventional concrete, high performance concrete, and UHPC is shown in Table 1.3 (Schmidt and Fehling 2005).

Table 1.3 Durability parameters of conventional concrete, high performance concrete, and UHPC.

Parameter	Conventional concrete (35 MPa)	High performance concrete (100 MPa)	UHPC (150 MPa)
Nitrogen permeability (m^2)	10^{-16}	10^{-17}	10^{-18}
Chloride-ion diffusion (mm)	23	8	1
Carbonation depth (after 3 years) (mm)	7	4	1.5
Freeze-salt-resistance (scaling in g/m^2)	≤ 1500	150	2050
Water absorption factor	60	11	1

1.2.5. Applications of UHPC in Precast Industry. UHPC with its superior strength combined with higher shear capacity results in a significant dead-load reduction and less limited shapes of its structural members.

UHPC can lead to longer span structures with reduced member sizes compared to conventional or high performance concrete, and to a significant reduction in the volume and the self-weight with UHPC members. For example, the UHPC beam requires only half the section depth of the reinforced or pre-stressed concrete beams, which in turn reduces its weight by 70% or more (Perry 2006). The UHPC beam also has a same section depth as the steel beam which, in this case, is only slightly lighter than the UHPC member (Graybeal 2006). In addition, the superior durability properties of UHPC are also advantageous in terms of service life and reduced maintenance costs.

The first UHPC structure (precast footbridge) was built in Sherbrooke, Canada in 1997 (Figure 1.2). This bridge has a span of 60 meters and a width of 3.3 m with compressive strength and flexural strength of 200 MPa and 25 MPa, respectively. Since it is composed of six prefabricated segments, the erection of the bridge only took four days.

Figure 1.2. Sherbrooke prefabricated pedestrian bridge, 1997, Canada. (ACI 239 C 2015)

The first UHPC-bridge in the United States is the Mars Hill Bridge in Wapello Country Iowa in 2006 (Figure 1.3). The structure consists of 33 m long prefabricated beams with 1.07 m depth, as can be seen in 1.4. The girders have shallower top and bottom flanges and narrower webs more than the standard Iowa Bulb-Tee.

Figure 1.3. Mars Hill Bridge in Wapello Country Iowa, 2006, USA. (Aaleti et al. 2011)

UHPC is also being investigated for use in a variety of other applications. These applications include precast concrete piles, prefabricated panels for bridge decks and building slabs, and security and blast mitigation precast applications (Massicotte and Boucher 2010). In general, UHPC has proven to be particularly suitable in precast applications.

1.3. RESEARCH OBJECTIVES AND SCOPE OF WORK

Given the understanding of the UHPC technology, a comprehensive program has been undertaken to design and develop cost-effective UHPC for prefabricated elements. The overall goal of the proposed research program is to develop and implement cost-effective UHPC in precast applications where enhanced durability, crack resistance, and extended service life are in demand. To this end, the proposed research program is developed with the following specific objectives.

1) To present a systematic method to design and prepare non-proprietary, sustainable, and cost-effective UHPC. High-volume supplementary cementitious materials (SCMs), locally available sand (i.e. masonry sand and river sand), and low-volume steel fibers are proposed to be utilized to design UHPC with reduced costs and impacts on the environment.

2) To evaluate and optimize material properties of the UHPC designed using the proposed method. The investigated material properties will include, but not limited to, the rheological properties, shrinkage, compressive strength, and flexural/tensile properties.

Internal curing agent, fiber-reinforced polymers (FRPs), hybrid reinforcing fibers such as steel fibers and polyvinyl alcohol (PVA) fibers, and nano materials such as carbon nano platelet and nano fibers will be employed. Emphases are placed on understanding the physics behind the tested properties. Techniques for microstructure characterization will be utilized to advance the understandings. Besides, the concept of rheology control is proposed to secure effective use of steel fibers in UHPC (i.e. control of fiber uniform distribution).

3) To carry out pioneer study on unique applications of the developed UHPC. Potential innovative applications include ultra-thin prefabricated stay-in-place (SIP) formwork for bridge construction and functional graded concrete (FGC) railway track slab. The superior properties of the developed UHPC can possibly enable new designs of structural systems with enhanced sustainability, improved mechanical performance, and reduced life-cycle costs. The UHPC prefabricated elements element in the modular construction can cut down construction period and facilitate accelerated construction and repair of civil infrastructure.

1.4. SIGNIFICANCE OF THE RESEARCH

The composition of UHPC contains a large amount of cement, usually between 900 and 1100 kg/m^3, which is circa three times more the cement content in normal concrete (Graybeal 2006; Richard an Cheyrezy 1995). As the sustainable development is currently a pressing global issue and various industries have strived to achieve energy savings, the high material cost, high energy consumption and CO_2 emission for UHPC are the typical disadvantages that restrict its wider application (Habert et al. 2013). Hence, how to efficiently produce UHPC, based on materials point of view, still needs further investigation.

1) UHPC is an advanced cementitious material with exceptional mechanical performance and improved durability compared with high-performance concrete. The enhanced durability of UHPC can particularly benefit infrastructure that undergoes serious environmental loadings. However, for the high contents of cement and steel fibers, UHPC mixtures with reduced impacts on the environment are desired. For example, strategies include partial substitution of cement by alternative or green binders and reduction in content of steel fibers. Furthermore, the high price of proprietary UHPCs

limits the application. As a result, environmentally-friendly, non-proprietary UHPC is needed to extend the applications of UHPC. In the proposed study, UHPC mixtures using high-volume SCMs and conventional concrete sand will be developed. The proposed mix design method to produce cost-effective UHPC will enable great extension of applications of UHPC to facilitate development of sustainable infrastructure.

2) Due to extremely low water-to-binder ratio (w/b), autogenous shrinkage of UHPC (i.e. 1000 μm/m) typically far exceeds that of conventional concrete. Large autogenous shrinkage increases the risk of early-age cracking, which can significantly affect the mechanical performance and durability of UHPC structures. Therefore, it is important to develop a method to reduce shrinkage without sacrificing strength. The proposed internal curing approach will greatly reduce autogenous shrinkage of UHPC, which can substantially promote wider acceptance of UHPC.

3) To increase the tensile strength of concrete will enable development of innovative structures with reduced use of materials. Concrete with enhanced tensile strength tends to exhibit less cracks, which leads to not only a higher load-carrying capacity but also decelerated deteriorations such as corrosion of rebar and freeze-thaw damage of concrete, thus extending the service life. The development of ductile UHPC that has substantially higher tensile strength and ductility compared with normal concrete contributes to improving the resilience and sustainability of infrastructure.

4) Due to superior mechanical performance and durability, UHPC is an exceptional candidate to produce prefabricated structural elements with significantly reduced thickness. However, there is a lack of studies on precast UHPC element in the literature. Pioneer study to explore extended applications of UHPC in precast industry is in demand. The proposed designs of UHPC SIP and FGC slab will enrich the methods of fast construction, retrofit, and rehabilitation.

1.5. ORGANIZATION OF THIS DISSERTATION

This dissertation consists of ten sections. Each main section (2-9) will be organized as one or two papers including a detailed technical review section. The structure of this dissertation is plotted in Figure 1.4.

Section 1 introduces the objectives and scope of work of this study, and the organization of the dissertation. Literature reviews on general concept of UHPC such as

basic information of UHPC technology, constituent materials of UHPC, UHPC main characteristics, and typical applications are presented. More details of literatures related to different technical tasks are addressed at the beginning of the following sections.

Section 2 deals with the development a mix design method for cost-effective UHPC prepared with high-volume supplementary cementitious materials and conventional concrete sand, the results has been published in *Materials and Structures* (Journal).

Section 3 discusses improvement of UHPC properties by internal curing using lightweight sand. A factorial design approach is also employed to evaluate the effects of multiple mix proportioning parameters, including lightweight sand content that are important for mixture optimization of UHPC. This section consists of results from two papers: one is submitted to Cement and Concrete Research (Journal), the other one is submitted to *ASCE Journal of Materials in Civil Engineering* (Journal).

Section 4 presents the development of a rheology control method to improve steel fiber distribution and flexural performance of UHPC by adjusting the rheological properties of the suspending mortar of UHPC before steel fibers are added. The results of this section come from a paper that has been published in *Composites Part B: Engineering* (Journal).

Section 5 reported the reinforced effect of hybrid micro-macro steel and micro steel blended with synthetic fibers and the fiber content on key properties of the developed UHPC, which is submitted to *ACI Materials Journal* (Journal).

Section 6 deals with the reinforcement effect of two types of nanoplatelets and one type of nano fibers on rheological properties, mechanical properties, shrinkage, and microstructure characteristics. The results of this section come from two papers: one has been published in *Composites Part B: Engineering* (Journal); the other one is submitted to *Cement and Concrete Research* (Journal).

Section 7 addresses the effects of loading rate and notch-to-depth ratio on flexural properties of UHPC notched beam specimens, in order to enable use of standardized laboratory test data to predict flexural properties of UHPC structures that have different dimensions and are subjected to a range of loading rates. The results are part of a paper submitted to *Cement and Concrete Composite* (Journal).

Section 8 deals with the development of UHPC prefabricated panels reinforced by fiber-reinforced polymers (FRP). Analytical and numerical derivations and experimental validation for FRP-reinforced UHPC panels are conducted. The results of this section are from two papers: one is submitted to *Cement and Concrete Composite* (Journal), the other one has been published in *Transportation Research Record: Journal of the Transportation Research Board* (Journal).

Section 9 shows the potential precast applications using the developed UHPC. A series of numerical simulations are conducted in this section. Two published conference papers comprise this section.

Section 10 summarizes the main research outcomes, findings, and future studies.
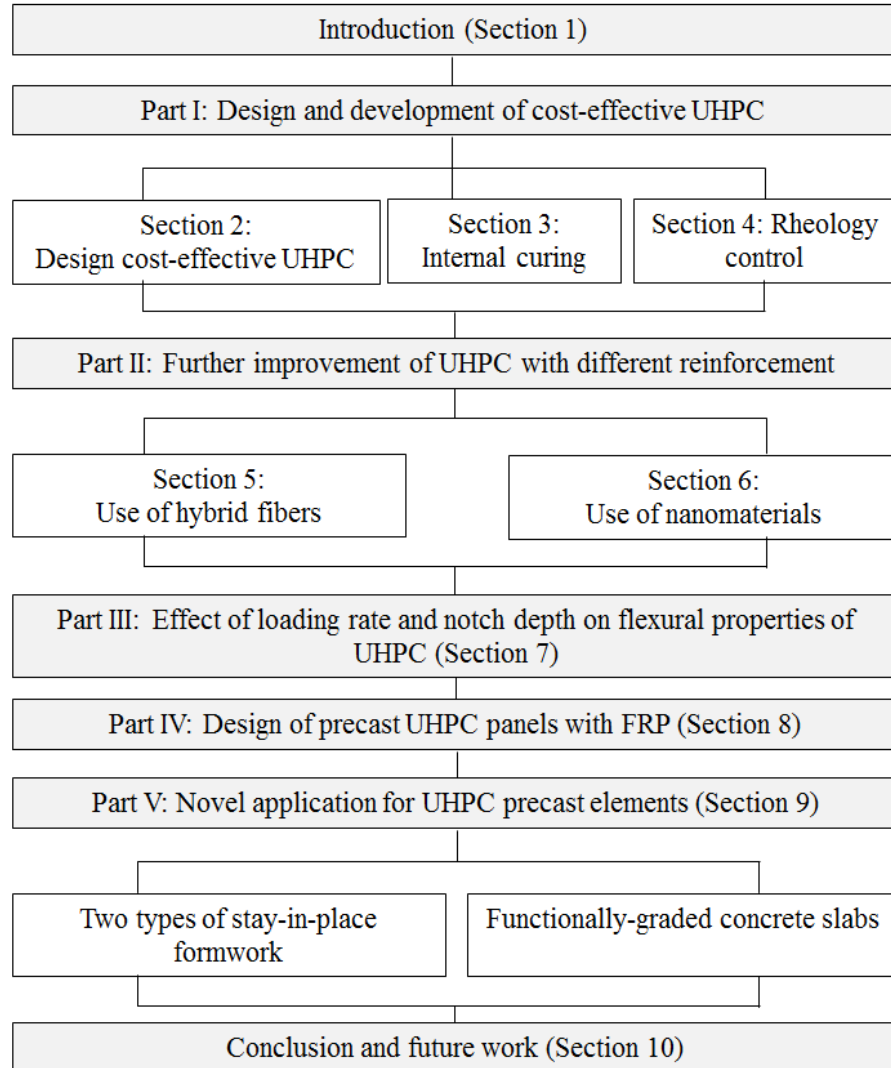
Figure 1.4. Organization of the dissertation.

2. OPTIMIZATION AND PERFORMANCE OF COST-EFFECTIVE UHPC

2.1. BACKGROUND

With appropriate combination of cementitious materials, adequate sand gradation, and incorporation of fiber reinforcement and high-range water reducer (HRWR), UHPC can be produced to deliver high flowability (self-consolidating), mechanical properties, and durability (De Larrard and Sedran 1994; Richard and Cheyrezy 1995). However, high material cost is restricting UHPC's wider acceptance worldwide (Brühwiler and Denarié 2008; Haber et al. 2013; Yu et al. 2014). Development of cost-effective UHPC is crucial for greater acceptance of this novel construction material.

However, the content of cement, which has high embodied energy and carbon footprint, is normally much higher than high-performance concrete. High-volume replacement of cement with SCMs or green binders, such as fly ash, ground granulated blast furnace slag (GGBS), and silica fume (SF), can be applied to reduce cement content without significantly sacrificing the mechanical strengths (El-Dieb 2009; Hassan et al. 2012; Wang et al. 2012; Yu et al. 2014). Mixtures containing 20–35% (vol.%) GGBS, 10–30% Class C fly ash (FAC), and 15–30% SF have been used in proportioning UHPC (El-Dieb 2009; Hassan et al. 2012; Wang et al. 2012; Yu et al. 2014). However, the substitution ratios were relatively low. A high-volume substitution of SCMs in proportioning UHPC needs to be investigated to further improve the sustainability.

Ground quartz sand (0–0.6 mm) is typically used in producing UHPC (Wille et al. 2011). Conventional concrete sand was used to replace quartz sand and reduce the initial unit cost. Yang et al. (2009) used two types of local natural sand to replace finely ground quartz sand. Experimental results indicated that the use of natural sand led to reduction in compressive strength and fracture energy of about 15% lower than those of UHPC made with quartz sand. Wang et al. (2012) reported that the 91-d compressive strength could achieve 150 MPa or higher strength when conventional concrete sand was used. However, high-volume SF (25%, by volume) was used. Besides, reducing the binder content can decrease unit cost of UHPC. The binder content can be reduced by optimizing the sand gradation to achieve a higher packing density (Le et al. 2015).

Appropriate binder contents need to be investigated in order to strike a balance between mechanical properties and unit cost of UHPC.

Reducing the steel fiber content is also vital in reducing unit cost of UHPC (Wille et al. 2011). While steel fibers greatly enhance tensile properties of UHPC, they import an adverse effect on flowability. An optimum content of steel fibers should be adopted to balance the workability, and mechanical performance (Graybeal 2011). An effective mix design method is of great importance for UHPC proportioning. The mix design should involve combining optimum proportions of all mixture constituents to fulfill the requirements of fresh and hardened concrete for a particular application (Khayat et al. 2007). In general, two methodologies exist for UHPC mix design. The first approach seeks to reduce porosity by decreasing the water-to-binder ratio, by mass, (w/b) (Richard and Cheyrezy 1994, 1995), and applying high temperature/pressure curing or vacuum mixing (Dils et al. 2015). However, the reduction in w/b may lead to a high amount of entrapped air, negatively affecting mechanical properties (Wille et al. 2011). High temperature/pressure curing or vacuum mixing may not be practical for cast-in-place applications. The second approach for UHPC mix design involves the increase in packing density (De Larrard and Sedran 1994; Yu et al. 2014). A modified Andreasen and Andersen model was employed to optimize UHPC mix design (Funk and Dinger 1994). The binder combinations and sand gradations were adjusted to achieve the best fit to the target particle size distribution proposed by the modified Andreasen and Andersen model using a least square method (Yu et al. 2014; 2015). However, the significant effects of water and chemical admixture on packing density of fine particles (< 100 μm) were not considered and only the solid materials were taken into account. The packing density of cementitious materials is strongly dependent on the water addition and dispersion imported by the use of HRWR (Li and Kwan 2014). Since the interparticle cohesive forces, especially electrostatic and Van der Waals forces, far exceed the gravitational forces, flocculation can form and compromise the packing (Iveson et al. 2001). A slight increase in free moisture content around fine particles can enhance packing. Water on particle surfaces can lead to lubrication and act as electrical conductor to relieve interparticle forces (Tomas 2004). Considering the presence of water, the packing density should be determined under wet conditions (Li and Kwan 2014). However, packing

models are still applicable for sand since sand particles are relatively large, and the gravitational forces far exceed the cohesive forces. Therefore, the packing densities of cementitious materials and sand should be analyzed separately.

A systematic mix design procedure was developed and implemented, incorporating preliminary testing and mathematical models. The mix design aims at achieving a densely-compacted cementitious matrix for UHPC with enhanced fresh and mechanical properties and relatively low cost. A number of cost-effective UHPC mixtures, which have high-volume SCMs, conventional concrete sand, and relatively low fiber content, are proposed and evaluated in terms of key workability, shrinkage, and durability characteristics.

2.2. MATERIALS, MIXERS, AND SPECIMEN PREPARATIONS

In this study, the cementitious materials included FAC, GGBS, SF, and Type III Portland cement. Fine SF with particles smaller than 1 μm in diameter was used; the mean diameter of the SF is about 0.15 μm, and the specific surface area determined using the Brunauer, Emmet, and Teller (BET) method is 18,500 m^2/kg. Missouri River sand (0-4.75 mm) and masonry sand (0-2.00 mm) were used under saturated surface dry (SSD) condition. The water absorptions of the river sand and masonry sands are 0.14% and 0.06%, respectively. A polycarboxylate HRWR was used to enhance the workability. The HRWR has a solid mass content of 23% and a specific gravity of 1.05. Straight steel fibers with 0.2-mm diameter and 13-mm length were used to enhance mechanical properties. The tensile strength and elastic modulus of the steel fiber are 1.9 and 203 GPa, respectively.

All mixtures were prepared and tested at room temperature (23 ± 2 ℃). Two mixers were used which were a 19-L Hobart mixer and a 150-L EIRICH mixer. The Hobart mixer was used for optimizing the individual components for UHPC, and the EIRICH mixer was employed for finalizing the UHPC mixtures. A specific mixing procedure was employed for each mixer. When the Hobart mixer was used, the mixing procedure was composed of three steps: (1) dry cementitious materials or/and sand were mixed for 2 min at 1 rps; (2) 90% of the mixing water and 90% of the HRWR were added and the mixture was mixed for 3 min at 2 rps; (3) the rest of water and HRWR were added and the mixture was mixed for 9 min at 2 rps. When the EIRICH mixer was used,

the mixing procedure was composed of five steps: (1) the mixer was pre-wetted; (2) the sand and cementitious materials were added into the mixer and mixed for 2 min at 1 rps; (3) 90% of the total liquid (water + HRWR), by volume, was added and mixed for 2 min at 6 rps; (4) the rest of the liquid was introduced, and the materials were mixed for 4 min at 6 rps; (5) the fibers were added gradually over a period of 1 min; (6) the materials were mixed for 2 min at 10 rps. While mixing, the pan speed of the mixer was fixed at 2 rps.

For each mixture, specimens were cast in one lift without mechanical consolidation. The molds were immediately covered after casting with wet burlaps and plastic sheets. They were demolded after 1 d, and then cured in lime-saturated water at 23 ± 1 ºC until the time of testing (standard curing). To investigate the effects of curing on compressive strength, two sets of UHPC specimens were prepared and tested, one set with standard curing and the other set with heat curing. Heat curing was performed at a maximum temperature of 90 ºC for 24 h. The specimens were then cured in lime-saturated water for 7 d, followed by air-curing at room temperature.

2.3. PROPOSED MIX DESIGN PROCEDURE AND EXPERIMENTAL PROGRAM

The proposed UHPC mix design method consists of six main steps, as illustrated in Figure 2.1: (1) determine binder candidates; (2) preliminarily select a w/b; (3) determine the sand combination; (4) assess the binder-to-sand volume ratio (V_b/V_s); (5) optimize the fiber content; and (6) evaluate and adjust the UHPC mixture. Step 1 is composed of three sub-steps: (1a) select binder combination candidates based on flow characteristics; (1b) narrow down the binder candidates according to the combined effects of minimum water content (MWC), relative water demand (RWD), and HRWR demand, as well as 1- and 28-d compressive strengths; (1c) finalize the binder combinations based on the rheological properties.

2.3.1. Step 1: Optimize Binder Combinations for Paste. With the initially-selected binder combinations, which aim at using high-volume SCMs in proportioning UHPC, flow tests are conducted to evaluate the MWC and RWD of binders under wet conditions in order to screen candidates for binders.

The paste mixtures with lower MWC are advantageous in terms of the packing density, and thus, the corresponding binders are selected for further optimization. To

further narrow down the candidates of the optimum binder combinations, the HRWR demand and compressive strength of the binders selected based on flow characteristics are then evaluated. For a given sand and fiber content, any change in the rheological characteristics are directly related to the changes of the paste matrix (Wu and An 2014). Therefore, final binder selection is based rheological properties of the successful binder systems. The three sub-steps are elaborated as follows.
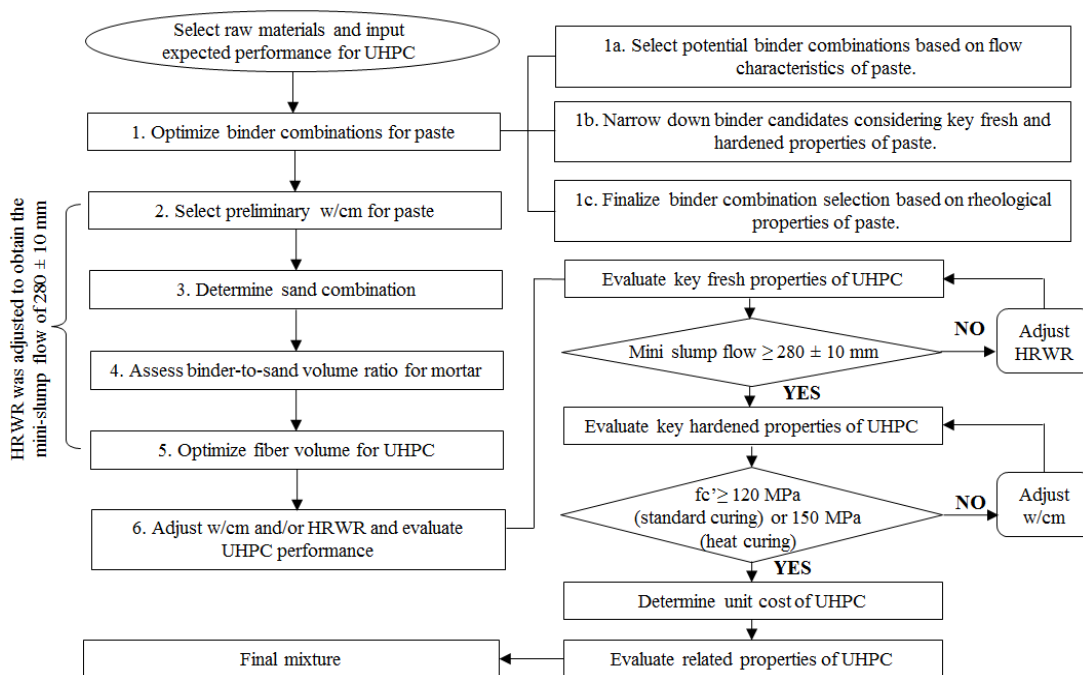
Figure 2.1. Procedure of mix design methodology for UHPC.

2.3.1.1 Sub-step 1a: Select binder candidates based on flow characteristics for paste. A mini-slump test is conducted in accordance with ASTM C 230/C 230M. For each of the test binders, seven mixtures are prepared with various water-to-binder ratio (w/b), by volume, values ranging from 0.4 to 1.0. This is carried out to establish a relationship between fluidity and w/b for each binder combination, as illustrated in Figure 2.2. The intercept on the vertical axis represents the MWC required to initiate flow, and the slope of the relationship represents the RWD. Assuming there is no air entrapped in the paste, the volume occupied by the water content can be taken as the minimum void content. Therefore, a low MWC represents a high packing density of the binder (Hwang and Khayat 2006). A high RWD indicates that a given increase in w/b can result in small

impact on the flowability. Thus, mixtures with high RWD are more robust to variations in water content (Hwang and Khayat 2006). Therefore, binder combinations with low MWC and high RWD are desirable for designing UHPC.
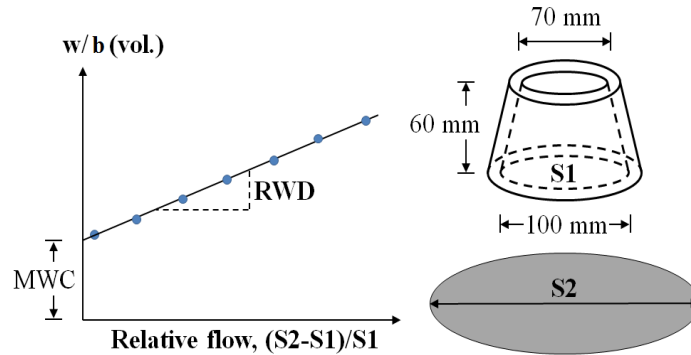
Figure 2.2. MWC and RWD in the mini-slump flow test.

2.3.1.2 Sub-step 1b: Narrow down binder candidates based on key fresh and hardened properties for paste. To further narrow down the binder combinations, key fresh and hardened properties of the selected binder combinations are evaluated. The 1- and 28-d compressive strengths are measured in accordance with ASTM C 109. The HRWR dosage is adjusted to obtain a mini-slump flow of 280 ± 10 mm, which is commonly adopted to ensure good flowability and low air entrapment (Dudziak and Mechtcherine 2008). The flow time is measured using a mini-V funnel in accordance with the EFNARC (2002). The mixtures with higher compressive strength and lower HRWR demand are preferred.

A radar chart is employed to display multivariate criteria for the selection of binder (Khayat et al. 2014). The criteria include the MWC, RWD, HRWR demand, and 1- and 28-d compressive strengths. The plot consists of a sequence of equi-angular spokes (radii), and each spoke represents one variable. The length of each spoke is proportional to the magnitude of the corresponding variable. Each variable is assigned with a specific weight factor. The data points of each spoke are sequentially connected and formed a specific area. A larger area indicates a better performance of the mixture (Khayat et al. 2014).

2.3.1.3 Sub-step 1c: Finalize the binder selection based on the rheological properties for paste. The rheological properties of paste mixtures with the selected

binders in Sub-step 1b are tested using a co-axial rheometer (Anton Paar MCR 302) at different ages, up to 60 min. The w/b (by volume) is fixed at 0.63, which corresponds to a w/b of 0.20, by mass, for mixture made with 100% Portland cement. The mini-slump spread value is fixed at 280 ± 10 mm by adjusting the HRWR dosage.

The plastic viscosity (μ_p) is measured at 20, 40, and 60 min after water addition. The paste in the rheometer undergoes a 60-s pre-shearing period at a shear rate of 100 s^{-1}. This operation could minimize the structural build-up of paste at rest. Then, the shear rate is reduced by 10 s^{-1} for every 5 s until zero. The dynamic yield stress (τ_0) and μ_p are calculated using the Bingham fluid model (Tattersall and Banfill 1983), as shown in Equation 2.1:

$$\tau = \tau_0 + \mu_p \dot{\gamma}$$

Equation 2.1

where $\dot{\gamma}$ denotes the shear rate. A relatively low value of μ_p is more desirable to ensure the proper filling capacity.

2.3.2. Step 2: Preliminarily Select a w/b for Paste. The w/b of UHPC is typically in the range of 0.15–0.25 (Wille et al. 2011).

Paste mixtures of the selected binder combinations were proportioned with w/b ranging between 0.18–0.23. The selection of the appropriate w/b is based on HRWR demand and 28-d compressive strength under standard curing. The selected w/b is applied in the later investigations to determine the optimum sand and fiber content (see Steps 3 and 4). The preliminary w/b may be slightly adjusted in the final UHPC mixtures to achieve good balance between flowability and strength which is elaborated in Step 6.

2.3.3. Step 3: Determine Sand Gradation. The modified Andreasen and Andersen model acts as a targeted function for the optimization of sand gradation, as shown in Equation 2.2 (Funk and Dinger 1994):

$$P(D) = \frac{D^q - D_{min}^q}{D_{max}^q - D_{min}^q}$$

Equation 2.2

where P(D) represents the weight percentage of sand passing the sieve with size D, D_{max} is the maximum particle size (μm), D_{min} is the minimum particle size (μm), and q is the distribution modulus which is related to the sand particle size. For fine particles, q can be set at 0.23 (q < 0.25) (Yu et al. 2014). The sand proportions are adjusted until the best fit is achieved between the composed gradation and the targeted curve, using an optimization algorithm based on the least square method. When the discrepancy between the targeted curve and the composed sand gradation is minimized, the sand combination can be considered as optimum.

According to the excess thickness theory (Li and Kwan 2011), the fluid paste volume should be high enough to fill voids between sand particles and provide a lubrication layer that envelops the particles to achieve a high flowability (Koehler and Fowler 2007). The bulk density of the compacted sand blend can be determined using a Gyrator compactor testing machine. A sand sample can be compacted by a continuous kneading action consisting of axial pressure and shear. The applied overhead air pressure is set at 4×10^5 Pa. The gyrator angle and cycle number are fixed at 2° and 200, respectively. The working speed is 1 rps. The void content (α) of the compacted sand blend can be then be calculated as:

$$\alpha = (1 - \gamma_{RM} / \rho_{RM}) \times 100\%$$

Equation 2.3

$$\rho_{RM} = \rho_{Ri} \times \sum\nolimits_{i-1}^{n} (V_{Ri} / V_{RM})$$

Equation 2.4

where γ_{RM} is the bulk density of dry sand blend, V_{Ri} and V_{RM} are absolute volumes of river sand and sand blend, respectively, and ρ_{Ri} and ρ_{RM} are the densities of river sand and sand blend, respectively.

2.3.4. Step 4: Determine V_b/V_s of Mortar. The primary paste volume, denoted by V_b, takes into account the paste volume that is necessary to fill the void content of the sand and lubricate the sand particles. The primary paste can be calculated using the approach proposed by Koehler and Fowler (2007):

$$V_b = V_{exp} + V_{void}$$

Equation 2.5

$$V_{\exp} = 8 + (16 - 8)/2(R_{S,A} - 1)$$

Equation 2.6

$$V_{void} = \alpha(100 - V_{\exp})/100$$

Equation 2.7

$$V_S = (V_{\exp} + V_{void})/(100 - V_{\exp} - V_{void})$$

Equation 2.8

where V_S expresses as the sand volume, $V_{\exp}$ denotes excess paste volume (vol.%), V_{void} is void content in mortar (vol.%), and $R_{S,A}$ is a coefficient related to the shape and the angularity of sand in the range of 1-5 (Koehler and Fowler 2007).

The minimum V_b/V_S value can provide the necessary paste for filling ability. However, the minimum value is not necessarily appropriate for a specific requirement of strength. Therefore, additional experiments need to be carried out to validate the optimum value of V_b/V_S using mortar mixtures. The 28-d compressive strength of each mortar mixture with a V_b/V_S value can be evaluated. The HRWR dosage is adjusted to obtain a mini-slump flow of 280 ± 10 mm.

2.3.5. Step 5: Determine Fiber Content of UHPC. The fiber content of UHPC commonly ranges from 2% to 5% (Park et al. 2012).

The optimum fiber content is determined based on key fresh and mechanical properties of UHPC mixtures made with different fiber contents. The mini-V-funnel and mini-slump tests are used to express workability. The HRWR dosage is adjusted to obtain a mini-slump flow of 280 ± 10 mm.

Flexural load-deflection relationships are determined in accordance with ASTM C 1609 to evaluate the first cracking strength and load capacity. Beam specimens (304.8 mm $\times$ 76.2 mm $\times$ 76.2 mm) are tested after 28-d standard curing.

2.3.6. Step 6: Adjust w/b and/or HRWR and Evaluate Performance of UHPC. In this step, trial batches are prepared to verify compliance of selected mixtures with mini-slump flow of 280 ± 10 mm and 28-d compressive strength ≥ 120 MPa under standard curing and/or ≥ 150 MPa under heat curing.

If the mixture does not achieve the targeted performance, either the HRWR dosage or w/b can be adjusted. For the selected mixture(s), key properties of the UHPC should be determined, as elaborated below.

2.3.6.1 Fresh properties. The HRWR dosage is adjusted to secure an initial mini-slump flow of 280 ± 10 mm. The unit weight and air content are measured in accordance with ASTM C 138 and ASTM C 231, respectively. The initial and final setting times are tested in accordance with ASTM A403.

A ConTech 5 viscometer can be employed to determine τ_0 and μ_p of the UHPC. Typically, the measurements begin at 10 min after water addition with samples subjected to pre-shear at a rotational velocity of 0.50 rps during 25 s, followed by a stepwise reduction in rotational velocity. The τ_0 and μ_p are then calculated using the Bingham fluid model (Tattersall and Banfill 1983), as shown in Equation 2.1.

2.3.6.2 Mechanical properties. Compressive strength and flexural properties can be tested at different ages.

The elastic modulus can be determined in accordance with ASTM C 469. The splitting tensile strength can be measured in accordance with ASTM C 496. Three samples are replicated in each test.

2.3.6.3 Autogenous and drying shrinkage. The autogenous shrinkage can be evaluated in accordance with ASTM C 1698 using samples in corrugated plastic tubes and stored immediately after casting at 20 ± 0.5 ℃ and 50 ± 2% RH.

The first measurement is taken as final setting. The second measurement is taken at 12 h after final setting. Other measurements are carried out daily within the first week, and then, weekly until 28 d after final setting. Drying shrinkage can be evaluated using prism specimens in accordance with ASTM 596, until 91 d after 7-d moist curing.

2.3.6.4 Durability. If deemed necessary, some durability characteristics of the optimized UHPC mixture can be investigated. For example, electrical resistivity can be measured in accordance with ASTM C 1760, and frost durability can be determined in accordance with the ASTM C 666, Procedure A.

2.4. EXPERIMENTAL VALIDATIONS

As stated earlier, the study aimed at using high-volume SCMs and locally available conventional concrete sand in proportioning UHPC to reduce the material's unit cost. An example of using the mix design method in detail is presented as follows.

2.4.1. Optimize Binder Combinations for Paste. The detail of the first step of the design is elaborated below:

2.4.1.1 Select binder candidates. The initial binder combinations contained SF ≤ 25%, vol.%, and FAC or/and GGBS ≥ 30%, vol.%, as listed in Table 2.1.

Table 2.1 Codification of initial investigated binders (vol. %).

Group	Code	Cement	GGBS	FAC	SF
1	Ref	100	-	-	-
2	G40	60	40	-	-
	G50	50	50	-	-
	G60	40	60	-	-
	G70	30	70	-	-
3	FAC30	70	-	30	-
	FAC40	60	-	40	-
	FAC50	50	-	50	-
	FAC60	30	-	60	-
4	SF5	95	-	-	5
	SF8	92	-	-	8
	SF11	89	-	-	11
	SF14	86	-	-	14
	SF20	80	-	-	20
	SF25	75	-	-	25
5	FAC40SF5	55	-	40	5
	FAC50SF5	45	-	50	5
	FAC50SF8	42	-	50	8
	FAC60SF5	35	-	60	5
6	G40SF5	55	40	-	5
	G50SF5	45	50	-	5
	G60SF5	35	60	-	5
	G50SF8	42	50	-	8
	G50SF11	39	50	-	11
7	F40S5G10	45	10	40	5
	F40S5G20	35	20	40	5
	F40S5G30	25	30	40	5

In total, 27 binder systems were investigated, which consisted of the reference, 14 binary, nine ternary, and three quaternary binders. The binary binders were categorized into three groups: (i) four GGBS systems, (ii) four FAC systems, and (iii) six SF systems. The ternary binders included four FAC-SF systems and five GGBS-SF systems. Three quaternary binders were prepared with FAC-SF-GGBS.

Figure 2.3 compares the MWC and RWD results of the 27 binder combinations, which are listed in Table 2.2. For the binary systems, the FAC and GGBS systems exhibited lower MWC values than that of the reference made with 100% cement. The

MWC value decreased with the increase of FAC's content due to the lubrication effects of FAC (Termkhajornkit et al. 2001). However, GGBS had an optimum amount that allowed the lowest MWC, due to its higher Blaine fineness than that of the cement, which improves the grain size distribution of the powder component and reduces the water demand (Parka et al. 2005). However, GGBS has irregular shapes and large specific areas that may result in increase of the MWC. The MWC values of the SF binary systems were close to that of the reference mixture. The small and spherical SF particles can fill the voids between cement particles, which reduce the water demand. However, the fine SF particles are highly chemically reactive and can adsorb HRWR, which is adverse for the MWC (Otsubo et al. 1980)

Figure 2.3 indicates that the use of SCMs could increase the RWD and lead to a greater robustness. For the binary systems, the FAC60 mixture provided the smallest MWC, and the largest RWD. For the GGBS binary system, the G50 mixture had the best performance (smallest MWC and largest RWD). For the SF binary system, the SF5 mixture gave the best performance. For the GGBS-SF ternary systems, the use of 5% SF slightly reduced the MWC and increased the RWD, compared with the corresponding GGBS binary systems. The fine SF particles filled the voids between the bigger cement and GGBS particles and formed gel that reduced the friction between the particles (Parka et al. 2005), thus reducing the MWC. However, using 5% or 8% SF in the FAC-SF ternary systems did not demonstrate significant improvement for the corresponding FAC binary systems. Particularly, the use of 5% SF led to a notable increase in MWC and reduction in RWD when 60% FAC was used. In summary, the G50SF5 mixture provided the highest packing density (smallest MWC) and robustness (largest RWD). All three quaternary systems offered relatively low MWC and high RWD, as indicated in Figure 2.3.

Out of the 27 binder combinations shown in Figure2.3, 18 binders that have relatively low MWC (high packing density) were selected. Aside from Group 1 (shown in Table 2.1 and Figure 2.3), two combinations having the lowest MWC were selected in each group. For Groups 2, 4, 5, 6, and 7, three mixtures were selected since the second and third mixtures have similar performance.
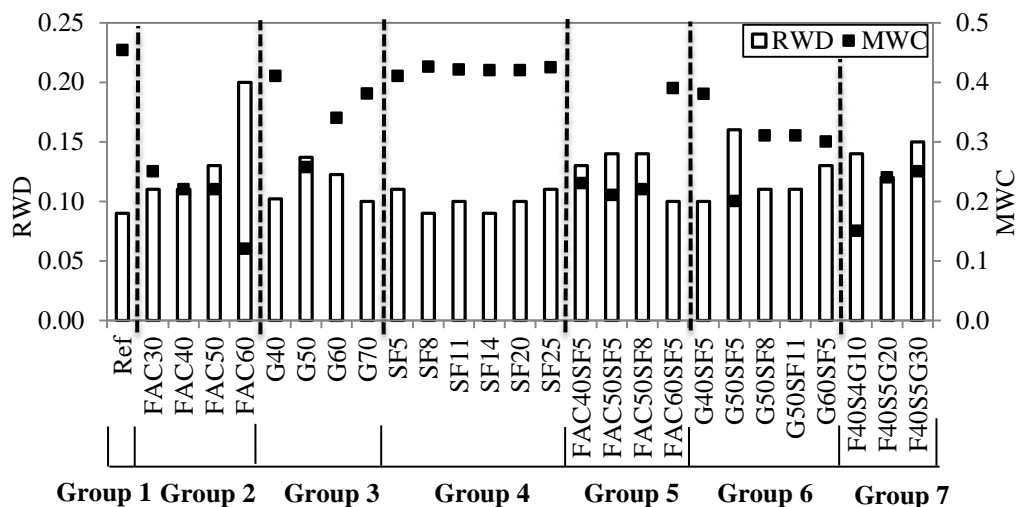
Figure 2.3. Effect of binder type on minimum water content and relative water demand.

2.4.1.2 Narrow down binder combinations. In this step, the w/b was fixed at 0.20. Figure 2.4 shows the results of HRWR demand (active solid material in HRWR divided by binder, wt.%), and 1- and 28-d compressive strengths of paste mixtures. Under standard curing, the FAC binary systems, except for the FAC60 mixture, achieved higher 1-d compressive strengths but lower 28-d compressive strengths than those of the GGBS binary systems. Using high-volume GGBS or FAC could lead to 75% lower HRWR demand compared with the reference mixture. The use of SF did not influence the HRWR demand and 28-d compressive strength significantly but increased considerably the 1-d compressive strength. For example, the use of 5% SF resulted in 95.8 MPa of the 1-d compressive strength which is more than twice that of the reference mixture (45.8 MPa). The SF binary systems demonstrated the highest 1-d compressive strength compared to other binary systems but also the highest HRWR demand. Except for the FAC40SF5G10 mixture, the 28-d compressive strength of the 17 binder combinations was in the range of 125–158 MPa. The HRWR demand of the binders with high-volume SCMs combinations was about one third of those of the reference and the SF binary systems.

In this study, the weighted factors that were used in radar chart analysis were selected to secure high performance of UHPC intended for precast application. The factors for the 1-d compressive strength, 28-d compressive strength, MWC, flow time,

RWD, and HRWR demand were 2, 4, 3, 3, 2, and 3, respectively. Figure 2.5 shows the area obtained from the radar charts. The FAC60 had the largest area, followed by G50SF5, G50, FAC40SF5, FAC40, and G50SF11 mixtures. The top six binder combinations were selected for evaluating the rheological properties.
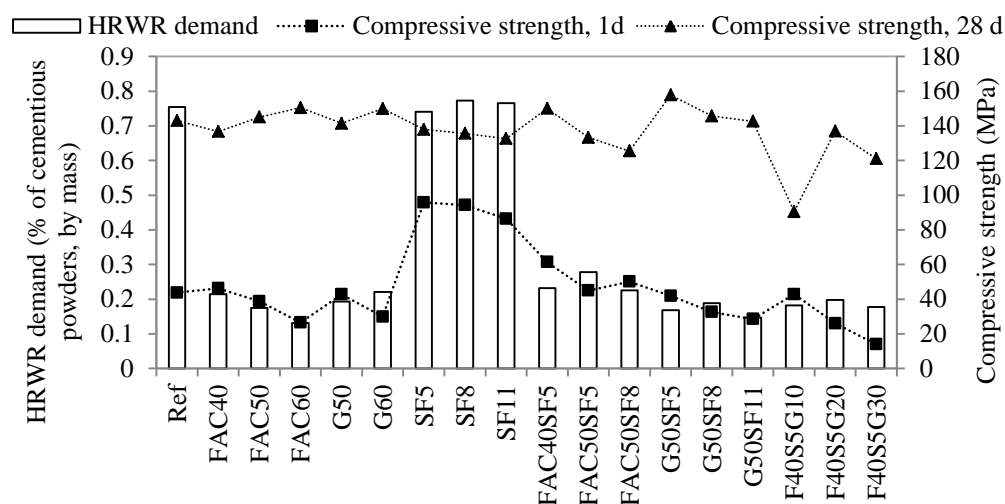
Figure 2.4. HRWR demand and 1- and 28-d compressive strength of paste.

2.4.1.3 Finalize binders. Seven binder combinations, including the reference (Ref) and six candidates selected from the previous steps, were further evaluated in terms of the rheological properties. Since the w/b and initial mini-slump flow were fixed for all mixtures, spreads of μ_p at 20 min between the mixtures were mainly due to their differences in packing densities and water film thicknesses that depend on the HRWR dosage and binder in use (Ferraris et al. 2001). Figure 2.6(a) shows an example of Bingham behavior of the reference mixture. Figure 2.6(b) shows the variation in μ_p from 20 to 60 min after water addition. At 20 min, the G50SF5 mixture achieved the lowest µp, whereas the reference paste had the highest μ_p. A lower μ_p of binders indicated more additional water amount, thicker water film, and lower friction between particles (Wong and Kwan 2008). Between 20 and 60 min, the μ_p values did not change significantly and had similar rates of increase in μ_p.

Low μ_p is desirable to achieve good filling capacity (Mechtcherin et al. 2015). Relatively low μ_p can also help fibers get evenly distributed in the matrix and improve the flexural performance. Mixtures that are highly viscous can entrap air, and, thus have

reduced strength. Therefore, based on the results presented in Figure 2.6, the G50SF5, FAC40SF5, G50, and FAC60 mixtures were select for further evaluation.

(a)

(b)
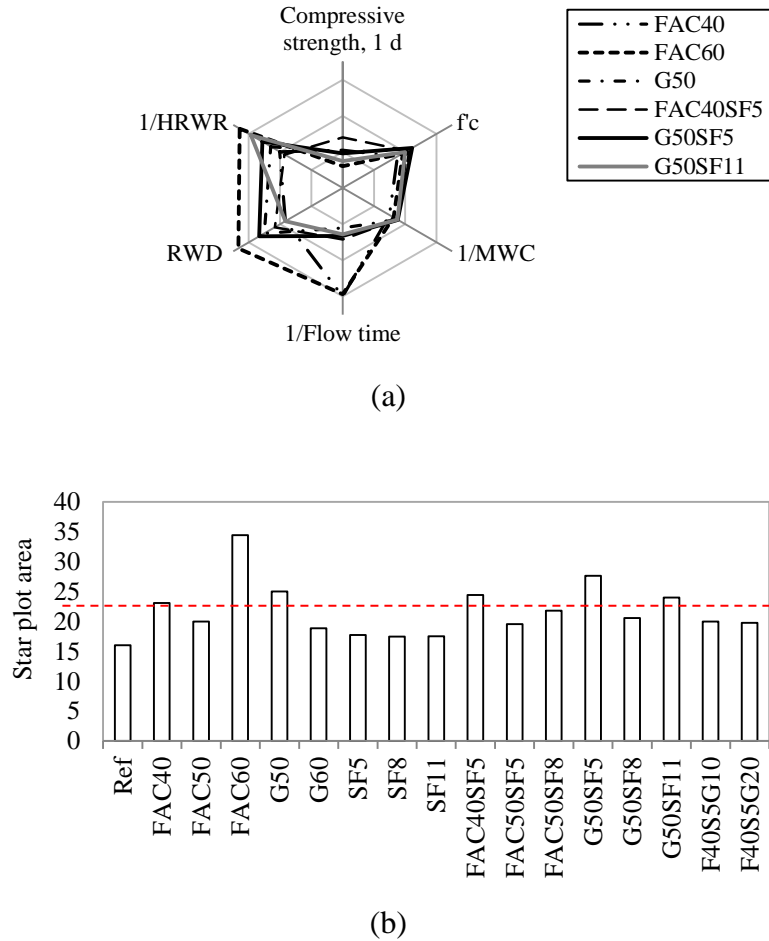
Figure 2.5. Multi-variable analysis: (a) radar chart and (b) areas in radar chart.

(a) (b)
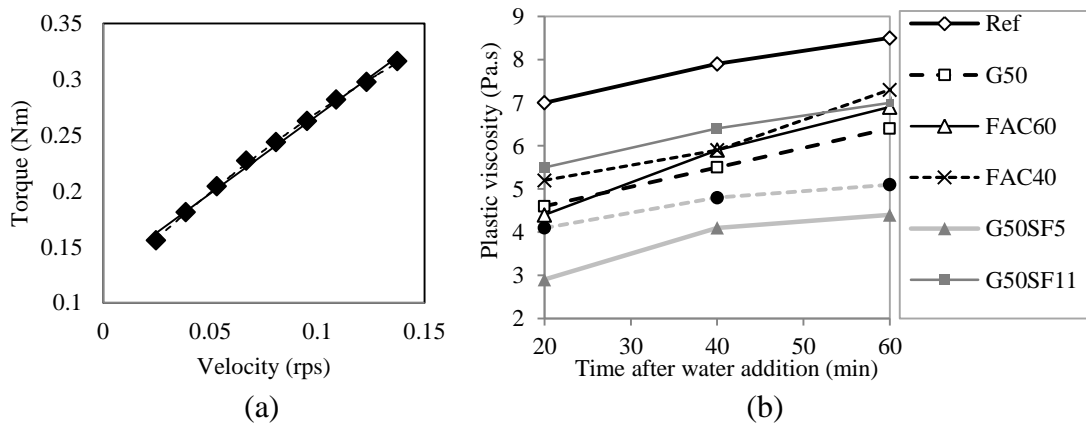
Figure 2.6. Rheology: (a) Torque versus rotational speed at 20 min for Ref and (b) Time versus plastic viscosity of paste mixtures.

2.4.2. Preliminarily Delect a w/b for Paste. A w/b in the range of 0.18–0.23 was investigated for the four optimum binders. As indicated in Figure 2.7, when the w/b was increased from 0.18 to 0.23, the 28-d compressive strengths under standard curing did not decrease significantly (< 10%), but the HRWR demand was reduced by about 40% to 60%. When the w/b was increased from 0.20 to 0.23, the HRWR demand did not change significantly. Therefore, a w/b of 0.2 was preliminarily selected, which allowed high compressive strength and flowability and relatively small temperature change.
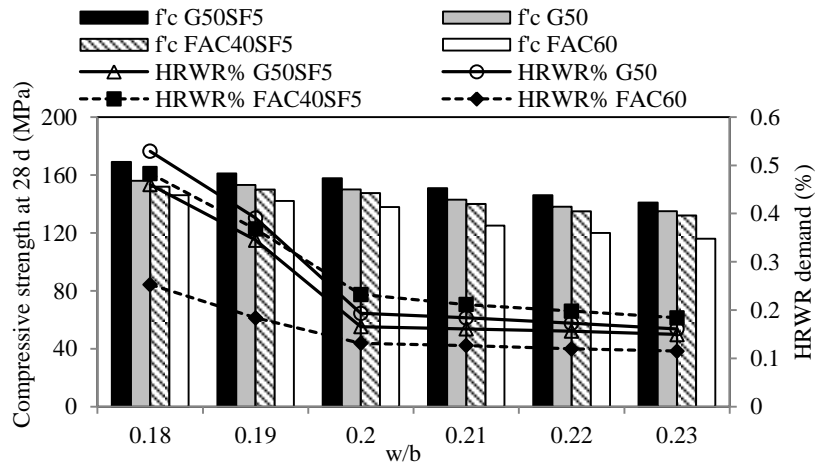
Figure 2.7. HRWR demand and compressive strength at 28 day for different w/b values.

2.4.3. Determine Sand Combination. The D_{max} and D_{min} values were determined by the sieve sizes of 4.75 and 0.15 mm, respectively.

The optimized sand combination can result in an optimized gradation curve that could be achieved with the minimum deviation from the target gradation curve, as shown in Figure 2.8. For the river sand and masonry sand employed in this study, the optimized sand combination to meet the targeted particle size distribution consisted of 70% of river sand and 30% of masonry, by mass.

In order to validate the suitability of the optimized sand to achieve high packing density, the densities of different sand combinations were measured using a gyrator compaction testing procedure.

The combination with 70% river sand and 30% masonry indeed resulted in the highest bulk packing density (1870 kg/m^3) compared to the density of other sand blends.

By applying the Equations 2.3 and 2.4, the void content (α) can be determined as: $\alpha = (1- 1870/2640) \times 100 = 30$. This value is required for evaluating the binder-to-sand volume ratio (V_b/V_S).
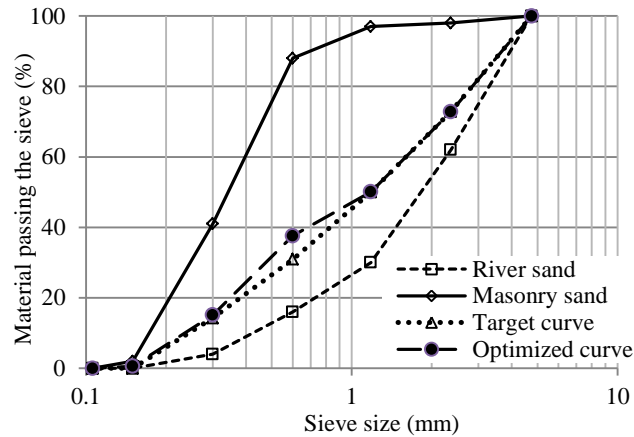
Figure 2.8. Sand gradations.

2.4.4. Determine V_b/V_s. The minimum V_b/V_s is determined to be 0.6 according to Equations 2.5-2.8, where $R_{S,A}$ equals 2 (Koehler and Fowler 2007).

The flow properties and compressive strength for mortars with V_b/V_s values of 0.6, 0.7, 0.8, 0.9, 1.0, and 1.3 were tested, as shown in Table 2.2.

The mixtures were prepared with the same binder made with 50% GGBS, 5% SF, and 45% cement. The w/b was set to 0.2. As V_b/V_s value was increased from 0.6 to 1.3, the HRWR demand and flow time were increased from 0.12% to 0.30% and from 46 to 129 s, respectively.

The corresponding 1-d compressive strength was increased from 40 to 42 MPa, respectively, and the 7- and 28-d compressive strengths were increased from 75 to 90 MPa and from 100 to 124 MPa, respectively.

Therefore, as V_b/V_s value increased from 1.0 to 1.3, the compressive strength results did not change considerably, but the HRWR demand and flow time were significantly increased.

The V_b/V_s value was determined to be 1.0, which resulted in optimized mixture with relatively low HRWR demand and viscosity, low paste content, and high compressive strength.

Table 2.2 Compressive strengths of different binder-to-sand ratio (V_b/V_s).

V_b/V_s	HRWR demand (%)	Flow time (s)	Compressive strength (MPa)		
			1 d	7 d	28 d
0.6	0.12	46	40	75	100
0.7	0.18	64	41	80	106
0.8	0.21	79	43	83	111
0.9	0.25	92	42	85	115
1.0	0.28	104	42	88	123
1.3	0.30	129	42	90	124

2.4.5. Determine V_b/V_s. Short steel fibers were used to enhance the post-cracking performance.

As the fiber content was increased from 0 to 2.5% with a step size of 0.5%, as shown in Table 2.3, the HRWR demand, which was required to ensure the slump flow of 280 ± 10 mm was increased from 0.28% to 0.69%, and the flow time was increased from 12 to 35 s. Particularly, when the fiber volume percentage, denoted by V_f, was increased from 2% to 2.5%, the HRWR dosage and flow time were increased by 72% and 94%, respectively. For the flexural properties, the first cracking load is expressed as f1, which corresponds to the load at the appearance of the first crack, as shown in Table 2.3.

Table 2.3 Performance of UHPC made with different fiber contents.

Code	V_f (%)	HRWR demand (%)	Slump flow (mm)	Flow time (s)	28-d compressive strength (MPa)	f_1 (MPa)	δ_1 (mm)	f_p (MPa)	δ_p (mm)	T150 (J)
Ref.-no fiber	0.0	0.28	29.0	12	123	13.7	0.10	13.7	0.10	1.0
Steel-0.5%	0.5	0.28	29.0	20	124	14.9	0.10	14.9	0.10	24.5
Steel-1.0%	1.0	0.28	28.5	22	124	15.9	0.07	16.5	0.61	38.4
Steel-1.5%	1.5	0.29	28.0	24	125	16.2	0.11	19.6	0.77	41.3
Steel-2.0%	2.0	0.40	28.0	18	125	16.5	0.08	20.3	1.05	50.2
Steel-2.5%	2.5	0.69	28.0	35	126	12.7	0.07	19.7	1.65	49.7

The peak load is denoted by f_p. The mid-span deflections corresponding to f_1 and f_p are denoted by and δ_1 and δ_p, respectively. The area under load versus deflection curve between deflection values of 0 to L/150 (L = 202 mm) is referred to as T150, which represents the toughness and is an indicator of energy dissipation. The fiber content increased from 0 to 2%, the f_1 and f_p increased by 20% and 48%, respectively. However, as the fiber content was further increased from 2% to 2.5%, without significantly change

in f_p and T150. A drop in f_1 was observed. The highest f_p and T150 were secured by the use of 2% steel fibers which is considered as the optimum fiber content.

2.5. EVALUATE AND ADJUST THE DESIGNED UHPC MIXTURES

Based on the above investigations, four mixtures were selected for further evaluation. Table 2.4 lists the four mixtures and a proprietary UHPC mixture taken as the reference mixture. These mixtures were prepared using the EIRICH mixer. The UHPC mixtures were designed to have a mini-slump flow diameter of 280 ± 10 mm, by adjusting the HRWR dosage, without consolidation. The w/b was not changed since all the mixtures achieved 28-d compressive strengths higher than 120 MPa under standard curing.

2.5.1. Fresh and Physical Properties. Table 2.5 summarizes the results of fresh properties. All the mixtures were self-consolidating and stable. The mini V-funnel flow times and plastic viscosities of the mixtures ranged from 12 s to 46 s and 23 Pa to 50 Pa, respectively. The reference mixture exhibited the lowest flow time and plastic viscosity, which were 12 s and 23 Pa·s, respectively. The highest flow time and plastic viscosity, which were 46 s and 50 Pa·s, respectively, were obtained by the G50 mixture. The HRWR demands of all the mixtures were in the range of 0.5% to 1.4%. The HRWR demand was the lowest for the FAC60 mixture and the highest for the G50SF5 mixture. The FAC40SF5 mixture demonstrated the longest initial setting time of 10 h and final setting time of 15 h. The G50SF5 had the shortest initial and final setting time of 2 h and 6 h, respectively.

Table 2.4 Proportioning of the designed UHPC mixtures (unit: kg/m^3).

Code	Cement	SF	FAC	GGBS	Quartz sand	Fine sand	River sand	Masonry sand	HRWR	Total water	Steel fibers
Ref.	712	231	-	-	1020	211	-	-	6.5	164	156
G50SF5	548	42	-	535	-	-	694	304	16.0	167	156
G50	593	-	-	546	-	-	698	295	12.5	182	156
FAC40SF5	663	42	367	-	-	-	703	308	12.0	171	156
FAC60	486	-	556	-	-	-	715	304	5.5	188	156

2.5.2. Compressive Strengths. Compressive strengths of the selected mixtures at 28 d under standard and heat curing methods were compared, as listed in Table 2.5.

The 28-d compressive strength of the reference mixture was 135 MPa and that of the designed mixtures was up to 125 MPa, under standard curing. The designed mixtures had slightly lower compressive strengths than that of the reference mixture. This may be due to the low silica fume content of the designed UHPC mixtures compared with the reference mixture. The designed UHPC mixtures achieved 28-d compressive strength up to 178 MPa under heat curing, which was 12% lower than that of the reference UHPC (202 MPa). The FAC60 mixture had 136 MPa under initial heat curing, which is under the target value of 150 MPa.

2.5.3. Unit Cost Per Compressive/Flexural Strength under Standard Curing. As stated before, one of the major obstacles for wider spread of UHPC is its high initial cost. By using high volume of SCMs as well as normal concrete sand, the material price of UHPC can be significantly reduced.

Figure 2.9 compares the unit cost ($/m^3) normalized by the 28-d compressive strength (MPa) and the flexural strength (MPa) of the UHPC mixtures subjected to standard curing. The unit cost included the costs of all ingredients for producing the UHPC mixtures, except for transportation costs. The unit cost of cement, SF, FAC, GGBS, river sand, masonry sand, quartz sand, HRWR, and steel fibers are 20, 660, 30, 50, 14, 7, 2200, 3800, and 1000 $/ton, respectively. Since the unit cost of FAC and GGBS are 75% lower than cement, and the cost conventional concrete sand is only around 0.5% that of quartz sand, the use of high-volume SCMs and conventional concrete sand was significantly reduced the cost of UHPC. The unit cost per compressive strength was 7.6 $/m^3/MPa for the reference mixture, and 3.5, 4.2, 4.3, and 4.7 $/m^3/MPa for the optimized FAC 60, G50, FAC40SF5, and G50SF5 mixtures, which corresponds to 40%-50% reduction in unit cost per compressive strength. As a key property of flexural performance, flexural strength demonstrates the capacity of UHPC beams. Compared with the reference mixture, the mixtures of G50SF5, G50, FAC40SF5, and FAC60 were observed 45%, 60%, 50%, and 65% reduction in cost per flexural strength. The optimized UHPC mixtures have significant benefits in cost in terms of flexural performance.

2.5.4. Other Mechanical Properties. Table 2.5 summarizes the test results of the splitting tensile strength, Young's modulus, and flexural properties of the investigated UHPC mixtures under standard curing.

The G50SF5 and FAC60 mixtures offered the highest and the lowest splitting tensile strengths of 14.3 MPa and 10.3 MPa, respectively. The FAC40SF5 and FAC60 gave the highest and the lowest elastic moduli of 51.6 GPa and 45.8 GPa, respectively. For the flexural properties, the flexural strengths of the five mixtures were close and ranged from 19.7 to 22.8 MPa. The G50 mixture had the highest first cracking and peak loads and toughness. The reference mixture had the lowest flexural strength and T150.

Table 2.5 Characteristics of the UHPC mixtures.

Code		Ref.	G50SF5	G50	FAC40SF5	FAC60
Flow time (s)		12	30	37	39	46
HRWR demand (%)		0.69	1.38	1.06	1.01	0.51
Mini slump flow (mm)		275	280	285	285	285
Yield stress (Pa)		39	35	37	34	30
Plastic viscosity (Pa·s)		23	39	50	44	29
Air content (%)		4	5	5	4	3.5
Specific gravity		2.47	2.45	2.43	2.44	2.41
Initial setting (h)		5	2	6	10	6
Final setting (h)		10	6	12	15	12
1 d – Standard curing (MPa)		53	52	64	65	69
28 d - Standard curing (MPa)		135	125	124	124	120
28 d – Heat curing (MPa)		202	178	170	168	136
Splitting tensile strength (MPa)		12	14	12	12	10
Modus of elasticity (GPa)		53	50	50	52	46
	First cracking load (kN)	22	21	24	21	20
	Peak load (kN)	21	29	33	31	28
Flexural	δ_1 (mm)	0.092	0.085	0.080	0.093	0.089
performance	δ_p (mm)	0.701	0.690	0.653	0.820	0.635
	Peak strength (MPa)	19.7	20.2	22.8	21.3	20.1
	T150 (J)	40.4	48.8	51.5	51.1	49.4
Surface conductivity (kΩ·cm)		45	30	28	38	34
Durability factor (%)		99.8	99.8	99.8	99.7	99.7
Autogenous shrinkage at 28 d (μm/m)		731	602	253	545	593
Drying shrinkage at 98 d (μm/m)		600	430	56	466	500

2.5.5. Shrinkage. Autogenous shrinkage, which is caused by volume reduction due to chemical reactions during hydration and self-desiccation, contributes mostly to the total shrinkage in UHPC (Bao et al. 2015).

Table 2.5 shows the results of 28-d autogenous shrinkage measured since the final setting. The reference mixture had the highest 28-d autogenous shrinkage, which was 730

µm/m, due to the high silica fume content. The lowest autogenous shrinkage of 250 µm/m was obtained by the G50 mixture. The G50SF5, FAC60 and FAC40SF5 mixtures had 28-d autogenous shrinkage values of 600, 595, and 545 µm/m, respectively.

The drying shrinkage values measured after 7 d of moist curing. The end of the moist curing was chosen as "time zero" (t = 0). The reference mixture reached a total drying shrinkage of 600 µm/m, which was the highest value compared with the other designed mixtures. The G50 mixture displayed the minimum drying shrinkage, which was only 55 µm/m. The total shrinkage of the UHPC can be considered as the initial autogenous shrinkage after 7 d, when autogenous shrinkage was stabilized, plus the drying shrinkage determined following 7 d of moist curing. The G50 mixture had the lowest total shrinkage of 310 µm/m. The reference mixture obtained the highest total shrinkage, which was 1330 µm/m.
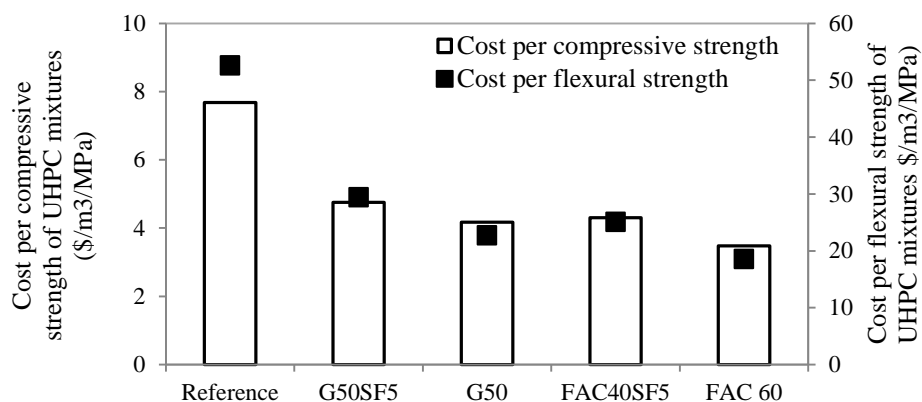
Figure 2.9. Unit cost per unit compressive strength/flexural strength of UHPC mixtures.

2.5.6. Durability. As the key properties of UHPC, the durability properties are presented below:

2.5.6.1 Electrical resistivity. The electrical resistivity affects the corrosion resistance of the material.

Test results of surface resistivity, which is an indicator of electrical resistivity, of the five UHPC mixtures determined at 28 d, are shown in Table 2.5 Mixtures with a surface conductivity greater than 20 kΩ·cm can be considered to have a low risk of corrosion rate (Broomfield 2011). Hence, all the mixtures that had surface conductivities of 30-38 kΩ·cm can be considered to exhibited a low risk of corrosion rate. The reference

mixture with high silica fume content had the highest electrical resistivity. The G50 mixtures had the lowest electrical resistivity.

2.5.6.2 Freezing and thawing. The variations in durability factor of the UHPC mixtures after 300 freeze-thaw cycles are shown in Table 2.5. All the UHPC mixtures exhibited adequate resistance to freezing and thawing with durability factors of nearly 100%. The freezing and thawing testing was initiated after 56 days of moist curing given the high volume of SCMs. The excellent frost durability is associated with the very low permeability of the material.

2.6. EVALUATION OF SUSTAINABILITY

The exceptional durability of UHPC makes it an sustainable materials in terms of prolonging the service life and reducing maintenance cost of infrastructure.

2.6.1. Evaluation Method. Sustainability of construction materials is the optimization of the materials in a way that has reduced harmful effect on resources, surroundings and living ecosystem. This investigation focuses on the carbon footprint and embodied energy of designed UHPC, which should be evaluated in a life cycle. In this study, GreenConcrete LCA tool was employed. This tool was developed for the analysis of cradle-to-gate environmental impacts of concrete and its constituents (including cement, aggregates, admixtures, and SCMs) as well as fuels and water consumption using spreadsheet. The tool converts weight information and mixture proportions taken from Table 2.5.

Environmental impacts attributed to the implementation of the materials on site (construction), structure use and replacement over time and end of-life scenarios are not included in this study. Emissions that originated from the production of all concrete constituents are incorporated in the analysis.

In this study, the unit embodied energies of quartz sand and other sands were not distinguished. The unit embodied energy and CO_2e of SF were taken as 0.036 MJ/kg and 0.014 kg/kg, respectively. The unit embodied energy and CO_2e of steel fiber were taken as 36.0 MJ/kg and 3.02 kg/kg, respectively.

2.6.2. Embodied Energy. The embodied energy results for concrete productions for 1-m^3 UHPC mixtures are listed in Table 2.6.

In the table, it can be found that the cement and steel fiber productions account for most of the total embodied energies. The reference mixture contains the most amount of cement, and thus, the embodied energy due to cement is largest for the reference mixture. Five mixtures have the same amount of steel fibers. FAC60 has the smallest embodied energy, due to the use of large content of fly ash.

Table 2.6 Embodied energy in 1-m^3 UHPC mixtures (Unit: MJ).

Phase	Reference	G50SF5	G50	FAC40SF5	FAC60
Sand	43.7	35.4	35.2	35.9	36.2
Fly ash	0	0	0	164.4	249.1
Ground blasted furnace slag	0	872.0	888.9	0	0
Silica fume	8.3	1.5	0	1.5	0
Steel fibers	5616	5616	5616	5616	5616
HRWR	530.7	1281.0	988.2	933.3	439.2
Cement	3691.9	2764.5	2990.7	3344.6	2451.7
Mixing and batching	52.2	52.2	52.2	52.2	52.2
Total	9942.8	10622.6	10571.2	10147.9	8844.4

2.6.3. Carbon Footprint. The CO2e results for concrete productions for 1-m^3 UHPC mixtures are listed in Tables 2.7. In the tables, and as shown from the embodied energy analysis, cement and steel fiber production accounts for most of the total CO2e in the investigated UHPC mixtures.

Table 2.7 GWP of in 1-m^3 UHPC mixtures (Unit: CO2e).

Phase	Reference	G50SF5	G50	FAC40SF5	FAC60
Sand	4.5	3.6	3.6	3.7	3.7
Fly ash	0	0	0	10.3	15.6
Ground blasted furnace slag	0	63.3	64.6	0	0
Silica fume	3.2	0.6	0	0.6	0
HRWR	22.2	53.7	41.4	39.1	18.4
Steel fibers	471.1	471.1	471.1	471.1	471.1
Cement	752.4	579.1	626.6	700.6	513.6
Mixing and batching	4.1	4.1	4.1	4.1	4.1
Transport to concrete plant	110.4	143.4	140.2	103.7	98.9
Total	1367.9	1318.9	1351.6	1333.2	1125.4
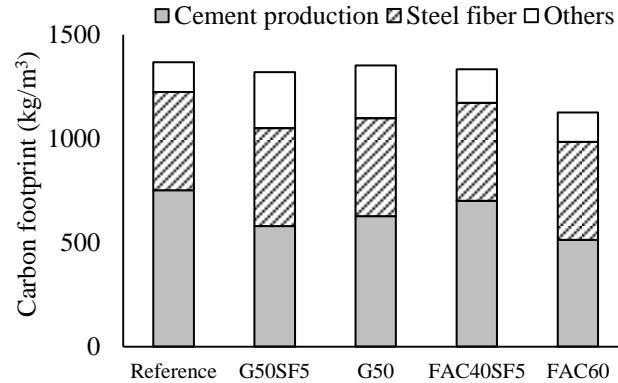
Figure 2.10. Carbon foot print results of the UHPC mixtures.

2.7. SUMMARY

A mix design methodology is presented for producing cost-effective UHPC with high-volume SCMs and conventional concrete sand. Based on the reported studies, the following conclusions can be drawn:

(1) The MWC can first be used as an indicator of the packing density of binders in wet condition to narrow down binder systems and reduce the required number of experiments. The binder composition of UHPC can then be optimized with consideration on the HRWR demand, rheological properties, MWC, RWD, and compressive strength properties. A radar chart can be then employed for the analysis. Based on this approach the following binder combinations were selected: G50, G50SF5, FAC60, and FAC40SF5.

(2) The second step is to determine the preliminary w/b based on the 28-d compressive strength and HRWR demand value for paste mixtures prepared with the optimum binder combinations with w/b values of 0.18–0.23. The optimum value for the selected binders was 0.20.

(3) The modified Andreasen and Andersen model can be used to optimize sand gradation. In this study, 70% river sand and 30% masonry sand were selected to achieve the highest packing density.

(4) The next step involves the determination of the binder-to-sand volume ratio (V_b/V_s). Mortar mixtures made with the selected w/b and G50SF5 binder were prepared with V_b/V_s values of 0.6, 0.7, 0.8, 0.9, 1.0, and 1.3. Based on flow properties and 28-d compressive strength, the optimum V_b/V_s was determined to be 1.0.

(5) The optimum fiber content for the UHPC is experimentally determined given the flowability and flexural properties of UHPC made with various fiber contents. For the steel fibers considered in this study, 2% fiber volume was selected.

(6) For the UHPC mixtures prepared with the various binder systems and optimized mixture proportioning, the UHPC mixtures were self-consolidating, stable, and had 28-d compressive strengths of 120-125 MPa under standard curing condition. The strength can reach up to 178 MPa by applying heat curing at a maximum temperature of 90 ℃ for one day followed by 7-d moist curing. For the selected UHPC mixtures, the 28-d splitting tensile strength, modulus of elasticity, flexural strength, and toughness (T150) were 11.6–14.3 MPa, 48.8–51.6 MPa, 20.2–21.3 MPa, and 50 ± 1.5 kN·mm, respectively.

(7) The designed UHPC mixtures exhibited relatively low autogenous shrinkage and drying shrinkage. The G50 mixture had the lowest autogenous and drying shrinkage of 255 μm/m at 28 d and 55 μm/m at 98 d, respectively. All tested UHPC mixtures exhibited a very high electrical resistivity and excellent frost durability.

(8) The unit cost per compressive strength of the UHPC mixtures designed with high volume of SCMs and concrete sand can range between 4.1–4.7 $/m^3/MPa. The mixture FAC60 was the most cost-effective mixture, which also developed better workability and lower unit cost per compressive strength of 3.7 ($/m^3)/MPa than other mixtures.

(9) The developed mixtures exhibited better sustainability compared with the reference mixture.

3. INTERNAL CURING OF UHPC BY LIGHTWEIGHT SAND

3.1. BACKGROUND

UHPC normally has extremely low water-to-binder ratio (w/b < 0.25) (Habel et al 2006). However, lacks of water and capillary pore space compromise the precipitation of hydration products, thus resulting in low degrees of hydration of cement, which is typically less than 50% (Justs et al. 2014). The unhydrated cement particles exist as expensive fillers that barely contribute to the development of mechanical properties. Besides, the low w/b leads to significant autogenous shrinkage, which tends to cause cracks in UHPC (Bao et al. 2015). The hydration products have smaller volume than the reactants, which results in chemical shrinkage. In a sealed curing condition, the hydration reactions consume water and reduce the internal relative humidity, i.e. self-desiccation, which increases the capillary tension in pore fluid and the compression on pore skeleton, resulting in autogenous shrinkage (Justs et al. 2015). Supplying additional water facilitates the hydration reactions and reduces self-desiccation. However, due to the low permeability of UHPC, limited amount of external curing water can penetrate the matrix and involve the hydration reactions. For such reasons, internal curing is a promising alternative to supply addition water for low w/b concrete to increase the degree of hydration (Bentz and Weiss 2011; De la Varga and Graybeal 2014).

Bentz et al. claimed that small inclusions dispersed in matrix store water during mixing and setting and then progressively release water for internal curing in the later hydration reactions (Bentz et al. 2005). De la Varga and Graybeal reported that supplying internal curing by utilizing pre-saturated lightweight aggregates resulted in a significant reduction in autogenous shrinkage of cementitious composites (De la Varga and Graybeal 2014). Justs et al. used superabsorbent polymer as an internal curing agent to reduce the autogenous shrinkage of UHPC (Justs et al. 2015). Rice husk ash was also proven to be a good internal curing agent and pozzolanic material for UHPC (Van et al., 2014; Nguyen, 2011). Internal curing has been gaining wide acceptance as an effective way to reduce shrinkage of high-performance concrete (Hwang et al. 2012; Bentur et al. 2001). However, employment of superabsorbent polymers was reported to significantly reduce the workability (Beushausen and Gillmer 2014) and compressive strength of concrete

(Justs et al. 2015). Mechtcherine et al. (2009) achieved complete autogenous shrinkage reduction by applying internal curing with superabsorbent polymers to a reference UHPC that experienced high autogenous shrinkage, which was about 1100 μm/m at 7 days (d). However, the high dosages of superabsorbent polymers, which were necessary to significantly reduce shrinkage, reduced the compressive strength from 150 MPa to lower than 100 MPa. Zhutovsky and Kovler (2009) claimed that the presence of excessively additional pores in internally cured concrete may cause reduction in the compressive strength. Habeeb and Fayyadh (2009) stated that fine rice husk ash increased the compressive strength of concrete but it also increased the autogenous shrinkage. Past studies in the literature indicate a trade-off between the mechanical properties and autogenous shrinkage of concrete with use of superabsorbent polymer or rice husk ash. On the other hand, lightweight aggregates were found to offer more effective and longer internal curing than superabsorbent polymers (Weiss et al. 2012). However, limited information is available on the effectiveness of lightweight sand (LWS) for internal curing of UHPC. There is a concern that the relatively large particle size of lightweight sand can potentially have adverse effect on mechanical properties of UHPC.

3.2. MATERIALS AND TEST METHODS

The materials investigated and test methods are introduced below:

3.2.1. Materials. Type III Portland cement, Class C fly ash (FAC), and silica fume (SF), well-graded river sand (NS), masonry sand (MS), and expanded shale LWS were employed to produce UHPC. The chemical compositions and physical characteristics of these materials are listed in Table 3.1.

The particle size distributions of the three types of sand (NS, MS, and LWS)are showed in Figure 3.1. The water absorption values of NS and MS were respectively measured to be 0.14% and 0.06% in accordance with ASTM C128. The water absorption value of LWS after soaking in water for 24 h and the relative desorption of the LWS using centrifuge method was determined to be 17.6% and 96.4%, respectively, in accordance with ASTM C1761. The 72 h water absorption was also measured as 18.4%. In addition, Henkensiefken et al. (2008) reported that 96% of water in this type of LWS was lost at a 92% RH, implying that water can be effectively transported from the LWS to cement paste at a high RH for internal curing. The moisture content of the bulk LWS

was measured in accordance with ASTM C128. The rest amount of water to be added in the LWS was calculated by subtracting the water content in the LWS from the total water demand of the LWS to secure a saturated-surface-dry (SSD) condition. After adding the rest amount of water to the LWS, the LWS was homogenized with water and then placed in a sealed plastic bag for 24 h before batching to secure the SSD condition (Bentz and Weiss 2011; Hwang et al. 2012). A polycarboxylate-based high-range water reducer (HRWR) and air de-training admixture was employed. Steel fibers with 0.2 mm in diameter and 13 mm in length were incorporated. The tensile strength and modulus of elasticity of the fibers were 1.9 and 203 GPa, respectively.

Table 3.1 Chemical and physical properties of cementitious materials and selected sands.

	Type III cement	Class C fly ash	Silica fume	Missouri river sand	Masonry sand	Lightweight sand
SiO_2(%)	19.72	36.50	95.50	80.30	86.50	57.60
Al_2O_3(%)	5.10	24.80	0.70	10.50	0.39	19.40
Fe_2O_3(%)	2.76	5.20	0.30	3.43	1.47	9.60
CaO (%)	64.50	28.10	0.40	1.72	9.42	3.40
MgO(%)	2.30	5.00	0.50	1.70	0	2.60
SO_3(%)	3.25	2.50	–	1.07	0	0.60
Na_2O eq. (%)	0.33	–	0.40	–	–	5.60
C_3S (%)	65.23	–	–	–	–	–
C_2S (%)	7.33	–	–	–	–	–
C_3A (%)	8.85	–	–	–	–	–
C_4AF (%)	8.40	–	–	–	–	–
Loss of Ignition (%)	1.50	0.50	2.00	1.28	0.24	–
Blaine surface area (m^2/kg)	562	465	–	–	–	–
B.E.T. (m^2/kg)	–	–	18,200	–	–	–
Specific gravity, SSD	3.15	2.70	2.20	2.65	2.64	1.80
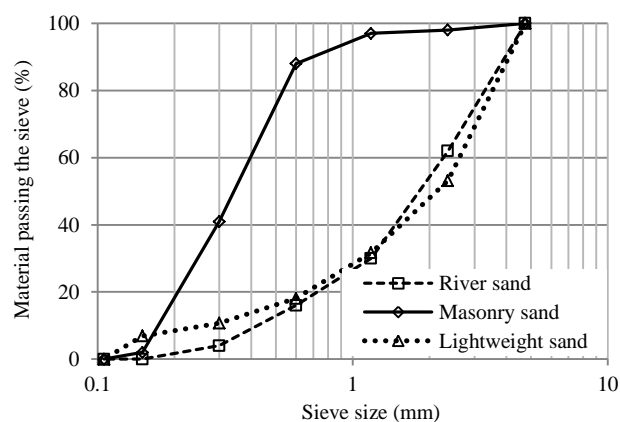
Figure 3.1. Sieve analyses of investigated sand.

3.2.2. Experimental Methods. The test methods of fresh and hardened properties of investigated UHPC are detailing below:

3.2.2.1 Mixing, casting, and curing of UHPC. A 19-L Horbart mixer was employed to prepare the UHPC mixtures in six steps: (1) homogenizing sand at 60 rpm for 60 s; (2) mixing dry cementitious materials at 60 rpm for 2 min; (3) adding 90% of the mixing water and HRWR and mixing at 120 rpm for 3 min; (4) introducing the rest of water and HRWR and mixing at 120 rpm for 5 min; (5) micro steel fibers were gradually added within 1 min at 60 rpm; and (6) the final mixing at 120 rpm for 2 min was applied. Given the self-consolidating property, all specimens were cast in one lift without mechanical consolidation. The specimens were immediately covered with wet burlap and a plastic sheet after casting, demolded after 1 d, and then cured in lime-saturated water at room temperature until the age of testing.

3.2.2.2 Heat of hydration. The rate and extent of hydration were monitored using an isothermal conduction calorimeter (Calmetrix I-CAL 8000), which was programmed to maintain the sample at a constant temperature of 20 °C ± 0.1 °C. About 75 g of fresh mixture was sealed in a plastic vials and placed into the calorimeter. The heat of hydration data were continuously measured from 2 min after completion of mixing the UHPC and continued for 72 h. The calorimetry results were normalized by mass of the binder.

3.2.2.3 Internal relative humidity. UHPC prism specimens measuring $75 \times 75 \times 285$ mm were prepared for IRH measurement. Two holes were created in each of the UHPC specimens by placing two plastic tubes in the formwork at a depth of 40 mm, which was the optimum depth to obtain stable and repeatable readings of IRH (Mehdipour and Khayat 2017). A rubber rod, of which the diameter is the same as the inner diameter of the tubes, was inserted in each tube to prevent intrusion of fresh concrete in the tube during placement. At final setting, the rubber rod was removed and a rotary drill was used to break the surface at the bottom of the hole. Then, a calibrated humidity sensor with a rubber cap to cover the top of the hole was then put in the hole to measure IRH until the age of 168 h. All specimens were sealed with multiple layers of aluminum tape and stored in a temperature and humidity controlled room at 23 °C ± 1°C and 50% ± 3% RH.

3.2.2.4 Autogenous shrinkage. Autogenous shrinkage was measured according to ASTM C1698. Shrinkage measurements were carried out starting at the final setting and at 12 h of age, then on daily basis for the first week and on weekly basis until the age of 28 d. Samples were cast in corrugated plastic tubes and stored at constant temperatures of 23 °C ± 1 ºC and 50% ± 1% RH immediately after casting.

3.2.2.5 Fresh and hardened properties of UHPC. The unit weight and mini slump flow values of fresh UHPC mixtures were measured in accordance with ASTM C138 and ASTM C230/C230M, respectively. The flow time was measured using a mini V-funnel according to EFNARC recommendations .The initial and final setting times were tested in accordance with ASTM C403. The compressive strengths at 1, 7, 28, and 91 d were evaluated using 50-mm cubes according to ASTM C109. The Young's modulus at 28 d was evaluated in accordance with ASTM C469. Flexural properties were evaluated using prism specimens measuring $305 \times 76 \times 76$ mm in accordance with ASTM C1609 at 28 d. Three samples replicates were prepared for each test. The average results are reported.

A ConTec Viscometer 5 was employed to test the dynamic yield stress (τ_0) and plastic viscosity (μ_p) of the UHPC mixtures. The viscometer is a wide gap concentric cylinder rheometer with an inner cylinder radius of 100 mm and an outer cylinder radius of 145 mm. The measurements were started 10 min after water was added in the mixer. The test started with a pre-shear period of 25 s at a rotational velocity of 0.5 rps, followed by a stepwise decrease in rotational velocity from 0.5 to 0.025 rps within ten 5-s steps. The torque and velocity were recorded by the rheometer. The yield stress and plastic viscosity were calculated using the Bingham fluid model (Tattersall and Banfill 1983)

3.2.2.6 Materials characterization. Thermogravimetric (TG) analysis was carried out using a thermal analyzer (Netzsch STA 409 PC) to evaluate the effect of LWS on hydration kinetics of cementitious materials. Mass loss versus temperature curve was obtained to indicate the degree of hydration and phases present in the UHPC. For each mixture, a UHPC specimen measuring approximately $25 \times 25 \times 25$ mm was grounded into fine power with a maximum grain size of 63 μm. Sand was included in the power and steel fibers were excluded. Then, powder sample weighing about 100 mg was heated to 1000 ºC in a nitrogen atmosphere at a heating rate of 10 ºC/min, with continuously

measured mass loss of the test sample. For each mixture, three different power samples from three different specimens were tested, and their average result is reported. In addition, TG tests of river sand, masonry sand, and lightweight sand were conducted and considered in the analysis.

The total porosity and pore size distribution of the samples were determined using mercury intrusion porosimetry (MIP). For each investigated UHPC mixture, three samples measuring approximately $5 \times 5 \times 5$ mm were tested. In the MIP testing, the applied low and high pressures were 0.28 and 414 MPa, respectively; the contact angle was 140º; the surface tension was 480 mN/m. For both the TG and MIP evaluations, the hydration reactions of UHPC samples were terminated at 28 d by soaking the samples in 99.8% isopropyl alcohol and drying at 50 ºC in an oven for 24 h before examination.

Small cube samples were carefully cut from intact bulk UHPC using a diamond saw for scanning electron microscope (SEM) analysis. The samples were prepared in accordance with ASTM C1723. All the UHPC were impregnated with a low viscosity epoxy to stabilize the microstructure during sample preparation. The impregnation involves evacuating air and other gasses and filling cracks and pores with epoxy, all while the specimen is under a vacuum. The impregnation was followed by cutting, lapping, and polishing the samples. Before examination, the samples were rinsed using 99.8% isopropyl alcohol, oven dried at 50 ºC for 24 h, and then coated with a very thin layer of gold for conduction.

3.3. EFFECTS OF SATURATED LIGHTWEIGHT SAND CONTENT ON KEY CHARACTERISTICS OF UHPC

In this part, LWS is for the first time employed as an internal curing agent to prepared UHPC, aiming to reduce autogenous shrinkage and increase mechanical properties. The mechanisms of the effects of LWS on material properties of UHPC are systematically evaluated. The kinetics of cement hydration, evolution of internal relative humidity (IRH), autogenous shrinkage, compressive and flexural properties, and microstructure were investigated for UHPC mixtures with LWS contents between 0 to 75% substitutions by volume of river sand. It is expected that LWS with coarse pore structure and well-interconnected pore can rapidly release water from the reservoirs while the IRH is still high. Self-desiccation and autogenous shrinkage can be alleviated, and the

degree of hydration of cement can be increased, in particular, for concrete that has high cement content and low w/b. Knowledge gained in this study can be used to develop mix design guidelines and curing provisions to promote a wider acceptance of LWS as a key component for UHPC with reduced shrinkage.

3.3.1. Mixture Design. In this study, a UHPC mixture designed by the authors in a previous study was used for the reference mixture (Meng et al. 2017). For the binder, the volume percentages of cement, FAC, and SF were 55%, 40%, and 5%, respectively. The contents of MS and NS for the reference mixture were 30% and 70%, respectively, of the total sand volume. The binder-to-sand ratio (b/s) was 1:1, by volume. The w/b was fixed at 0.20, by mass. The mixture designs are listed in Table 3.2. The dosages of active solid component of HRWR and air de-training admixture were fixed at 1% and 0.8%, respectively, by mass of binder. The volume fraction of 2% of steel fibers was incorporated in all investigated mixtures.

Table 3.2 Investigated UHPC mixtures.

Code	LWS/(NS+LWS), (vol. %)	Cement (kg/m^3)	FAC (kg/m^3)	SF (kg/m^3)	MS* (kg/m^3)	NS* (kg/m^3)	LWS* (kg/m^3)
LWS00	0					703	0
LWS12.5	12.5					615	60
LWS25	25.0	663	367	42	308	527	120
LWS37.5	37.5					440	180
LWS50	50.0					352	240
LWS75	75.0					176	360

A theoretical model was presented in ASTM C1761 to predict the minimum amount of internal curing agent required to provide additional water to counteract the effects of self-desiccation and chemical shrinkage during the hydration of cement paste (Bentz and Snyder 1999). Water introduced by internal curing agent is gradually released to sustain a relatively high IRH, and ensures the capillary porosity in the cement paste is water-filled at the maximum degree of hydration. The hydration reactions of cement are terminated due to lack of space for precipitation of hydration products (Jensen and Hansen 2001, Bentz and Snyder 1999). The presented model has been applied in various concretes and demonstrated great effectiveness (De la Varga and Graybeal 2015; Bentz and Weiss 2011). In this study, the chemical shrinkage of the reference mixture was determined to be 0.055 g of water/g of cement, according to ASTM C1608; the saturation

degree of LWS was measured to be 1.0. Given a w/b of 0.20, the maximum potential degree of hydration of cement was calculated to be 0.50 according to the model (Bentz and Synder 1999). Thus, the minimum percentage of NS to be replaced by LWS for compensating the chemical shrinkage and maintaining SSD condition of concrete at the maximum hydration degree was calculated to be 25%, by volume, using the model recommended in ASTM C1761.

However, Justs et al. (2015) claimed that the model for determination of internal curing agent content might not allow appropriate prediction for that of UHPC. Because the amount of internal curing agent calculated using the model was insufficient to prevent self-desiccation and compensate chemical shrinkage (Justs et al. 2015). The reason was likely because the pores of the internal curing agent that provided additional space for precipitation of hydration products were not taken into account in the model. The space introduced by internal curing agent might be insignificant for normal concrete, but for UHPC that has very low w/b and limited space for precipitation, the additional space could allow a higher degree of hydration, which could not be neglected. For this reason, a greater amount of internal curing agent may be required. In addition, the travel distance of internal curing water is limited in UHPC due to the low permeability associated with the very low w/b. The content of internal curing agent may need to be carefully considered to ensure that a majority of the paste is within the travel distance of curing water. Under such circumstances, investigations on LWS with higher volume fraction ($\geq$ 25%) for internal curing of UHPC are highly desired. Therefore, a wide range of LWS/(NS+LWS), referred to as LWS content, from 0 to 75% were considered in this study.

3.3.2. Fresh and Hardened Properties. Table 3.3 summarizes the fresh and hardened properties of the investigated UHPC mixtures.

All of the investigated mixtures appeared to be self-consolidating and stable with mini-slump spread values that were no less than 275 mm. As the LWS content was increased from 0 to 75%, the unit weight gradually decreased from 2.5 to 2.3, which can be attributed to the relatively low unit gravity of LWS, as shown in Table 3.1. The mini slump value was slightly increased from 275 to 290 mm with the addition of LWS. However, the mini V-funnel flow time was considerably reduced from 40 to 12 s, when

the LWS content was increased from 0 to 75%, indicating substantial drop in plastic viscosity. Both the initial and final setting times increased gradually with the increase of LWS. The initial and final setting times of the LWS75 mixture were 8.2 and 16.2 h, respectively, compared with 5.6 and 9.0 h of the reference mixture.

As the LWS content was increased from 0 to 75%, the compressive strength at 1 d was reduced from 80 to 60 MPa. However, the LWS50 mixture achieved the highest 7-d compressive strength, which was 12% higher than that of the LWS00 mixture. At 28 d and 91 d, the LWS25 mixture achieved the highest compressive strengths that were about 22% greater than the corresponding compressive strengths of the LWS00 mixture. As the LWS content was increased from 0 to 75%, the 28-d Young's modulus was reduced from 52 to 40 GPa.

Table 3.3 Fresh and hardened properties of the UHPC mixtures with different LWS contents.

	LWS00		LWS12.5		LWS25		LWS37.5		LWS50		LWS75	
	Mean	SD*	Mean	SD	Mean	SD	Mean	SD	Mean	SD	Mean	SD
Unit weight (g/cm^3)	2.50	0.04	2.46	0.0.02	2.42	0.01	2.38	0.0.03	2.34	0.02	2.30	0.05
Mini slump flow (mm)	275	2.0	280	1.3	285	1.6	290	1.8	290	2.0	290	3.0
Mini V-funnel flow time (s)	40	1.0	32	0.6	26	1.2	21	0.5	18	0.6	16	0.4
Initial setting time (h)	5.6	0.1	5.9	0.1	6.4	0.1	6.6	0.2	7.0	0.2	8.2	0.2
Final setting time (h)	9.0	0.0.2	10.6	0.2	12.1	0.2	13.2	0.3	14.0	0.2	16.2	0.1
1-d compressive strength (MPa)	80	1.5	77	2.0	75	1.6	72	2.3	70	1.8	60	1.4
7-d compressive strength (MPa)	122	0.9	127	1.0	135	0.8	136	0.9	137	1.2	129	0.8
28-d compressive strength (MPa)	130	0.5	140	0.5	158	0.4	142	0.5	140	0.7	130	0.6
91-d compressive strength (MPa)	138	0.5	149	0.6	168	0.3	146	0.4	140	0.6	130	0.5
28-d Young's modulus (GPa)	52	0.5	52	0.5	51	0.5	47	0.4	44	0.6	40	0.8
28-d flexural strength (MPa)	21	1.2	23	1.3	24	1.5	16	0.9	15	0.8	9	0.6
28-d toughness-T150 (J)	51	1.8	54	2.0	57	2.5	33	1.6	31	1.3	18	0.9

Figure 3.2 shows the load-deflection relationships of the UHPC mixtures, which demonstrated ductile and strain-hardening behaviors. The LWS25 mixture achieved the largest flexural strength, which was 24 MPa and 14% higher than that of the LWS00 mixture. The area under load versus deflection curve between the deflection values of 0 and L/150 (L = 202 mm) is referred to as T150, which represents the toughness and is an indicator of energy dissipation. The LWS25 mixture achieved the largest T-150 toughness, which was 57 J and12% higher than that of the LWS00 mixture. Therefore,

based on the mechanical properties, the LWS25 mixture offered the best overall performance.
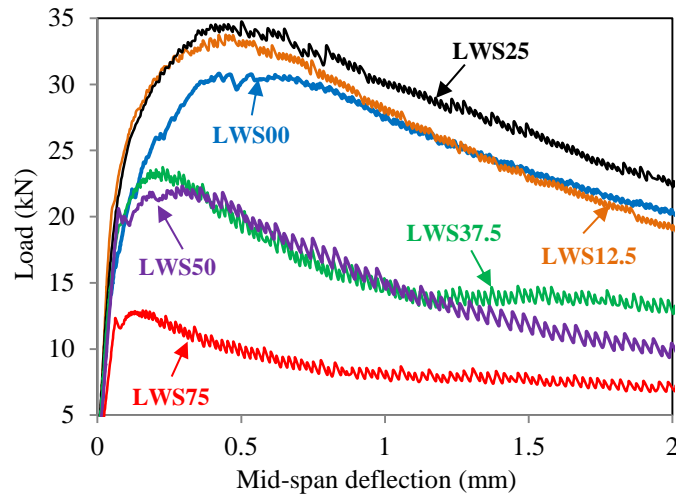
Figure 3.2 Load-deflection relationships of the investigated UHPC mixtures.

3.3.3. Internal Relative Humidity and Autogenous Shrinkage. Figure 3.3(a) shows the evolution of IRH of the UHPC mixtures for a period up to 168 h.

Within the first 24 h, the reduction in IRH is 12% in the reference mixture (i.e. LWS00) without any LWS due to consumption of water in hydration, while the reduction is only 0.2% in the LWS75 mixture with a LWS content of 75%, given the presence of internal curing water in LWS. However, it is remarked that even with 75% of LWS, the saturation condition (IRH = 100%) should not be expected. The IRH at 72 h was about 85% in the LWS00 mixture and 97% in the LWS75 mixture. Similar phenomenon of reduction in IRH with use of high volume internal curing agent was observed by other researchers using superabsorbent polymer to prepare UHPC, and the primary reasons why the saturation condition was not sustained were believed to be associated with the extremely low w/b of UHPC and the extra hydration precipitation space provided by the pores of internal curing agent, as elaborated in the section of Mixture Design.

The autogenous shrinkage of the UHPC mixtures is shown in Figure 3.3(b). As the LWS content is increased from 0 to 75%, the autogenous shrinkage is reduced from 489 to 196 μm/m (by 60%), which represents a significant reduction. The reduction in autogenous shrinkage is primarily because the IRH is sustained at a relatively high level,

mitigating the self-desiccation. Another observation is that the autogenous shrinkage is not completely eliminated, even with the use of a high LWS content (75%). This is because the self-desiccation is not eliminated, due to the fact that the IRH is not sustained at 100% over time, even with a LWS content of 75%, as shown in Figure 3.3(a).
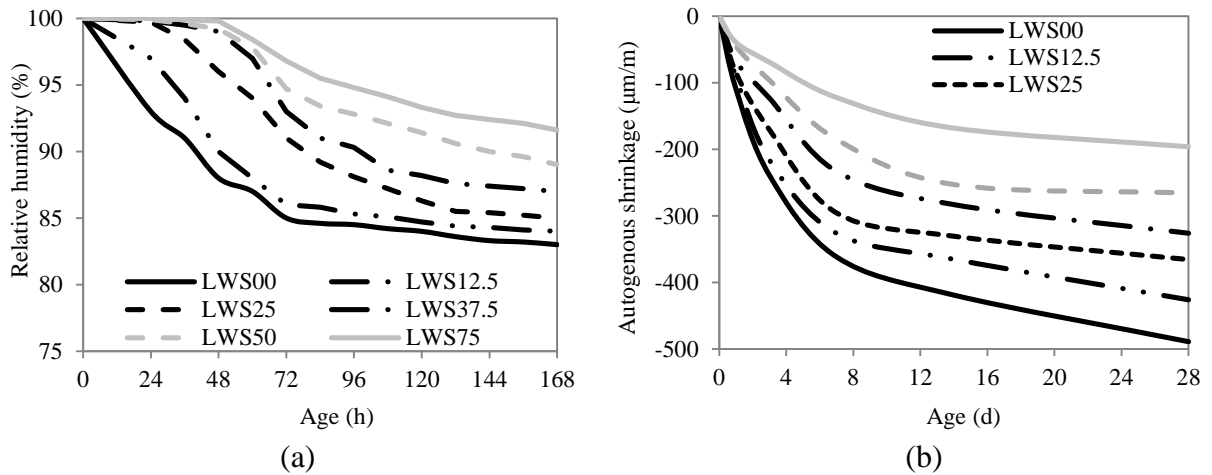
Figure 3.3. Experimental results of relative humidity and autogenous shrinkage: (a) IRH in the first 7 d and (b) autogenous shrinkage in the first 28 d.

Figure 3.4 plots the relationship between IRH and autogenous shrinkage. Autogenous shrinkage decreased with IRH, following a parabolic equation with a coefficient of determination (R^2) of 0.96. A relatively high IRH was sustained by using the pre-saturated LWS that was incorporated to reduce the autogenous shrinkage of the UHPC mixtures.
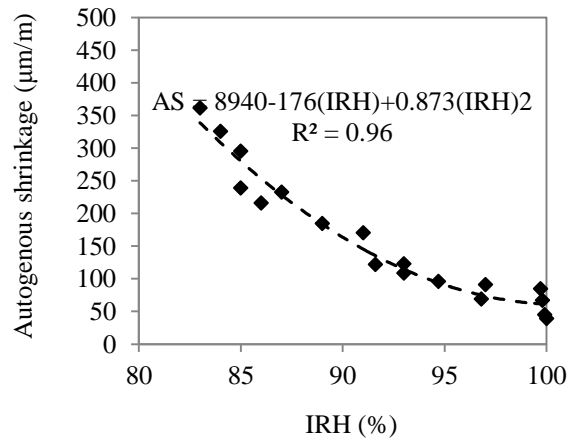
Figure 3.4. Correlation of IRH and autogenous shrinkage (AS) up to 7 d.

3.3.4. Radar Chart Analysis. Figure 3.5(a) plots a multivariate radar chart to select the optimum UHPC mixture.

The plot consists of a sequence of equi-angular spokes (radii), and each spoke represents one variable. The length of each spoke is proportional to the magnitude of the corresponding variable. Each variable is assigned with a specific weight factor. The data points of each spoke are sequentially connected, forming an enclosed area for each of the mixtures. A larger area indicates a better overall performance of the mixture. The optimum mixture is expected to have good flowability (high mini slump spread value and low mini V-funnel flow time), high mechanical properties, and low autogenous shrinkage. The assigned weight factors for the mini slump flow, mini V-funnel flow time, compressive strengths at 1 d, and Young's modulus at 28 d was 1. And the weighted factors was assigned to 2 for compressive strength at 91 d, flexural strength and toughness at 28 d, and autogenous shrinkage at 28 d. Figure 3.5(b) shows the areas obtained from the radar charts of the mixtures. A higher value represents a better performance of the corresponding UHPC mixture. The LWS25 mixture had the largest area, followed by LWS12.5, LWS50, LWS75, LWS37.5, and LWS00 mixtures. The LWS25 mixture can therefore be considered as the optimum UHPC mixture.
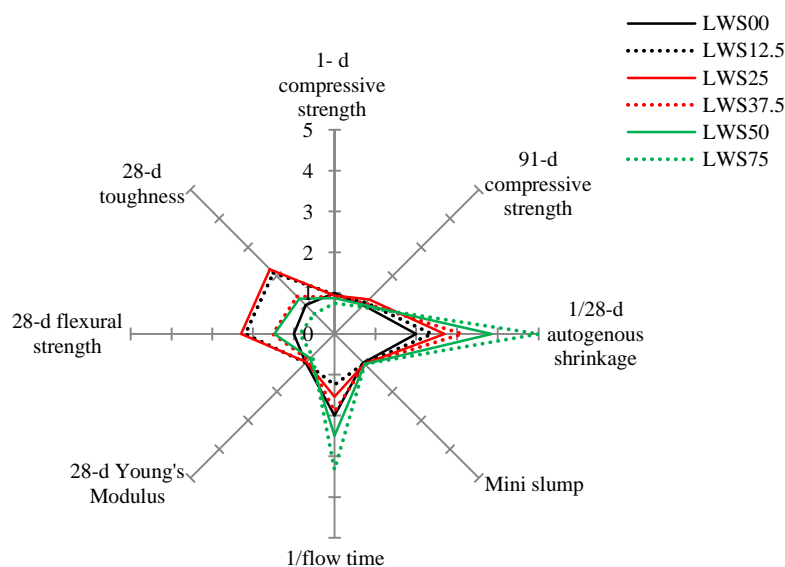
(a)

Figure 3.5. Radar chart analysis: (a) radar chart and (b) enclosed areas.
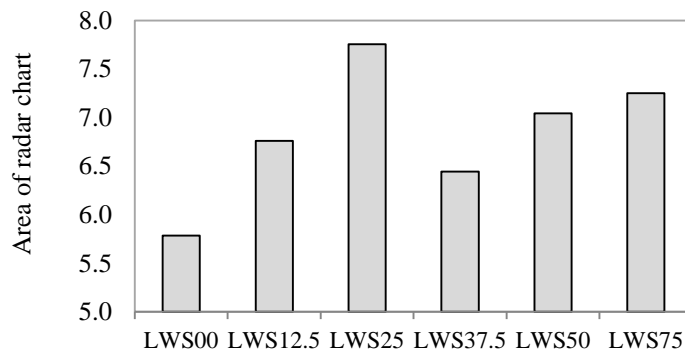
(b).

Figure 3.5. Radar chart analysis: (a) radar chart and (b) enclosed areas. (cont.)

3.3.5. Heat of Hydration. As shown in Figure 3.6(b), the LWS content does not have significant effect on the cumulative heat of hydration within the first 15 hours after mixing; however, after 15 hours, the use of LWS greatly increases the cumulative heat, and thus increases the degree of hydration of the UHPC mixtures with LWS. The increased degree of hydration leads to more hydration products, which in turn contribute to the development of strength. Such effect of LWS tends to offset its effect to reduce strength due to the initial additional porosity introduced by LWS. This is indeed reflected in compressive strength gain of UHPC with LWS up to 25% at 28 d and 91 d (see Table 3.3). However, beyond a LWS content of 25%, the compressive strength decreased with the LWS content. The mechanism of such decrease phenomenon is discussed later.

(a)   (b)
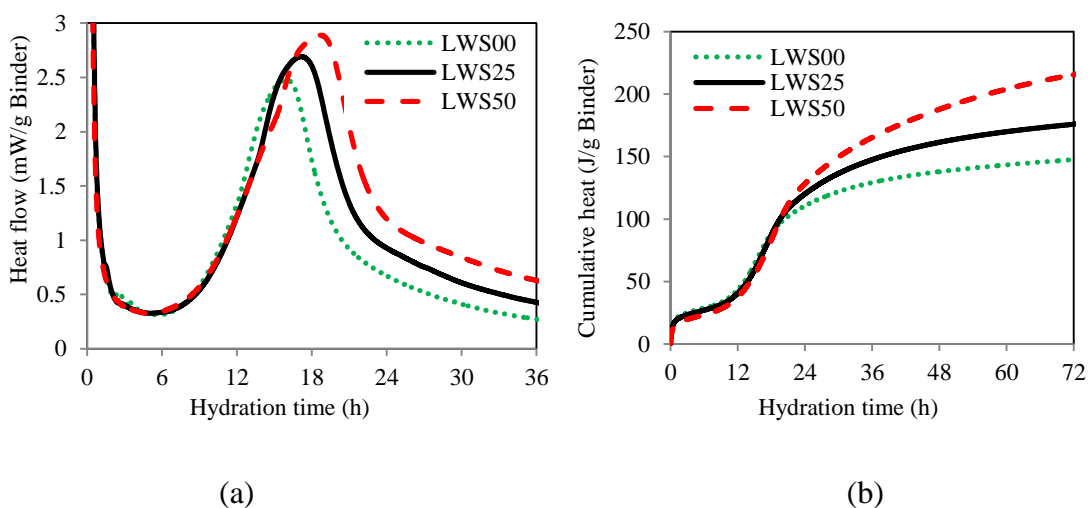
Figure 3.6. Isothermal calorimetry results of cementitious materials at 20 ℃ for the UHPC mixtures: (a) hydration heat flow; (b) cumulative heat.

3.3.6. Thermal Analysis. The TG curves of the LWS00, LWS25, and LWS50 mixtures at 28d are plotted in Figure 3.7. The TG curves of the three mixtures followed similar trends of mass loss. Three sudden mass loss events occurred at about100, 450, and 680 ℃, respectively, for all the investigated UHPC mixtures. The mass loss events are attributed to evaporation of free water at about100 ℃, dehydroxylation of $Ca(OH)_2$ at about 450 ℃, and decomposition of $CaCO_3$ at about 680 ℃ (Yu et al. 2014). Overall, the mass loss increased with the LWS content, which implies that more $Ca(OH)_2$ was produced and carbonated in the mixtures that contained more LWS.
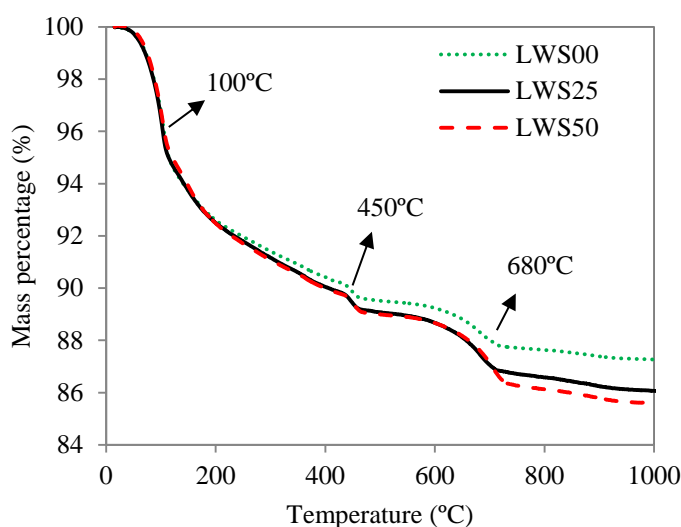
Figure 3.7. TG test results of UHPC samples at 28 d.

In the TG tests of raw materials, the percentages of the mass loss of the river sand, masonry sand, and LWS between 380 and 550 ℃ are used to characterize the mass loss at the 450 ℃ level, and their values are 0.06%, 0, and 0.14% respectively.

Since the UHPC specimens used for TG test were ground into very fine power, the samples for TG test are considered to be homogenous in terms of sand content. Thus, the mass loss between 380 and 550 ℃ due to the three types of sand can be removed from the total mass loss shown in Figure 3.7. The remaining mass loss represents the amount of non-evaporated water per gram of binder at the 450 ℃ level, which is an indicator of the amount of hydration products in the hardened UHPC specimens with different LWS contents.

Figure 3.8 shows the changes of mass loss due to non-evaporated water at the 450 ºC level with the LWS contents. As the LWS content was increased from 0 to 25%, the value of mass loss of non-evaporated water was increased from 0.09 to 0.107 g H_2O/g binder (by 19%). As the LWS content was increased from 25% to 50%, the value of mass loss of non-evaporated water was increased to 0.111 g H_2O/g binder (by 4%). The majority of the mass loss was achieved by the LWS25 mixture. The increases in mass loss implies that more $Ca(OH)_2$ was produced in hydration due to the use of more LWS.
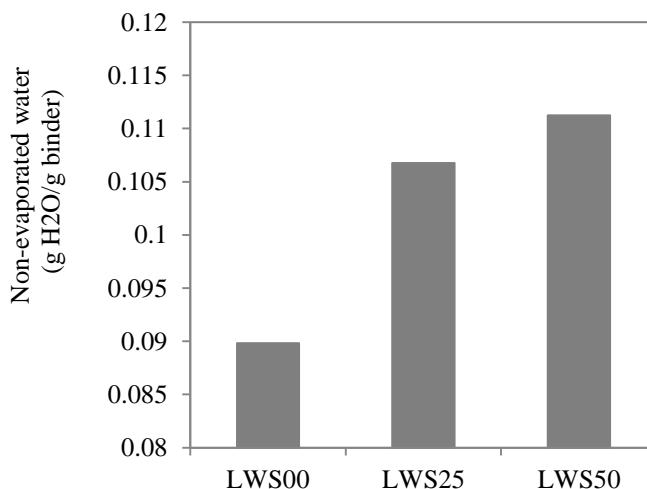
Figure 3.8. Non-evaporated water of investigated UHPC mixtures at 28 d.

3.3.7. Pore Structure. Figure 3.9(a) shows the pore size distribution of the UHPC mixtures covering pores with apparent diameter of 4 nm to 105 μm. A peak was observed for each of the three curves with pore diameters in between 10 and 50 nm.

The peak corresponding to the most probable diameter shifted towards finer pore sizes and the value was increased from 0.018 to 0.046 cc/g as for LWS was increased from 0 to 50%. Figure 3.9(b) plots the cumulative porosity results, which shows that the total porosity is reduced by about 20% as the LWS increased from 0 to 25%, the total porosity increased by about 100% for LWS increased from 25% to 50%.

The results of pore size distribution, including gel micro-pores (< 10 nm), capillary pores (10–5000 nm), and macro-pores (>5000 nm), are summarized in Figure 3.10. The porosity of gel micro-pores, which are mainly influence the shrinkage behavior of concrete, is more than 50% of the total porosity, thus dominating the pore structure.

For capillary pores, which significantly affect the mechanical behavior of concrete, decreased when LWS content increased from 0 to 25% and then increased when LWS content increased from 25% to 50%. The reduction in capillary pores of LWS 25 resulted in higher performance in all the mechanical properties, compared with that of UHPC without LWS or 50% LWS.

(a)   (b)
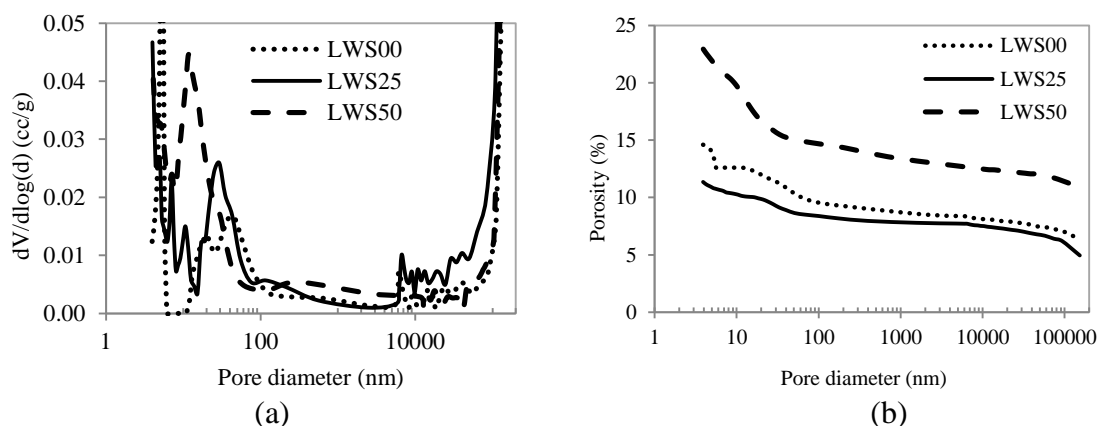
Figure 3.9. Effect of LWS content on (a) pore size distribution and (b) porosity of UHPC after hydrating 28 d.
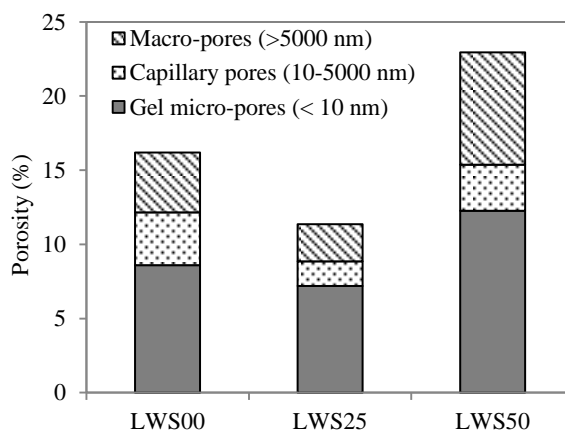
Figure 3.10 Effect of LWS content on pore parameters.

Significant effects of the LWS content on porosity are demonstrated. Intuitively, to increase the LWS content leads to an increase in the total porosity due to the porous structure of LWS. However, as the LWS content was increased from 0 to 25%, the total porosity was reduced by 18%. The reduction total porosity to some extent explains the

increases in compressive strengths at 28 and 91 d (see Table 3.3) (Mehta 1986). The increase in capillary pores (10–5000 nm) can be attributed to the promoted degree of hydration due to the use of LWS (see Figure 3.8), since capillary pores are mainly present among hydration products. The reduction in total porosity might be due to three mechanisms: (1) LWS promoted the hydration reactions and led to refined microstructures. (2) The hydration products filled a significant part, if not all, of the pores introduced by the LWS. (3) The hydration products partially sealed the surface pores of the LWS, preventing intrude of mercury in MIP measurement and leading to a reduction in the measured porosity.

As the LWS content was increased from 25% to 50%, the total porosity was increased by 110%. The effects to reduce the total porosity and macro pores were overwhelmed due to the addition of excessive amount of LWS. The additional water and space introduced by LWS increases the degree of hydration, thus increasing the capillary pores. Due to the excessive amount of water released from the LWS, a matrix that is not as dense and impermeable as that of the LWS25 tends to form, in particular, at the zones close to LWS. The less impermeable matrix has larger porosity. Besides, increasing LWS content introduces more pores in UHPC and decreases the Young's modulus, and thus led to considerable reduction in compressive strengths, in spite of the slightly increased degree of hydration.

3.3.8. Image Observation. Figures 3.11(a) and 3.11(b) illustrate the interface between matrix and sand particles embedded in the cementitious matrix of LWS25 UHPC. Compared with the river sand, lightweight sand is porous, as depicted in Figure 3.11(a). While a distinct interface can be observed between the relatively smooth river sand and the matrix, as shown in Figure 3.11(b), there is not a well-defined interface between LWS and matrix, because of the uneven and porous surface of LWS. The matrix seems to encapsulate the LWS, forming a well-integrated sand-matrix interface. The existence of the large quantities of voids indicates that the hydration products did not fill all the internal voids of LWS.

To corroborate the above statement, an energy dispersive spectroscopy (EDS) image corresponding to Figure 3.11(a) is shown in Figure 3.11(c). According to the chemical compositions (Table 3.1), the SiO_2 content in the LWS is much higher than that

in cement, while the chemical composition of cement is dominated by CaO. Therefore, elementary mappings of Si (representing LWS) and Ca (representing cement matrix) could enable a clearer observation of the interaction between these two phases. The hydration products of cement, most likely C-S-H gel, protrude into the micro-pores in the LWS. On one hand, the nano-porous C-S-H gel tends to seal the surface of the lightweight sand particles, and separate the micro-pores inside from the well-connected capillary network in the matrix.
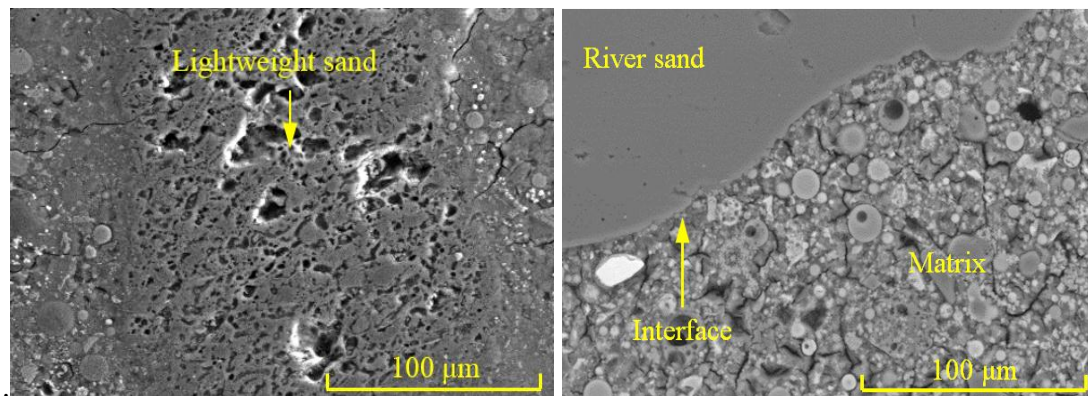
(a)   (b)
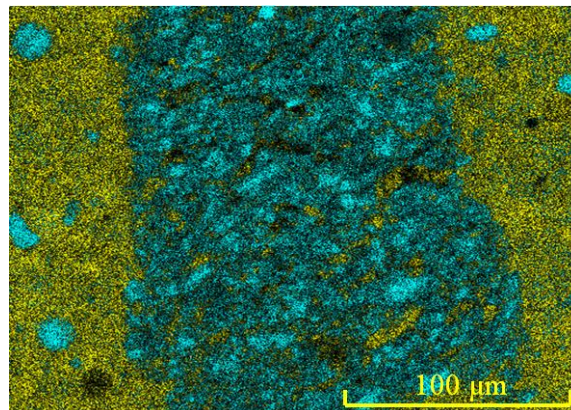
(c)

Figure 3.11. SEM pictures of interfaces between sand and matrix of LWS25: (a) lightweight sand at 500X, (b) river sand at 500X, and (c) elementary mapping of (a), where cyan color indicates Si and yellow color indicates Ca.

This explains the almost equal porosities of LW25 and LW00 mixtures as characterized by MIP. On the other hand, such an inter-penetrated microstructure eliminates the interfacial transition zone between the LWS and matrix, strengthens the LWS, and tends to enhance the interfacial bonding strength, thus enhancing the mechanical properties of UHPC. However, when more than 25% of LWS was used in UHPC, the pores introduced by LWS might be overwhelmed (as shown in MIP results), and thus reduced the mechanical properties (Table 3.3).

The interface between steel fiber and UHPC matrix was also examined. Large amount of inter-connected micro cracks and inter-particle voids near the steel fiber were observed in the LWS00 (Figure 3.12(a)). This may be attributed to relatively low degree of hydration and high autogenous shrinkage that lead to micro cracking (Bao et al. 2015). Figure 3.12(b) shows steel-matrix interface of LWS25 mixture. The matrix is in good contact with the steel fiber at the interface, a more densified matrix is demonstrated, and reduced numbers of micro cracks are observed. This to some extent explains why the first cracking strength and post cracking behavior of the LWS25 mixture were improved compared with those of the LWS00 mixture.

(a)   (b)
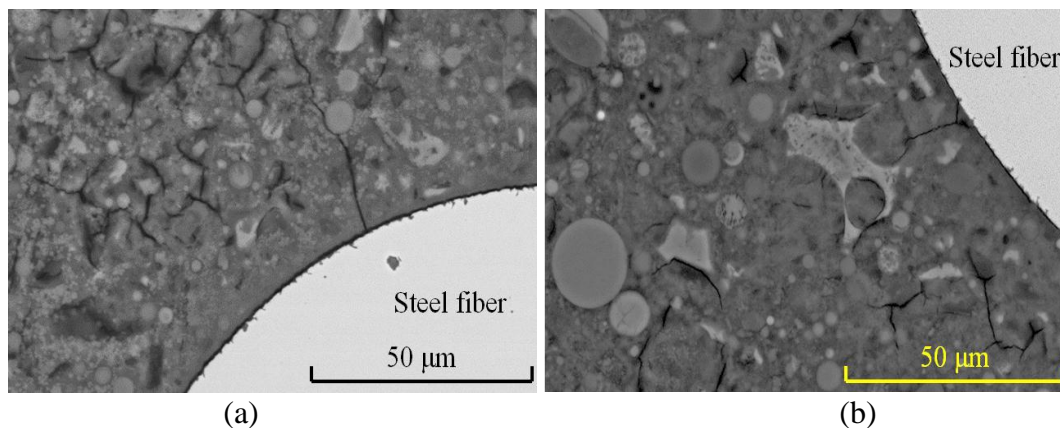
Figure 3.12. SEM pictures of interfaces between the steel fiber and matrix: (a) LWS00 at 1000X; (b) LWS25 at 1000X.

3.4. OPTIMIZATION OF UHPC USING LIGHTWEIGHT SAND BY FACTORIAL DESIGN APPROACH

In this part, a statistical fractional factorial experimental design approach was employed to evaluate the influence of the primary mix design parameters and their

coupling effects on the key material properties of UHPC. The investigated key mix design parameters included the w/b, lightweight sand replacement ratio (LWS/NS), and cementitious materials-to-sand ratio (b/s). The key material properties of UHPC included the flow time, plastic viscosity, high-range water reducer (HRWR) demand, compressive strength, and autogenous shrinkage. The formulae of the material properties were derived by regression analysis considering three mix design parameters and used for optimizing UHPC mixtures.

3.4.1. Mixture Design. A total of 16 UHPC mixtures were prepared and tested.

The investigated UHPC had a fixed binder composition consisting of 55% Portland cement, 40% fly ash, and 5% silica fume, by volume, which was optimized in the authors' previous study (Meng et al. 2016). The volume ratio of masonry sand to river sand was fixed at 3/7.

A statistical fractional factorial design approach was used to formulate the 16 UHPC mixtures shown in Table 3.4 for evaluating the three primary proportioning parameters, which are the w/b, LWS/NS, and b/s. The LWS/NS was calculated by volume ratio of the lightweight sand to the sum of lightweight sand and the river sand. Each parameter was evaluated at two distinct values, coded as -1 and +1, which correspond to the minimum and the maximum levels, respectively.

Table 3.4 Details of experimental program.

Mixture No.	Coded value			Type	Absolute value		
	w/b	LWS/NS	b/s		w/b	LWS/NS	b/s
1	-1	-1	1	Fractional factorial points	0.17	0	1.20
2	-1	1	-1		0.17	0.250	0.80
3	-1	-1	-1		0.17	0	0.80
4	-1	1	1		0.17	0.250	1.20
5	1	-1	-1		0.23	0	0.80
6	1	1	1		0.23	0.250	1.20
7	1	-1	1		0.23	0	1.20
8	1	1	-1		0.23	0.250	0.80
9	0	0	0	Central points	0.20	0.125	1.00
10	0	0	0		0.20	0.125	1.00
11	0	0	0		0.20	0.125	1.00
12	0	0	0		0.20	0.125	1.00
13	-1/3	1	-1/3	Validation points	0.19	0.250	0.93
14	1/3	1/3	-1		0.21	0.167	0.80
15	-1/3	-1/3	1		0.19	0.083	1.20
16	1/3	-1	1/3		0.21	0	1.07

Eight UHPC mixtures were investigated to establish a 23 factorial design for the three parameters. Four UHPC mixtures were prepared to represent the center points in the design obtaining a measure of experimental error. Another four mixtures were prepared for validating the statistical models. In accordance with ASTM C 230, the initial mini-slump flow of all mixtures was regulated to 280 ± 10 mm by adjusting the HRWR dosage. The dosage of de-air entraining admixture was fixed at 0.8% for all mixtures.

The absolute values corresponding to the coded values of the primary variables are presented in Table 3.5. The coded values were calculated as the difference between the absolute values and the values corresponding to the center points divided by half the spread between the maximum and minimum values, as shown in Equation 3.1:

$$\text{Coded w/cm} = (\text{absolute w/cm} - 0.20) / 0.03$$
$$\text{Coded LWS/NS} = (\text{absolute LWS/NS} - 0.125) / 0.125 \qquad \text{Equation 3.1}$$
$$\text{Coded cm/s} = (\text{absolute cm/s} - 1) / 0.2$$

Table 3.5 Absolute and coded values of modeled parameters (from -1 to +1).

Coded value	Absolute value		
	w/b	LWS/NS	b/s
-1	0.17	0	0.80
0	0.20	0.125	1.00
+1	0.23	0.250	1.20

3.4.2. Experimental Results and Statistical Models. Table 3.6 summarizes the experimental results of the 16 UHPC mixtures, including the specific gravity, air content, HRWR demand, flow time, plastic viscosity, dynamic yield stress, mini-slump flow, autogenous shrinkage at 1, 3, 7, and 28 d, and compressive strength at 1, 3, 7, 28, and 91 d.

Statistical analysis of the effects of the LWS/NS, w/b, and b/s on the material properties of UHPC was performed using the Design-Expert® software (Vaughn and Polnaszek 2007). The investigated properties were modeled as functions of the test parameters by performing multiple linear regression analysis using the least square method. The derived statistical models are reported in Table 3.7. The statistical models are established in three steps:

Table 3.6 Summary of test results.

Mixture No.	1	2	3	4	5	6	7	8	9	10	11	12	13	14	15	16
Fresh properties																
Specific gravity	2.52[**]	2.40	2.46	2.41	2.42	2.40	2.49	2.36[*]	2.41	2.40	2.39	2.42	2.35	2.37	2.49	2.38
Air content (%)	2.5[**]	2.5	2.0	2.0	2.5	2.5	2.5	2.5	1.5	1.0[*]	1.0	1.5	2.0	2.5	2.0	1.5
HRWR demand (%)	0.9	1.0[**]	1.0	0.9	0.7	0.6[*]	0.6	0.7	0.7	0.7	0.7	0.8	0.8	0.8	0.8	0.7
Flow time (s)	30.2[**]	26.1	29.6	28.2	8.5	7.7[*]	12.3	8.1	18.1	17.6	17.4	17.2	21.2	15.1	23.3	17.2
Mini-slump flow (mm)	270	270	290	270	290	290	280	280	290	270	270	270	280	290	270	280
Rheological properties																
Plastic viscosity (Pa·s)	28.8[**]	21.6	26.6	23.2	4.4	3.9[*]	7.2	4.1	16.1	11.6	12.3	15.4	20.5	14.6	25.5	17.6
Yield stress (Pa)	6.5	9.6	3.9	4.6	16.1	13.0	6.5	19.1	14.3	19	10.4	15.2	4.2	6.0	15.8	14.4
Autogenous shrinkage (μm/m)																
1 d	502[**]	100	226	165	168	94	388	23[*]	223	206	213	241	100	95	336	350
3 d	693[**]	135	345	310	280	152	520	34[*]	349	338	353	323	168	176	425	462
7 d	831[**]	187	558	436	388	240	627	47[*]	462	421	432	444	210	218	592	600
28 d	893[**]	200	609	440	406	260	676	72[*]	492	456	465	479	226	233	611	632
Compressive strength (MPa)																
1 d	59[**]	46	59	48	42	44	38[*]	47	50	53	50	52	50	47	51	42
3 d	86[**]	70	83	65[*]	79	62	78	80	73	78	69	75	80	69	77	80
7 d	124	126	115	132[**]	103[*]	121	111	119	116	114	118	115	121	121	121	118
28 d	145	148	135	160[**]	123[*]	140	132	136	144	142	140	141	143	136	138	139
91 d	151	156	139	170[**]	125[*]	147	135	141	156	150	150	152	152	146	145	146

* Minimal value ** Maximal value

(1) For each material property, a multiple linear regression analysis was performed to establish the mathematical equations, taking the three mix design parameters (w/b, LWS/NS, and b/s) and their products as input variables.

(2) After the mathematical equation of each material property is generated, the probability value (p-value) is examined for each variable to ensure the variable has statistically significant influence on the material property. If the p-value of a variable is larger than 0.05, the variable is identified as a statistically insignificant variable, and thus removed from the equation. This step is repeated until all insignificant variables are removed from the statistical equations.

(3) All influencing parameters are expressed using the coded values (-1 to +1). In the derived equations in Table 3.7, the variables are listed in a descending order in terms of the degree of significance, which is represented by the coefficient in front of the variable. The positive or negative sign of each coefficient manifests the property increases or decreases with the corresponding variable.

The products of influencing parameters, for instance, (w/b)×(b/s), indicates the coupling effect of the mix design parameters. The coefficients of determination (R^2) of the derived models ranged from 0.85 to 0.98, indicating adequate agreement between the

test data and the statistical models. The relative errors were determined using mixtures corresponding to the central point of the experimental domain.

Table 3.7 Derived statistical models for UHPC properties (based on coded value).

Derived equations	R^2	p-value
HRWR demand (%)		
0.78 - 0.16 w/b - 0.05 b/s	0.92	<0.0001
Flow time (s)		
18.42 - 9.69 w/b - 1.31 LWS/NS	0.98	<0.0001
Plastic viscosity (Pa·s)		
14.60 - 10.08 w/b - 1.78 LWS/NS	0.96	<0.0001
Autogenous shrinkage (μm/m)		
1 d 210.92 - 112.75 LWS/NS + 81.25 b/s - 46.25 w/b - 45.00 (LWS/NS)×(b/s)	0.94	0.0002
7 d 413.58 - 190.50 LWS/NS + 113.00 b/s - 82.50 w/b	0.95	<0.0001
28 d 442.75 - 205.88 LWS/NS + 115.13 b/s - 88.63 w/b	0.95	<0.0001
Compressive strength (MPa)		
1 d 49.00 − 5.13 w/b + 4.38 (w/b)×(LWS/NS)	0.85	0.0003
3 d 74.83 - 6.13 LWS/NS - 3.12(b/s)×(LWS/NS) - 2.63 b/s + 2.38(w/b)×(LWS/NS) - 2.12(w/b)×(b/s)	0.90	0.0075
7 d 117.83 + 5.62 LWS/NS - 5.38 w/b + 3.12 b/s	0.91	0.0002
28 d 140.50- 7.13 w/b + 6.12 LWS/NS + 4.37 b/s	0.95	<0.0001
91 d 147.67 - 8.50 w/b + 8.00 LWS/NS + 5.25 b/s	0.90	0.0003

3.4.2.1 Fresh properties. As shown in Table 3.6, the values of specific gravity of the mixtures in fresh condition slightly decreased with the increasing content of lightweight sand. The variation range was 2.39–2.52, which is relatively small and insignificant. The air content was in the range of 1%–2.5%; the larger entrapped air content was associated with mixtures of greater viscosity. The HRWR demand (mass ratio of active solid HRWR to cementitious materials) for achieving the targeted mini-slump spread value of 280 ± 10 mm was in a range of 0.5%–1.0%. A lower HRWR indicates better flowability prior to the addition of HRWR. The mini V-funnel flow time of the investigated mixtures was in a range of 7.7–30.2 s.

As indicated in Table 3.7, the w/b has the most significant effect on the HRWR demand. The w/b also has the highest impact on flow time, which far exceeds the effects of the LWS/NS and b/s on the flow time. Increasing the w/b can reduce the flow time, thus enhancing the filling capacity of the UHPC. Therefore, it is critical to balance the mechanical properties and fresh properties by adjusting w/b of the UHPC.

3.4.2.2 Rheological properties. Reducing plastic viscosity (μ_p) is essential to facilitate placement and enhance the filling ability of self-consolidating materials, such as UHPC.

The derived statistical models in Table 3.7 indicate that the w/b has the most significant effect on μp and tf. The influences of LWS/NS on μp and tf can be considered as secondary effects compared with w/b.

3.4.2.3 Autogenous shrinkage. Figure 3.13 shows the autogenous shrinkage of the investigated UHPC mixtures made with different combinations of w/b-LWS/NS-b/s in the first 28 d.

The autogenous shrinkage of the 0.17-0-1.2 mixture (w/b-LWS/NS-b/s: 0.17-0-1.2) is shown to increase dramatically after final setting. The autogenous shrinkage reached approximately 500 μm/m at 1 d and 800 μm/m at 28 d. The autogenous shrinkage was substantially reduced when the w/b and LWS/NS were increased and/or the b/s was reduced. For instance, the 28-d autogenous shrinkage of the 0.23-0.25-0.8 mixture was 50 μm/m, which is 90% lower than that of the 0.17-0-1.2 mixture. As the LWS/NS increased from 0 to 0.25, the 28-d autogenous shrinkage decreased by 70% compared with the 0.17-0-0.8 and 0.17-0.25-0.8 mixtures, by 50% for the 0.17-0-1.2 and 0.17-0.25-1.2 mixtures, by 70% for the 0.23-0-0.8 and 0.23-0.25-0.8 mixtures, and by 75% for the 0.23-0-1.2 and 0.23-0.25-1.2 mixtures. This indicates that the addition of LWS can significantly reduce autogenous shrinkage. Due to internal curing effect from the LWS, self-desiccation is reduced, resulting in proportionally lower self-induced stresses (Lura et al. 2001; Lura et al. 2003).

Table 3.7 indicates that the LWS/NS has the most significant influence on the 1-, 7-, and 28-d autogenous shrinkages of the UHPC mixtures, followed by the b/s. The w/b demonstrates more impact on the 28-d autogenous shrinkage than that on the 1-d autogenous shrinkage.
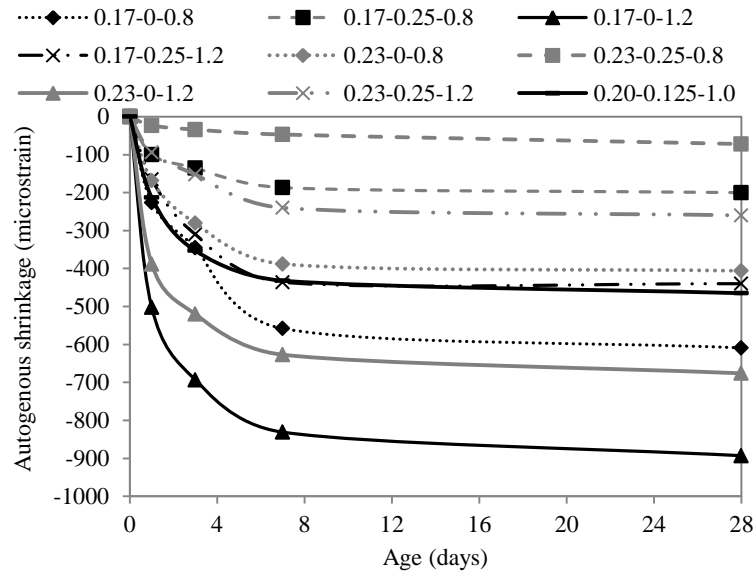
Figure 3.13. Autogenous shrinkage of UHPC mixtures with different w/b-LWS/NS-b/s combinations.

Figures 3.14(a) and 3.14(b) respectively show the contour diagrams of the 1- and 28-d autogenous shrinkages of the UHPC mixtures with 0.20 w/b. The trade-off between the b/s and the LWS/NS is illustrated. The 1- and 28-d autogenous shrinkage results decreased with the LWS/NS and increased with the b/s.
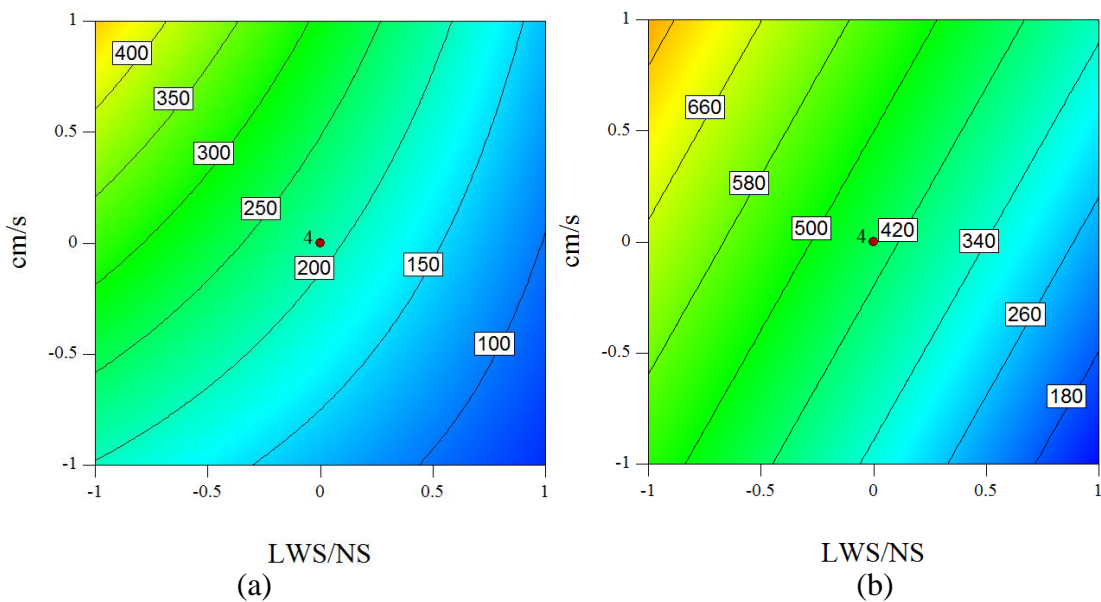
Figure 3.14. The b/s-LWS/NS (coded value) contour diagrams of autogenous shrinkage at: (a) 1 d and (b) 28 d (w/b coded as 0).

3.4.2.4 Compressive strength. For the compressive strengths at 1 and 3 d, the LWS/NS demonstrated negative effects (Table 3.7), meaning the use of LWS reduced the compressive strength at early ages.

Figure 3.14(a) shows that, as the LWS/NS was increased from 0 to 0.25, the 1-d autogenous shrinkage was reduced by about 150 μm/m; as the b/s was reduced from 1.20 to 0.80, the 1-d autogenous shrinkage decreased by about 360 μm/m.

Figure 3.14(b) shows that, as the LWS/NS was increased from 0 to 0.25, the 28-d autogenous shrinkage was reduced by about 400 μm/m; as the b/s was reduced from 1.20 to 0.80, the 28-d autogenous shrinkage was reduced by 380 μm/m.
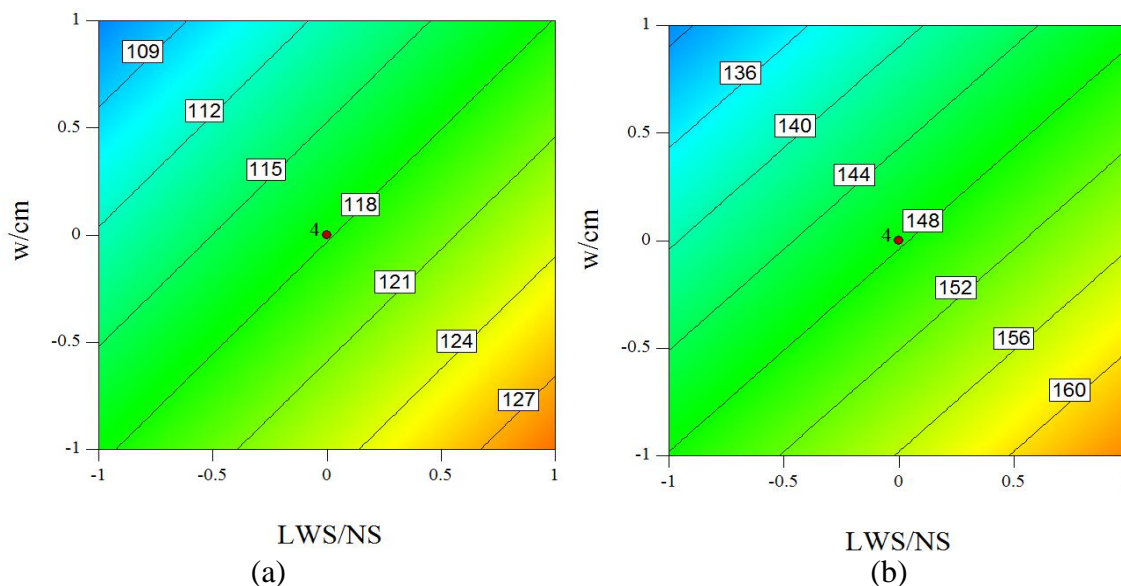
Figure 3.15 The w/b-LWS/NS (coded value) contour diagrams of compressive strength at: (a) 7 d, and (b) 91 d (b/s coded as 0).

However, the LWS/NS demonstrated positive effects on the compressive strength at 7, 28, and 91 d. The coefficient of the LWS/NS increased monotonically from +5.62 at 7 d to +8.00 at 91 d, indicating the use of LWS enhanced the compressive strength of the UHPC mixtures and the enhancement becomes more significant at latter ages. Figures 3.15(a) and 3.15(b) show the contour diagrams of the 7- and 91-d compressive strengths of the UHPC mixtures associated with the LWS/NS and w/b, with the b/s fixed at 1.0. The 7- and 91-d compressive strengths increased with the LWS/NS and decreased with the w/b. With a w/b of 0.17, as the LWS/NS was increased from 0 to 0.25, the 7- and 91-

d compressive strengths were increased by approximately 10% (from 118 to 132 MPa) and 15% (from 146 to 170 MPa), respectively.

With the addition of LWS, the compressive strength was significantly increased. At early ages, the porous LWS and water released from the pre-saturated LWS increased the porosity of the hydraulic UHPC system, thus reducing the compressive strength. However, at latter ages, the released water promoted the hydration reactions of cementitious materials, thus increasing compressive strength of UHPC (Jesen and Hansen 2001). The released water during the curing process help sustain a relatively high humidity in UHPC for extended periods, which is necessary for continued hydrations of Belite (C_2S) and pozzolanic reactions of fly ash and silica fume (Bentz et al. 2005; Duran-Herrera et al. 2007).

The w/b has a negative effect on the compressive strength, and the negative effect becomes magnified at the latter ages. Significant positive coupling effects of the w/b and LWS/NS on the 1- and 3-d compressive strength are demonstrated, indicating that the negative effect of w/b was suppressed by using LWS which results in a greater level of hydration. The b/s has negative effects on the compressive strength at 3 d, but positive effects at latter age. At early age, the strength of cementitious materials matrix was lower than that of sand, due to the relatively low degree of hydration, and, therefore, increasing the b/s reduced the compressive strength. However, at the latter ages, the matrix gained substantially high strength, due to the increased degree of hydration. Thus, increasing the b/s increased the compressive strength.

3.4.3. Evaluation and Validation of Statistical Models. The four mixtures (mixtures No. 9–12) corresponding to central points were used to evaluate the error (i.e. the discrepancy between the test data and predicted values from the statistical models) at 95% confidence level. These values are listed in Table 3.8. The relative error is defined as the ratio of the error to the mean value.

The predicted and measured values of the HRWR demand, flow time, autogenous shrinkage, and compressive strength at different ages of 16 mixtures (mixture No. 1–16) are compared in Figures 3.16(a)–3.16(d).

In each figure, the solid line represents the 1:1 line; the two dash lines correspond to the upper and lower limits, respectively of the material property at 95% confidence

level. Any data point above the solid line represents an overestimated value of the property, and any data point below the solid line represents an underestimated value.

Table 3.8 Mean values and relative errors of central points at 95% confidence level.

Property	Age (d)	Mean	Error	Relative error (%)
HRWR demand (%)	-	0.74	0.03	5.8
Flow time (s)	-	17.6	0.8	4.8
Plastic viscosity (Pa·s)	-	13.9	0.8	5.4
Autogenous shrinkage	1	220.8	9.8	4.5
(μm/m)	7	439.8	26.2	6.0
	28	473.0	30.3	6.4
Compressive strength	1	51.3	2.3	4.4
(MPa)	3	73.7	1.1	1.5
	7	115.8	2	1.8
	28	141.8	1.3	0.9
	91	152	4.3	2.9

The majority of the data points are shown to fall into the range between the dash lines, indicating that the proposed models allow adequate prediction of the material properties.

3.4.4. Optimization of UHPC Mixtures. The validated statistical models were employed to optimize the UHPC mixtures using a numerical optimization technique with desirability functions (Montgomery 2012; Lotfy et al. 2014), according to the responses of the materials properties.

Table 3.9 lists the optimization criteria and seven material properties that were taken into account for the evaluation of the overall performance of the various UHPC mixtures (Montgomery 2012). A goal was set as either minimal or maximal for each materials property according to the desired response. In the case of HRWR demand, plastic viscosity, and autogenous shrinkage, a minimum goal was set. On the other hand, in the case of compressive strength, maximum goal was desired.

Since the optimization was based on the formulated statistical models, which were valid within a specific range of each proportioning variable, a lower and an upper limit should be set for each material property. The lower and upper limits of any material property correspond to minimal and maximal experimental results of that property, respectively. These values are reported in Table 3.9. Any predicate response of material property that lies outside of the lower and upper limits was not taken into consideration in

the mixture optimization. The weight factors of the lower and upper limits were taken as 1. The significance of each material property was empirically valued from 1 to 5. A larger significance value represents a more important material property.
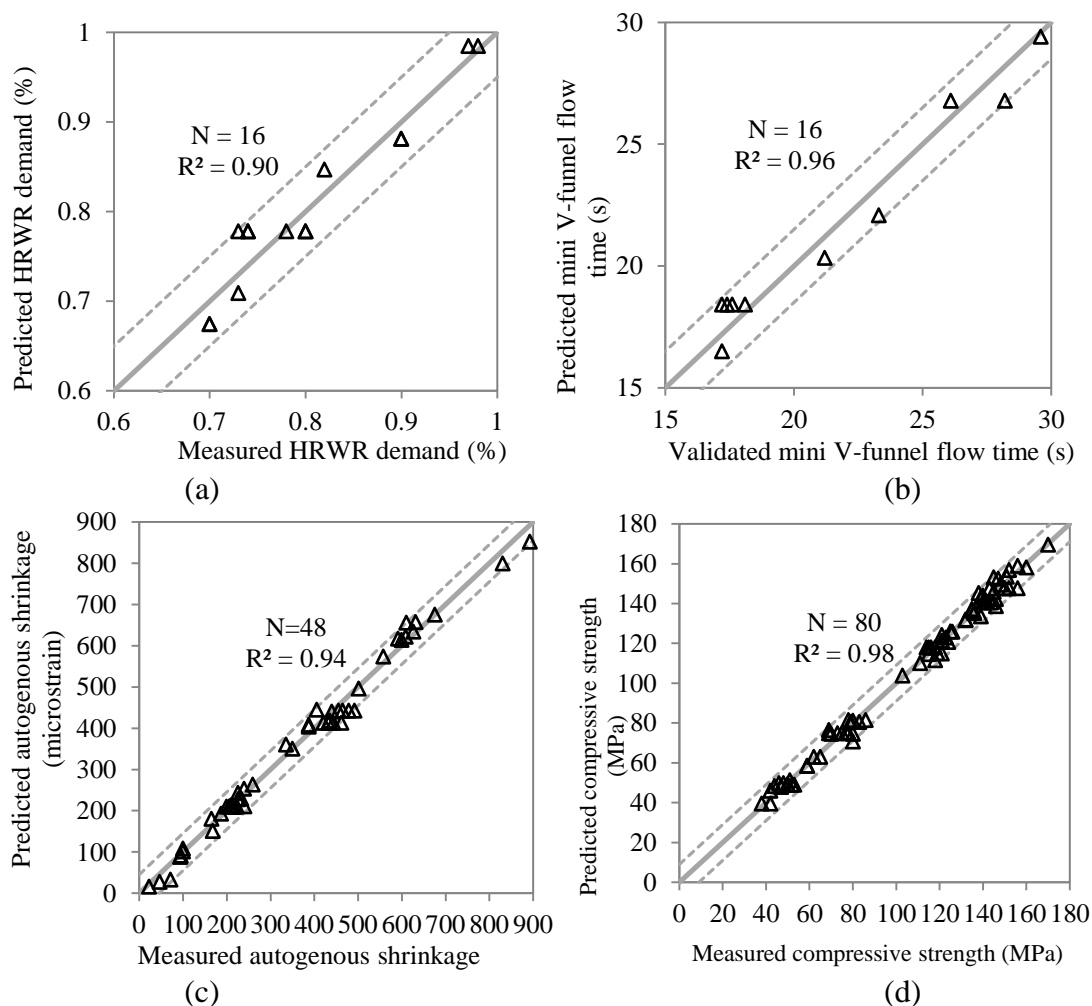
Figure 3.16 Comparison between predicted and measured values for: (a) HRWR demand, (b) mini V-funnel flow time, (c) autogenous shrinkage at 1, 7, and 28 d, and (d) compressive strength at 1, 3, 7, 28, and 91 d. "N" denotes the number of data points.

Table 3.9 Criteria for optimizing UHPC mixtures.

No.	Material property	Goal	Lower limit	Upper limit	Significance
1	HRWR demand	Minimal	0.6	1.0	5
2	Plastic viscosity	Minimal	3.9	28.8	5
3	1-d autogenous shrinkage	Minimal	23	502	5
4	28-d autogenous shrinkage	Minimal	72	893	5
5	1-d compressive strength	Maximal	38	59	1
6	28-d compressive strength	Maximal	123	160	3
7	91-d compressive strength	Maximal	125	170	5

According to the goals of the material properties, a desirability index (d_i) ranging from 0 to 1 was introduced for each of the seven material properties (Montgomery 2012). For a material property with a goal of minimal value, the desirability is linearly changed from 1 at the lower limit to 0 at the upper limit. Similarly, for a material property with a goal of maximal value, the desirability is linearly changed from 1 at the upper limit to 0 at the lower limit (Montgomery 2012). A higher desirability value indicates higher performance level. With the seven desirability indices (d_1–d_7), an overall desirability (D) was defined to represent the overall performance of each UHPC mixture, as indicated in Equation 3.2 (User's Manual 2013):

$$D = (\prod_{i=1}^{7} d_i^{r_i})^{\frac{1}{\sum r_i}}$$

Equation 3.2

where r_i represents the significance value, and i represents the number of material properties (Table 3.9).

Within the ranges of mixture proportioning variables (0.17–0.23 for the w/b, 0.8–1.2 for the b/s, and 0–0.25 for the LWS/NS), w/b, b/s, and LWS/NS were changed with a step size of 0.01, 0.1, and 0.01, respectively. The overall desirability values of a total of 910 UHPC mixtures were calculated and compared. The highest overall desirability value is 0.795. Table 3.10 lists the top six candidate mixtures, in terms of the value of the overall desirability. For the six candidates, the LWS/NS corresponds to 0.25, the w/b is in the range of 0.21 to 0.23, and the b/s is various between 0.90 and 1.20. In particular, the 0.23-0.25-1.2 mixture (w/b = 0.23, LWS/NS = 0.25, b/s=1.2) was ranked the best mixture (No. 1).

Table 3.10 Top candidates of optimized UHPC mixtures.

Rank	LWS/NS	cm/s	w/cm	Desirability
1	0.25	1.20	0.23	0.795
2	0.25	1.10	0.23	0.783
3	0.25	1.20	0.21	0.762
4	0.25	1.00	0.23	0.758
5	0.25	0.90	0.22	0.754
6	0.21	1.20	0.22	0.731

The properties of the 0.23-0.25-1.2 mixture were: HRWR demand of 0.6%, the plastic viscosity of 3.9 Pa·s, the 1-d autogenous shrinkage of 94 μm/m, the 28-d autogenous shrinkage of 260 μm/m, the 1-d and 28-d, and 91-d compressive strengths were 44 MPa, 140 MPa, and 147 MPa, respectively.

3.5. SUMMARY

In this study, LWS was used as an internal curing agent to prepare UHPC for the first time. Knowledge gained in this study can be used to develop mix design guidelines and curing provisions to promote a wider acceptance of LWS as a key component for UHPC with reduced shrinkage. Based on the above investigations, the main findings can be summarized as follows:

(1) The use of LWS can slightly increase the mini-slump spread and significantly reduce the mini V-funnel flow time of UHPC. As the LWS content was increased from 0 to 25%, the mini-slump spread was increased from 275 to 285 mm, and the mini V-funnel flow time was reduced from 40 to 26 s. As the LWS content was increased from 25 to 75%, the mini-slump spread was increased to 290 mm, and the mini V-funnel flow time was reduced to 16 s.

(2) The increase in LWS content reduced was increased from 0 to 25%, the autogenous shrinkage at 28 d. As the LWS content was increased from 0 to 75%, the autogenous shrinkage at 28 d was approximately reduced from 489 to 196 μm/m, and the IRH at 72 h was increased from 85% to 97%. The IRH and autogenous shrinkage are correlated, and their relationship can be fitted using a parabolic equation.

(3) The LWS25 mixture can be considered as the optimum UHPC mixture, in terms of the fresh and hardened properties. The compressive strength at 91 d, flexural strength, T-150, and Young's modulus at 28 d were measured to be168 MPa, 24 MPa, 57 J, and 51 GPa, respectively was increased by 10%. As the LWS content was increased from 25% to 75%, the compressive strength at 91 d, flexural strength, T-150, and Young's modulus at 28 d were reduced by 23%, 63%, 68%, and 22%, respectively. The LWS25 is considered as the optimum UHPC mixture, while the weight factors of the mini slump flow, mini V-funnel flow time, compressive strengths at 1, 28, and 91 d, Young's modulus at 28 d, flexural strength and toughness at 28 d, and autogenous shrinkage at 28 d are taken as 1, 1, 1, 2, 1, 1, 2, 2, and 2, respectively.

(4) The isothermal calorimetry measurements and TG results demonstrated that LWS can promote cement hydration. As the LWS content was increased from 0 to 25%, the value of mass loss of non-evaporated water was increased from 0.100 to 0.118 g H_2O/g binder (by 18%). Further increasing the LWS content from 25% to 50% increased the value of mass loss of non-evaporated water from 0.118 to 0.123 g H_2O/g binder (by 4%).

(5) Based on the MIP test results, the use of LWS had substantial effect on porosity. Increasing the LWS content from 0 to 25% reduced the total porosity by 18%. The reduction in total porosity explains the increase in mechanical properties. As the LWS content was increased from 25% to 50%, the porosity of macro pores was increased by 100% and total porosity was increased by 110%. Such increase in porosity reduced mechanical properties for LWS with high LWS content.

(6) By partially replacing river sand with lightweight sand, UHPC mixtures can be produced to achieve improved flowability, plastic viscosity, compressive strength, and autogenous shrinkage properties. As the LWS/NS was increased from 0 to 25%, the compressive strength at 91 d was increased by up to 15%, and the autogenous shrinkage at 28 d was reduced by up to 75%.

(7) Among the w/b, LWS/NS, and b/s, the w/b was the most significant parameter influencing the compressive strength after 7 d, followed by the LWS/NS and then the b/s. The compressive strength decreased with the w/b and increased with the LWS/NS and b/s. The coupling effects of the three parameters on compressive strength were significant for the first 3 d and then become insignificant after 7 d.

(8) The LWS/NS was the most significant parameter influencing the autogenous shrinkage, followed by the b/s and then the w/b. The autogenous shrinkage decreased with the increase of LWS/NS and b/s, and increased with the increase of w/b. The coupling effects of the three parameters on autogenous shrinkage were insignificant at 7and 28 d.

(9) When the w/b was 0.17 and the b/s was 1.2, increasing the LWS/NS from 0 to 25% reduced the 28-d autogenous shrinkage from 890 to 440 μm/m, and increased the 91-d compressive strength from 150 to 170 MPa. When the w/b was 0.23 and the b/s was

1.2, increasing the LWS/NS from 0 to 25% reduced the 28-d autogenous shrinkage from 680 to 260 μm/m, and increased the 91-d compressive strength from 135 to 145 MPa.

(10) The developed statistical models allow prediction of the material properties of the UHPC mixtures with relative errors less than 10%. Using the validated formulae, UHPC mixtures can be optimized in terms of the desirability of material properties, given the optimization criteria for different applications. With the objective to minimize autogenous shrinkage and maximize the compressive strengths, an optimized UHPC mixture 0.23-0.25-1.2 (w/b-LWS/NS-b/s) was recommended.

4. IMPROVING FLEXURAL PERFORMANCE OF UHPC BY RHEOLOGY CONTROL OF SUSPENDING MORTAR

4.1. BACKGROUND

Steel fibers are commonly employed as reinforcement to enhance the tensile and flexural performance of UHPC. The fibers crossing cracks can restrain the widening and propagation of cracks and allow cracked UHPC to carry sustain load. The tensile and flexural properties of UHPC are closely related to the orientation and spatial dispersion of fibers in UHPC matrix (Grünewald 2004; Li and Li 2013; Kang and Kim 2011). Well-oriented and uniformly-dispersed fibers have greater chance to bridge cracks. Thus, improving the fiber distribution is critical for increasing the tensile and flexural performance of UHPC (Yoo et al. 2016). The fiber orientation in UHPC matrix was associated with the casting scheme (Li and Li 2013; Kang and Kim 2011; 2012). Due to the high viscosity and fluidity of UHPC, during the casting, the velocity ingredient of the flow (shear flow) of fresh UHPC mixture drives the fibers orient along with the flow direction (Ferrara et al. 2008). Thus, fresh UHPC that was placed at one end of the mold and flowed to the other end in the longitudinal direction demonstrated more favorable fiber orientation (Barnes et al. 2011). In the literature, UHPC specimens that were cast in the proper way exhibited more than 60% higher flexural strengths than other UHPC specimens (Kang and Kim 2011; Kang et al. 2011; Abrishambaf et al. 2013). However, the casting scheme demonstrated little influence on the dispersion of fibers in UHPC (Kang and Kim 2011; Ferrara et al. 2008). On the other hand, the rheological properties of concrete demonstrated significant effects on the fiber orientation and dispersion (Ferrara et al. 2008; Tosun-Felekoğlu et al. 2014). The mini-slump flow and plastic viscosity of concrete should be controlled at a proper level to ensure the concrete has adequate flowability but no fiber segregation occurs (Li and Li 2013). Effects of plastic viscosity on the dispersion of polyvinyl alcohol fibers and the tensile performance of engineered cementitious composites were studied (Li and Li 2013; Tosun-Felekoğlu et al. 2014). Increasing the plastic viscosity by using viscosity modified admixture (VMA) was found to have two opposite effects on the mechanical properties of engineered cementitious composites. On one hand, increasing the plastic viscosity improved the fiber dispersion and thus increased the tensile properties of engineered cementitious

composites (Li and Li 2013). A plastic viscosity greater than 10 Pa·s secured uniform dispersion of polyvinyl alcohol fibers and improved tensile properties (Li and Li 2013). On the other hand, increasing the plastic viscosity tended to reduce the mechanical properties by introducing more air voids (Tosun-Felekoğlu et al. 2014). The optimum plastic viscosity needs to be determined to ensure both fiber distribution and flaws are at adequate levels, in order to enhance the tensile/flexural performance. Governing the dispersion and the orientation of fibers in concrete through a suitable balance of rheological properties is a promising approach to achieve a superior tensile/flexural performance and reduce the fiber content for fiber-reinforced composites (Ferrara et al. 2008). So far, there has been a lack of studies on improving fiber distribution and mechanical properties of UHPC by controlling the rheological properties. Besides, the effects of the VMA content on hydration kinetics of UHPC and the steel-matrix interfacial properties has not been fully studied. The objective of this study is to develop a robust and easy-to-apply approach to improve fiber distribution and resulting flexural performance of UHPC by controlling the rheological properties of the suspending mortar before fiber addition. The study seeks to establish correlations among the rheological properties of the suspending mortar, the resulting fiber distribution in the UHPC, and flexural performance of corresponding UHPC. The plastic viscosity is correlated with the mini V-funnel flow time, which provides a simple alternative to evaluate the plastic viscosity. For UHPC mixtures with 2% micro steel fibers, the optimal plastic viscosity of UHPC mortar is determined and validated to achieve the optimized steel fiber distribution and the greatest flexural performance of UHPC. In addition, the effect of increasing plastic viscosity by adding VMA on the hydration kinetics, compressive strength, and the fiber-matrix interfacial properties of UHPC were investigated.

4.2. MATERIALS AND MIX DESIGNS

The materials investigated in this study is presented below:

4.2.1. Raw Materials. The cementitious materials were used.

The binder materials used in this study included ASTM Type III Portland cement, Class C fly ash, ground granulated blast furnace slag, and silica fume. The lightweight sand was saturated for 24 hours (h) before use and had a desorption value of 96% under 92% relative humidity. More details of the materials can be seen in Section 3.2.1.1.

Straight steel fibers with 0.2-mm diameter and 13-mm length were used. The steel fibers have tensile strength and modulus of elasticity of 1.9 and 203 GPa, respectively. A polycarboxylate-based high-range water reducer (HRWR, i.e. MasterGlenium 7500) was incorporated to enhance workability of UHPC. A VMA (i.e. RHEOMAC® VMA 362) with a specific gravity of 1.00 was employed to adjust the viscosity of UHPC.

4.2.2. Mix Design of UHPC Mixtures. Two types of UHPC mixtures designated as UHPC-F and UHPC-G were employed in this study. The optimized UHPC mixtures (Meng et al. 2017) had a fixed w/b of 0.23, by mass. The sand-to-binder ratio was set to 1.0, by volume. The sand consisted of 30% masonry sand, 45% river sand, and 25% lightweight sand, by volume. The mixtures had 2% steel fibers, by volume of UHPC.

For the UHPC-F, the binder consisted of 55% cement, 40% fly ash, and 5% silica fume, by volume. The HRWR dosage was fixed at 0.3% (active portion to binder ratio, by mass) obtain 280 ± 10 mm mini slump flow.

By changing the VMA dosage from 0 to 2.0% at 0.5% intervals, by mass of binder, five UHPC-F mixtures were prepared and designated as VMA-0, VMA-0.5, VMA-1.0, VMA-1.5, and VMA-2.0.

For the UHPC-G, the binder consisted of 45% cement, 50% ground granulated blast furnace slag, and 5% silica fume, by volume. The VMA dosage was increased in three increments, in order to secure different rheological properties.

The mixtures were designated as FT-12, FT-48, and FT-93, and had mini V-funnel flow times of 12, 48, and 93 seconds (s) for the suspending mortar before adding fibers.

The HRWR dosage of the three mixtures was 0.8%, which yielded slump values of 290, 280, and 270 mm, respectively. The flexural properties of the UHPC-G were investigated to validate the developed rheology control method.

4.2.3. Mixing, Casting, and Curing. All mixtures were prepared and tested at room temperature (23 ± 2 ºC). A 19-L Hobart mixer was used. The mixing procedure was followed the same way as presented in Section 3.2.2.1.

For each UHPC mixture, specimens were cast in one lift without any mechanical consolidation. For beam specimens, UHPC was cast from one end of the mold using a chute with an inclined angle of 30º and naturally flowed to the other end of the mold. In

this way, the fibers have a greater tendency for alignment parallel to the longitudinal direction of the beam (Ferrara et al. 2007). After casting, the specimens were covered with wet burlaps and plastic sheets, demolded at 1 day (d), and then, cured in lime-saturated water at room temperature until the time of testing.

4.3. EXPERIMENTAL PROGRAM

The test methods for fresh properties, mechanical properties, single fiber pull out test, determination of fiber distribution, and microstructure characterization are introduced below:

4.3.1. Fresh Properties. The mini-slump test was performed in accordance with ASTM C 230/C 230M. The mini V-funnel flow time was measured according to the EFNARC recommendations (2002).

The mini V-funnel is illustrated in Figure 4.1(a). The unit weight and air content were measured in accordance with ASTM C 138 and ASTM C 231, respectively. The rheological properties of the suspending mortars and UHPC mixtures were evaluated using co-axial viscometers ConTech 6 and ConTech 5, respectively, as shown in Figure 4.1(b) and 4.1(c), respectively. The measurement was started at 15 min after water addition. The samples were subjected to pre-shear at a rotational velocity of 0.50 rps during 25 s, followed by a stepwise reduction in rotational velocity till zero. The dynamic yield stress (τ_0) and μ_p were calculated using the Bingham model (1983). In order to evaluate the repeatability of the rheological properties, each UHPC mixture was batched. The fresh properties therefore correspond to mean values of three sets of measurements.

4.3.2. Mechanical Properties. The 28-d compressive strength was tested using three 50-mm cubes in accordance with ASTM C 109. The loading rate was kept at 1.8 kN/min. This was done for the UHPC-F mixtures.

The 28-d flexural properties of both sets of UHPC mixtures (UHPC-F and UHPC-G) were evaluated with four-point bending test in accordance with ASTM C 1609.

The beam specimens were $305 \times 76 \times 76$ mm in dimension and with a span of 203 mm. Three beams were tested for each mixture. The same load frame (model: MTS 880) was used to apply loads at a controlled displacement rate of 0.05 mm/min. The deflection of the beam specimens and settlement of the two roller supports were recorded using linear variable differential transformers. The applied loads were recorded by a load

transducer embedded in the load frame. The flexural tests were continued until the mid-span deflection reached 3 mm, when the carried load was significantly reduced compared with the peak load (El-Hacha and Chen 2012).

(a)   (b)   (c)
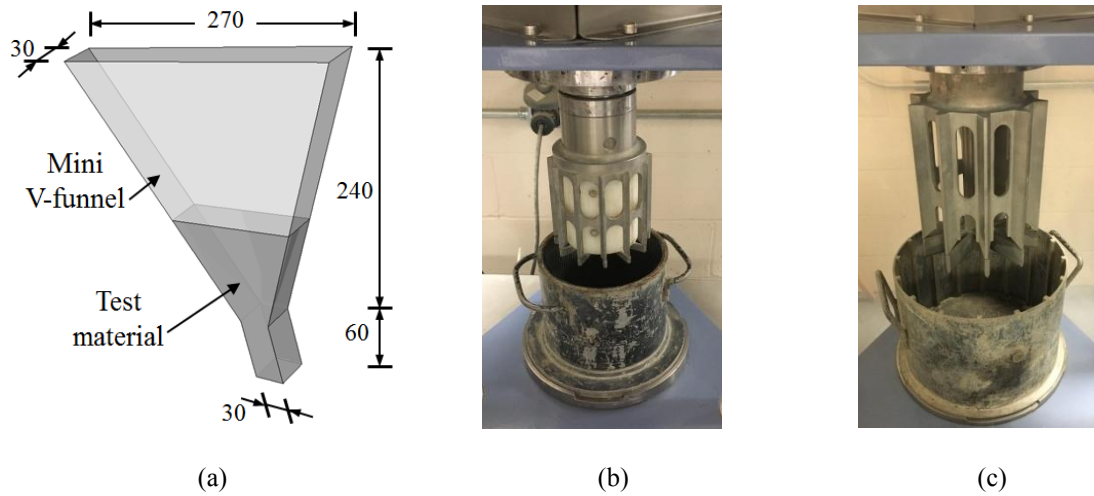
Figure 4.1. Equipment for rheology measurement: (a) mini V-funnel (unit: mm), (b) ConTech 6 viscometer for mortar, and (c) ConTech 5 viscometer for concrete.

The flexural strength was calculated using Equation 4.1, in accordance with ASTM C1609. The area between the load-deflection curve and horizontal axis (from 0 to 3 mm of mid-span deflection) represents the dissipated energy.

$$F = PL/(bd^2)$$ Equation 4.1

where $P, L, b,$ and d corresponds the peak load, span length, beam width, and beam depth, respectively.

4.3.3. Heat of Hydration and Setting Time. The heat of hydration was measured for the UHPC-F mixtures to evaluate the impacts of VMA on cement hydration.

An isothermal conduction calorimetry (model: Calmetrix I-CAL 8000), which was programmed to maintain the samples at 20 ± 0.1 °C, was employed to measure the heat flow and cumulative heat of hydration.

The measurement was started as 15 min after the introduction of water in the mixture, and continued for 48 h when the heat flow was substantially reduced. The initial and final setting time were investigated in accordance with ASTM A403.

4.3.4. Single Fiber Pull-Out Tests. Single fiber pull-out tests were performed for the UHPC-F mixtures to evaluate the influence of VMA on the bond properties of the fiber-matrix interface.

A customized setup was employed (Meng and Khayat 2016). A half of steel fiber was embedded in a 50-mm cube specimen that was tightly constrained by the steel frame system. The other half of the fiber outside of the UHPC matrix was gripped by a low-capacity load frame (model: Instron 5965) for applying pulling force. The force and displacement were recorde by a load cell and a linear variable differential transformer embedded in the load frame. The test was performed under displacement control at a rate of 0.05 mm/min. Three mixtures were investigated with variable VMA dosage rate of 0, 1%, and 2%, by mass of binder, which were VMA-0.0, VMA-1.0, and VMA-2.0, respectively.

4.3.5. Evaluation of Fiber Distribution and Orientation. After flexural testing for the five UHPC-F mixtures, two thin slices (width × depth × thickness = $76 \times 76 \times 5$ mm) were cut from the two sides of the major crack of the beam that failed in flexure.

The cut planes were parallel to the cross section of beam, and in the vicinity of the major crack section. A high-resolution image ($23,005 \times 23,005$ pixels) for each slice was examined. An image processing technique proposed by Lee et al. (2009; 2016) was adopted to quantitatively evaluate the fiber dispersion and orientation in the UHPC matrix, based on the coordinates of fibers and the shape of the fibers in the cutting plane. The RGB images were converted into binary images using Imagej (Rueden et al. 2016), which enables the fibers to be distinguished from the surrounding matrix according to the brightness. The 76×76 mm image corresponding to the total cross sectional area was divided into 21×21 units. Then, the number of fibers per unit was counted. The uniformity of fiber distribution of the whole cross section was quantified using a fiber dispersion coefficient (α). This coefficient expresses the deviation of the number of fibers in a unit area from the average number of fibers, as expressed by Equation 4.2 (Li and Li 2013; Kobayashi 1981):

$$\alpha = \exp\left[-\frac{1}{x_0}\sqrt{\frac{\Sigma(x_i - x_0)^2}{n}}\right]$$

<div style="text-align:right">Equation 4.2</div>

where n is the number of the units, x_i denotes the number of fibers in the i-th unit, and x_0 represents the average number of fibers in each unit. The α value approaches to 1 for uniformly-dispersed fibers in the matrix, or 0 for a severely-biased dispersion.

Figure 4.2 illustrates the geometry of an inclined fiber and the section in the cut plane, where θ, D, and L correspond to the inclined angle ($0 \leq \theta \leq \pi/2$), diameter of the fiber, and the major axis length of the fiber image, respectively. The major axis length (L) and the diameter (D) of each fiber were measured by specifying the lengths (in pixels) of the major and minor axes of the ellipse. High-resolution images were employed to prevent false detection of fiber orientation (Lee et al. 2016). In this study, the resolution was 60 pixels, in order to accommodate the 0.2-mm diameter of the steel fibers.
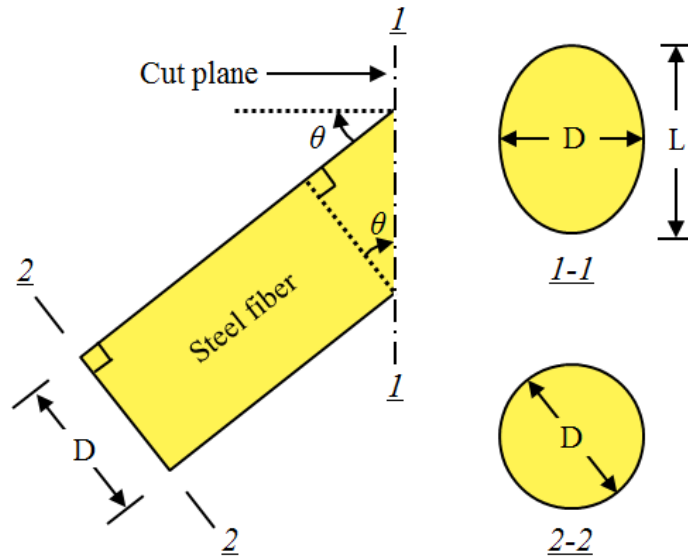
Figure 4.2. Illustration of an inclined fiber.

Fiber orientation was defined as the angle between the fiber axis and the normal direction which is perpendicular to the cutting plane, as shown in Equation 4.3:

$$\theta = \arccos(D/L)$$

<div style="text-align:right">Equation 4.3</div>

In order to evaluate the effect of fiber orientation on flexural properties of UHPC, a fiber orientation coefficient (η) was introduced, considering the probability density distribution of the fiber orientation (Xia et al. 1995, Piggott 1994):

$$\eta = \int_{\theta_{min}}^{\theta_{max}} p(\theta) \cos^2\theta \, d\theta \qquad \text{Equation 4.4}$$

where η approaches to 1 when all of the fibers are aligned perpendicular to the cross section, and η equals to 0 when all of the fibers are aligned parallel to the cross section. $p(\theta)$ represents the probability density distribution for the fiber orientation (Kang et al. 2011, Lee 2009).

4.4. EXPERIMENTAL RESULTS AND DISCUSSIONS

The test results of fresh properties, mechanical properties, single fiber pull out test, determination of fiber distribution, and microstructure characterization are introduced below:

4.4.1. Fresh Properties. The mean values and coefficients of variation (COV) of the fresh properties of the UHPC-F mixtures are summarized in Table 4.1.

As the VMA dosage was increased from 0 to 2.0%, the plastic viscosity, yield stress, and mini V-funnel flow time of the suspending mortar and the corresponding UHPC were monotonically increased. The mini V-funnel flow time of the suspending mortar before fiber addition and the UHPC increased linearly with the VMA dosage, as shown in Figure 4.3(a).

The UHPC mixtures demonstrated higher plastic viscosity, yield stress, and flow time than the corresponding suspending mortar. During flow, mechanical contacts between fibers and sand particles increase the resistance to flow, thus increasing the plastic viscosity. Figure 4.3 shows that the mini V-funnel flow time can be used as a simple and reliable indicator for the plastic viscosity of the suspending mortars and UHPC mixtures.

The air content of the UHPC mixtures increased with the VMA dosage. This can be attributed to the increase in plastic viscosity of the materials that can lead to greater entrapment of air during mixing. Both the initial and final setting time increased with

increase of VMA content. The VMA-2.0 mixture demonstrated the longest initial setting time of 10 h and final setting time of 15 h. The controlled VMA-0.0 mixture had the shortest initial and final setting time of 7 and 13 h, respectively.

Table 4.1 Fresh properties of the UHPC-F mixtures (mini slump flow = 280 ± 10 mm).

Code	VMA-0.0		VMA-0.5		VMA-1.0		VMA-1.5		VMA-2.0	
	Mean	COV(%)	Mean	COV(%)	Mean	COV(%)	Mean	COV(%)	Mean	COV(%)
Mini slump flow (mm	290	4	285	3	280	5	275	6	270	8
Plastic viscosity (Pa·s) – Mortar	12	1	32	2	53	2	74	3	98	3
Plastic viscosity (Pa·s) – UHPC	20	2	36	2	60	3	78	4	112	4
Yield stress (Pa) – Mortar	10	1	13	1	16	2	19	2	22	2
Yield stress (Pa) – UHPC	14	1	16	1	19	2	20	2	26	3
Mini V-funnel flow time (s) – Mortar	10	3	25	4	46	4	66	5	91	5
Mini V-funnel flow time (s) – UHPC	14	3	30	5	51	5	73	5	95	5
Air content (%)	3.0	4	3.5	4	4.0	5	4.5	6	5.0	6
Initial setting time (h)	7.2	2	7.4	3	7.8	2	8.1	4	9.6	4
Final setting time (h)	12.5	2	12.7	2	13.2	1	13.6	4	14.5	3
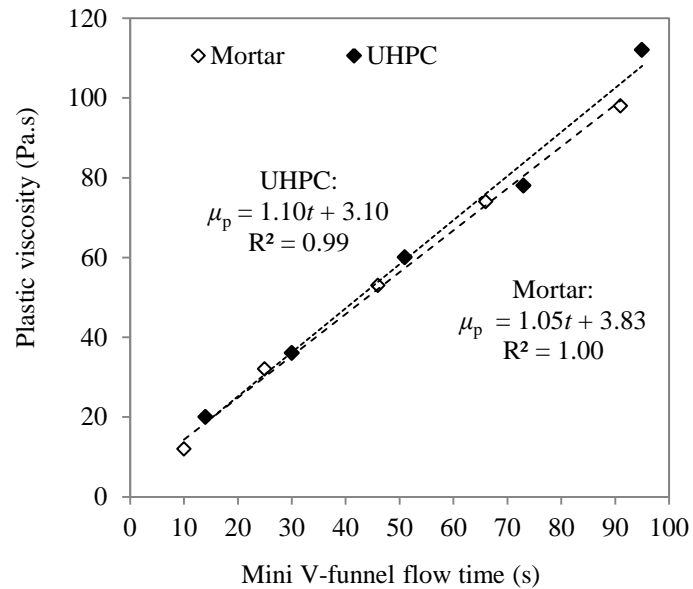
Figure 4.3. Correlation between mini V-funnel flow time (t) and plastic viscosity (μ_p) for suspending mortar and UHPC.

4.4.2. Mechanical Properties. The flexural test results of the five UHPC-F mixtures are compared in Figure 4.4.

Each of the load-deflection curves can be divided into three zones: (1) elastic zone, (2) cracking zone, and (3) post-cracking zone (Gesoglu et al. 2016). In the elastic zone, the carried load approximately linearly increases with the deflection.

In the cracking zone, the carried load increases with the deflection with a decreasing slope that is accompanied with the occurrence of multiple cracks in the test beam. In the post-cracking zone, the load approximately linearly decreases with the deflection.
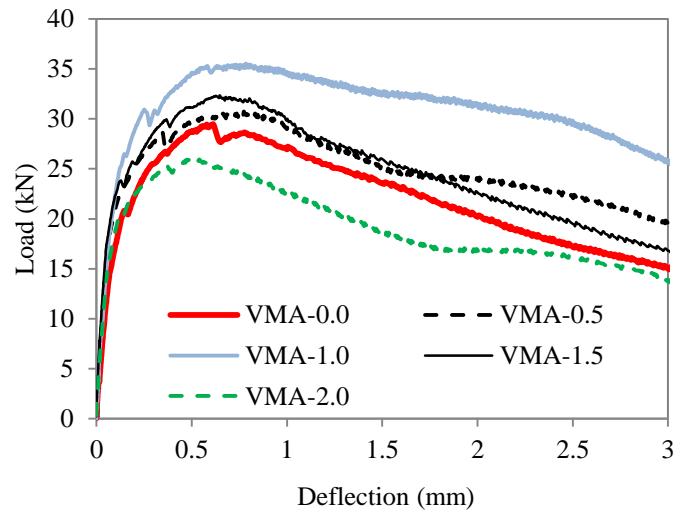
Figure 4.4. Load-deflection curves of UHPC-F mixtures with different VMA contents.

The flexural strength and dissipated energy (i.e. area under the load and deflection curve) are plotted in relation to VMA dosage in Figure 4.5. As the VMA dosage increased up to 1%, overall, the flexural strength and dissipated energy increased with the VMA dosage. As the VMA dosage increased from 1% to 2%, the flexural strength and dissipated energy decreased with the VMA dosage. Both the flexural strength and the dissipated energy reached the highest values at the VMA dosage of 1%. This can be attributed to the optimum fiber distribution was guaranteed when 1% of VMA was used in the suspending mortar, which is explained in later section. The 28-d compressive strength values of the UHPC mixtures are plotted in relation to VMA dosage in Figure 4.6. As the VMA dosage was increased from 0 to 2%, the compressive strength was

decreased by 24% (from 126 to 96 MPa). This can be attributed to more air was entrapped in and introduced more voids in UHPC when more VMA was incorporated (Tosun-Felekoğlu et al. 2014).
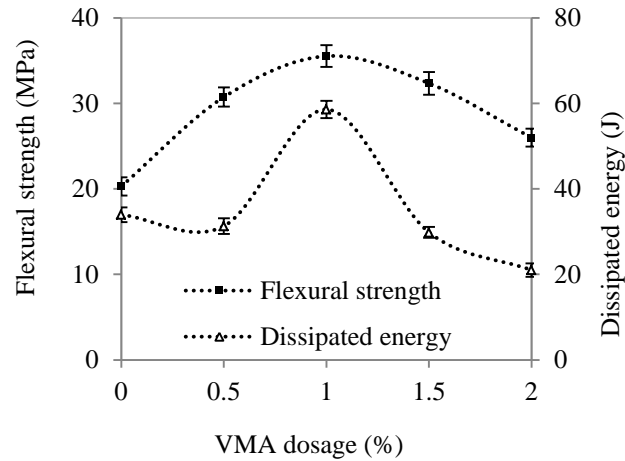
Figure 4.5. Flexural strength and dissipated energy of UHPC-F mixtures with different VMA dosages. The error bars represent the standard deviations of three specimens.
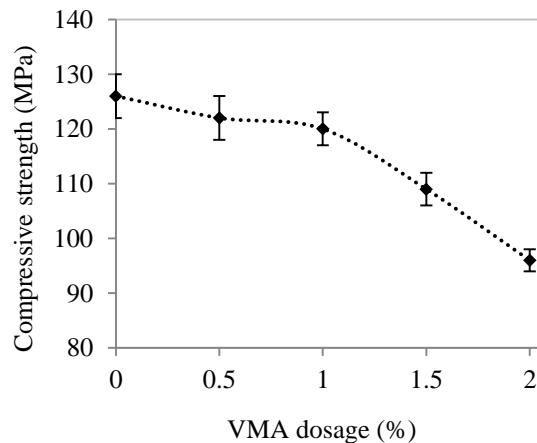
Figure 4.6. Compressive strength of UHPC mixtures with different VMA contents at 28 d. The error bars represent the standard deviations of three specimens.

4.4.3. Fiber Distribution and Orientation. The RGB and binary images of the cutting planes of the VMA-0.0, VMA-1.0, and VMA-2.0 mixtures are shown in Figures 4.7(a)–4.7(f).

In Figures 4.7(a) and 4.7(d), more steel fibers are observed at the bottom of the beam, indicating fiber segregation, which can be attributed to the relatively low viscosity of the suspending mortar of the VMA-0.0 mixture during casting and the relatively high

density of steel compared with the mortar. In Figures 4.7(b) and 4.7(e), the steel fibers seem to be uniformly distributed in the matrix of VMA-1.0 mixture. In Figures 4.7(c) and 4.7(f), fiber agglomeration is observed due to high viscosity of the mortar of VMA-2.0. Overall, the VMA-1.0 mixture shows the best performance in fiber dispersion.

Figure 4.8 plots the values of α and η determined by image analysis (Li and Li 2013; Lee 2009). Increased the VMA dosage from 0 to 1%, α increased from 0.45 to 0.86, thus improving the uniformity of fiber dispersion in the UHPC. However, when the VMA dosage increased from 1% to 2%, α decreased to 0.76, thus reducing the uniformity of fibers in UHPC. The increase of VMA dosage from 0 to 2% increased η from 0.64 to 0.77. This indicates that increasing the viscosity of the suspending mortar tended to make the steel fibers perpendicular to the cross section of the corresponding UHPC beam. However, the change in η is smaller than the change in α.

| (a) | (b) | (c) |
| (d) | (e) | (f) |
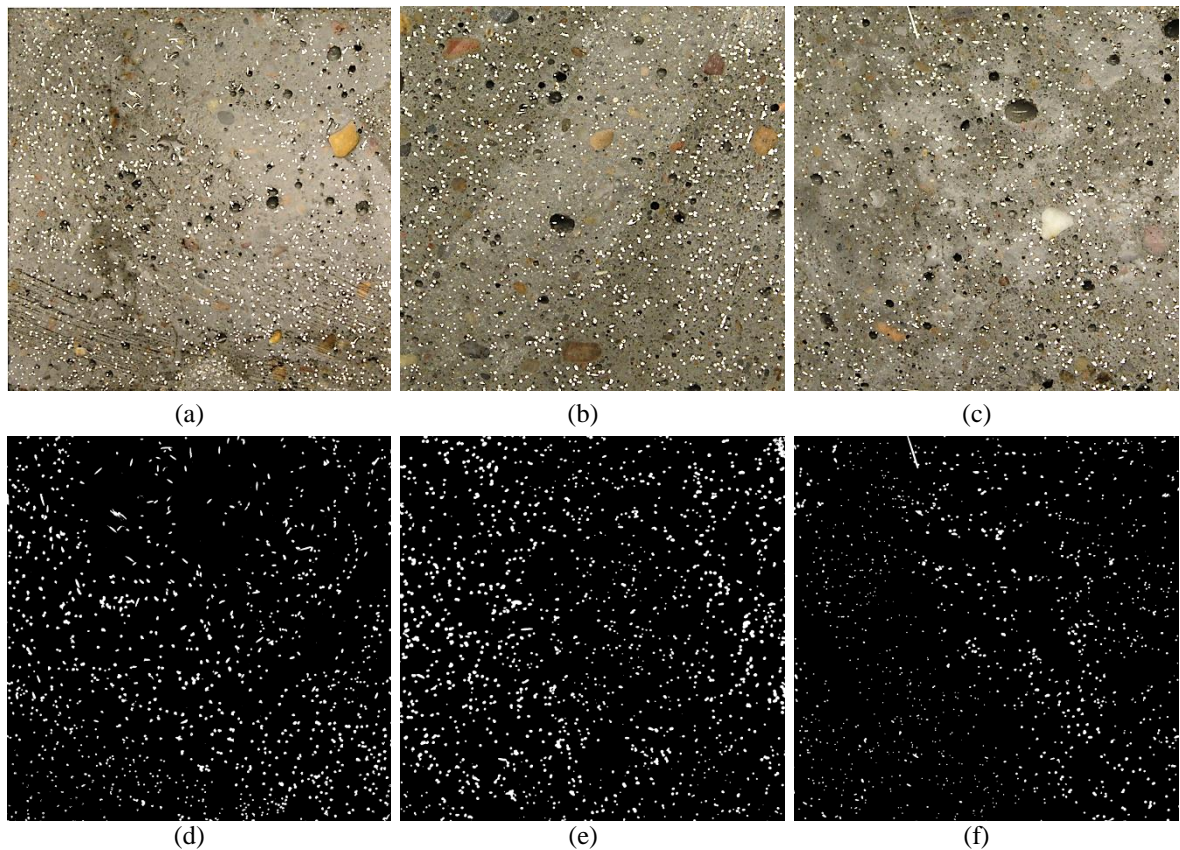
Figure 4.7. Cut plane images of the UHPC-F mixtures: (a) RGB image of VMA-0.0, (b) RGB image of VMA-1.0, (c) RGB image of VMA-2.0, (d) binary image of VMA-0.0, (e) binary image of VMA-1.0, and (f) binary image of VMA-2.0.
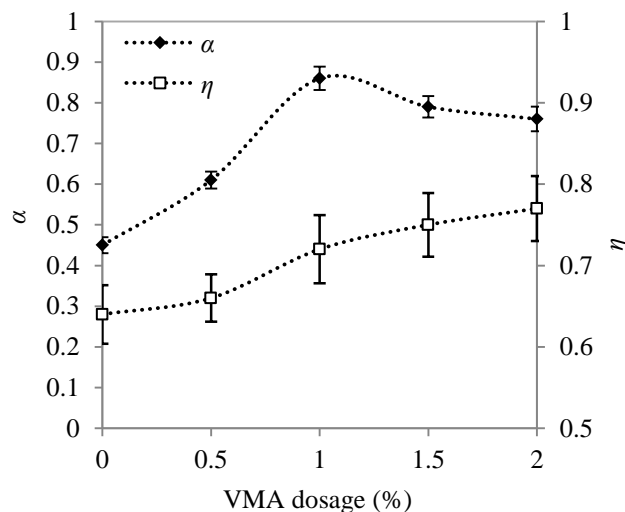
Figure 4.8. Relationships of fiber dispersion and orientation coefficients with the VMA dosage.

4.4.4. Rheological Properties, Fiber Distribution, and Flexural Properties of UHPC. The relationships among the mini V-funnel flow time of the suspending motar, fiber dispersion coefficient, and dissipated energy in flexure of UHPC mixtures are plotted in Figure 4.9.

As the mini V-funnel flow time was increased from 10 to 46 s, both the fiber dispersion coefficient and dissipated energy increased. As the mini V-funnel flow time was increased from 46 to 91 s, both the dispersion coefficient and dissipated energy decreased. Both the highest fiber dispersion coefficient and dissipated energy were achieved at the mini V-funnel flow time of 46 s. Therefore, the highest fiber dispersion coefficient corresponded to the highest dissipated energy of the UHPC beam, which can be attributed to the improved bridge effect due to the improvement in the fiber distribution.

4.4.5. Heat of Hydration. Figures 4.10(a) and 4.10(b) show the influence of VMA dosage on the hydration kinetics of cementitious materials of the investigated UHPC-F mixtures.

As the VMA dosage was increased from 0 to 0.2%, the main hydration peak was delayed with lower heat flow peak values, as shown in Figure 4.10(a). The cumulative heat of hydration decreased with the increase in VMA dosage, as shown in Figure 4.10(b).
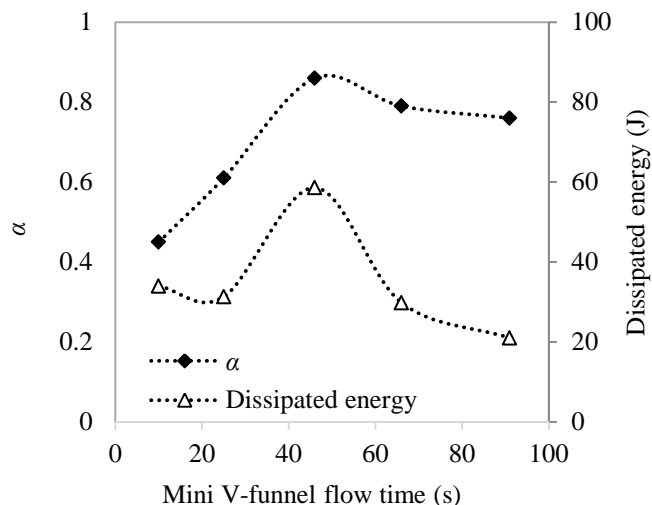
Figure 4.9. Correlation among flow time, fiber dispersion coefficient, and flexural toughness.

| (a) | (b) |
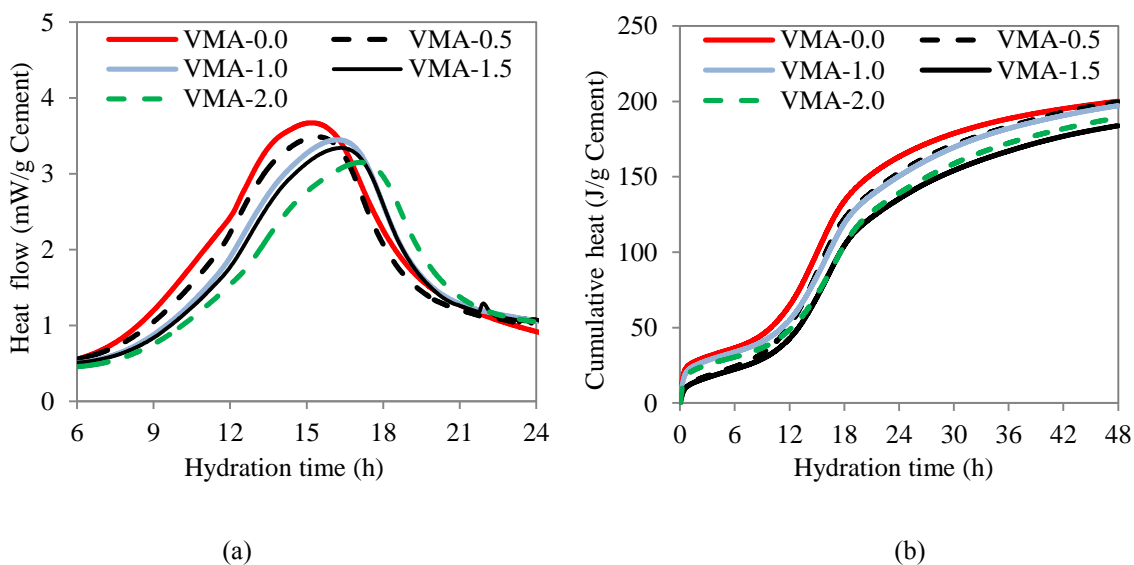
Figure 4.10. Heat of hydration and cumulative heat for UHPC-F mixtures: (a) heat flow and (b) cumulative heat.

It can be hypothesized that the suppression of cement hydration by VMA is primarily due to adsorption of VMA molecules on the surfaces of cement particles. The adsorbed VMA molecules inhibit the surface dissolution sites, thus, delaying the time needed to reach the critical super-saturation for Portlandite precipitation. Beyond the induction period, the adsorbed VMA molecules continue to inhibit cement dissolution

sites, as well as sites for nucleation of calcium silicate hydrates, thus resulting in delayed hydration of cement even at later ages. In addition, the lower values of cumulative heat of mixtures with higher VMA dosages indicate that the VMA can suppress the cement degree of hydration, and thus, reduce the compressive strength of UHPC.

4.4.6. Single Fiber Pull-Out Behavior. The pull-out load-slip curves of three UHPC mixtures (VMA-0.0, VMA-1.0, and VMA-2.0) are shown in Figure 4.11. Before debonding occurs, the bond of the interface between a steel fiber and the matrix is composed of chemical adhesive bond, friction, and mechanical interlock effect due to surface roughness of the steel fiber.

The mean values and COV of the pull-out results are reported in Table 4.2. As the VMA dosage was increased from 0 to 1%, the peak pull-out force and dissipated energy were reduced by about 10% and 15%, respectively. As the VMA dosage was increased from 1% to 2%, the peak pulling force and dissipated energy were reduced by 25% and 35%, respectively. Overall, the peak pulling force and area under the load-slip curves decreased with the VMA dosage. Thus, adding VMA was detrimental for the bond properties of the fiber-matrix interface, and the adverse effect became more significant as the VMA dosage was increased.
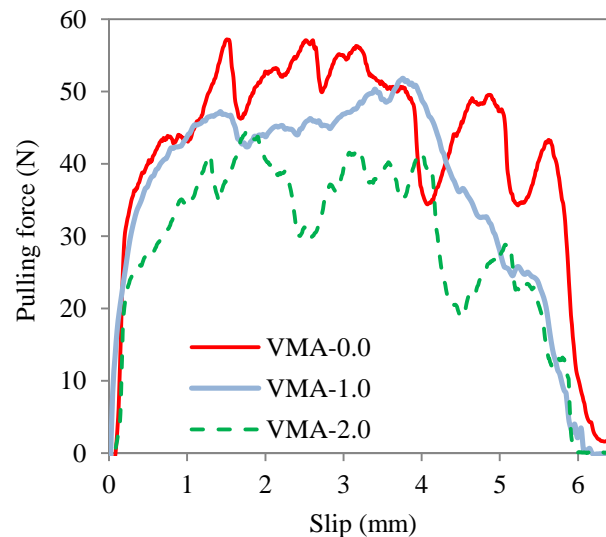
Figure 4.11. Single fiber pull-out test results of UHPC mixtures: VMA-0.0, VMA-1.0, and VMA-2.0.

Table 4.2 Single fiber pull-out test results.

Matrix	Maximum force (N)		Dissipated energy (mJ)	
	Average	COV (%)	Average	COV (%)
VMA-0.0	57	6	270	6
VMA-1.0	52	5	230	7
VMA-2.0	44	7	180	9

4.5. VALIDATION OF RHEOLOGY CONTROL CONCEPT

Establishing the relationship between the rheological properties of the suspending mortar of UHPC and the flexural properties of the UHPC product, as shown in Figure 4.9, can facilitates the optimization of the flexural performance of UHPC. Given the correlation between the plastic viscosity and mini V-funnel flow time, the flow time of the suspending mortar can be tested to indirectly evaluate the steel fiber distribution and optimize the flexural properties of UHPC.

In order to validate the rheology control approach, the UHPC-G mixture had a HRWR of 0.8% to secure an initial mini-slump flow of 280 ± 10 mm, was prepared to evaluate the effect of rheology of the suspending mortar on flexural performance of UHPC. The VMA dosages of 0, 0.8%, and 1.6% were incorporated to increase viscosity of the suspending mortar. The corresponding mixtures are referred to FT-16, FT-48, and FT-93 and achieved the mini V-funnel flow times of 16, 48, and 93 s, respectively. Figures 4.12(a) and 4.12(b) show the flexural testing results of the UHPC-G mixtures. Among the three mixtures, the FT-48 mixture, whose flow time is closest to the optimal flow time (46 s) in Figure 7.9 of the UHPC-F mixtures, achieved the best flexural performance.

This evaluation indicates that the proposed rheology control method is promising for improving flexural performance of UHPC where adapted rheology can enhance steel fiber distribution.

It should be noted that the optimum mini V-funnel flow time of 46 ± 2 s can indeed change with changes of the steel fiber volume and types. A similar approach can be followed to identify the optimum range of the plastic viscosity and the mini V-funnel flow time of UHPC.
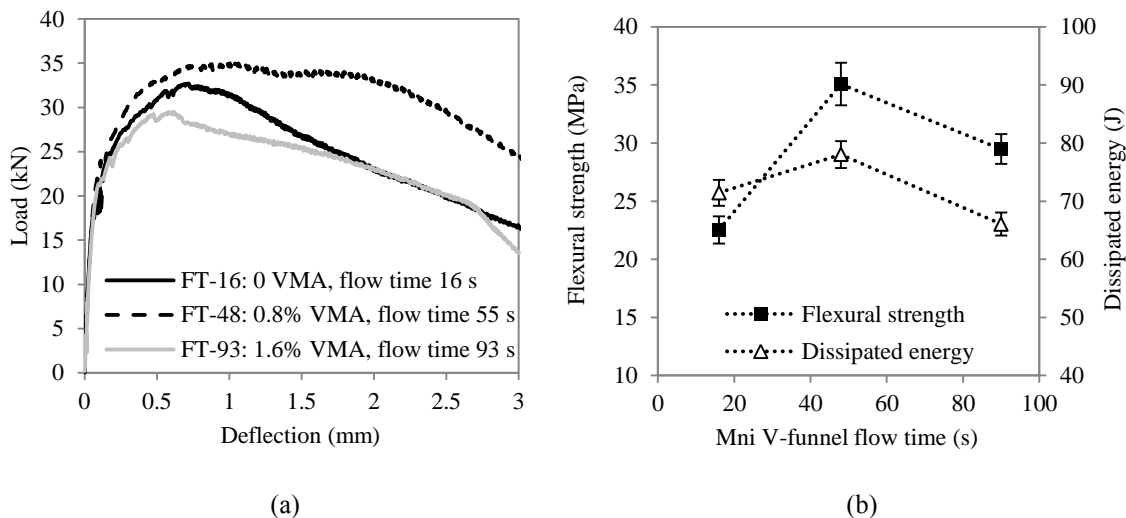
Figure 4.12. Effect of rheology control on (a) flexural load-deflection relationship and (b) flexural strength and toughness for the UHPC-G mixture.

4.6. SUMMARY

Based on the above investigation, the following conclusions can be drawn:

(1) The dispersion and orientation of steel fibers in UHPC are dependent on the rheological properties of the suspending mortar. For UHPC containing 2% of micro steel fibers, the fiber dispersion coefficient increased first and then decreased with the plastic viscosity of the suspending mortar. The peak fiber dispersion coefficient was achieved at a plastic viscosity of 53 ± 3 Pa·s. The fiber orientation coefficient monotonically increased with plastic viscosity up to about 100 Pa·s.

(2) Improving the fiber distribution in UHPC by adjusting the rheological properties of the suspending mortar enhanced the flexural performance of UHPC. The greatest flexural strength and dissipated energy of UHPC were obtained when the fiber dispersion coefficient achieved the peak value.

(3) Mini V-funnel flow time can be used as an indicator of plastic viscosity to adjust rheological properties of UHPC suspending mortar before the addition of steel fibers, in order to improve fiber distribution and enhance flexural properties of the UHPC. For the UHPC containing 2% micro steel fibers, the greatest flexural properties were achieved when the mini V-funnel flow time was around 46 ± 2 s. This was validated by the experiments of UHPC-G mixtures.

(4) Increasing the plastic viscosity of UHPC mortar by adding VMA at a dosage up to 2% of binder reduced the compressive strength of the UHPC at 28 d by 24% (from 126 to 96 MPa), retarded the hydration kinetics, and reduced the degree of hydration of the UHPC at 48 h.

(5) Increasing the VMA dosage decreased the fiber-matrix interfacial bond properties. As the VMA dosage increased from 0 to 2%, the bond strength and pull-out energy were shown to drop by 25% and 35%, respectively. This can have adverse effect on post-cracking behavior of UHPC.

5. REINFORCEMENT OF UHPC BY HYBRID FIBERS

5.1. BACKGROUND

Through appropriate combination of high-range water reducer (HRWR), adequate gradation of sand, fiber reinforcement, cement, and supplementary cementitious materials, ultra-high-performance concrete (UHPC) can be produced to deliver exceptional mechanical properties and durability. Due to the superior material properties, fiber reinforced cementitious composites have been proposed to repair deteriorated structural components (Li et al. 2017), construct bridge closure joints (Perry and Weiss 2009), and stay-in-place formwork (Meng and Khayat 2016). However, in spite of remarkable fresh and hardened material properties, UHPC is susceptible to cracking (Yoo et al. 2013; Bao et al. 2015). To extend the service life of UHPC, the crack tolerance and high tensile/flexural strengths can be improved by appropriately utilizing fibers as reinforcement (Park et al. 2012).

Behloul et al. (1996) used 2.5% straight steel fibers that are 12 mm in length (l_f) and 0.15 mm in diameter (d_f) to develop a UHPC mixture with a tensile strength of 7.8 MPa. Benson and Karihaloo (2004) proposed a UHPC mixture with a tensile strength of 13.5 MPa using 13 mm long straight steel fibers at a fiber content of 6%. Yoo et al. (2013, 2016) reported that increasing the fiber content increased the flexural/tensile properties of UHPC when other components are fixed. Unfortunately, the increase in fiber content can substantially increase material cost. Low fiber contents are preferred to produce cost-effective and workable UHPC (Meng et al. 2017). In order to further enhance material properties and reduce material cost, hybrid fibers have been proposed to prepare UHPC. For example, Wille et al. (2011) developed a UHPC with a tensile strength of 13 MPa by blending 1% deformed fibers (l_f = 30 mm, d_f = 0.38 mm) and 1.5% micro straight steel fibers (l_f = 13 mm, d_f = 0.2 mm). Park et al. (2012) produced a UHPC with a tensile strength of 15 MPa using 1% 30-mm deformed steel fibers and 1.5% 13-mm straight steel fibers. By incorporating 1% straight fibers (l_f = 6 mm, d_f = 0.16 mm) and 2% hooked fibers (l_f = 30 mm, d_f = 0.38 mm), Kwon et al. (2014) achieved a UHPC mixture with a tensile strength of 20 MPa. On the other hand, synthetic polymeric fibers such as polyvinyl alcohol (PVA) and polyethylene fibers can be

incorporated with steel fibers in proportioning UHPC. Kang et al. (2016) adopted 1% steel fiber (l_f = 16.3 mm, d_f = 0.2 mm) and 0.5% polyethylene fiber (l_f = 12 mm, d_f = 0.04 mm) in UHPC, and obtained 15% higher tensile strength than that of the reference UHPC with 1.5% mono steel fibers. Hannawi et al. (2016) observed that the interfacial zone between synthetic fiber and matrix was more porous than that of steel fiber and matrix. This was attributed to the fact that synthetic fibers are made of hydrophobic materials. The volume of steel fiber replacement by synthetic fiber is typically restricted to minimize the adverse effect on the mechanical properties of UHPC. Nevertheless, synthetic fibers can reduce drying shrinkage and cracking potential of concrete (Mesbah and Buyle-Bodin 1999; Passuello et al. 2009). However, limited information exists about the effect of synthetic fibers on shrinkage characteristic of UHPC.

These improvements due to use of hybrid fibers are mainly due to the mechanisms of multi-scale reinforcement and improved mechanical bond through fiber deformation (Lawler et al. 2005). However, in most studies reported in the literature, rheological properties of the mixtures are not considered and flowability of the UHPC can change with fiber content. While UHPC mixtures are expected to be utilized in complex structural elements, proper filling capacity is expected by optimizing the rheological properties. Although the mixtures achieved high mechanical properties, the reduced flowability could hinder wide constructability of the mixtures. As a matter of fact, the addition of fibers can increase the surface areas that need to be wetted, hence reducing the amount of free water for the lubrication of cement particles (Grünewald and Walraven 2011). Therefore, the use of fibers could significantly reduce flowability of UHPC. Reduction in flowability can in turn affect the hardened properties and cost-effectiveness of the UHPC. On one hand, more voids tend to form in less flowable mixtures and significantly reduce the mechanical strengths and durability of the mixtures (Boulekbache et al. 2010; Wee et al. 2006). On the other hand, reduced flowability requires the use of high-power mixers and consumption of more energy during mixing, especially when long deformed fibers and/or high amount of fibers is used. Moreover, most of the UHPC mixtures reported in the literatures subjected to heat curing at a temperature around 90 ºC, which to some extent restrained wider applications of this technology in cast-in-place applications.

Based on these premises, there is lack of knowledge on the effect of fibers content and fiber combination on material properties of highly flowable UHPC under standard curing conditions. This study systematically investigates the key material properties of a UHPC made with both hybrid steel (micro-macro) and steel-synthetic fibers. Of special interests are the HRWR demand for obtaining a mini-slump flow around 280 mm, rheological properties, tensile and flexural properties, compressive strength, and autogenous shrinkage of such concrete that is cured under standard curing (no heat curing).

5.2. MATERIALS AND EXPERIMENTAL PROGRAM

The materials investigated in this study and experimental program are detailing below;

5.2.1. Materials. The investigated UHPC is based on a cost-effective mixture developed by the authors (Meng et al. 2017), in which the key mix proportioning parameters were optimized through a systematical experimental study to deliver excellent material properties and cost-effectiveness. The cementitious materials included Class C fly ash, silica fume, and Type III Portland cement. All UHPC mixtures were prepared with 40% fly ash, 5% silica fume, and 55% cement, by total volume of binder. The water-by-binder ratio was fixed at 0.20. More details of the raw materials can be seen in Section 3.2.1.1. Three types of sand, including river sand, masonry sand, and lightweight sand, were pre-treated to secure a saturated surface dry (SSD) condition. A polycarboxylate-based HRWR was used to improve the flowability of the UHPC. An air detraining agent was fixed at 0.8% to reduce the air content of the UHPC.

Figures 5.1(a)–5.1(c) show the straight steel fibers (SF), hooked-end steel fibers (HF), and PVA fibers respectively investigated in this study. The straight fibers are 0.2 mm in diameter and 13 mm in length. The hooked fibers are 0.5 mm in diameter and 30 mm in length. The tensile strength and the Young's modulus of elasticity of the both types of steel fibers are 1.9 and 203 GPa, respectively. The PVA fibers are 38 μm in diameter and 8 mm in length; their specific gravity and tensile strength are 1.3 and 1400 MPa, respectively.

Autogenous shrinkage was evaluated in accordance with ASTM C 1698. Three specimens were cast in standard corrugated plastic tubes for autogenous shrinkage measurements for each UHPC mixture. The specimens were stored at room temperature ($23 \pm 1°C$) and a relative humidity of $50\% \pm 2\%$. Shrinkage measurements were performed at final setting, and then on daily basis for the first week and on weekly basis until the age of 56 d.

Table 5.1 Mix designs of investigated UHPC mixtures.

Mixtures	Cement (kg/m³)	Silica fume (kg/m³)	Fly ash (kg/m³)	River sand* (kg/m³)	Masonry sand* (kg/m³)	lightweight sand* (kg/m³)	PVA fibers (kg/m³)	SF (kg/m³)	HF (kg/m³)	Total Fiber (%)
S0	675	43	422	558	312	122	-	-	-	0
S1	668	42.5	418	553	308	121	-	78	-	1
S2							-	156	-	
PVA0.5S1.5							6.5	117	-	
H0.5S1.5	663	42	367	527	308	120	-	117	39	2
H1S1							-	78	78	
H1.5S0.5							-	39	117	
H2							-	-	156	
S3	654	41.7	409	542	302	118	-	234	-	3
S4	648	41.3	405	536	299	117	-	312	-	4
S5	641	40.8	401	531	296	116	-	390	-	5

* Saturated-surface dry condition.

5.3. EXPERIMENTAL RESULTS AND DISCUSSIONS

The test results of fresh properties, mechanical properties, single fiber pull out test, and development of autogenous shrinkage are introduced below:

5.3.1. Fresh Properties. To ensure proper flowability and filling capacity of UHPC, the mini-slump flow was fixed at 280 ± 10 mm by adjusting the HRWR dosage. As shown in Table 5.2, the HRWR demand increased with the increase of fiber content.

Taking the S2 mixture as the reference mixture, increasing the fiber content from 2% to 5% led to a 300% increase in HRWR demand. The replacement of 0.5% straight fibers by PVA fibers (PVA0.5S1.5 mixture) resulted in a 25% greater HRWR demand compared with that of the S2 mixture. Greater contents of PVA fiber attempted; however, this led to significant reduction in flowability due to high water adsorption of PVA fiber. Increasing the substitution ratio of straight fibers by hooked fibers increased the HRWR

demand. For example, the incorporation of 1% hooked-end fiber (i.e. the H1S1 mixture) resulted in 10% greater HRWR demand than that of the S2 mixture. When hooked fibers were completely replaced by straight fibers (i.e. the H2 mixture), the HRWR demand was increased by 60%.

Table 5.2 Fresh properties of investigated UHPC mixtures.

Mixtures	HRWR demand (%)[*]	Plastic viscosity (Pa·s)	Flow time (s)
S0	0.8	35	29
S1	0.9	40	34
S2 (reference)	1.0	45	39
PVA0.5S1.5	1.2	56	48
H0.5S1.5	1.0	50	42
H1S1	1.1	58	50
H1.5S0.5	1.6	63	55
H2	2.2	66	59
S3	2.5	55	47
S4	3.0	62	55
S5	4.0	70	63

* The symbol "%" refers to mass ratio of active powder of HRWR to cementitious materials.

Plastic viscosity can influence the filling capacity of concrete mixtures. The viscosity and flow time increased with the increase of fiber content from 0 to 5% (Table 5.2). Compared with the reference UHPC mixture (i.e. the S2 mixture), the increase in fiber content from 2% to 5% resulted in 55% increase in plastic viscosity. The incorporation of 0.5% PVA fiber increased the plastic viscosity by 25%. The use of 1%, 1.5%, and 2% of hooked-end fibers led to increase in plastic viscosity by 10%, 30%, 40%, and 45%, respectively, compared with that of UHPC with 2% straight steel fibers.

During UHPC mixing, fiber agglomeration was observed for the mixtures containing hooked-end fibers at volume content greater than or equal to 1.5% or straight fibers with more than 3%. With increase in fiber content, greater level of fiber agglomeration was observed during mixing and casting. Such agglomeration can present adverse effects on mechanical properties (Swamy and Mangat 1974).

5.3.2. Single Fiber Pull-Out Behaviour. Figure 5.2 compares the pull-out curves of the straight steel fiber and hooked-end steel fiber partially embedded in the UHPC matrix.

The pull-out results are summarized in Table 5.3 and correspond to mean of nine single fiber pullout results. The pull-out energy represents the area under the pull-out curves in Figure 5.2.
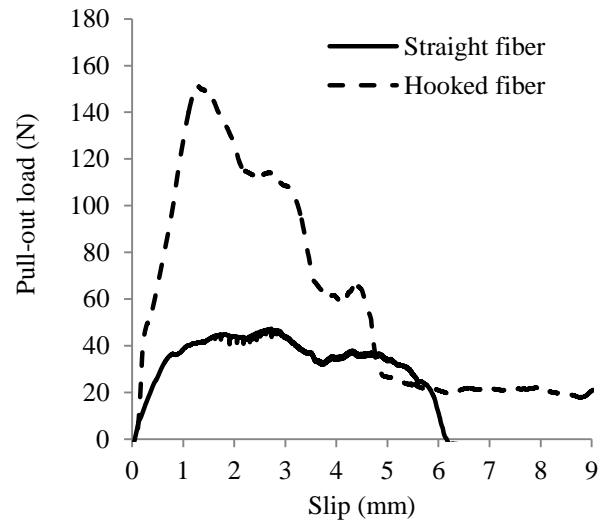
Figure 5.2. Mean values of nine single fiber pull-out tests for straight steel fiber and hooked-end steel fiber.

The peak pull-out load and dissipated energy of hooked-end fibers were 275% and 300%, respectively, greater than those of straight fibers. Before debonding occurred, the pullout load increased linearly with the slip. The bond of the fiber-matrix interface comprises of adhesive bond, friction, and mechanical interlock effect due to surface roughness of the steel fiber. After the peak load, fiber was gradually debonded and finally pulled out from the UHPC matrix. The pull-out test results indicate that the fiber geometry has a significant effect on the pullout response. The hooked ends of hooked-end fibers mechanically anchored the fibers in matrix, thus allowing the fibers to provide higher resistance to pull-out loads than that of straight fibers. The high resistance to the pull-out load and longer length of hooked-end fibers enables them to effectively bridge crack interfaces (Kwon et al. 2014). Therefore, the quantity of hooked-end fibers is crucial for controlling crack expansion and enhancing the tensile and flexural behaviors.

However, compared with the straight fibers, the hooked-end fibers produce higher contacting pressure and more damages at the fiber-matrix interface to activate mechanical bond resistance. Consequently, overwhelm content of hooked-end fibers may lead to much higher degree of matrix damage (Park et al. 2012). Moreover, straight fibers can provide effective reinforcement for UHPC matrix by improving the stiffness and crack resistance to stabilize the pull-out behavior of the hooked-end fibers (Miahashi and Kohno 2007).

Table 5.3 Single fiber pull-out test results.

Fiber type	Maximum force (N)		Pull-out energy (mJ)	
	Mean	C.O.V.	Mean	C.O.V.
SF	45	3%	188	6%
HF	148	5%	750	9%

5.3.3. Mechanical Properties. Different mechanical properties were reported as follows:

5.3.3.1 Compressive strength. Table 5.4 shows the mechanical properties of the investigated UHPC mixtures. As the fiber content was increased from 0 to 5%, the compressive strengths did not monotonically increase with fiber content. Among the six S0–S5 mixtures, the S3 mixture made with 3% fibers achieved the highest 7-d and 28-d compressive strengths of 140 and 158 MPa, respectively. The 7-d and 28-d compressive strengths of the S5 mixture were lower than those of the S2 mixture. This can be attributed to the high dosage of HRWR needed to maintain high fluidity, as shown in Table 5.2. This resulted in high volume of entrapped air, which in turn reduced the compressive strength of UHPC. In addition, when a large amount of fibers were used, fiber agglomeration was observed and indicated that high mixing energy was needed to uniformly disperse fibers in UHPC. The UHPC mixtures were all cast without any mechanical consolidation. Therefore, at high volume fraction of fibers, the mixtures may not be truly self-consolidating (Khayat et al. 2014).

For the mixtures with hybrid fibers at a total fiber content of 2%, the H1S1 achieved the highest 7-d and 28-d compressive strengths of 145 and 168 MPa, respectively. Further increase in the content of hooked-end fibers reduced compressive strength. For example, the 7-d and 28-d compressive strengths of the H1.5S0.5 mixture

were lower than those of the H1S1 mixture. Overall, proper use of hybrid fibers (micro-macro steel fibers) was shown to be more effective in increasing compressive strength than simply increasing the fiber content.

5.3.3.2 Flexural properties. Figures 5.3(a) and 5.3(b) compare the representative load-deflection curves of different mixtures.

The results of the first cracking strength, flexural strength, and T150 toughness are summarized in Table 5.4 The flexural strength was calculated using Equation 5.1 in accordance with RILEM recommendations (RILEM 2002).

$$f_u = \frac{3P_u L}{2bd^2}$$

Equation 5.1

where f_u and P_u represent the flexural strength and the peak load in the load-deflection curves; L, b, and d denote the span, width, and depth of the test beam, respectively.

Furthermore, this equation was used to determine the first cracking strength; however, the load corresponding to the appearance of first crack in the test beam is used rather than the peak load.Except for the S0 mixture that did not contain any fibers, all of the investigated UHPC mixtures showed hardening behaviors after initial cracking. In the post-cracking stage, the tensile load was primarily carried by the steel fibers crossing the crack interfaces, which is mainly associated with fiber pull-out behavior. Higher fiber-matrix bond strength resulted in better post-cracking performance.

Table 5.4 Mechanical properties of investigated mixtures.

Mixtures	Compressive strength at 28 d (MPa)		Flexural strength at 28 d (MPa)		T150 (J)		Tensile strength at 28 d (MPa)		Tensile dissipated energy at 28 d (J)	
	Mean	C.O.V.	Mean	C.O.V.	Mean	C.O.V.	Mean	C.O.V.	Mean	C.O.V.
S0	140	5%	9.6	4%	1.5	8%	-	-	-	-
S1	143	5%	12.5	3%	38.5	5%	-	-	-	-
S2(control)	153	3%	21.3	1%	51.9	4%	6.8	5%	11.8	7%
PVA0.5S1.5	160	3%	23.4	2%	58.5	5%	-	-	-	-
H0.5S1.5	160	3%	23.4	2%	61.7	5%	7.3	6%	14.2	7%
H1S1	166	3%	26.5	2%	66.9	6%	8.0	6%	14.7	8%
H1.5S0.5	150	4%	21.6	3%	53.4	4%	6.7	7%	11.2	8%
H2	145	4%	20.4	4%	49.8	5%	6.0	8%	10.4	9%
S3	158	4%	22.4	3%	51.1	6%	-	-	-	-
S4	150	5%	23.0	4%	48.1	7%	-	-	-	-
S5	146	6%	22.0	5%	44.2	7%	-	-	-	-

Figure 5.3(a) plots the load-deflection curves of UHPC mixtures proposed with different fiber contents. As the fiber content was increased from 0 to 5%, the highest first cracking strength was 16.0 MPa, which was obtained by the S3 mixture with 3% fiber. The highest flexural strength was 23.0 MPa, which was obtained with the S4 mixture containing 4% fibers. The highest T150 toughness was 51.9 J corresponding to the S2 mixture with 2% fibers. Increasing the fiber content from 2% to 5% reduced toughness by 15%. The overall flexural performance did not monotonically increase with fiber content. As mentioned previously, the use of a higher HRWR dosage associated with greater fiber content resulted in increase in entrapped air, which in turn increased the porosity of matrix, thus reducing the compressive strength of UHPC (Meng et al. 2017). Also, fiber agglomeration was observed when high fiber contents were used, which can adversely affect flexural properties.

(a)   (b)
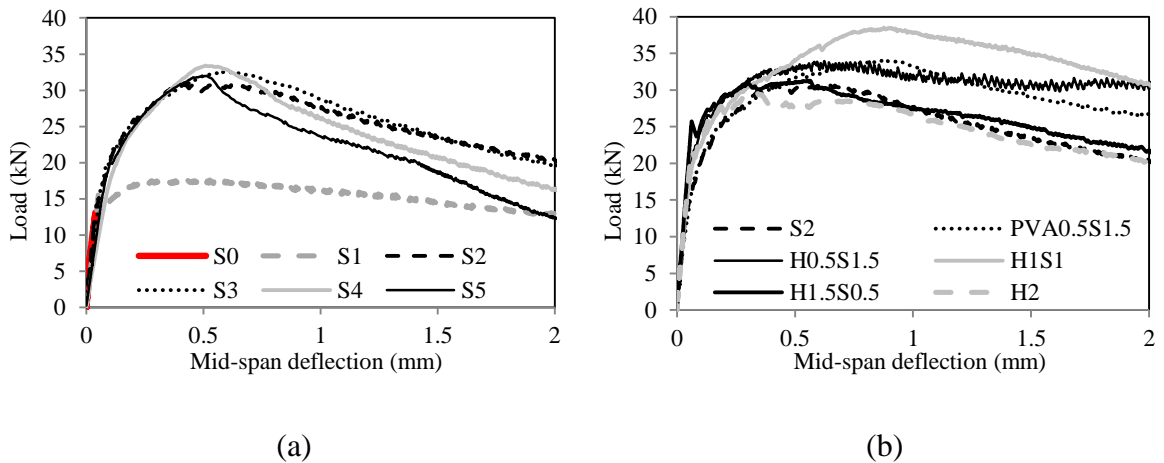
Figure 5.3. Load-deflection curves of: (a) mixtures with different fiber contents; (b) mixtures with different fiber combinations.

Figure 5.3(b) plots the load-deflection curves of the UHPC mixtures containing 2% fibers of different combinations. The increase in hooked-end fiber content from 0 to 1% resulted in an increase in flexural properties; however, further increase in such fiber content led to drop in flexural performance. For example, the highest first cracking strength was obtained with the mixture made with 1.5% hooked-end fibers (H1.5S0.5). The H1S1 mixture presented the highest flexural strength and T150 toughness. Compared with the reference UHPC mixture, the flexural strength and T150 of the H1S1 mixture

made with 1% straight fibers and 1% hooked-end fibers increased by 25% and 30%, respectively; the flexural strength and T150 of the H2 mixture with 2% hooked fibers decreased by about 5%; and the flexural strength and T150 of the PVA0.5S1.5 mixture increased by 10% and 15%, respectively. These results indicate that at a given total fiber content of 2%, proper combination of different fibers can increase flexural performance. As greater content of hooked-end fibers is introduced, an increase in flexural properties is observed due to the enhancement of pull-out force exhibited with hooked fibers (Figure 5.2). Again, further increasing the content of hooked-end fibers reduces flexural properties, which can be associated with fiber agglomeration.

   5.3.3.3 Tensile properties. Figure 5.4 shows the load-elongation curves obtained from direct tensile testing of UHPC containing 2% fibers made with different fiber combinations. Similar to the flexural curves, first cracking is followed by strain hardening behavior. The tensile strength and tensile dissipated energy are listed in Table 5.3. The dissipated energy represents the area under load versus elongation curve between elongation values of 0 to 2 mm.
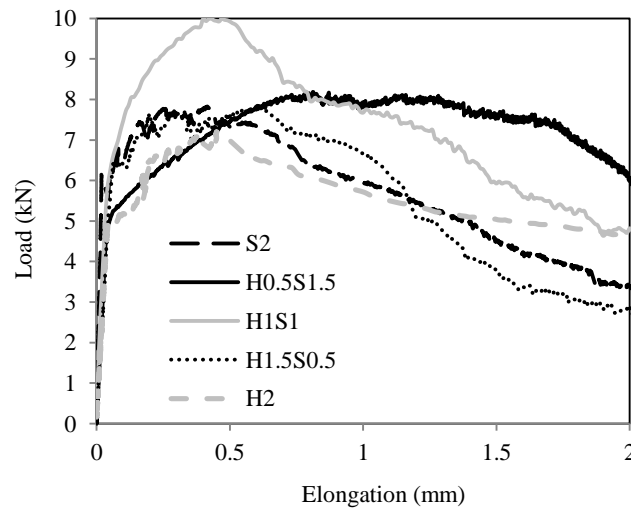
Figure 5.4. Load-elongation relationship of UHPC with different fiber combinations.

   Compared with the S2 mixture, the tensile strength and dissipated energy of the H0.5S1.5 mixture increased by 7% and 20%, respectively, and the tensile strength and dissipated energy of the H1S1 mixture increased by 20% and 25%, respectively. The increase is because of the high resistance to pull-out force of the hooked-end fibers

(Figure 5.2). However, as the hooked-end fiber content was exceeded 1%, the tensile strength and dissipated energy started to drop. Compared with the H1S1 mixture, the tensile strength and dissipated energy of the H1.5S0.5 mixture were reduced by 16% and 24%, respectively, and the tensile strength and dissipated energy of the H2 mixture dropped by 25% and 29%, respectively. Such reduction can again be mainly attributed to fibers agglomeration, as discussed in the last section.

5.3.3.4 Autogenous shrinkage. Figure 5.5(a) shows autogenous shrinkage of UHPC made with straight steel incorporated 0–5%, by volume. The increase of fiber content from 0 to 5% led to significant reduction in autogenous shrinkage. Compared with the S0 mixture, the 56-d autogenous shrinkage values of the mixtures S1, S2, S3, S4, and S5 were reduced by 15%, 30%, 35%, 45%, and 60%, respectively. This can be attributed to the fact that steel fibers do not shrink and have high elastic modulus compared with the matrix; when steel fibers are added and bonded with the matrix, they provided mechanical resistance to deformation and restrain the development and propagation of microcracks of the matrix (Bischoff 2003), thus, reducing autogenous shrinkage of UHPC.

Figure 5.5(b) shows that the use of hybrid fibers can potentially reduce autogenous shrinkage compared with the S2 mixture with mono straight steel fibers. The PVA0.5S1.5 mixture achieved a 56-d autogenous shrinkage of 220 μm/m, which is only 60% of the S2 mixture. Although the PVA fibers could not effectively restrain shrinkage deformation of the cement paste and maintain the volume stability, due to their low elastic modulus, they could effectively bridge microcracks and restrain crack propagation at early age (Sun et al. 2001; Passuello et al. 2009).

This behavior helped reduce shrinkage induced by microcracks, which could lead to a relaxation of the matrix and increase in shrinkage (Bouziadi et al. 2016). In case of mixtures with steel fibers, the H1S1 mixture achieved the lowest autogenous shrinkage at 56 d (271 μm/m), which is 72% that of the S2 mixture. However, an adverse effect of hooked fibers on autogenous shrinkage was observed for UHPC mixtures with hooked fiber contents greater than 1% (i.e. H1.5S0.5 and H2). The adverse effect can be associated with fiber agglomeration and lack of self-consolidation. Compared with the S2 mixture, the 56-d autogenous shrinkage of the H2 mixture was increased by 15%. This

may be due to lack of micro fibers to restrain microcracks in the matrix. The results indicate that using 0.5% PVA fibers or hooked fibers of 1% or less can effectively reduce autogenous shrinkage, and thereby reduce the risk of cracking of UHPC.

(a)   (b)
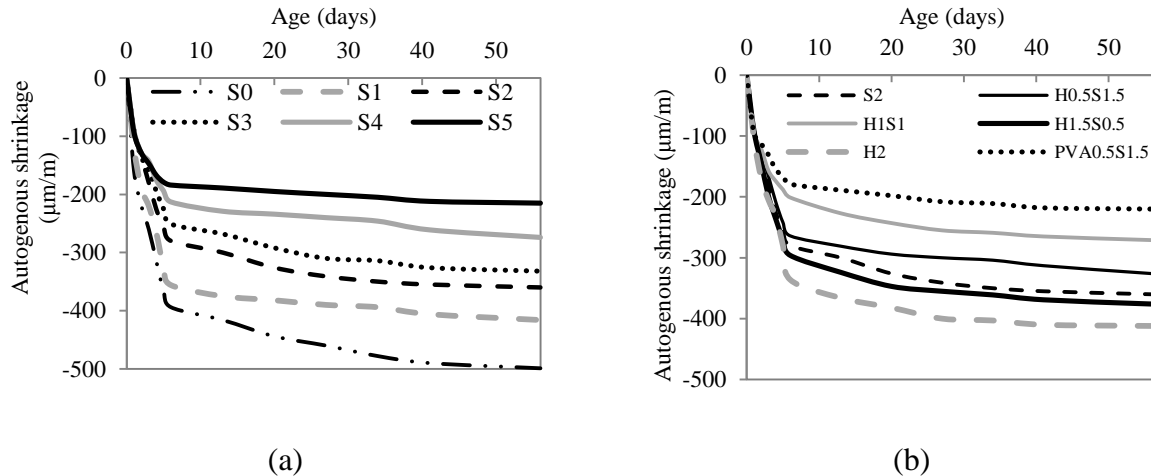
Figure 5.5 Autogenous shrinkage of: (a) mixtures with different fiber contents; (b) mixtures made with different fiber combinations.

5.4. SUMMARY

Based on the results of above investigations, the following conclusions can be drawn:

(1) As steel fiber content increased from 0 to 5%, the workability of UHPC mixtures decreased significantly, thus necessitating greater HRWR demand. The increase of fiber content from 2% to 5% increases HRWR demand by 300%. At the constant fiber content of 2%, compared with the UHPC mixture with 2% straight steel fiber, the incorporation of 0.5% PVA fibers, 1% hooked-end fiber, and 2% hooked-end fibers increased the HRWR demand by 25%, 10%, and 60%, respectively.

(2) Increase of the fiber content from 2% to 5% increased plastic viscosity by 55%. At the constant fiber content of 2%, compared with the UHPC mixture with 2% straight steel fiber, using 0.5% PVA fibers increased the plastic viscosity by 25%; using 0.5%, 1%, 1.5%, and 2% hooked fibers increased the plastic viscosity by approximately 10%, 30%, 40%, and 45%, respectively.

(3) The flexural performance depends on the fiber volume. The increase in steel fiber content enhanced flexural properties; however, after critical fiber content, the

flexural performance dropped, which is mainly due to fiber agglomeration and lack of self-consolidation, albeit with high mini-slump flow of 280 ± 10 mm was secured. As the fiber content was increased from 0 to 5%, the highest first cracking strength was 16.0 MPa (S3); the highest flexural strength was 23.0 MPa (S4); the highest T150 toughness was 51.9 J (S2). The overall flexural performance did not monotonically increase with the fiber content.

(4) Compared with the S2 (reference), the flexural strength and T150 of the H1S1 and PVA0.5S1.5 mixtures increased by 25% and 30%, 10% and 15%, respectively. However, the flexural strength and T150 of the H2 mixture reduced by about 5%.

(5) Compared with the S2 mixture, the tensile strength and dissipated energy of the H0.5S1.5 and H1S1 mixtures increased by 7% and 20%, 20% and 25%, respectively. However, as the hooked-end fiber content was exceeded 1%, the tensile strength and dissipated energy started to drop. Such reduction can again be mainly attributed to fibers agglomeration and lack of self-consolidation.

(6) Compared with the reference UHPC mixture containing 2% straight steel fiber, the 56-d autogenous shrinkage of mixtures with straight steel fiber contents of 1%, 2%, 3%, 4%, and 5% were reduced by approximately 15%, 30%, 35%, 45%, and 60%, respectively.

(7) Proper use of hybrid fibers can further reduce autogenous shrinkage. Compared with the reference UHPC mixture with 2% straight steel fibers, using 0.5% PVA fibers and 1.5% straight steel fibers achieved a 56-d autogenous shrinkage of 220 μm/m, which represents a 40% reduction of autogenous shrinkage. The incorporation of 1% macro hooked-end fibers and 1% micro straight steel fibers exhibited a 56-d autogenous shrinkage of 270 μm/m, which represents a 28% reduction compared with the reference mixture (S2).

6. REINFORCEMENT OF UHPC BY CARBON NANOMATERIALS

6.1. BACKGROUND

By incorporating steel/polymeric fiber reinforcements, UHPC can exhibit strain hardening behavior in tension and in flexure, exhibiting ductile failure modes. Park et al. (2012) found that the strain hardening behavior of UHPC can be observed for tension with multiple cracking, by incorporating micro steel fibers at 1.5% by volume of UHPC. Meng et al. (2017) reported that under four-point bending, the post-cracking behavior of UHPC exhibited strain hardening when the content of micro steel fibers exceeded 1% by volume of UHPC. However, the micro fibers were found to be ineffective in delaying the initiation and propagation of microcracks, which can be due to the relatively large spacing between fibers (Sbia et al. 2014). The presence of cracks can make UHPC vulnerable to ingress of moisture and undesired ions, thus resulting in accelerated deterioration. Therefore, to enhance the cracking resistance and the fracture toughness of UHPC is of great importance.

Carbon nanomaterials, such as carbon nanotubes (CNTs), carbon nanofibers (CNFs), and graphite nanoplatelets (GNPs), have been used to enhance mechanical properties of cementitious composites, due to their high elastic modulus and tensile strength (Liang et al. 2016, Wille and Loh 2010, Han et al. 2015). For example, Li et al. (2005) found an addition of CNT at 0.5% by weight of binder increased the flexural tensile strength, compressive strength, and failure strain of a cementitious composite by 25%, 20%, and 30%, respectively. Gao et al. (2009) observed that the compressive strength of a cementitious composite containing 0.16 % CNFs was 40% higher than that of the plain cementitious composite. With an addition of 0.13% GNPs, Peyvandi et al. (Pevandi et al. 2013) obtained a 70% increase in the flexural tensile strength of a cement paste. The nanoscale spacing and high specific surface areas of the nanomaterials make them effective in suppressing inception and propagation of microcracks (Konsta-Gdoutos et al. 2010; Sun et al. 2016). On the other hand, carbon nanomaterials were found to be able to enhance the packing density of cementitious materials and accelerate the nucleation and growth of calcium-silicate-hydrate. This can be attributed to the increase in nucleation sites due to the nanomaterials, thus refining the microstructure and

improving the mechanical properties (Han et al. 2015; Sanchez and Sobolev 2010). However, due to the small size, agglomeration of nanomaterials can potentially compromise their reinforcing performance (Metaxa et al. 2010; Kirgiz 2015). Ultra-sonification has been used to undermine agglomeration and facilitate their dispersion in aqueous media (Konsta-Gdoutos et al. 2010). Surfactants were incorporated to convert the hydrophobic surface of nanomaterials into hydrophilic surface (Peyvandi et al. 2013). Uniformly-dispersed CNTs at relatively low content (≤ 0.5 % by weight of binders) were found to effectively improve the flexural behavior without affecting flowability (Metaxa et al. 2012).

Compared with CNTs, CNFs and GNPs have 40% lower unit cost (Breuer et al. 2004), more favorable surface that enhances interfacial bonding to cement paste (Sbia et al. 2014; Lu et al. 2016; Le et al. 2014), and mechanical properties (Han et al. 2015). For example, by adding 0.2% CNTs by weight of binder, Luo et al. (2009) obtained a 35% increase in flexural strength; Al-Rub et al. (2011) achieved a 130% increase in fracture toughness, compared with cementitious composite without CNT. With the same amount of CNFs (0.2% by weight of binder), Tyson et al. (2011) achieved an 80% increase in flexural strength and a 270% increase in fracture toughness, compared with the cementitious composite without CNF. Huang (Huang 2012) obtained an increase of 80% in flexural strength by using 0.2% GNPs in cementitious materials. In past studies, nanomaterials were incorporated in paste or cementitious mortars, which are typically brittle in tension. There is a lack of studies on UHPC, which contains micro fiber reinforcement to enhance crack resistance and ductility.

Based on the above review, researches on carbon nanomaterials (i.e. CNF and GNP) in the existing studies focused on two main aspects: (1) how to make nanomaterials uniformly dispersed in cementitious matrix; (2) whether the use of nanomaterials offers substantial improvement to the cementitious matrix, and what content range of nanomaterials should be recommended. Both of the aspects were studied in this section. In addition, It is reported that the introduction of CNF or GNP could potential affect compatibility between cementitious particles and chemical admixture (Nochaiya and Chaipanich 2011), thus affecting the rheological properties of UHPC mixtures. To date, effects of CNF and GNP on rheological properties of UHPC have not been reported.

Besides, due to the very low w/b, which is typically less than 0.25, UHPC is generally subjected to large early-age autogenous shrinkage, which can possibly cause cracks (Bao et al. 2015). Thus far, investigations on the effects of CNF and GNP on autogenous shrinkage, hydration kinetics, and pores structure have been limited.

In this study, the effects of incorporating two types of GNP and one type of CNF on rheological properties, hydration kinetics, autogenous shrinkage, mechanical properties, and pores structure of UHPC containing 0.5% steel fibers, by volume, are investigated. The content of the nanomaterials is increased from 0 to 0.3% by weight of binders. Four dispersion methods were compared to seek for the best way to disperse the nanomaterials. The evaluated mechanical properties of UHPC include compressive strength, tensile strength, and flexural strength. To explore the reinforcing mechanism of CNFs and GNPs for UHPC, a single fiber pull-out test and optical microscopy examination were conducted. The microstructures of the UHPC mixtures containing nanomaterials were also examined by scanning electron microscopy (SEM).

6.2. EXPERIMENTAL PROGRAM

The materials investigated in this study and experimental program are presented as follows:

6.2.1. Materials and Mix Design. The UHPC matrix adopted in this study is based on an optimized mixture developed by the authors (Meng et al. 2017). The w/b was set to 0.2, by mass. The sand-to-binder volume ratio was 1.0. The binder was composed of ASTM Type III Portland cement, Class C fly ash, and silica fume, of which the volume fractions were 55%, 40%, and 5%, respectively, of total binder. The Blaine finenesses of the cement and the fly ash are 560 and 465 m2/kg, respectively. Fine silica fume with particles smaller than 1 μm in diameter was used, the mean diameter is about 0.15 μm, and the specific surface area determined using the Brunauer, Emmet, and Teller (BET) method is 18,200 m^2/kg. The silica fume has a SiO_2 content of 95%.
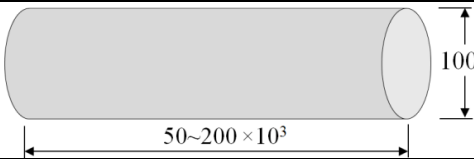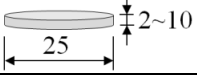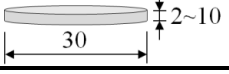
A polycarboxylate-based HRWR was used to enhance the workability. The HRWR has a solid mass content of 23% and a specific gravity of 1.05. The sand was composed of 70% Missouri River sand (0–4.75 mm) and 30% masonry sand (0–2 mm). The fineness moduli of the river sand and the masonry sand are 2.71 and 1.76, respectively. The water absorptions of the river sand and the masonry sand are 0.14% and

0.06 %, respectively. The specific gravities of the river sand and the masonry sand are 2.64 and 2.63, respectively. Straight steel fibers measuring 0.2 mm in diameter and 13 mm in length were used at 0.5% by volume of the UHPC mixture. The fibers have a tensile strength and modulus of elasticity of 1.9 and 203 GPa, respectively.

Two types of GNPs and one type of CNFs were investigated in this study. Their dimensions and material properties are listed in Table 6.1. The illustrations of CNF and GNPs are not in scale. The GNPs were obtained by exfoliation of natural graphite.

The investigated contents of the nanomaterials were 0, 0.05%, 0.10%, 0.15%, 0.20%, and 0.30%, by weight of binder. The UHPC mixture that does not contain nanomaterial is taken as the reference mixture and is coded as "Ref". A total of 16 mixtures were investigated.

Table 6.1 Properties of the investigated NCMs.

Fiber type	Specific gravity (g/cm^3)	Dimensions (nm)	Specific surface area (m^2/g)	Elastic modulus (GPa)	Tensile strength (GPa)	Carbon content (%)
CNF	2.00	100; 50~200×10^3	45	240	30	>95.0
GNP-C	1.95	2~10; 25	300	1000	5	>99.5
GNP-M	1.95	2~10; 30	150	1000	5	>99.5

6.2.2. Dispersion of Nanomaterials. In this study, in order to secure uniform dispersion of nanomaterials, four different treatment methods were used to prepare four UHPC mixtures with 0.3% CNFs by weight, which were designated as T-0, T-1, T-2, and T-3.

(1) T-0: CNFs were directly added into the mixing water, without applying any other treatment. The liquid (CNF + water) was directly used in batching the UHPC mixture. (2) T-1: after CNFs were added into the mixing water, the liquid (CNF + water) was stirred for 4 h before batching UHPC. (3) T-2: The CNFs, HRWR, and polyacrylic acid were added into the mixing water with a mass ratio of 1:4:0.1. The liquid (CNF +

HRWR + polyacrylic acid + water) was stirred for 4 h before batching. (4) T-3: the nanomaterials, HRWR, and polyacrylic acid were added into the mixing water with a mass ratio of 1:4:0.1 in 600-ml water. The liquid (CNF + HRWR + polyacrylic acid + water) was stirred for 4 h, and, then, sonification was applied to the liquid for 70 min using a 500-W (Konsta-Gdoutos 2010), cup-horn high-intensity ultrasonic processor. In every 60 s, ultra-sonification was paused for 30 s to prevent overheating of the suspensions. Note that the polyacrylic acid is a high-molecular-weight polyelectrolyte that can be physically adsorbed on the surface of nanomaterials (Peyvandi et al. 2013).

Flexural tests were conducted to evaluate the flexural properties of the four UHPC mixtures. A higher flexural strength indicates more uniform dispersion of nanomaterials. The investigated UHPC mixtures contained 0.3% CNFs and 0.5% steel fibers, by weight of binder. Table 6.2 shows the results of the flexural properties, which were determined in accordance with ASTM 1609 C. It can be observed that the flexural strength was increased due to the treatment of CNFs before batching. Compared with T-0, the flexural strength and toughness (T150) of T-3 were approximately increased by 65% and 200%, respectively. Proper treatment can significantly improve the uniformity of nanomaterials dispersed in the UHPC matrix, thus increasing the flexural properties and other mechanical properties. Based on the experimental investigation, the treatment method corresponding to T-3 was selected to disperse nanomaterials in this study.

Table 6.2 Effects of different treatments on flexural properties of UHPC.

Code	Flexural strength (MPa)		T150 (J)	
	Average	C.O.V. (%)	Average	C.O.V. (%)
T-0	6.9	1.3	8.1	1.8
T-1	7.6	1.2	10.4	1.4
T-2	9.3	0.9	16.2	1.6
T-3	11.3	0.6	24.0	1.6

6.2.3. Mixing, Casting, and Curing of Nanocomposites. All mixtures were prepared using a 19-L Hobart mixer at room temperature (23 ºC).

The mixing procedure was composed of three steps: (1) dry cementitious materials and sand were mixed at 60 rpm for 3 min; (2) the liquid (i.e. nanomaterials, HRWR, polyacrylic acid, and 600 ml mixing water) was added and mixed at 60 rpm for 3 min; (3) the remaining mixing water and HRWR were added and mixed at 120 rpm for 5

min; (4) micro steel fibers were gradually added within 1 min at 60 rpm; and (5) the final mixing at 120 rpm for 2 min was applied. In total, the mixing time was 14 min to ensure adequate homogeneity. The amount of water in the HRWR, water used for the dispersion of nanomaterials, and a portion of water evaporated (determined by mass loss before and after stirring of liquid with nanomaterials) are accounted for to maintain a fixed w/b of 0.20. For each mixture, specimens were cast in one lift without any mechanical consolidation. Immediately after casting, the specimens were covered with wet burlap and plastic sheets. The specimens were cured at 23 °C and demolded after 1 d. Heat curing at 90 ℃ was then applied for 24 h. Then, the specimens were cured in lime-saturated water at 23 ℃ for 7 d, followed by air-curing at 23 ℃ until the testing at 28 d.

6.2.4. Experimental Program. The detailing experimental program is presented below:

6.2.4.1 Fresh and physical properties. The HRWR dosage was adjusted to ensure that the initial mini-slump is maintained at 280 ± 5 mm, which enables the mixture to be self-consolidating. The mini-slump was measured in accordance with ASTM C 230/C 230M. The air content was measured in accordance with ASTM C 231.

As for the rheological properties, the yield stress (τ_0) and plastic viscosity (μ_p) was evaluated using co-axial viscometer ConTech 5 and determined by Bingham model. The measurement was initiated at 15 min after water addition. The samples were subjected to pre-shear at a rotational velocity of 0.5 rps during 25 s, followed by a stepwise reduction in rotational velocity till zero.

6.2.4.2 Heat of hydration. The rate and extent of hydration were measured using an isothermal conduction calorimeter (Calmetrix I-CAL 8000), which was programmed to maintain the sample at 20 ± 0.1 °C.

The heat of hydration data were continuously recorded from 2 min after completion of mixing the UHPC and continued for 72 h.

6.2.4.3 Autogenous shrinkage. Autogenous shrinkage was measured in accordance with ASTM C1698. Samples were cast in corrugated plastic tubes and stored at constant temperatures of 23 ± 1 ℃ and $50\% \pm 1\%$ RH immediately after casting. The starting time of shrinkage measurements was at the final setting, which was about 12 h

after the contact of binder and water. The frequency of shrinkage measurement was every 12 hours in the first day, then daily in the first week, and weekly until the age of 28 d.

6.2.4.4 Mechanical properties. The compressive strength was determined using 50-mm cubes in accordance with ASTM C 109. Three samples are replicated in each test. The loading rate was maintained at 1.8 kN/min until failure.

Direct tensile tests were conducted using dog-bond specimens with a load frame (MTS 880 with load capacity of 250 kN) operating at displacement control at a rate of 0.5 mm/min, as depicted in Figure 6.1. The thickness of the specimen is 25 mm. Three samples are replicated in each test. During the test, the tensile load was continuously measured using a load cell embedded in the load frame. The tensile deformation was controlled by an extensometer embedded in the load frame. The elongation of the specimen was measured using two linear variable differential transformers (LVDTs) attached to the two sides of the specimens. The results obtained from the two LVDTs were averaged.
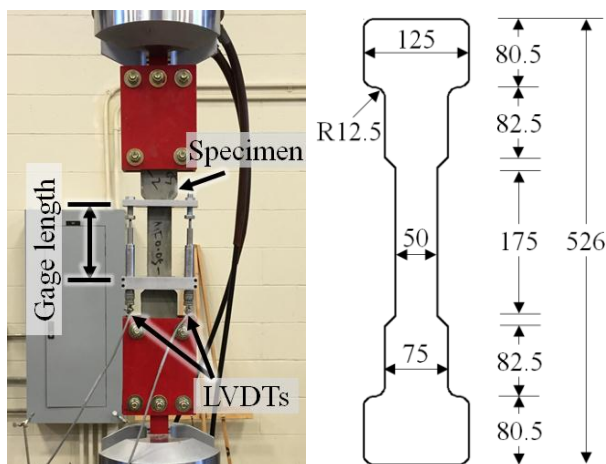
Figure 6.1. Test setup and dog-bone specimen (thickness = 25 mm) for direct tensile test. Unit: mm.

The flexural performance of beam specimens was evaluated under four-point bending test in accordance with ASTM C 1609. Specimens with 76×76 mm cross section were 305 mm long and had a span length of 203 mm. Three replicated samples were used for each test. The same load frame (MTS 880) was used to apply loads at a displacement rate of 0.05 mm/min. A 1-kN preload was applied to allow accommodation

of the loading apparatus. The deflections of the specimens were measured using two linear variable differential transformers LVDTs. The applied loads were recorded by a load transducer embedded in the load frame.

6.2.4.5 Single fiber pull-out test. Single fiber pull-out tests were carried out using a customized setup, as shown in Figure 6.2. During casting, a known length of steel fiber was embedded in 50-mm cube specimens that were tightly constrained by the steel frame system. The load and the pull-out displacement were simultaneously measured using a load cell (load capacity: 1000 N) and a LVDT that were embedded in the load frame. The test was performed under displacement control mode at a rate of 0.05 mm/min. Three identical steel fibers were deployed on each cube specimen. A half length of each steel fiber was embedded in matrix, and a 4-mm length outside of matrix was gripped by the load frame for applying tensile force. Three mixtures were applied, which were Ref, the UHPC mixture containing 0.15% GNP-C, and the UHPC mixture containing 0.30% GNP-C.
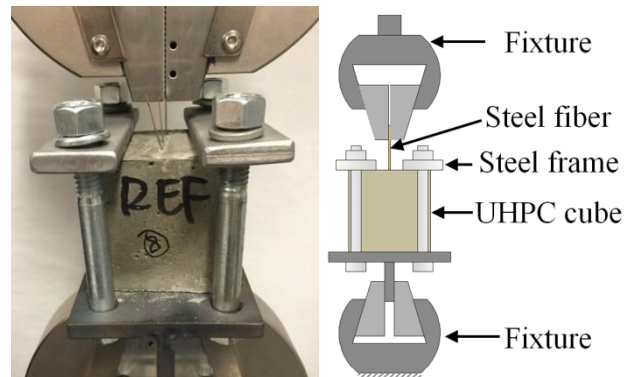
Figure 6.2. Test setup and specimen of single fiber pull-out test.

6.2.4.6 Mercury intrusion porosimetry. The total porosity and pore size distribution of the samples with CNFs were determined using mercury intrusion porosimetry (MIP).

For each investigated UHPC mixture, three samples were tested. In the MIP testing, the applied low and high pressures were 0.28 and 414 MPa, respectively; the contact angle was 140º; the surface tension was 480 mN/m. The hydration reactions of UHPC samples were terminated at 28 d by soaking the samples in 99.8% isopropyl alcohol and drying at 50 ºC in an oven for 24 h before examination.

6.2.4.7 Scanning electron microscopy. The microstructures and morphology of fractured specimens were inspected using an S-4700 FE-SEM (Hitachi High Technologies Inc.). The fractured surfaces of the UHPC matrix were cleaned by performing ultra-sonification in 99% isopropyl alcohol for 20 min. Fractured specimens were then coated with a very thin layer of gold using an ion sputtering coater for conduction.

6.3. EXPERIMENTAL RESULTS

The results are detailed as follows:

6.3.1. Fresh and Physical Properties. The effects of nanomaterials on flowability of UHPC mixtures are associated with the nanomaterials content, as shown in Table 6.3.

Table 6.3 Fresh and physical properties of UHPC with different content of nanomaterials.

Type	Content (%)	HRWR demand (%)	Air content (%)	Yield stress (Pa)	Plastic viscosity (Pa·s)
CNF	0	0.97	2.5	15	40.7
	0.05	0.78	2.5	13	37.6
	0.10	0.92	2.5	16	41.8
	0.15	0.99	2.8	16	46.4
	0.20	1.01	3.0	17	52.2
	0.30	1.04	3.2	19	55.5
GNP-C	0	0.97	2.5	15	40.7
	0.05	0.69	2.4	10	35.6
	0.10	0.71	2.5	14	36.0
	0.15	0.74	2.5	16	37.6
	0.20	0.74	2.5	18	38.1
	0.30	0.92	3.0	20	39.4
GNP-M	0	0.97	2.5	15	40.7
	0.05	0.74	2.5	12	36.8
	0.10	0.78	2.5	18	37.4
	0.15	0.83	2.6	19	38.0
	0.20	0.85	3.0	19	39.1
	0.30	0.87	3.0	22	40.2

The HRWR demand, which allows the mixtures to achieve an initial mini-slump of 280 ± 5 mm for securing self-consolidating property, is given as the active powder weight percentage of the cementitious materials. The HRWR demand is a key parameter to evaluate flowability of UHPC. A low HRWR demand indicates good flowability. The nanomaterials have two opposite effects on flowability. On one hand, certain amount of

nanomaterials can improve the packing density of the cementitious particles. The extra water by packing improvement can lubricate solid particles of the cementitious materials and sand, which improves flowability and reduces the HRWR demand. The lubrication effect is dominant when the content of the nanomaterials is no more than 0.05%. The HRWR demands of CNF mixtures are higher than those of the corresponding GNP mixtures at the same nanomaterials content, indicating that CNFs had less lubrication effects than the GNPs because the CNFs have greater aspect ratios (fiber length / diameter) than those of GNPs. On the other hand, the nanomaterials adsorb the HRWR and water, which represents an adverse effect on the flowability and increases the HRWR demand. When the content of nanomaterials is increased from 0.05% to 0.3%, the adsorption effect becomes dominant, which explains why the HRWR demand was increased.

Table 6.3 lists the air content of the UHPC mixtures. Overall, the air content increased with the nanomaterials content. As the nanomaterials content was increased from 0 to 0.3%, the air content was increased by 30% for the UHPC mixture with CNFs, and by 20% for the UHPC mixtures with GNPs. Substantial increase in air content may be detrimental for mechanical properties.

For the rheological properties, while the mini-slump flow was fixed, the yield stresses of UHPC did not significantly change. For the three types of carbon nanomaterials, the plastic viscosity decreased when the nanomaterials content was no more than 0.05% due to the enhancement of packing density, and increased when the nanomaterials content was increased from 0.05% and 0.3%. For UHPC with CNFs, increasing the CNF content to 0.3% led to 35% increase in plastic viscosity, compared with that of the reference mixture.

The addition of CNF accelerates the re-agglomeration of cement particles due to its high aspect ratio. CNF is adsorbed on the surface of cement particles through intermolecular forces, which partially weaken the steric hindrance and electrostatic repulsion of HRWR (Meng et al. 2016), resulting in the formation of flocculation structures. The re-agglomeration action of CNF becomes more obvious with the increase of CNF content, thus increasing the viscosity.

Nevertheless, for the GNP-C and GNP-M, the plastic viscosity values were less than those of the reference mixture. This is likely because the addition of GNPs increases the packing density of the cementitious materials. It should be noted that, a low plastic viscosity is preferred for UHPC to achieve a high filling capacity (Khayat 1999).

6.3.2. Autogenous Shrinkage. Figure 6.3 shows the evolution of autogenous shrinkage of the investigated UHPC mixtures until 28 d.
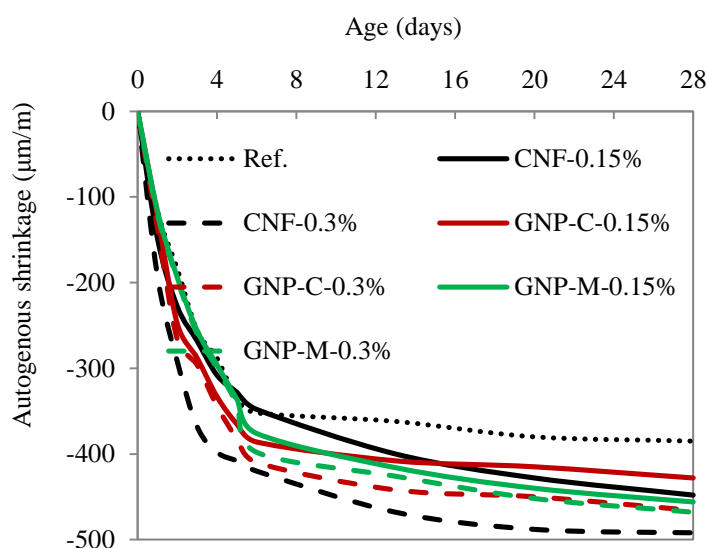
Figure 6.3. Results of autogenous shrinkage of UHPC with different types and contents of nanomaterials.

Overall, the addition of nanomaterials increased the autogenous shrinkage at all ages. This could be mainly due to the refinement of pore size and increase of mesoporous (pore diameter: 2–50 nm) volumes which is directly related with the autogenous shrinkage caused by self-desiccation, as can be seen in Section 3.5. Moreover, the cement degree of hydration increased with the increase of nanomaterials, the chemical shrinkage which contributed to autogenous shrinkage was also increased. For addition of 0.15% nanomaterials, the UHPC incorporating GNP-M resulted in the highest 28-d autogenous shrinkage (456 μm/m), which increased by 20% compared with that of the reference mixture without nanomaterials. The addition of 0.15% GNP-C led to very high early age shrinkage of UHPC (< 7 d), but after 7 d, the shrinkage stabilized. When the addition of nanomaterials increased to 0.3%, the autogenous shrinkage of UHPC with CNF, GNP-C, and GNP-M increased by 30%, 20%, and 20%, respectively, compared with that of the

reference mixture. In general, the UHPC with 0.3% CNF resulted in the highest 28-d autogenous shrinkage. It can be mainly due to the larger length and aspect ratio and small stiffness of CNF compared with CNPs that can result in higher self-desiccation induced shrinkage (Polat et al. 2015).

6.3.3. Compressive Strength. The variations of compressive strength of UHPC mixtures with different nanomaterials content at 28 d are shown in Figure 6.4.

It can be seen that the compressive strength of the UHPC slightly increases (5 to 8 MPa) with the content of nanomaterials. The increase in compressive strength can be attributed to the "bridging effect" of the CNFs and GNPs for microcracks and the "filler effect" for accelerating the hydration reactions of the cementitious materials (Han et al. 2015). Compared with the CNF and the GNP-M, the GNP-C had slightly higher compressive strength of the UHPC.
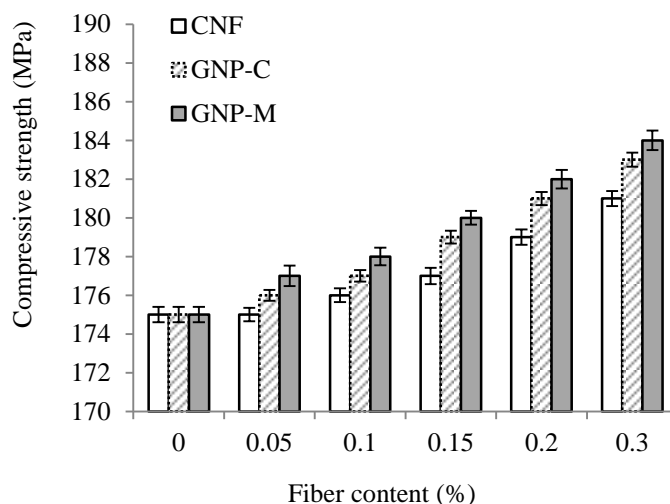
Figure 6.4. Effect of nanomaterials content on (a) compressive strength at 28 d, (b) tensile strength at 28 d, and (c) energy dissipation at 28 d of UHPC.

6.3.4. Direct Tensile Responses. Figure 6.5(a) shows the measurement results from extensometer of load frame, LVDTs, and force sensor attached to the load frame, respectively, for the reference UHPC mixture made without any nanomaterials.

The reading from the extensometer linearly increased with time at a constant rate of 0.05 mm/min. The direct tensile response is analyzed at three zones that are shown in Figure 6.6:
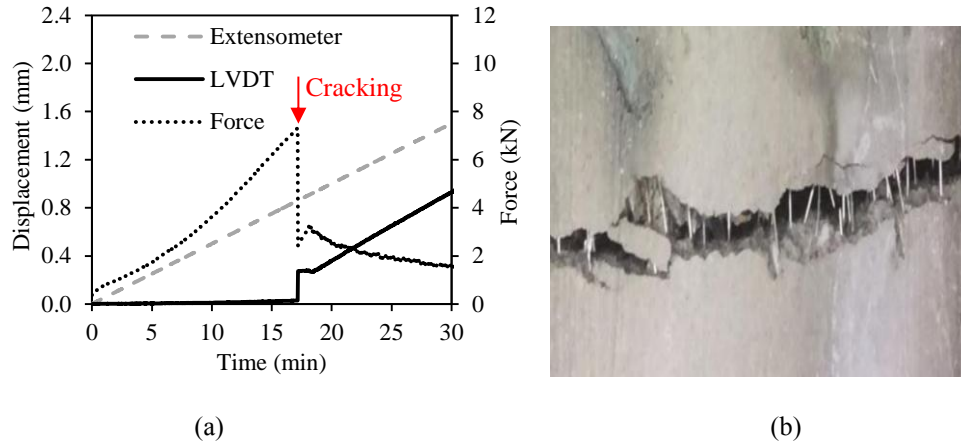
Figure 6.5. Direct tensile test results of a reference sample: (a) time histories and (b) bridging effect of steel fibers after cracking.

(1) Elastic zone. Before fracture occurred, the readings from the LVDTs were associated with elastic deformation of the specimen within the gage length (Figure 6.1), which was very small in comparison with the deformation measured from the extensometer. This is because the displacement from the extensometer includes the elastic deformation of the setup and any displacement of the specimen gripping to the load frame, in addition to the elastic deformation of the specimen. The load increased nonlinearly with an increasing slope.

(2) Cracking zone. At the onset of "major" cracking of the specimen, the displacements measured from LVDTs abruptly jumped to a relatively large value. The tensile load dropped to a small, but nonzero value, given that steel fibers can bridge crack interfaces and allow the cracked specimen to carry a sustained load, as depicted in Figure 6.5(b). In the vicinity of the crack faces, steel fibers and the nano-reinforcements were pulled out from the cementitious matrix. The microstructures of fracture interface are inspected, as discussed latter.

(3) Post-cracking zone. After major cracking, readings from the extensometer and LVDTs increased at the similar rates, as depicted in Figure 6.5(a). The discrepancy was due to the accommodation of specimen to the setup and elastic deformation of the specimen length beyond the gage length of the LVDT. The carried load was mainly associated with the interfacial bond and friction between steel fibers and matrix, which is elaborated in a latter section.
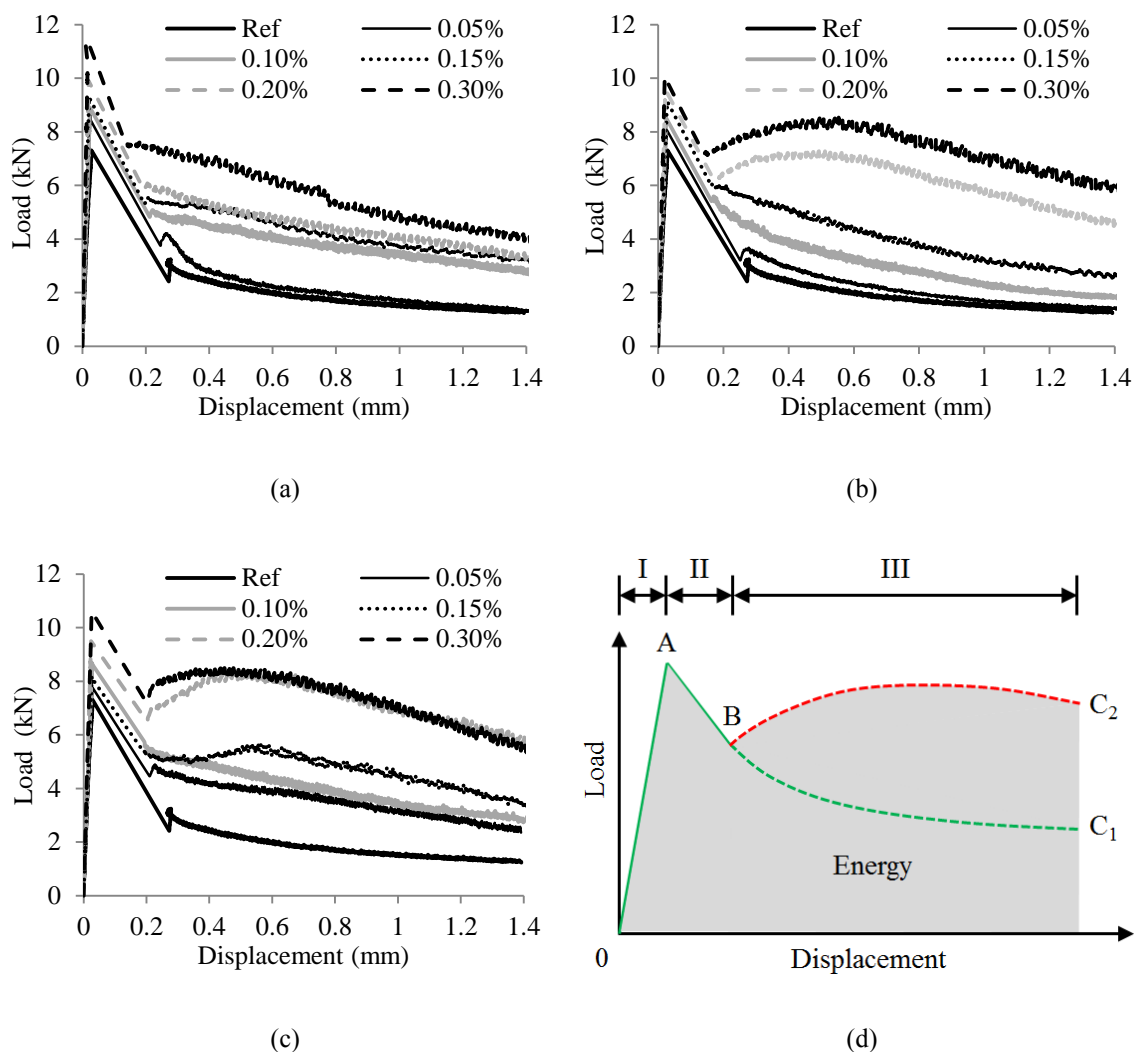
Figure 6.6. Direct tensile test results of mixtures incorporating: (a) CNF, (b) GNP-C, (c) GNP-M, and (d) the three stages along the load-displacement curve.

The load-displacement relationships of the UHPC mixtures reinforced by CNF, GNP-M, and GNP-C are plotted in Figures 6.6(a)–6.6(c), respectively. The load was measured with the load cell and the displacement was taken as the average of the two LVDTs. In the case of the reference mixture (Ref) without nanomaterials, the load-displacement curves of UHPC with nanomaterials can be divided into three zones (I–III), as depicted in Figure 6.6(d):

(1) Elastic zone (I): the tensile load increased linearly with displacement until cracking occurs. The use of nanomaterials increased the cracking load, which can be attributed to the combination of "bridging effect" and "filler effect". The addition of

nanomaterials can provide more preferable sites for the initiation and growth of nucleation of hydrates, thus accelerating hydration reactions.

(2) Cracking zone (II): the tensile load decreases with displacement to a relatively low value after cracking. Due to the presence of steel fibers, which can arrest cracking, the load does not drop to zero.

(3) Post-cracking zone (III): as the displacement is further increased after cracking, different mixtures demonstrate different post-cracking behaviors. The mechanical performance of the UHPC mixtures in the post-cracking regime is mainly associated with fiber pull-out behavior. For the UHPC mixtures without nanomaterials or with low content of nanomaterials, a "softening" behavior is observed (i.e. following B-C_1). For the UHPC mixtures incorporating GNP-M or GNP-C, when the GNP content is higher than 0.20 %, a "hardening" behavior is observed (i.e. following B-C_2).

The cracking load at the peak point "A" (Figure 6.6(d)) corresponds to tensile strength of the specimenThe displacement range for integration was 0–1.4 mm, which is a well-accepted range in the literatures of tensile tests of fiber reinforced cementitious composites (Nguyen et al. 2014). The tensile strength and energy absorption capacity of the tested dog-bone specimens are summarized in Table 6.4.

Table 6.4 Tensile strength and energy absorption capacity in tension.

Type	Content (%)	Tensile strength (MPa)		Energy absorption capacity (J)	
		Average	Standard deviation	Average	Standard deviation
CNF	0	5.84	0.66	3.77	0.59
	0.05	7.01	0.75	4.13	0.68
	0.10	7.65	0.82	5.79	0.87
	0.15	7.97	0.91	6.32	0.77
	0.20	8.36	0.78	7.28	0.91
	0.30	9.09	0.98	7.85	0.88
GNP-C	0	5.84	0.66	3.77	0.59
	0.05	6.21	0.74	5.26	0.68
	0.10	6.67	0.81	5.84	0.85
	0.15	6.49	0.90	6.62	0.76
	0.20	7.68	0.78	8.95	0.91
	0.30	8.50	0.95	9.53	0.86
GNP-M	0	5.84	0.66	3.77	0.59
	0.05	6.49	0.74	4.62	0.68
	0.10	6.99	0.79	5.37	0.87
	0.15	7.32	0.88	6.96	0.77
	0.20	7.67	0.77	9.39	0.92
	0.30	8.17	0.95	10.80	0.88

As the content of CNF is increased from 0 to 0.30%, the tensile strength is increased by 56% and the energy absorption capacity is increased by 108%. As the content of GNP-C increases from 0 to 0.30%, the tensile strength is increased by 40%, and the energy absorption capacity is increased by 187%. As the content of GNP-M is increased from 0 to 0.30%, the tensile strength is increased by 45%, and the energy absorption capacity is increased by 153%.

6.3.5. Flexural Responses. The flexural test results of beam specimens are compared in Figures 6.7(a)–6.7(c).

(a)

(b)

(c)
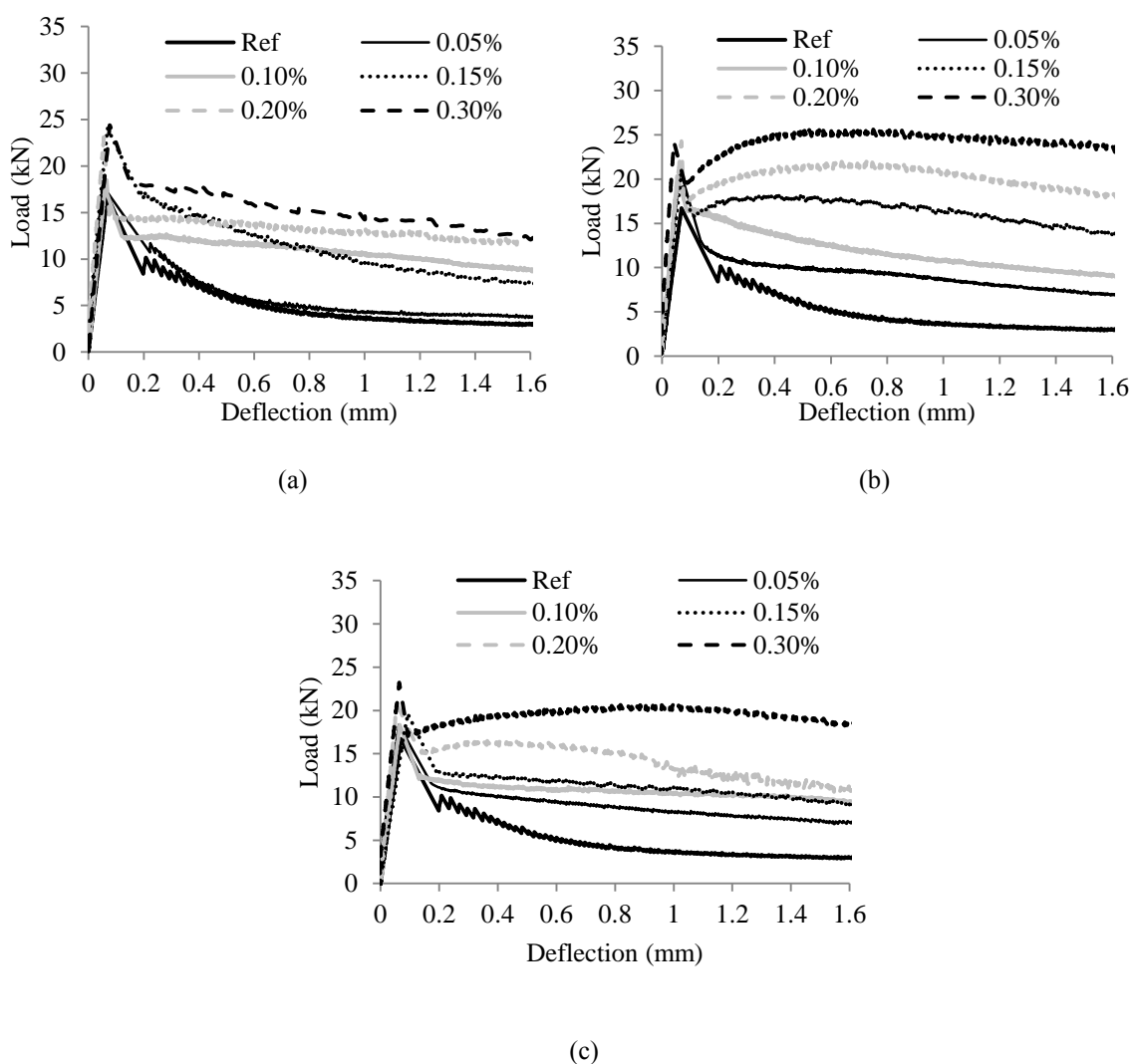
Figure 6.7. Flexural test results of mixtures incorporating: (a) CNF, (b) GNP-C, and (c) GNP-M.

Similar to the tensile load-displacement curves, each load-deflection curve can be divided into: (1) elastic zone, (2) cracking zone, and (3) post-cracking zone. In the elastic zone, the carried load approximately linearly increases with the mid-span deflection. In the cracking zone, the carried load decreases with the deflection to a relatively low value when cracking occurs. As in the case of tensile strength, in the post-cracking zone, different mixtures demonstrate different post-cracking behaviors. For the UHPC mixtures made without nanomaterials or with low content of nanomaterials, a "softening" behavior was obtained. For the UHPC mixtures incorporating GNP-M or GNP-C, when the GNP content achieved 0.20 %, a "hardening" behavior was observed.

The flexural strength is calculated in accordance with ASTM C1609. The area under load versus deflection curve between deflection values of 0 to L/150 (L = 203 mm) is referred to as T150, which represents the toughness and is an indicator of energy dissipation. The results of flexural strength and T150 are summarized in Table 6.5. The use of 0.3% CNF can increase flexural strength by 46% and the T150 by 174%. Compared with no GNP, 0.3% GNP-C can increase flexural strength by 59%, and the T150 by 276%. As the content of GNP-M is increased from 0 to 0.30%, the flexural strength is increased by 39% and the T150 is increased by 203%.

Table 6.5 Flexural strength and T150 values.

Type	Content (%)	Flexural strength (MPa)		T150 (J)	
		Average	Standard deviation	Average	Standard deviation
CNF	0	7.73	0.43	8.75	0.65
	0.05	8.17	0.58	10.05	0.59
	0.10	8.28	0.38	15.46	0.96
	0.15	10.70	0.45	17.65	1.10
	0.20	11.12	0.54	18.47	1.38
	0.30	11.26	0.62	23.99	1.56
GNP-C	0.05	9.35	0.41	13.85	0.68
	0.10	9.69	0.40	17.00	0.79
	0.15	10.58	0.52	22.71	1.26
	0.20	11.23	0.50	27.50	1.18
	0.30	12.31	0.70	32.88	1.80
GNP-M	0.05	8.49	0.27	13.46	0.51
	0.10	8.94	0.35	15.15	0.72
	0.15	9.53	0.42	16.32	0.39
	0.20	10.02	0.47	20.19	1.01
	0.30	10.74	0.53	26.53	1.39

6.4. DISCUSSION

6.4.1. Heat of Hydration. Figures 6.8(a) and 6.8(b) show the influence of different types and contents of nanomaterials on the hydration kinetics of the UHPC mixtures.

The addition of CNFs retarded the cement hydration and increased the cumulative heat (i.e. degree of cement hydration), while the addition of GNP-C and GNP-M slightly accelerated the heat of hydration. Among the three types of nanomaterials, the GNP-M most effectively increased the cumulative hydration heat. A higher cumulative heat indicates a higher degree of cement hydration, which could have positive effect on UHPC's properties. The nanomaterials possess the "nano size effect" that enables them to serve as nuclei, thus accelerating the hydration reactions of cementitious materials and reducing the porosity of concrete (Singh et al. 2013). Due to the relatively larger specific surface area of the GNPs compared with the CNFs, more hydrates may form in the UHPC mixtures containing GNPs.

(a)   (b)
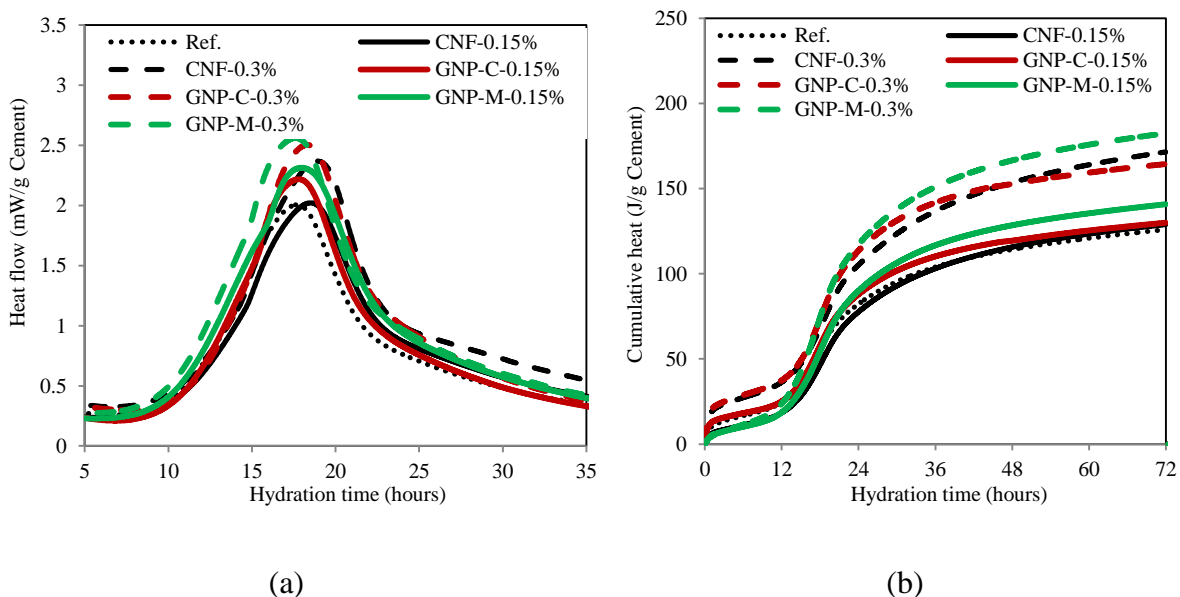
Figure 6.8. Isothermal calorimetry results of cementitious materials at 20 ℃ for the investigated UHPC mixtures: (a) hydration heat flow and (b) cumulative heat.

For more information of hydration, the detailed results of cement hydration in the presence of different contents of carbon nanomaterials are listed in Table 6.6, where Q_{min} and $t(Q_{min})$ represent the minimum heat release rate and the time when Q_{min} is achieved,

respectively. This specific time is considered as representative of the duration and end of the induction period. The maximum heat release rate and the time corresponding to the peak of hydration are denoted as Q_{max} and $t(Q_{max})$, respectively. It can be observed that the use of CNF prolonged the induction period. The retardation of the primary peak of hydration heat flow can be attributed to the higher dosage of HRWR compared with that of other mixtures. The adsorbed HRWR molecules inhibit the surface dissolution sites, thus, delaying the time needed to reach the critical super-saturation for Portlandite precipitation. It can also because that the CNFs are susceptible to adhere on the surface of cement particles and thus hinder the hydration of cement. Compared with the reference mixture, the use of 0.30% CNF retarded the end of induction period by 5%, but increased the cumulative heat at 72 h by 35%. In the cases of GNP-C and GNP-M, less HRWR was in demand, which can be attributed to the improvement in packing density due to the presence of fine particles. Both of the GNPs shortened the induction period, which was because the high surface area of nanoparticles increased the number of nucleation sites for precipitating hydration products. A greater content of GNPs led to a higher cumulative heat. By adding 0.30% GNP-M, the end of induction period was 205 min, which is only 50% that of the reference mixture. Moreover, the addition of 0.30% GNP-M increased the cumulative heat at 72 h by 45%, compared with that of the reference mixture.

Table 6.6 Results of heat of hydration.

Type	Content (%)	End of induction period		Peak of hydration		Cumulative heat at 72 h (J/g)
		Q_{min} (mW/g)	$t(Q_{min})$ (min)	Q_{max} (mW/g)	$t(Q_{max})$ (min)	
CNF	0	0.258	384	2.001	1058	126
	0.05	0.246	380	2.006	1052	126
	0.10	0.238	386	2.014	1084	128
	0.15	0.231	392	2.022	1110	130
	0.20	0.284	395	2.188	1121	146
	0.30	0.326	400	2.369	1136	171
GNP-C	0	0.258	384	2.001	1058	126
	0.05	0.238	380	2.056	1056	128
	0.10	0.222	374	2.111	1060	130
	0.15	0.211	366	2.218	1062	132
	0.20	0.256	358	2.337	1083	142
	0.30	0.301	320	2.496	1097	164
GNP-M	0	0.258	384	2.001	1058	126
	0.05	0.256	360	2.109	1063	130
	0.10	0.260	333	2.235	1070	165
	0.15	0.266	312	2.313	1078	141
	0.20	0.265	300	2.476	1064	160
	0.30	0.265	205	2.561	1052	182

6.4.2. Single Fiber Pull-Out Responses. The pull out load-slip curves of three UHPC mixtures incorporating different contents of GNP-C are compared in Figure 6.9.

The average and standard deviations of the pull-out results are listed in Table 6.7. Before debonding occurs, the bond of the interface between a steel fiber and the matrix is composed of chemical adhesive bond, friction due to shrinkage of the matrix, and interlock effect due to surface roughness of the steel fiber.

The incorporation of nanoplatelets enhances bond strength, which can be attributed to the modification of the interface due to the presence of nanoplatelets that can provide additional sites for the nucleation of hydrates. When debonding takes place at the interface, the chemical adhesive bond is destroyed, and, hence, the fiber pull-out behavior is primarily dependent on the friction and mechanical interlock effects. As illustrated in Figure 6.10(a), the surface of the intact steel fiber is rough and uneven, which can enhance bond to the highly flowable UHPC mixture. The shrinkage of the mixture during hydration and curing further enhances the holding force applied on the steel fiber (Wille and Naaman 2013). The slip of steel fiber in the UHPC matrix can lead to particle abrasion in the fiber tunnel, wedging of the particles, scratching the fiber surface and partly or full delamination of the brass coating, as indicated in Figure 6.10(b) (Wille and Naaman 2013), which can enhance roughness and bond between steel fibers and UHPC matrix. The area under the pull-out load-slip curve represents the pull-out energy, which increases with the content of nanomaterials, as shown in Table 6.7. The fluctuations of the curves are attributed to the different roughness conditions of the surface of steel fibers and the fiber tunnels in the matrix.
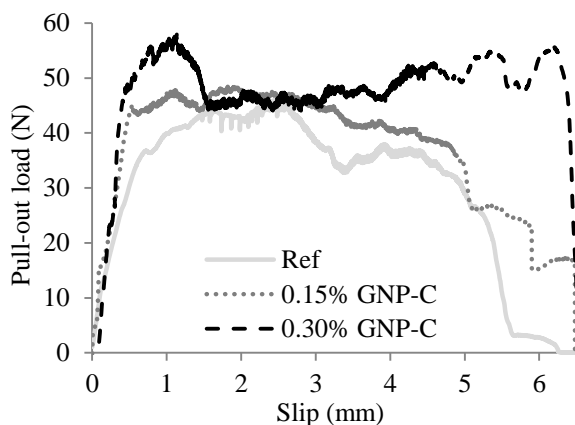
Figure 6.9. Single fiber pull-out test results.

Table 6.7 Single fiber pull-out test results.

Matrix	Maximum force (N)		Energy (mJ)	
	Average	Standard deviation	Average	Standard deviation
Ref	46.2	3.5	169	18
0.15% GNP-C	52.6	5.1	246	22
0.30% GNP-C	58.5	6.6	302	29
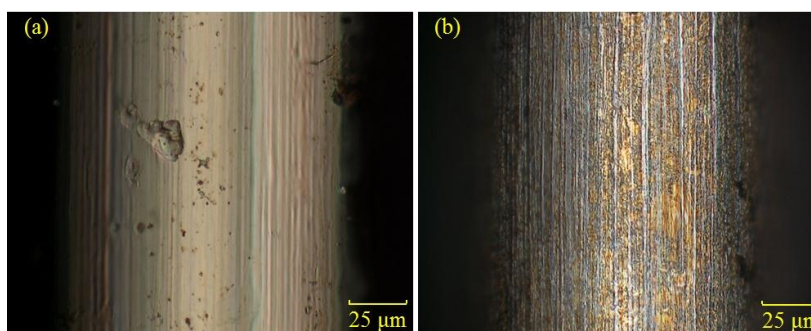
Figure 6.10 Optical microscopy of steel fiber: (a) before pull-out test and (b) after pull-out test.

6.4.3. Microstructures. Figure 6.11shows the pore size distribution of the UHPC mixtures covering pores with apparent diameter of 4 nm to 105 μm.

A peak was observed for each of the three curves with pore diameters in between 10 and 100 nm. The peak corresponding to the most probable diameter shifted towards finer pore sizes and the value was decreased from 0.045 to 0.017 cc/g as for CNF was increased from 0 to 0.3%. This decrease led to an increase in mechanical properties. The decrease in capillary pores indicated more hydration products were produced to fill the pores when more nanomaterials were added. Figure 6.11shows that the total porosity is reduced by about 35% as the CNF increased from 0 to 0.3%.

The results of pore size distribution, including gel micro-pores (< 10 nm), capillary pores (10–5000 nm), and macro-pores (> 5000 nm), are indicated in Figure 6.11(b). The porosity of macro-pores, which are mainly due to entrapment of air, is ranged from around 2.5% to 4.5% of the investigated mixtures. The addition of CNF significantly decreased the volume fraction of capillary pores and increased the gel micro-pores porosity. As the CNF content was increased from 0 to 3%, the total porosity was reduced from 13.4% to 8.6%. As the CNF content was increased from 0 to 0.3%, the

porosity of capillary pores reduced by 76%, and the gel pores increased by 68%. This is indicating a refinement of the pore structure. The increase in gel pores can be attributed to the enhanced degree of hydration of binder in the presence of high-volume CNFs. The reduction in capillary pores porosity might be due to the fact that CNFs promoted the hydration reactions and led to refined microstructures of the hydration products.

Microstructure image of the fracture interfaces of mixtures with 0.3% nanomaterials are shown in Figures 6.12(a)–6.12(d). Fiber agglomerates are observed in the UHPC mixture (Figure 6.12(a)), in which the CNFs were directly added in the mixing water, without applying any treatment for better dispersion. After the treatment of CNFs, the CNFs are observed to be more uniformly dispersed in the matrix (Figure 6.12(b)).

Partially embedded CNFs and GNPs were observed in the matrix, as shown in Figures 6.12(b)–6.12(d).

Immediately when micro cracks are initiated in the matrix, the CNFs and GNPs can bridge the crack interfaces. With the increase in applied load, eventually, the CNFs and GNPs were pulled out from the matrix, dissipating energy at the nanomaterial-matrix interfaces. The bridging effects for cracks at nano- or micro-level greatly enhance the cracking loads of the UHPC mixtures, which can be a significant compensation for the bridge effects of steel fibers at meso-level.
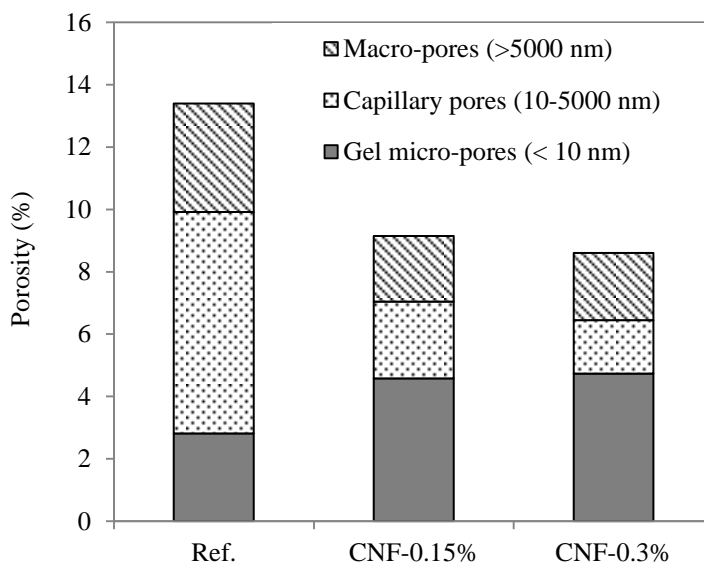
Figure 6.11. Effect of CNF content on porosity of UHPC after hydrating for 28 d.

6.4.4. Enhancement Mechanisms. Generally, the mechanical properties of nanocomposite UHPC are associated with the intrinsic mechanical properties of CNFs and GNPs, nano size effect and filler effect of CNFs and GNPs (Makar and Chan 2009), improvement to the microstructures and the interfacial transition zones of the nanocomposite, stronger bond between steel fiber and matrix, and bridging effect for microcracks (Wille and Loh 2010). The different morphological properties of CNF and GNPs caused different mechanical properties of the nanocomposite UHPC. The mechanisms can be discussed in terms of the chemical reactions and mechanical behaviors:

(1) The nanomaterials possess the "nano size effect" that enables them to serve as nuclei that accelerate the hydration reactions of cementitious materials and reduce the porosity of concrete (Singh et al. 2013). Due to the relatively larger specific surface area of the GNPs compared with the CNFs, more hydrates can form in the UHPC mixtures containing GNPs. Therefore, the UHPC mixtures containing GNPs exhibited higher compressive strengths than the UHPC mixtures mixed with the CNFs.

(2) Overall, the CNFs have larger length and aspect ratio and smaller rigidity/stiffness, compared with the GNPs, as shown in Table 6.1. Thus, CNFs are more effective than the GNPs in bridging microcracks and enhancing the cracking stress/load due to the large length. The enhancement of CNFs on the properties of UHPC mainly results from the extensively-distributed enhancement network of CNFs in the matrix (Wille and Naaman 2013). Therefore, the UHPC mixtures containing CNFs demonstrated higher tensile strength than the UHPC mixtures mixed with GNPs. However, the CNFs have smaller rigidity/stiffness than the GNPs, and thus are less effective in the steel fiber pull-out process. The mechanical performance of the UHPC mixtures in the post-cracking stage is mainly associated with fiber pull-out behavior. Therefore, the UHPC mixtures mixed with GNPs demonstrated higher load resistance in the post-cracking part of the curves in Figures 6.6 and 6.7. In addition, the GNPs have the "surface effect", which leads to enormous interface area, thus ensuring intimate bond between the GNPs and the matrix due to Van der Waals forces. The platelet shapes of GNPs enable them to block and divert microcracks, thus slowing the crack propagation and formation of the crack network. The bridging effect of GNPs can delay the initiation and opening up of cracks.

In addition, GNPs enhance the mechanical properties of nanocomposites via crack-arresting effect and the improvement to the interfacial transition zone of composites (Le et al. 2014).

(a)   (b)

(c)   (d)
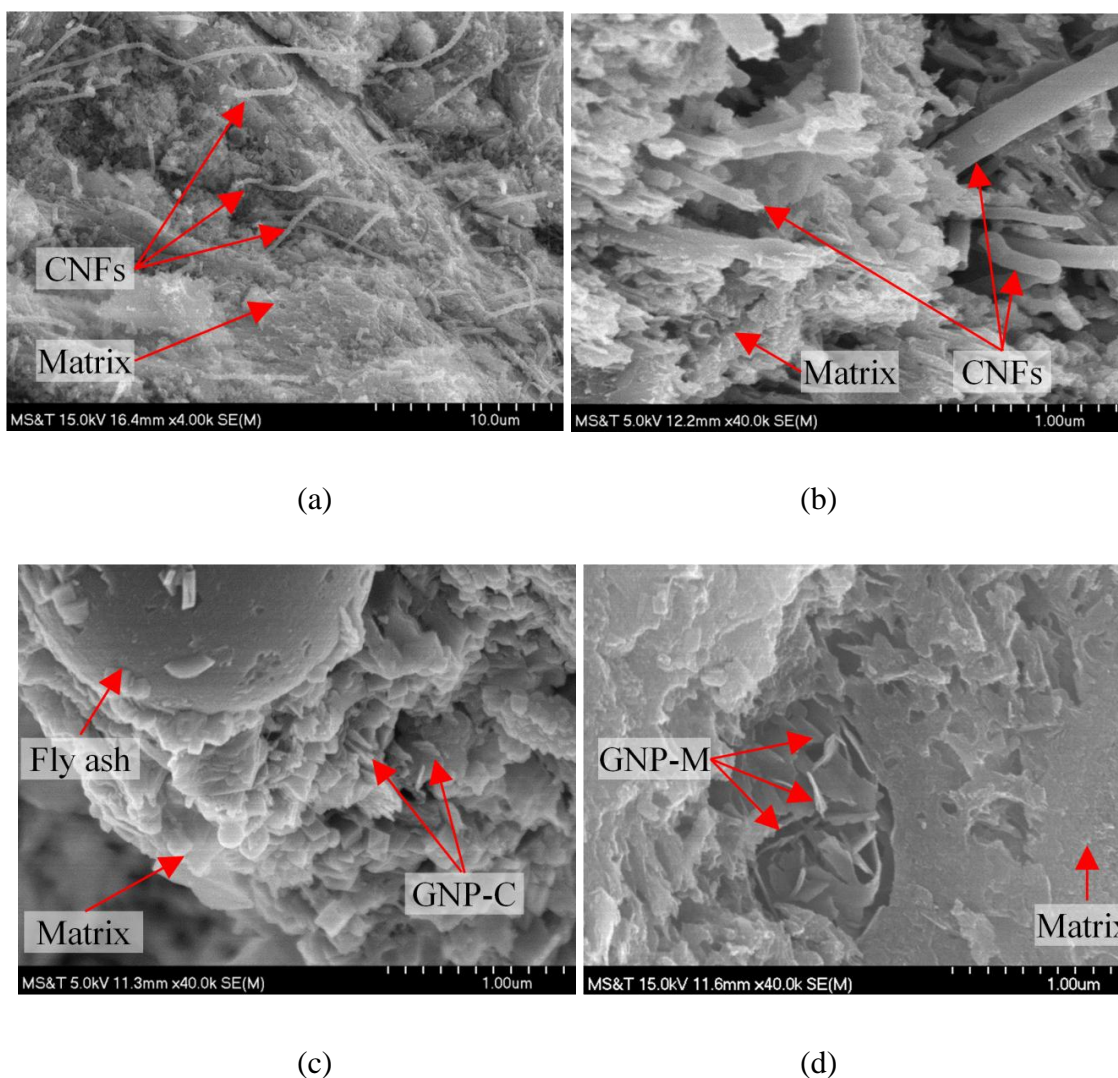
Figure 6.12. Microstructures at fracture interfaces of UHPC with different nanomaterials: (a) CNF at 4,000X, (b) CNF at 40,000X, (c) GNP-C at 40,000X, and (d) GNP-M at 40,000X.

6.5. SUMMARY

Based on the above investigation, conclusions can be drawn below:

(1) As the nanomaterials content was increased from 0 to 0.3%, the air content was increased by 20%−30%. When the nanomaterial content was no more than 0.05%,

the HRWR demand decreased with the addition of the nanomaterials, meaning the use of small amount of nanomaterials could improve the flowability of the UHPC mixture. However, as the nanomaterial content was more than 0.05%, further addition of nanomaterials had adverse effects on the flowability.

(2) When the mini-slump flow was fixed at 280 ± 5 mm, the addition of nanomaterials did not substantially influence the yield stress, but changed the plastic viscosity. The plastic viscosity decreased with the nanomaterials content when the content was no more than 0.05%, and increased with the nanomaterials content when the content was more than 0.05%. The addition of CNFs led to higher viscosity, while adding GNPs reduced the plastic viscosity, compared with the reference mixture.

(3) The increase of nanomaterials content increased the autogenous shrinkage at all ages. The autogenous shrinkage of UHPC with 0.3% CNF, GNP-C, and GNP-M was increased by 30%, 20%, and 20%, respectively, compared with that of the reference UHPC mixture.

(4) The incorporation of nanomaterials increased the direct tensile strength of UHPC. As the content of CNF was increased from 0 to 0.30%, the tensile strength and energy absorption capacity were increased by 56% and 108%, respectively. As the content of GNP-C was increased from 0 to 0.30%, the tensile strength and energy absorption capacity were increased by 40% and 187%, respectively. As the content of GNP-M was increased from 0 to 0.30%, the tensile strength and energy absorption capacity were increased by 45% and 153%, respectively.

(5) The incorporation of nanomaterials enhanced flexural strength of UHPC. Compared with the UHPC mixture without nanomaterial, the use of 0.3% CNF increased the flexural strength and the T150 by 46% and 174%, respectively; the use of 0.3% GNP-C increased the flexural strength and the T150 by 59% and 276%, respectively; the use of 0.3% GNP-M increased the flexural strength and the T150 by 39% and 203%, respectively.

(6) The duration of induction period was extend by the use of CNFs, and shortened by the use of GNPs. The cumulative heat release was increased by increasing the nanomaterials content.

(7) As revealed in the single fiber pull-out test, the incorporation of the nanomaterials enhances bond strength and post-debonding performance of the interface between steel fiber and the matrix.

(8) The use of nanomaterials reduced the total porosity of the UHPC. As the CNF content increased from 0 to 0.3%, the total porosity was reduced by 35%, the capillary pores was reduced by around 75%, and the gel pores was increased by around 70%.

7. UNIQUE MECHANICAL PERFORMANCE CHARACTERIZATION OF UHPC

7.1. BACKGROUND

In addition to quasi-static loads, UHPC can be used to resist short-duration loads or impact loads due to earthquake, wind, blast, or collision (Xu and Wille 2015). Ranade et al. (2015) studied the effects of strain rate on the direct tensile properties of a high-strength, high-ductility concrete. As the tensile strain rate was increased from 10^{-4} /s to 10 /s, the cracking strength and the tensile strength were increased by 53% and 42%, respectively. Zhang et al. (2014) investigated the effects of loading rate on the flexural tensile strength and fracture energy of a steel fiber reinforced concrete. As the increasing rate of mid-span deflection was increased from 10^{-3} mm/s to 10^{3} mm /s, the flexural tensile strength and fracture energy were increased by 248% and 152%, respectively. Pyo et al. (2015) and Tran et al. (2016) studied the effects of tensile strain rate on the direct tensile strength and fracture energy of UHPC mixtures. Smooth and twisted steel fibers were blended at different volume ratios in the UHPC mixtures. Pyo et al. (2015) reported that the tensile strength and fracture energy of the UHPC mixtures were respectively increased by up to 36% and 96%, as the strain rate was increased from 10^{-4} /s to 10^{-1} /s. Tran et al. (2016) reported that the tensile strength and fracture energy were respectively increased by up to 190% and 920%, as the strain rate was increased from 5 /s to 92 /s.

While the structural dimensions in many projects vary significantly, the practical sizes of test specimens in the laboratory are limited to a relatively small range. However, mechanical properties of fiber reinforced composites correlate with the geometry of the test specimen (Yoo et al. 2016; Mahmud et al. 2013; Nguyen et al. 2013). In general, the flexural tensile strength of fiber reinforced composites decreases with the depth or thickness of the specimen (Kim et al. 2010). The depth and width are the primary geometrical parameters for unnotched specimens, while the notch-to-depth ratio (N/D) is a primary geometrical parameter for notched specimens with a specified cross section (Vydra et al. 2012). Size effects of fiber reinforced composites have been studied by different researchers, aiming at utilizing the mechanical properties obtained from standardized laboratory tests to predict structural behavior of fiber reinforced composites with different dimensions. Reineck and Frettlöhr (2010) reported that the width-to-depth

ratio of UHPC prism was the key parameter that influenced the flexural strength. Spasojevic et al. (2008) claimed that thick UHPC specimens were more sensitive to size effect than thin specimens in flexure. The abovementioned studies were all based on prism specimens loaded at a single loading rate. Size effect for UHPC specimens has not been fully investigated at different loading rates.

Three-point bending tests using notched beam specimens are easy to conduct and allow more stable cracking with reproducible results compared with unnotched beams, since the notch helps localize the fracture plane. As a crack is initiated at the notch tip and propagates through the beam section, the load-carrying capacity of the section gradually diminishes and the carried load decreases with the increasing deflection. Thus, in this study, notched beam specimens are used to evaluate the post-cracking behavior of fiber reinforced composites. However, different specimen geometries are recommended in different codes. For example, the RILEM committee issued RILEM TC 162-TDF (2002), which specifies concrete beams of 150×150 mm cross section with a minimum length of 550 mm and a notch to depth (N/D) ratio of 1/6; the loading rate for deflection control is 0.2 mm/min. The specimen dimension recommended for normal concrete might be inappropriate for UHPC, which is relatively homogeneous due to removal of coarse aggregates. In addition, the ultra-high strength property of UHPC increases the requirement of load-carrying capacity of the test setup for large specimens. A wide range of specimen size and notch depth are permitted in Japan (2003), in order to accommodate various fiber-reinforced concretes that have different maximum aggregate sizes. The depth (D) of the beam specimen shall be no less than four times of the maximum aggregate size; the loading rate shall be 0.0005D to 0.001D/min; the N/D is 0.3. However, the loading rate is too low to characterize the flexural/tensile behavior of UHPC, which has high impact resistance property. European Committee for Standardization issued EN 14651:2005+A1 (2007), which gives recommendations that are similar to the RILEM recommendations.

In this study, notched UHPC beams with the dimensions in accordance with the JCI recommendations were used (2003). The notched beam specimens had a 75×75 mm cross section and a 400 mm length, with a 5 mm wide notch at mid-span. Three notch-to-depth ratios were respectively applied, which are 1/6, 1/3, and 1/2, corresponding to

recommendations by RILEM, JCI, and thin UHPC element application perspective, respectively. A baseline loading rate of 0.05 mm/min, (in the range of 0.0375 to 0.075 mm/min by JCI recommendations (2003)), was used and extended to 0.50, 1.25, 2.50, and 5.00 mm/min to study the effect of loading rate. The main objective of this study is to investigate the effects of loading rate and N/D on the flexural performance of UHPC notched beams. The direct tensile and compressive properties of a UHPC mixture were characterized. Single fiber pull-out tests of straight and hooked steel fibers, which are partially embedded in the UHPC matrix, were conducted to assess the post-cracking behaviors of the UHPC mixture.

7.2. EXPERIMENTAL PROGRAM

The materials investigated in this study and experimental program are presented as follows:

7.2.1. Materials, Specimens, and Curing Regime. An optimized UHPC mixture as shown in Table 7.1 was used (Meng et al. 2017). The w/b of 0.20, by mass, and sand-to-cementitious materials ratio of 1.0, by volume, was used. The cementitious materials consisted of tertiary blend of 45% Type III Portland cement, 50% Class C fly ash, and 5% silica fume, by volume. The lightweight sand was pre-treated to secure saturated surface-dry condition to an internal absorption of 17% prior to batching.

Table 7.1 Optimized UHPC mixtures.

Raw materials	UHPC (kg/m^3)
Cement	663
Silica fume	42
Fly ash	367
River sand (SSD)	452
Masonry sand (SSD)	308
Lightweight sand (SSD)	120
Mixing water	214
HRWR (including water)	40
Air detrainer	9
Straight steel fibers	78
Hooked-end steel fibers	78

A polycarboxylate-based high-range water reducer (HRWR) was adjusted to ensure an initial mini-slump flow of 280 ± 10 mm, in accordance with ASTM C 230/C 230M thus ensuring self-consolidation. The flow time was measured using a mini-V

funnel in accordance with the EFNARC (2002). An air-detraining admixture with a specific gravity of 0.97 was employed to decrease the volume of entrapped air during mixing and casting in the viscous UHPC mixture.

Figure 7.1 shows the steel fibers that had electro-plated brass coating to enhance corrosion resistance. The steel fiber's Young's modulus and tensile strength are 203 and 1.9 GPa, respectively. A blended mixture, containing 50 vol.% straight microfibers (diameter: 0.2 mm, length: 13 mm) and 50 vol.% hooked-end fibers (diameter: 0.5 mm, length: 30 mm) were used at a total volume content of 2%. The details of mixing and casting procedures can be seen in Section 3.2.2.1.

(a)   (b)
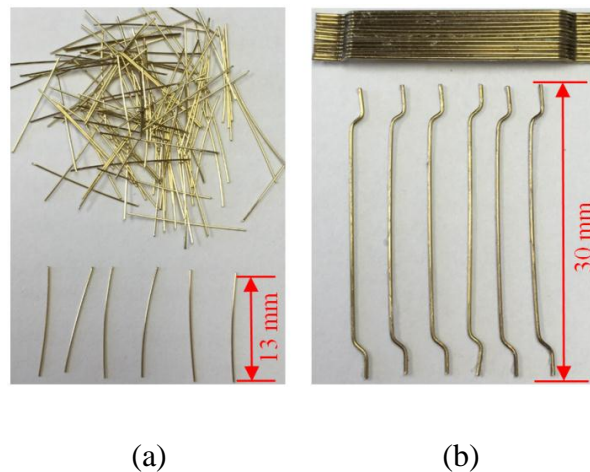
Figure 7.1. Photograph of steel fibers: (a) straight fibers, and (b) hooked-end fibers.

7.2.2. Mechanical Properties Tests. The compressive strength was evaluated using 50 mm cube specimens at 28 d at a loading rate of 1.6 kN/s, in accordance with ASTM C109.

The modulus of elasticity and Poisson's ratio were measured using 100×200 mm cylinders at 28 d in accordance with ASTM C469.Direct tensile tests. Direct tensile tests were conducted using dog-bone specimens, as can be seen in Section 6.2.4.4. Single fiber pull-out tests were performed using a customized setup (Meng and Khayat 2016). The details can be seen in Section 6.2.4.5. Figure 7.2 illustrates the notched beam specimen with notch-to-depth ratios N/D= 1/6, 1/3, and 1/2, corresponding to notch depths of 12.5, 25.0, and 37.5 mm, respectively. The mid-span deflection was measured as the average of two LVDTs mounted at two sides of the beam. A frame with a 250 kN capacity was used

and the load measured by an strain gage based load cell. The test was controlled by a constant rate of the mid-span deflection. A baseline loading rate of 0.05 mm/min was used and extended to 0.50, 1.25, 2.50, and 5.00 mm/min to study the effect of loading rate on the flexural properties.
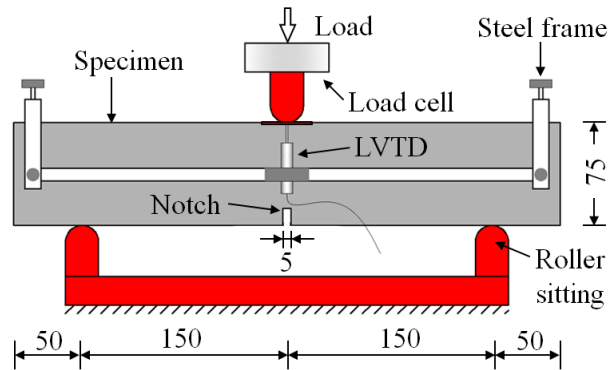
Figure 7.2. Flexural test setup and notched beam specimen. Unit: mm.

The specimens and loading protocols are shown in Table 7.2. A total of 15 test cases and 6 replicate specimens per case were used to address the effect of loading rate and the N/D on the flexural properties of UHPC.

Table 7.2 Notched beam specimens and loading rates in flexural tests.

Code	Notch depth (mm)	Loading rate (mm/min)
S-12.5-0.05	12.5	0.05
S-12.5-0.50	12.5	0.50
S-12.5-1.25	12.5	1.25
S-12.5-2.50	12.5	2.50
S-12.5-5.00	12.5	5.00
S-25.0-0.05	25.0	0.05
S-25.0-0.50	25.0	0.50
S-25.0-1.25	25.0	1.25
S-25.0-2.50	25.0	2.50
S-25.0-5.00	25.0	5.00
S-37.5-0.05	37.5	0.05
S-37.5-0.50	37.5	0.50
S-37.5-1.25	37.5	1.25
S-37.5-2.50	37.5	2.50
S-37.5-5.00	37.5	5.00

7.3. EXPERIMENTAL RESULTS

The detailing experimental results including fresh and hardened properties are presented below:

7.3.1. Fresh Properties. The mini-slump flow of the mixtures for all 90 specimens was adjusted to be 280 ± 10 mm. The mini V-funnel flow time was 18 ± 3 s. The air content and unit weight of representative UHPC samples were 2.5% and 2450 ± 30 kg/m^3, respectively.

7.3.2. Elastic Properties, Compressive Strength, and Tensile Properties. The compressive strength at 28 d was determined to be 158 ± 5 MPa. The modulus of elasticity and Poisson's ratio were 50 ± 2 GPa and 0.20 ± 0.02, respectively. With the steel fibers distributed in the UHPC matrix, the specimens gain enhanced ductility in tension. After cracks are initiated, the steel fibers crossing the crack interfaces can bridge the cracks, preventing abrupt drop in the load-carrying ability. Figure 7.3 shows the load-elongation curves of three out of six tested UHPC specimens and their average. In the other three specimens, the cracks did not occur within the gauge length. At the beginning of loading, the applied load increased linearly with elongation until cracks were initiated when the tensile stress in matrix reached the cracking limit. After cracking, the applied load continued to increase with a decreasing rate until the cracks were substantially developed, reaching peak values. Then, the load decreased with further elongation of the specimen until the specimen completely failed. In the post-cracking stage, the majority of the tensile load was carried by the steel fibers across the cracks via a load transfer mechanism that depends on the fiber-matrix interfaces. Therefore, the post-cracking behavior of the UHPC is primarily controlled by fiber pull-out mechanisms. Multiple cracks appeared progressively with increases in elongation. At the completion of testing, the widths of cracks were in a range of 0.05 to 1.10 mm.
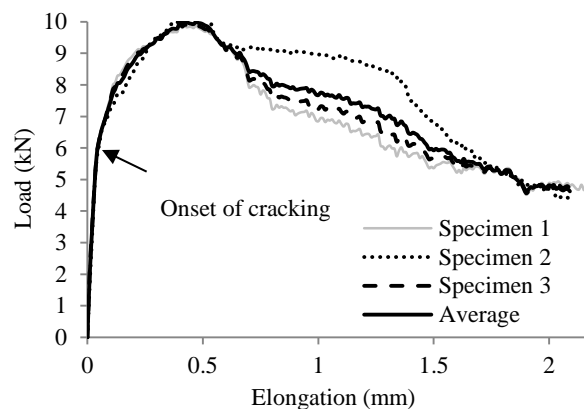
Figure 7.3. Load-elongation relationship of tensile tests.

7.3.3. Single Fiber Pull-Out Tests. Effect of loading rate on fiber pull-out behavior was studied by means of single fiber pull-out tests at the displacement rates of 0.05 and 5 mm/min, respectively. The two values of loading rate correspond to the lower and upper limits of the loading rates used for the notched beams. The mean results of nine straight microfibers and hooked-end fibers are shown in Figures 7.4(a) and 7.4(b), respectively. Results indicate that within the range of tested samples, the fiber geometry has a significant effect on the pullout response; however the loading rate is not as significant in the ranges studied. The peak pull-out loads and areas under the load-slip curves are shown to increase with the displacement rate.
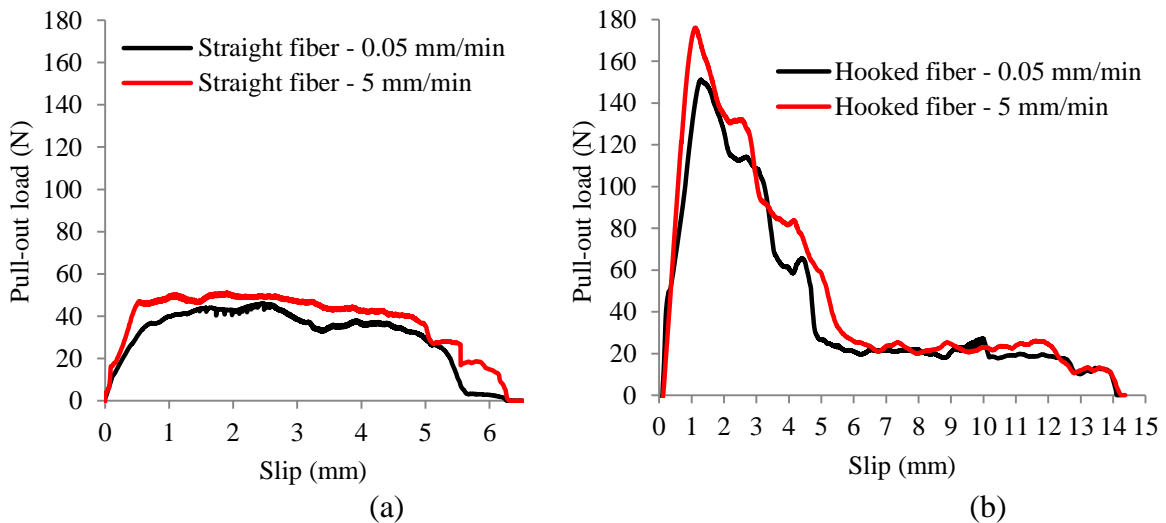
Figure 7.4. Mean values of nine single fiber pull-out tests for: (a) straight microfiber and (b) hooked-end fiber.

Figure 7.5 shows an intact hooked fiber that was not embedded in the UHPC matrix during the pull-out testing with uneven and rough surface. This surface roughness can cause substantial friction and interlock at the interface between the fibers and the UHPC matrix.

After the embedded fibers are pulled out from the UHPC matrix, abrasion and scratches can be observed at the fiber surface. The hooked end of the fiber is deformed during testing, as shown in Figure 7.5.
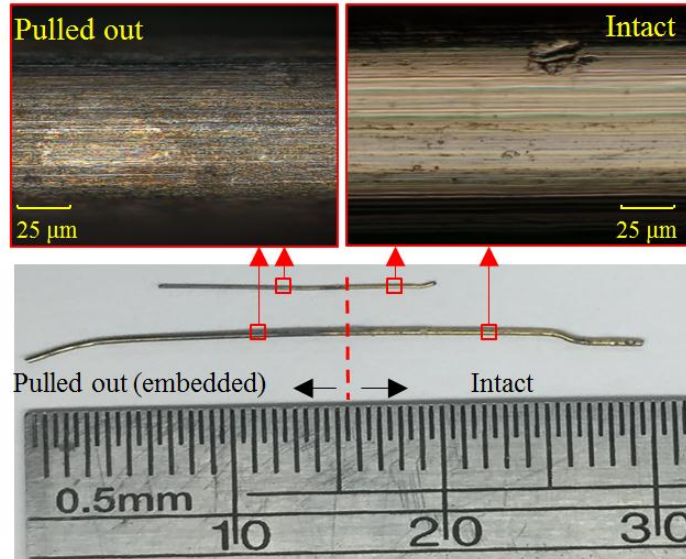
Figure 7.5. Surface conditions of steel fibers before and after pull-out testing for two portions of each fiber; with left side representing the section embedded in the UHPC matrix.

7.3.4. Flexural Tests. For the notched beam specimens, cracks are initiated in the vicinity of the notch tips, due to the reduced cross section and stress concentration. The steel fibers then bridge the cracks and cause multiple cracks, which greatly enhance the ductility of the beams. For this reason, after cracks are initiated, the load carried by the beam does not drop abruptly. Instead, higher loads are carried, demonstrating a hardening behavior. In the post-cracking stage, the tensile force is primarily carried by the steel fibers crossing the crack interfaces, which is mainly associated with the fiber pull-out mechanisms. At the completion of testing, the widths of cracks were in a range of 0.05–2.50 mm.

Figures 7.6(a)–7.6(c) show representative load-deflection curves of the notched beam specimens. As the N/D is increased from 1/6 to 1/2 (i.e. increasing the notch depth from 12.5 to 37.5 mm), the peak load is reduced by 58% at the loading rate of 0.05 mm/min, and 78% at the loading rate of 5.00 mm/min. The peak load increased with the loading rate at each N/D level; however, significant discrepancies among beams with different N/D were observed. As the loading rate was increased from 0.05 to 5.00 mm/min, the peak loads at N/D = 1/6 and 1/2 were respectively increased by 10 kN

(56%) and 1.1 kN (18%). This indicates that the increase of the N/D suppresses the loading rate effect on the load-carrying capacity.
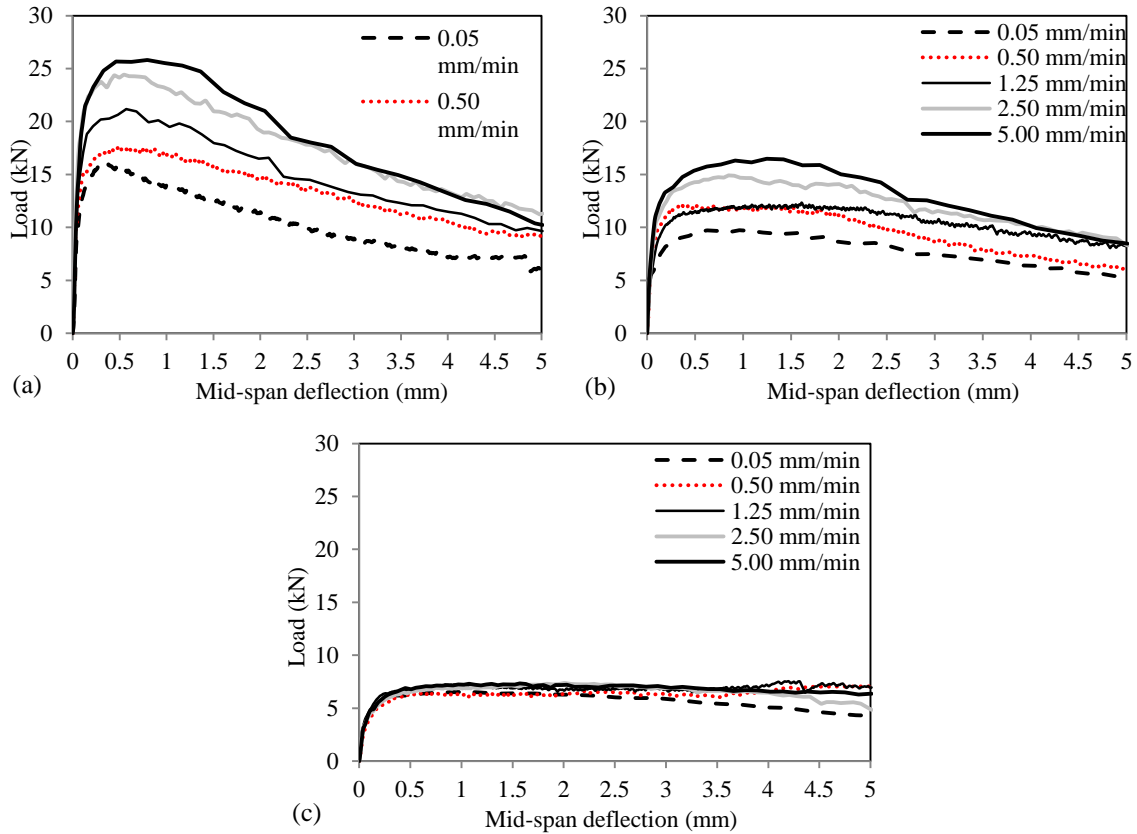
Figure 7.6. Load-deflection curves of notched beams with N/D of: (a) 1/6, (b) 1/3, and (c) 1/2.

7.4. DISCUSSIONS

The analysis of the flexural behaviors were further evaluated as follows:

7.4.1. Flexural Strength and Residual Strength. The flexural strength of UHPC notched beam is calculated using Equation 7.1 in accordance with RILEM recommendations (2002):

$$f_u = \frac{3P_u L}{2b(D-N)^2}$$

Equation 7.1

where f_u and P_u represent the flexural strength and the peak load in the load-deflection curves; L, b, D, and N denote the span, width, depth, and notch depth respectively. The test results of flexural strength from six specimens were averaged.

Figures 7.7(a) and 7.7(b) show the correlation of flexural strength with the loading rate and N/D, respectively. As the loading rate was increased from 0.05 to 5.00 mm/min, the flexural strength for N/D of 1/6, 1/3, and 1/2 was increased by 62%, 71%, and 19%, respectively. The increases in the flexural strength due to higher loading rates may be partially attributed to the increase in interfacial bond strength as corroborated by the single fiber pull-out tests in Figure 7.4, which also agrees well with the study by Xu et al. (Xu et al. 2016).
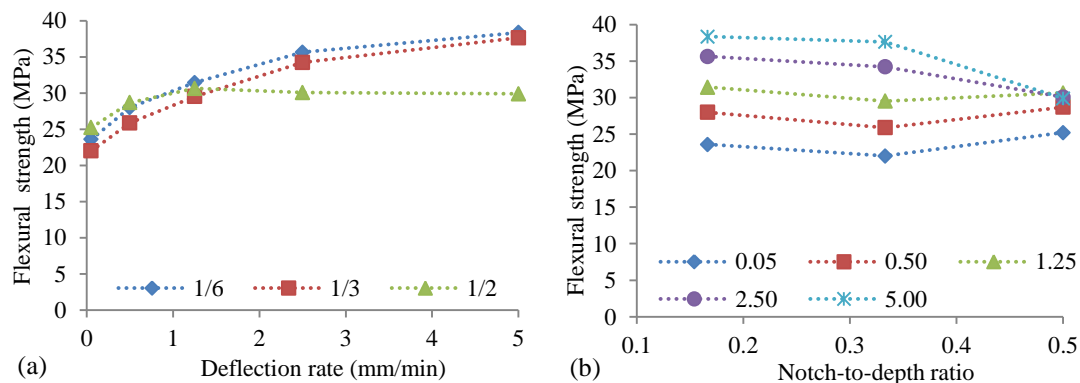
Figure 7.7. Flexural strength versus: (a) loading rate and (b) N/D.

The results of flexural strength demonstrate interaction coupling of the loading rate and N/D, and Figure 7.7(a) indicates a marginal effect of N/D when the loading rate is not more than 1.25 mm/min. As the N/D is increased from 1/6 to 1/2, the strength variations at different loading rates are up to ±6%. However, at the loading rates of 2.50 and 5.00 mm/min, increasing the N/D from 1/6 to 1/2 reduces the flexural strength by 20%−30%, meaning the effect of the N/D on the flexural strength can be significantly magnified by applying higher loading rates.

The residual strengths are calculated by Equation 7.2 in accordance with RILEM TC 162-TDF recommendations (2002):

$$f_{R,i} = \frac{3P_{R,i}L}{2b(D-N)^2}$$

Equation 7.2

where $f_{R,i}$ and $P_{R,i}$ respectively denote the residual strength and residual load corresponding to various mid-span deflections $\delta_{R,i}$ (i = 2, 3, and 4). The deflections $\delta_{R,2}$, $\delta_{R,3}$, and $\delta_{R,4}$ are 1.31, 2.15, 3.00 mm, respectively, according to the RILEM recommendations (2002). The test results of residual strengths from six specimens were averaged.

The residual strengths obtained from the load-deflection responses as shown in Figures 7.8(a)–7.8(c) observed the coupling between the loading rate and the N/D.
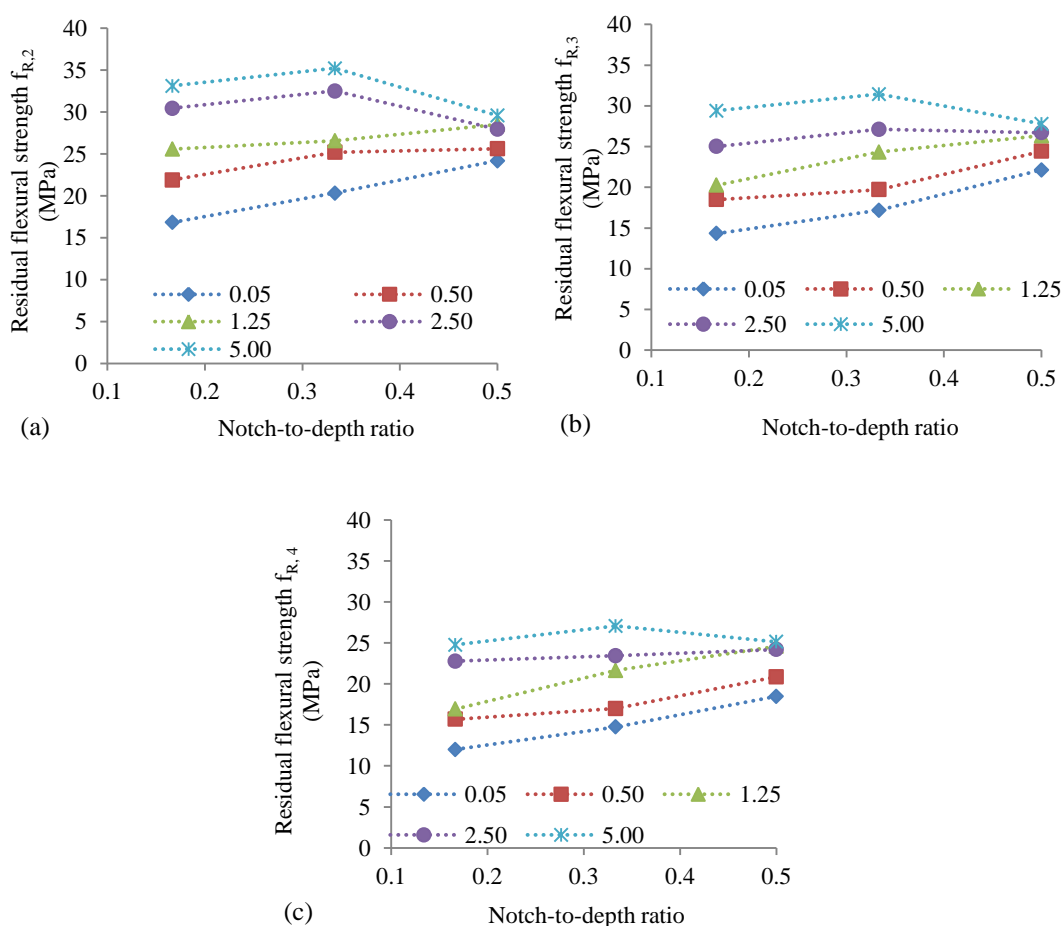
Figure 7.8. Residual flexural strengths versus N/D: (a) $f_{R,2}$, (b) $f_{R,3}$, and (c) $f_{R,4}$.

At the loading rate of 0.05 mm/min, the residual strengths increased with the N/D. However, with the increase in the loading rate, different tendencies were demonstrated.

At the loading rate of 5.00 mm/min, $f_{R,2}$ and $f_{R,3}$ decreased with the N/D, while the value of $f_{R,4}$ was relatively sustained.

Table 7.3 Summary of flexural test results.

Code	f_u		$f_{R,2}$		$f_{R,3}$		$f_{R,4}$	
	Average (MPa)	C.O.V. (%)	Average (MPa)	C.O.V. (%)	Average (MPa)	C.O.V. (%)	Average (MPa)	C.O.V. (%)
S-12.5-0.05	23.59	3.25	16.84	3.01	14.34	8.39	11.99	9.68
S-12.5-0.50	28.00	3.26	21.90	3.32	18.50	6.24	15.69	7.60
S-12.5-1.25	31.43	4.69	25.58	3.92	20.27	5.67	16.93	12.01
S-12.5-2.50	35.64	3.13	30.44	5.68	25.01	7.92	22.78	7.61
S-12.5-5.00	38.36	4.53	33.11	6.11	29.40	7.95	24.76	6.35
S-25.0-0.05	22.01	3.14	20.34	5.31	17.18	5.44	14.76	10.61
S-25.0-0.50	25.88	2.92	25.19	5.66	19.72	6.89	16.99	6.13
S-25.0-1.25	29.53	5.66	26.57	5.17	24.32	9.09	21.64	9.48
S-25.0-2.50	34.22	3.12	32.51	3.43	27.12	7.75	23.44	11.62
S-25.0-5.00	37.64	3.79	35.21	6.22	31.44	6.53	27.07	9.87
S-37.5-0.05	25.22	5.03	24.19	5.33	22.13	8.83	18.48	10.03
S-37.5-0.50	28.68	3.06	25.61	3.95	24.43	6.56	20.87	6.95
S-37.5-1.25	30.65	3.27	28.51	4.84	26.33	5.50	24.59	9.12
S-37.5-2.50	30.06	3.57	27.95	5.61	26.70	9.93	24.20	8.77
S-37.5-5.00	29.90	3.61	29.58	5.74	27.78	5.64	25.13	8.19

Using a linear fit on the curves in Figures 7.7(b) and 7.8(a)–7.8(c), the sensitivity of the flexural or residual strengths to N/D is measured. The slope is denoted as kfS and mathematically expressed using a differentiation equation as given in Equation 7.3:

$$k_{fS} = \frac{\partial f}{\partial (N/D)}$$

Equation 7.3

where f represents the flexural or residual strengths. This equation is applicable to both the flexural tensile strength and the residual strength. When k_{fS} is equal to zero, the strength can be considered to be independent on N/D.

Noting that the changing rates of the flexural or residual strengths to N/D are different at different loading rates, the changing rates k_{fS} are plotted against loading rate, as shown in Figure 7.9. As the loading rate is increased from 0.05 to 5.00 mm/min, the values of k_{fS} are shown to decrease, indicating that k_{fS} is associated with the loading rate. The relationship between k_{fS} and loading rate can be expressed using a differential equation as given in Equation 7.4:

$$k_{fSL} = \frac{\partial k_{fS}}{\partial \dot{\gamma}} = \frac{\partial^2 f}{\partial(N/D)\partial \dot{\gamma}} \qquad \text{Equation 7.4}$$

where k_{fSL} is the changing rate of k_{fS} with regard to loading rate. A non-zero value of k_{fSL} indicates that the relationship between the flexural or residual strengths to N/D is associated with the loading rate, i.e. coupling or interactive effect of loading rate and N/D on the flexural or residual strengths. Taking the flexural tensile strength (f_u) for example, as the loading rate increased from 0.05 to 5.00 mm/min, the changing rate of the flexural strength to N/D was changed from 4.96 to -25.78 MPa at a rate (k_{fSL}) of -6.48 MPa·min/mm. A larger k_{fSL} indicates a more significant coupling effect.
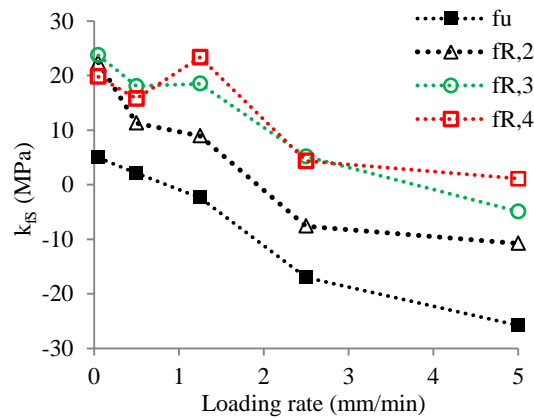
Figure 7.9. Coupling effects of loading rate and N/D on flexural strength and residual strengths.

7.4.2. Analytical Modelling of Flexural Responses. A modelling approach to simulate the flexural responses based on a developed equivalent tensile stress-strain relationship (Soranakom and Mobasher 2008) is also presented.

The modelling procedure correlates the flexural load-deflection and tensile stress-strain responses through moment-curvature analysis. Parameterized multi-linear compressive and tensile stress-strain constitutive laws are used in the derivations. The compression law is assumed to be elastic-perfectly plastic governed by Young's modulus, compressive strength, and ultimate compressive strain. The tension law is characterized by Young's modulus, tensile strength, and constant residual tensile residual strength. The cross sectional moment-curvature analysis is based on the assumption of plane section remains plane such that the linear distribution of strain is obtained. The stress profiles in

linear elastic and cracked stages are therefore derived using the stress-strain constitutive laws. By solving the static equilibrium equations along the cross section, neutral axis depth ratio is calculated which is subsequently used to derive geometric parameters including size of tension/compression zones and the moment arm of each force term. The total bending moment is then computed as the summation of the contributions from all force terms while the curvature is related to the strain and neutral axis depth. In order to obtain the full range load-deflection responses, moment-area method is employed to calculate the mid-span deflection at each load step. Details about the constitutive laws and complete derivations can be found in the original work (Soranakom and Mobasher 2008). The procedure has been applied to various types of materials including fiber-reinforced concrete reinforced by polypropylene and glass fiber, textile reinforced concrete reinforced by polypropylene and aramid textiles, high-performance fiber-reinforced concrete reinforced by steel fibers (Bakhshi et al. 2014; Mobasher et al. 2014).

Figures 7.10(a), (b), and (c) compare the simulated and experimental flexural stress-deflection responses of the UHPC beams with different notch depths and loading rates. Compressive strength of 158 MPa and modulus of elasticity of 50 GPa measured from compressive tests were used. The tensile material properties illustrated as multi-linear stress-strain diagrams were back-calculated by fitting the experimental flexural responses for N/D of 1/6, as shown in Figure 7.10 (d).The results show that in order to fit the experimental loading rate effect, the tensile and residual strength of have to increase from 9.5 to 15.9 MPa (67%) and 3.1 to 5.2 MPa (67%), respectively. The loading rate effects revealed by the increasing strength in tensile stress-strain laws agree with the experimental investigations on tensile properties of UHPC under varying strain rates (Zhang 2014). The percentages of improvement are consistent with those of flexural strength measured from experiment. It can be seen that the simulated responses agree well with the experimental results for N/D of 1/6 and 1/3, while discrepancies are observed when N/D increases to 1/2. As previously discussed, the loading rate effects on ultimate flexural strength and residual strength are suppressed for the beams with notch of 37.5 mm compared to those with shallow notches. Since the proposed modelling procedure correlates the tension and flexural responses by means of moment-curvature analysis, the back-calculated stress-strain responses from load-deflection curves at

different rates are equivalent tension laws and consistent with the loading rate sensitivity of experimental results (N/D=1/6). These may require further investigation into the coupled effects of stress intensity due to deep notch and loading rate. One possible explanation is the relationship between the stress rate and displacement rate. Since the fracture tests in present study were controlled by displacement, the same displacement rates may result in varying stress rates when the bending stiffness changes (due to changing notch depth). The coupled loading rate and notch depth effects on failure mechanisms of UHPC are not considered in the analytical model, which may require further investigation in future study. Since the present tests were performed using displacement control, as the notch depth changes, the bending stiffness of beam specimen decreases quadratically such that the stress rate obtained along the cross section may not be proportional to the displacement rate. The size of the potential fracture process zone (FPZ) may be several times larger than what can be possibly developed in the samples as the net section size decreases. This limits the full capability of the material for samples with exceedingly small effective depths.

On the other hand, the tensile stress-strain laws for simulations are found to overestimate the average stress-strain responses from experiment. This phenomenon may be explained by the loading rate effects and the different mechanisms between tension and flexure tests. While the magnitudes of displacement rates are similar, the loading rates of bending and tension tests are in terms of different parameters. The rate of actuator displacement does not necessarily lead to same strain rates due to the different strain distributions in bending and uniaxial tension samples. In addition, the tensile property of UHPC was only evaluated at a rate of 0.05 mm/min in this study, while the loading rate of bending test differed by two orders of magnitude. On the other hand, studies have shown that use of uniaxial tension data underpredicts the flexural response for this class of material (Soranakom and Mobasher 2008; Bakhshi et al. 2014) by a significant margin. This is attributed to differences in the stress distribution profiles of the two test methods. In the tension test, the entire volume of the specimen is a potential zone for transverse crack initiation. Comparatively, in the flexural test, only a small fraction of the tension region is subjected to an equivalent ultimate tensile stress.
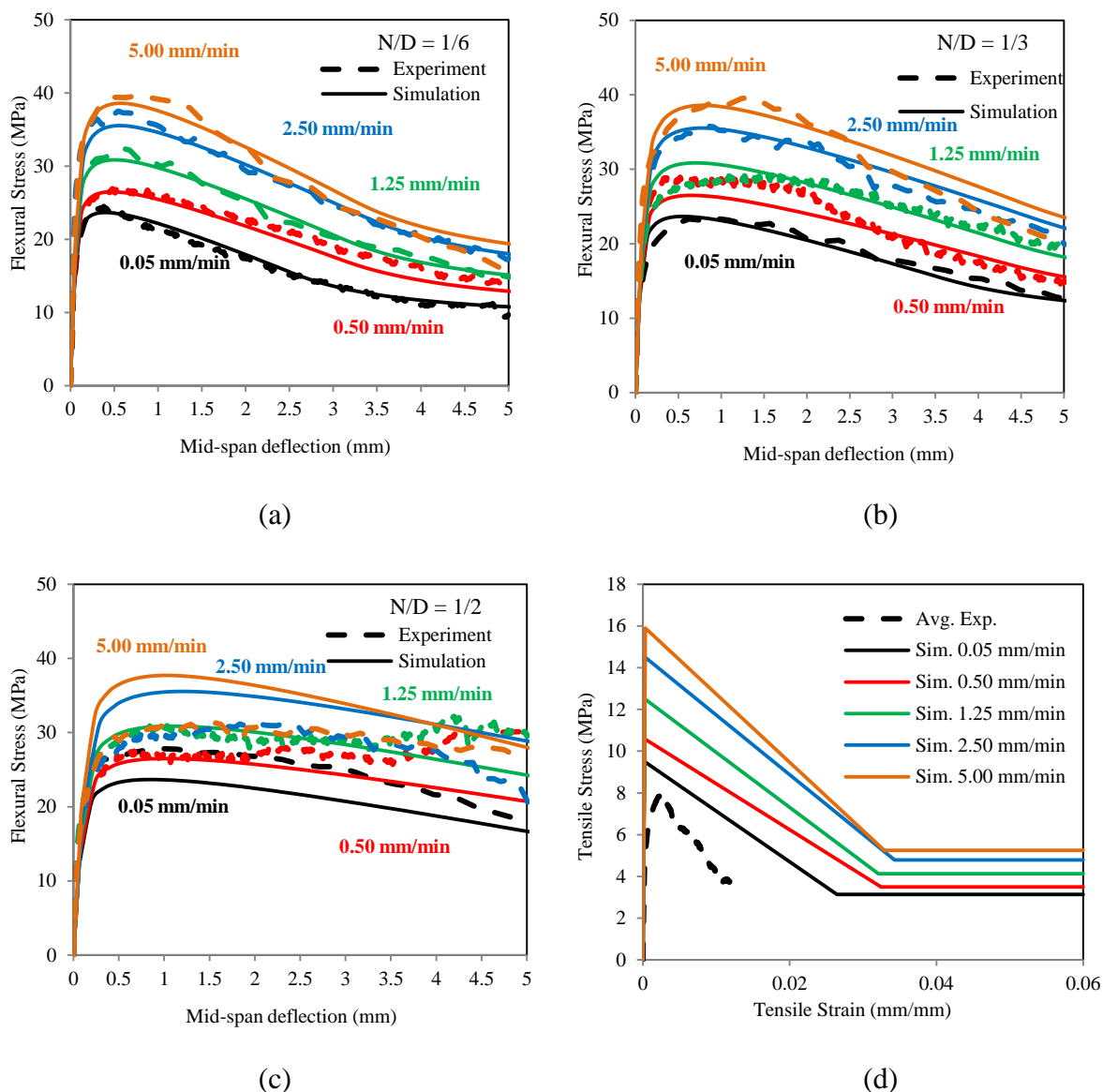
Figure 7.10. Comparisons between simulated and experimental flexural stress-deflection responses for the UHPC beams with N/D of: (a) 1/6, (b) 1/3, (c) 1/2, and the (d) tension laws used for simulation.

This also explains the fact that the residual strength obtained from the model tension laws underestimates the residual strength ($f_{R,i}$) measured and calculated from experimental flexural responses (see Table 7.3). The discrepancies are traced back to the inherent assumption of the standard method by RILEM, which assumes that the neutral axis is at the centroid of the specimen and the stress distribution is linear throughout at cracked stage. But the present model predicts the movement of neutral axis towards

compression zone and the reduced flexural stiffness as flexural crack propagates. Details of comparisons and correlations between the two methods can be found elsewhere (Bakhshi et al. 2014; Mobasher et al. 2014).

7.4.3. Fracture Energy. Fracture energy, denoted by G_F, is the energy necessary to create a crack of unit area and can be calculated from the area under the load-deflection curves by Equation 7.6, to allow for the self-weight of specimen, in accordance with the RILEM (2002) and JCI (2003) recommendations. In this study, the specimens were not deformed till complete failure (Xu and Wille 2015), and each specimen was loaded to reach a mid-span deflection of 5 mm, causing a slight underestimation of the fraction energy. The fracture energy is calculated as:

$$G_F = \frac{W + mg\delta}{b(D-N)}$$

Equation 7.6

where G_F is the fracture energy, W is the energy absorption, m is the total mass of the test beam, g is the acceleration of gravity, δ is the mid-span deflection.

The fracture energy results are plotted and compared in Figures 7.11(a) and 7.11(b), which manifest the trends of how the fracture energy changes with the loading rate and N/D, respectively. Figure 7.11(a) indicates that the fracture energy increased nonlinearly with the loading rate from 0.05 to 5.00 mm/min at a decreasing rate. Figure 7.11(b) indicates the fracture energy approximately linearly changed with the N/D.
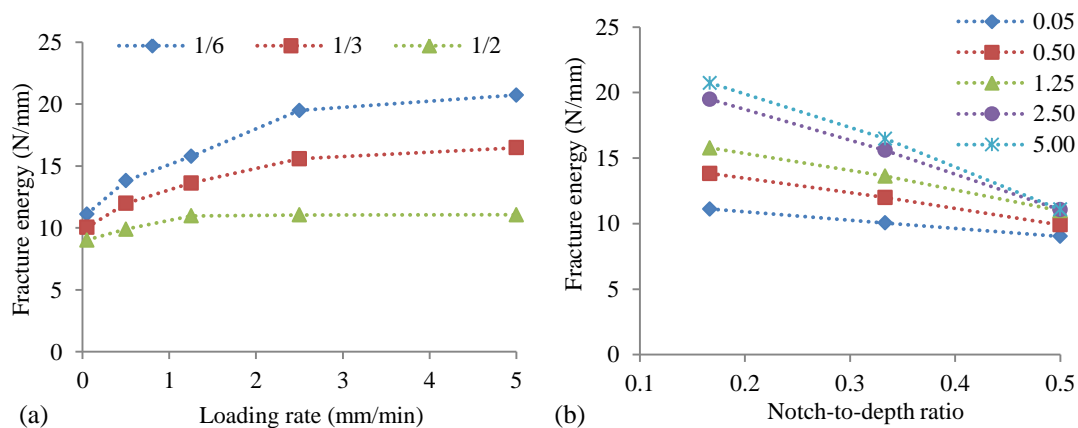
Figure 7.11. Fracture energy versus: (a) loading rate and (b) N/D.

As the loading rate increased from 0.05 to 5.00 mm/min, the fracture energy at N/C of 1/2, 1/3, and 1/6 increased by 23%, 64%, and 87%, respectively, indicating that the relationship between the fracture energy and loading rate is dependent on N/D. On the other hand, as the N/D is reduced from 1/2 to 1/6, the fracture energy is increased by 23% at a loading rate of 0.05 mm/min, and by 87% at a loading rate of 5.00 mm/min, indicating that the relationship between the fracture energy and N/D is also dependent on loading rate. The slopes of the variations of the fracture energy versus N/D shown in Figure 7.11(b) are plotted in Figure 7.12 with the increase of loading rate. The values of the slopes represent the changing rate or sensitivity of the fracture energy to the change of N/D. As the loading rate was increased from 0.05 to 5.00 mm/min, the sensitivity of the fracture energy to the N/D changed from -6.36 to -29.43 N/mm. The negative sign means that the fracture energy decreases with N/D. The absolute value represents the magnitude of the sensitivity, and a larger absolute value indicates a higher sensitivity of the fracture energy to N/D. Figure 7.12 shows that the magnitude of sensitivity of the fracture energy to N/D increases as the loading rate increases.
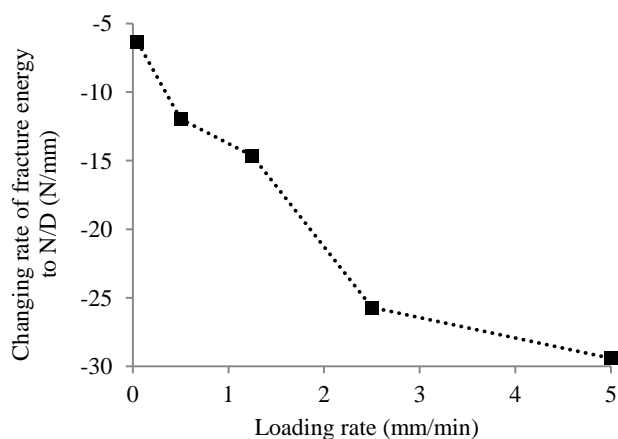
Figure 7.12. Coupling effect of loading rate and N/D on fracture energy.

7.4.4. Regression and Analysis of Variance. Based on the investigation above, the flexural strength and the fracture energy are found to be associated with the loading rate $\dot{\gamma}$ and N/D, as well as their coupling effects.

Based on the experimental results, regression analyses are conducted to formulate the flexural strength and the fracture energy. In this study, for the sake of simplicity of

formulation, the flexural strength and fracture energy are assumed to vary linearly with the loading rate and the N/D, as shown in Equation 8.7.

$$f_u = a_{f0} + a_{f1}(N/D) + a_{f2}\dot{\gamma} + a_{f3}(N/D)\dot{\gamma}$$
$$G_F = b_{G0} + b_{G1}(N/D) + b_{G2}\dot{\gamma} + b_{G3}(N/D)\dot{\gamma}$$

Equation 7.7

where, a_{f0} and b_{G0} are respectively constant terms of the flexural tensile strength and fracture energy; a_{f1}, a_{f2}, and a_{f3} represent the sensitivity coefficients of the flexural strength to N/D, loading rate, and coupling term of N/D and loading rate, respectively; b_{G0}, b_{G1}, b_{G2}, and b_{G3} represent the sensitivity coefficients of the fracture energy to N/D, loading rate, and coupling term of N/D and loading rate, respectively. These coefficients are determined by regression analysis of testing data using the least square method.

The coefficients for the flexural strength are: a_{f0} = 24.66 MPa, a_{f1} = 4.42 MPa, a_{f2} = 4.24 MPa·min/mm, and a_{f3} = -6.48 MPa·min/mm. The coefficients for the fracture energy are: b_{G0} = 14.27 N/mm, b_{G1} = -9.07 N/mm, b_{G2} = 2.63 N·min/mm^2, and b_{G3} = -4.57 N·min/mm^2. Then, Equation 7.7 can be rewritten as:

$$f_u = 24.66 + 4.42(N/D) + 4.24\dot{\gamma} - 6.48(N/D)\dot{\gamma}$$
$$G_F = 14.23 - 9.07(N/D) + 2.63\dot{\gamma} - 4.57(N/D)\dot{\gamma}$$

Equation 7.8

where, $1/6 \leq N/D \leq 1/2$, and 0.05 mm/min $\leq \dot{\gamma} \leq$ 5.00 mm/min.

The positive values of a_{f1} and a_{f2} indicate that the flexural strength increases with N/D and loading rate. The negative value of a_{f3} indicates that the sensitivity of flexural strength to N/D decreases with loading rate, and vice versa.

The negative value of b_{G1} and the positive value of b_{G2} indicate that the fracture energy decreases with N/D and increases with loading rate. The negative value of b_{G3} indicates that the sensitivity of fracture energy to N/D decreases with loading rate, and vice versa.

The regression analysis results were examined by analysis of variance (ANOVA) using the F-test criteria (Anderson 2001) with a significance level of 5% ($\alpha = 0.05$). For the regression analysis of the flexural tensile strength, the coefficient of determination (R^2) is 0.795, and the standard error is 2.48 MPa.

The P-value of F-significance is 4.2×10^{-4}, which is far smaller than the significance level 0.05, indicating the regressed formula has high significance. For the regression analysis of fracture energy, the coefficient of determination (R^2) is 0.909, and the standard error is 1.21 N/mm. The P-value of F-significance is 5.2×10^{-6}, which is far smaller than the significance level 0.05, indicating the regressed formula has high significance.

The formulae in Equation 7.8 are plotted in design charts to facilitate engineers to implement in engineering practice, as shown in Figure 7.13.

Since the formulae were obtained from the test results of specimens with N/D in the range of 1/6 to 1/2 at loading rates in the range of 0.05 to 5 mm/min, interpolation and extrapolation of data points should be within the specified ranges, to ensure the validity of the design charts.

(a)

(b)
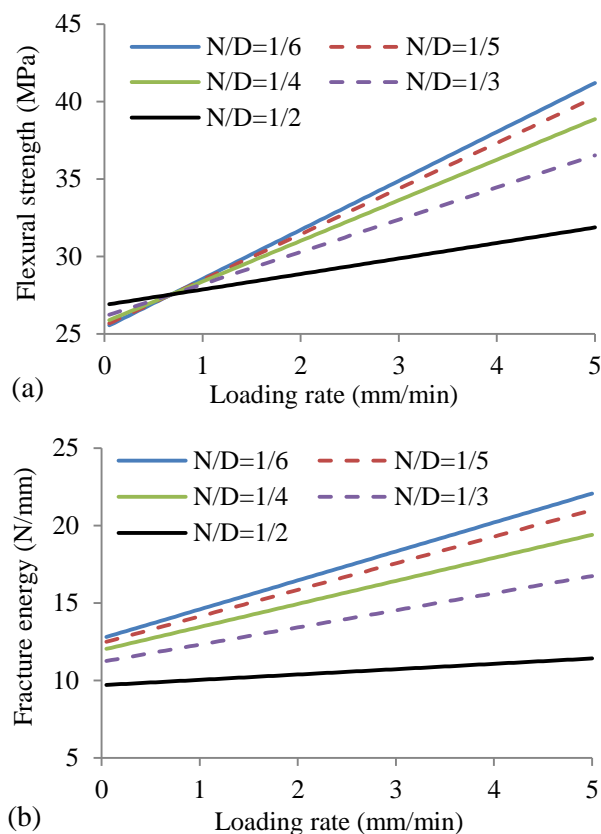
Figure 7.13. Design charts: (a) flexural strength and (b) fracture energy.

7.5. SUMMARY

Based on the above investigations, main findings are summarized as follows.

(1) In general, the flexural strength and residual strengths of UHPC notched beam increase with loading rate and the notch-to-depth ratio. The fracture energy of UHPC notched beam increases with loading rate and decreases with notch-to-depth ratio. The effects of the notch-to-depth ratio are associated with the loading rate. For a notch-to-depth ratio in the range of 1/6 to 1/2, the effect of notch-to-depth ratio on the flexural strength is less than 10% at a deflection rate up to 1.25 mm/min. However, as the deflection rate is increased to 2.5 mm/min, the effect of notch-to-depth ratio on the flexural strength of the UHPC mixture is increased to 30%. As the deflection rate is increased from 0.05 to 5.00 mm/min, the fracture energy is increased by 87% for the beam with a notch-to-depth ratio of 1/6, and by 23% for the beam with a notch-to-depth ratio of 1/2.

(2) Based on the experimental results, the flexural tensile strength and fracture energy of the UHPC notched beams are formulated with the loading rate and the notch-to-depth ratio by regression analyses. The regressed formulae of the flexural tensile strength and fracture energy are evaluated by analysis of variance, and reasonable significance of the regressed formulae is corroborated. The regressed formulae have reasonable quality and are plotted in design charts that can be conveniently used in engineering practice to predict the flexural properties of UHPC that is subjected to different loading rates or used in structures with different dimensions.

(3) The UHPC mixture proportioned with high-volume fly ash and 2% blend steel fibers demonstrate high ductility in tension and strain-hardening behavior. The steel fibers can bridge cracks and allow the UHPC to carry sustained load and have multiple cracks. The post-cracking performance is primarily dependent on the fiber pull-out mechanisms, which are characterized using single fiber pull-out tests. After debonding is initiated at the interface between the steel fibers and the UHPC matrix, the interface can carry substantial load before the steel fiber is completely pulled out. The bond strength and the post-debonding behaviors are associated with the loading rate.

8. REINFORCMENT OF UHPC BY FIBER-REINFOCED POLYMERS GRIDS

8.1. BACKGROUND

The effectiveness of fiber-reinforced polymer (FRP) used as internal reinforcement in concrete has been extensively investigated (Baena et al. 2013; Milani 2011; Sharbatdar et al. 2011). Compared with conventional steel reinforcement, FRP can provide higher tensile strength, lower self-weight and greater resistance to corrosion (Al-Sunna et al. 2012; Mias et al. 2013; Nanni 1993). FRP bars have been extensively implemented as one-dimensional reinforcement in concrete structures, such as bridge girders and decks (Sonobe et al. 1997). Effective enhancement in flexural strength and ductility was demonstrated by fiber reinforced concrete panels with embedded FRP bars (Kim 2006). The flexural capacity of the permanent formwork panel could be increased by nearly four times (Kim 2008). FRP bars were incorporated with UHPC in bridge deck, which demonstrated good promise to replace the conventional steel grid deck (Saleem et al. 2011). Two-dimensional FRP grids have been used in retrofitting or strengthening of damaged structures (Bakis 2002). Compared with FRP bars, FRP grids are more flexible and provide multi-dimensional enhancement, and thus can be used to develop thin prefabricated panels (Bakis 2002; Bank 2006). However, there is a lack of study on using FRP grids to strengthen UHPC elements in the literature.

The objective of this study is to develop UHPC panels reinforced with FRP grids for the development of permanent formwork. Such thin and highly-durable element can serve as stay-in-place panels and thus accelerate infrastructure construction. The use of fibers as reinforcement can provide good resistance to cracking and enhance the durability. The durability is also assured by using UHPC that is highly impermeable. Besides the improvement in construction efficiency, concrete permanent formwork can reduce site waste in comparison with the use of wooden formwork (Leung and Cao 2010). However, the design of such panels requires the development of sections that can be lightweight, durable, ductile, and maintenance-free. Research is needed to fully understand the behavior of FRP grids reinforced concrete panels (Kim 2009), including the development of reliable analysis tools to predict failure modes of FRP reinforced

UHPC panels (2004). This is critical for the development of design guidelines for concrete members reinforced with FRP grids.

When FRP grids are embedded in UHPC panels, their performance will strongly depend on the bond condition between the FRP and UHPC matrix. Bond characteristics influence the mechanism of load transfer between reinforcement and concrete, and therefore control the concrete crack spacing, crack width, required concrete cover to the reinforcement, and reinforcement development length (Matthys and Taerwe 2000; Yost et al. 2001). Two-dimensional FRP grids can provide a mechanical anchorage within the concrete matrix due to interlocking effects, and thus can provide proper load transfer (Björn and Thomas 2007; Francesca et al. 2014).

This study presents experimental, mechanical, and numerical investigations on the flexural behavior of thin UHPC panels reinforced with FRP grids. The flexural performance of the panels was evaluated in three-point bending tests. The bond between the matrix and embedded FRP grids is investigated using push-pull tests. The study also presents a mechanical model and a three-dimensional finite element model (FEM) to predict the flexural performance of the composite panels. Parametric studies were carried out using the numerical model to investigate the effect of panel thickness and reinforcement configuration on peak flexural load, first cracking load, and energy dissipation of reinforced UHPC panels.

8.2. MATERIAL PROPERTIES OF FRP GRID AND MORTAR

The materials investigated in this study and experimental program are presented as follows:

8.2.1. FRP Grid Type and Tensile Properties. Two types of FRP grids were investigated: GFRP and CFRP grids, as shown in Figures 8.1(a) and 8.1(b).

The dimensions and mechanical properties are listed in Table 8.1. The values of tensile strength and Young's modulus are obtained from the tensile tests, and the dimensions and other properties are nominal values provided by the manufacturer. Their constitutive relations were determined under uniaxial tensile testing (Bentayeb et al. 2008). Single strip specimens were cut from the orthogonal grids, as indicated in Figures 8.1(a) and 8.1(b). The strip specimens were tested using a low capacity load frame with a capacity of 5 kN, under displacement control at a rate of 1 mm/min. In order to avoid

local damage caused by stress concentration, each end of the tested strip was mounted onto a steel plate using a two-part epoxy. The steel plates were then directly gripped using the load frame for tensile testing.
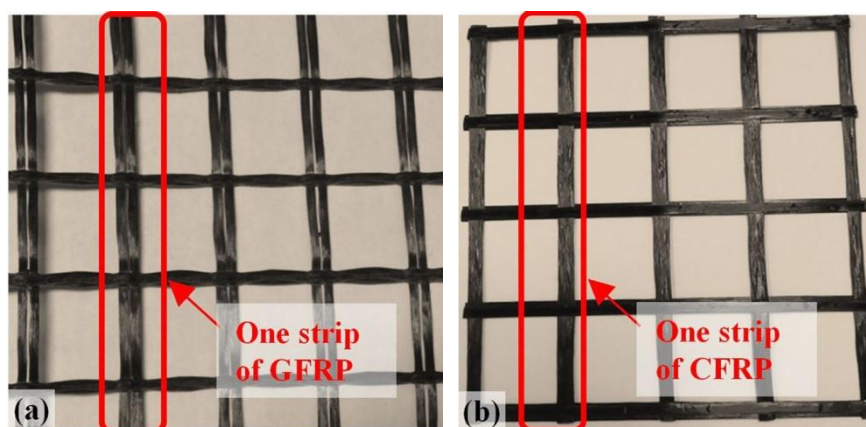
Figure 8.1. FRP grids: (a) GFRP and (b) CFRP.

Table 8.1 Properties of FRP grids provided by the manufacture.

Name	Size of grid (mm)	Cross section (mm)	Tensile strength (kN/m)	Young's modulus of elasticity (GPa)	Poisson's ratio	Unit weight (g/m2)
GFRP	25×25	5×2	45	25	0.26	225
CFRP	46×41	10×1	97	40	0.26	225

The load-displacement data were recorded using a load transducer and an extensometer, respectively, which were embedded in the load frame, with a sampling frequency of 10 Hz. Given the initial length of each specimen, the load-deformation relationships were converted into equivalent force-strain relationships, as shown in Figure 8.2.

The equivalent force-strain relationship remained linear until shortly before rupture. The slopes of these lines represent the tensile stiffness of the FRP grids. The CFRP specimens demonstrated larger tensile stiffness and tensile strength than the GFRP specimens. However, the GFRP specimens had larger tensile strain limits (or rupture strain) than the CFRP specimens. The average slopes corresponding to the force versus strain were 60 and 480 kN/ε for the GFRP and CFRP samples, respectively. The average tensile peak load was 1.2 and 3.8 kN for the GFRP and CFRP, respectively. The rupture

strains were approximately 2×104 and 1×104 μm/m for the GFRP and CFRP materials, respectively.

Figure 8.2. Force-strain relationships of single strip of: (a) GFRP, and (b) CFRP.

8.2.2. Proportioning and Properties of Investigated Mixtures. Two mixtures were investigated: (1) a UHPC mixture with micro steel fibers, and (2) an ultra-high-strength mortar (HSM) without any fiber. Table 8.2 shows the mixture proportions of the UHPC and HSM. The water-to-binder ratio (w/b) was fixed at 0.20. The volume fractions of ground granulated blast-furnace slag (GGBS) and silica fume (SF) were 50% and 5%, respectively, of the binder. A Type III Portland cement with Blaine fineness of 560 m^2/kg was employed. The Blaine fineness of the GGBS was 590 m^2/kg. Masonry sand (0–2 mm) and the river sand (0–4.75 mm) were used. A polycarboxylic-based high-ranged water reducer (HRWR) was used to enhance the workability. The fiber volume fraction of the UHPC was set at 2%. The mixture was poured into the mini-slump cone to full capacity, in accordance with ASTM C 230/C 230M. The HRWR dosage was adjusted to insure that the initial mini slump flow values of all the mixtures were kept at 280 ± 5 mm. All test samples were cured for 24 hours in the molds that were covered with wet burlap and plastic sheet and kept at 23 °C. After demolding, the samples were cured in lime-saturated water at 23 °C until the age of testing.Table 8.3 summarized the 28-day mechanical properties. The compressive strength of the mixtures was tested according to ASTM C 109 at 28 days using 50-mm cubes.

Table 8.2 Mixture proportioning of UHPC and HSM.

	Type III cement (kg/m^3)	Silica fume (kg/m^3)	GGBS (0–2 mm) (kg/m^3)	River sand (0–5 mm) (kg/m^3)	Masonry sand (kg/m^3)	HRWR (l/m^3)	Water* (kg/m^3)	Steel fiber (kg/m^3)
UHPC	548	42	535	708	310	70	146	156
HSM	546	42	559	722	316	26	149	-

* Total water: including water in high range water reducer.

Flexural performance (flexural strength and T-150) of the mixtures was evaluated using beams with three-point bending testing in accordance with ASTM C 1609. The beam specimen is 304.8 × 76.2 × 76.2 mm with a span of 203.2 mm. The modulus of elasticity and Poisson's ratio of the mixtures were measured in compression in accordance with ASTM C469 at the age of 28 days using cylinders with 100-mm diameter and 200-mm height. The compressive strengths of the two mixtures were close (up to 1.6% differences). However, the flexural strength (stress corresponding to peak load) of the HSM mixture was 44% lower than that of the fiber reinforced UHPC. Unlike the non-fiber reinforced HSM, the UHPC was ductile and exhibited strain-hardening behavior after cracking, which resulted in greater flexural strength.

Table 8.3 Properties of UHPC and HSM at 28 days.

	Compressive strength (MPa)	Flexural strength (MPa)	T-150 (kN-mm)	Young's modulus of elasticity (GPa)	Poisson's ratio	Unit weight (kg/m^3)
UHPC	125	20.2	1.0	50.1	0.20	2500
HSM	123	11.3	50.2	49.2	0.20	2430

8.3. BOND BETWEEN FRP GRID AND MORTAR

A customized set-up was fabricated for evaluating the bonding behavior between the FRP and concrete matrix.

8.3.1. Test Specimens and Setup. To evaluate the interfacial bond between the FRP grids and the mortar matrix, push-pull double lap tests were carried out (Francesca et al. 2014).

The FRP grids were embedded in the HSM or the UHPC bricks in a 'U' shape, and tested using a special test rig as shown in Figure 8.3. One layer of CFRP grids was

used in each of the specimens to evaluate the bond between CFRP and the cementitious matrix, while two layers of GFRP grids were used to evaluate the bond. This was done since a single layer of CFRP grids can provide comparable strength with two layers of GFRP grids. The embedded length of the FPR grid was set at 200 mm. The cover thickness over the grid was 8 mm. The dimensions of the brick were $250 \times 80 \times 120$ mm (length $\times$ thickness $\times$ width). Within the width of the specimen, five GFRP or three CFRP strips were placed. Therefore, either 20 (5 strips $\times$ 2 layers $\times$ 2 sides) GFRP strips or 6 (3 strips $\times$ 1 layer $\times$ 2 sides) CFRP strips can exist in a given cross section of the push-pull specimens. The non-embedded free length of FRP grids was about 455 ± 5 mm.

The specimens were tested using a load frame with a capacity of 250 kN at a displacement rate of 1 mm/min. When the FRP grid is pulled upward by the steel cylinder, the steel bar constrains the brick. A 1-kN preload was applied to the specimen. Load and deformation were recorded by load transducers and extensometers embedded in the load frame.

(a)   (b)
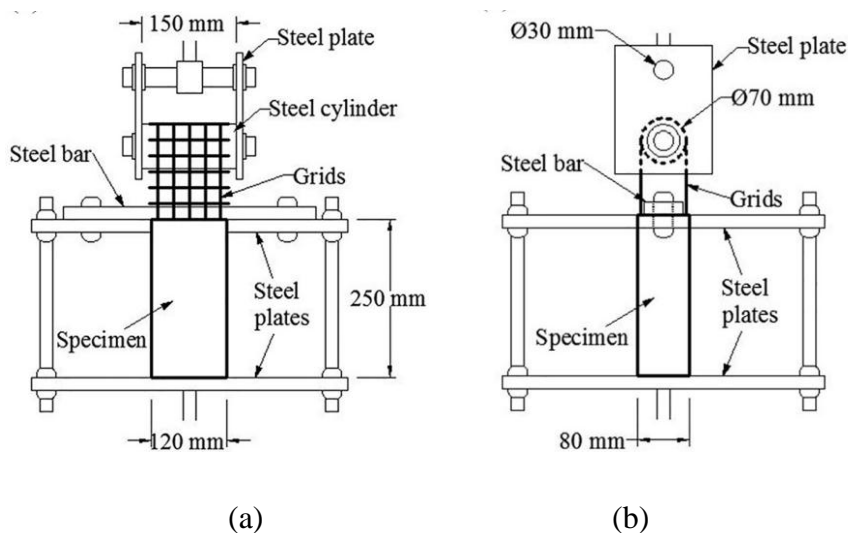
Figure 8.3. Setup of push-pull test: (a) front view and (b) side view.

8.3.2. Results and Discussion. Figures 8.4(a) and 8.4(b) show the load-displacement relationships for the GFRP and CFRP grids, respectively.

No significant difference was observed between HSM and UHPC specimens. This is because the failure was due to the rupture of the FRP grids. The HSM and UHPC provided sufficient embedment for the FRP grids.The FRP strips were not pulled out

from the cementitious matrix during the push-pull tests. The failure mode was rupture of the CFRP or GFRP grids, as shown in Figure 8.5. Since the FRP strips were not pulled out, the bond strength of the interfaces between FRP and matrix was not determined quantitatively. However, it can be deducted that the failure mode is FRP rupture when the embedded length of the FRP grids is no less than 200 mm.

(a)   (b)
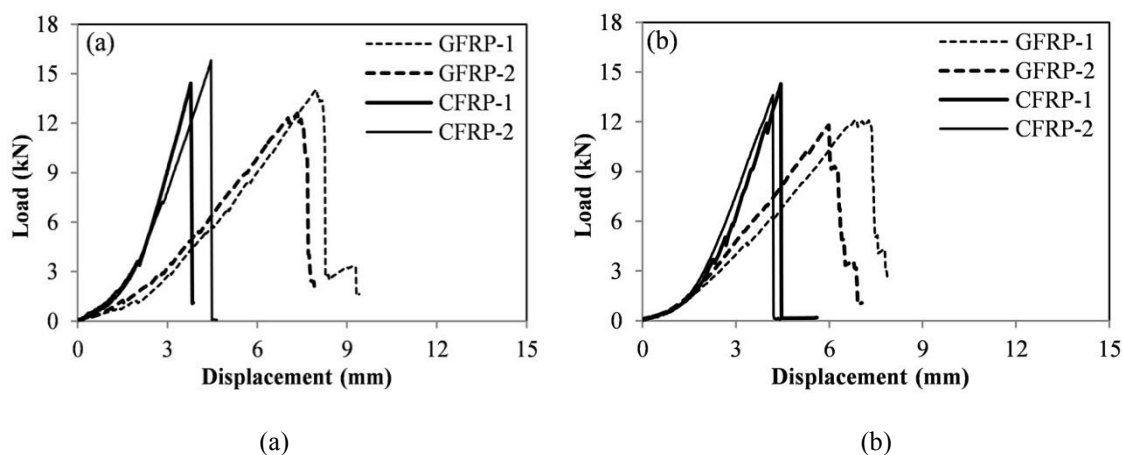
Figure 8.4. Load-deflection for two layers of GFRP grids and one layer of CFRP in push-pull tests (a) HSM made without fibers and (b) UHPC made with fibers.
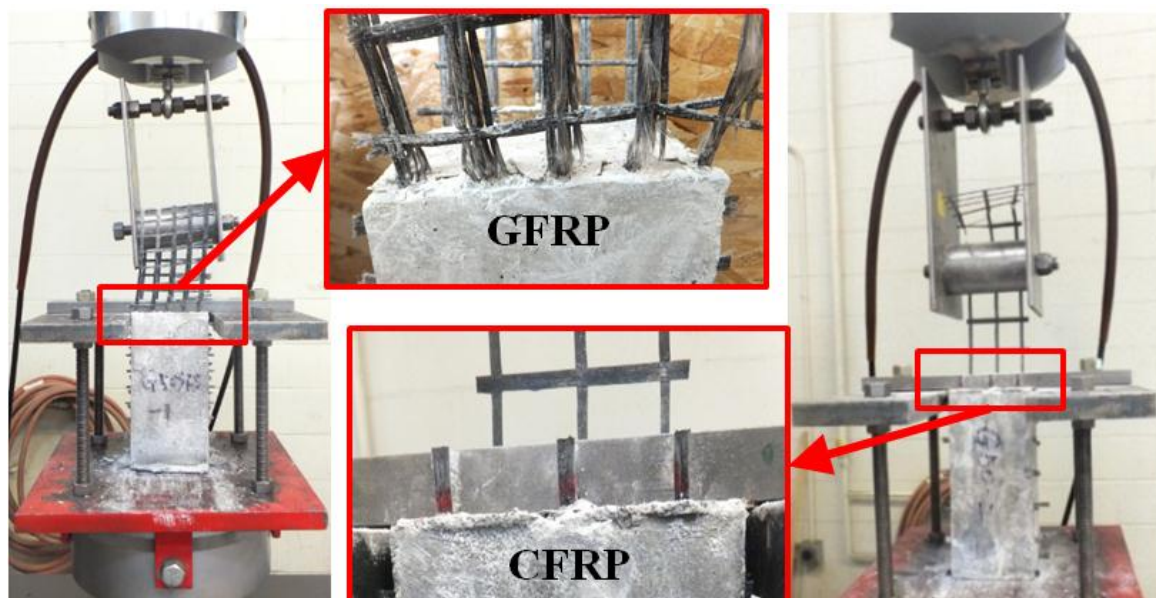
Figure 8.5. Rupture of dual-layer GFRP grids and single-layer CFRP grids.

Figure 8.6 shows four stages in the load-displacement curve: the first stage is to establish contact between the FRP grids and loading cylinder. During this stage, loose strips are gradually tightly stretched, which is reflected by the increasing slope of the load-displacement curve (Stage I). Once the contact is established, the slope becomes stabilized (Stage II). Rupture can then appear in some short strips that are stretched earlier than others, but overall the grids consisting of multiple strips can resist higher load until the peak point (Stage III). Then, rupture can occur in an increasing number of strips, and thus progressive failure takes place (Stage IV). Therefore, multiple strips in each sample do not rupture simultaneously, and, hence, the ultimate load capacity cannot be simply estimated by multiplying the capacity of a single strip by the number of strips in a given grid. For example, there were 20 GFRP strips in the cross section of a panel reinforced by two layers of GFRP grids. The tensile strength of a single strip of GFRP is about 1.2 kN. Theoretically, the strength of 20 strips can provide a load-carrying capacity of 24.0 kN; however, the tested peak load was only about 12.0–14.5 kN, which was 50%–60% of 24.0 kN.
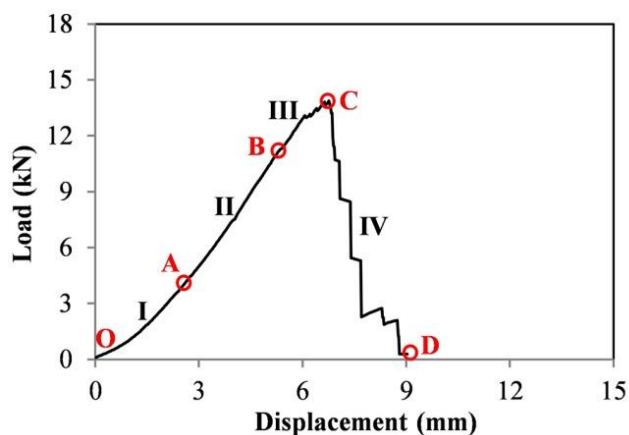
Figure 8.6. A representative load-displacement relationship of FRP grids consisting of multiple strips.

Based on this observation, the installation of FRP grids is of critical importance to mechanical performance of the specimen. FRP strips installed under the same stress-free condition resist load together and rupture at the same time. In order to improve the ductility, additional FRP strips that have different levels of pre-stresses can be added to enable progressive failure, since the FRP strips with different levels of initial stresses do

not fail simultaneously. The increase in load-carrying capacity due to the use of additional FRP strips can be determined, given the pre-stress in each of the FRP strips.

8.4. FLEXURAL TESTING

The sample preparation and test set-up of flexural testing of the panels were illustrated below:

8.4.1. Panel Specimens and Test Setup. Panel specimens measuring $500 \times 450 \times 40$ mm were prepared, as illustrated in Figure 8.7. The FRP grids were cut and fixed on the formwork before casting HSM or UHPC. A cover thickness of 5 mm was left between the grids and the formwork to ensure proper embedment of the grids in the cementitious material. The self-consolidating HSM and the UHPC were cast from the top of the panels without any mechanical consolidation.
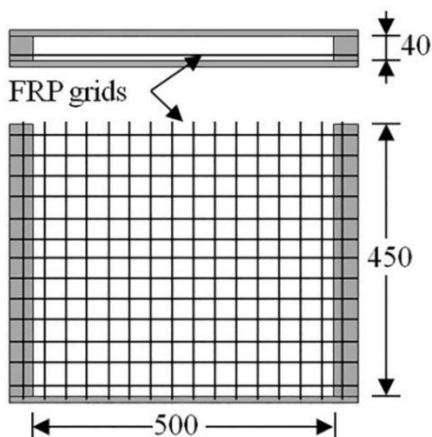
Figure 8.7. Preparation of panel specimens (unit: mm).

A total of 24 panels were prepared and tested, including 12 panels with the HSM mixture and 12 panels with the UHPC, as shown in Table 8.4. For each mixture, 3 panels had no FRP reinforcement, 3 panels had a single layer of GFRP, 3 panels had two layers of GFRP, and 3 panels had a single layer of CFRP. The HSM panels without FRP were considered as reference panels.

After 28 days of curing, the panels were tested in flexure under three-point bending, as illustrated in Figure 8.8. The panels were loaded at mid-span using a load frame with a capacity of 250 kN at a controlled displacement rate of 0.25 mm/min. A 1-kN preload was applied. The mid-span deflection and displacements of the two supports

were recorded using linear variable differential transformers (LVDTs). The applied load at the mid-span was recorded using a load transducer embedded in the load frame.

Table 8.4 Codification of specimens in three-point bending tests.

Code	Mixture	Reinforcement	Quantity
M (reference)		None	3
M1G	HSM	Single-layer GFRP	3
M2G		Dual-layer GFRP	3
M1C		Single-layer CFRP	3
ST		None	3
U1G	UHPC	Single-layer GFRP	3
U2G		Dual-layer GFRP	3
U1C		Single-layer CFRP	3
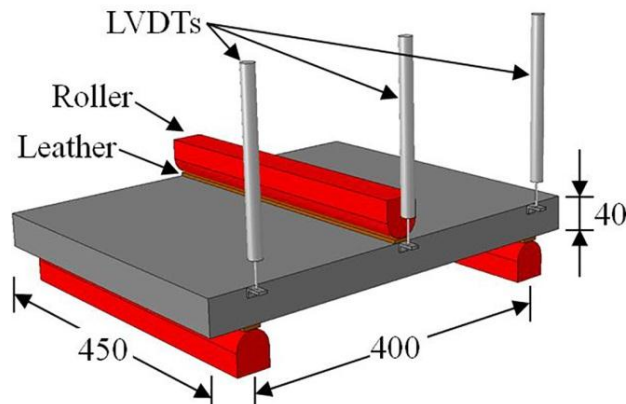
Figure 8.8. Flexural test setup (unit: mm).

8.4.2. Test Results and Discussion. The cracking scenarios of different panels are illustrated in Figures 8.9(a) – 8.9(d).

Panels made with HSM and no FRP grids exhibited brittle behavior. With the increase of load, a major crack occurred at the bottom of panel and propagated quickly through the panel thickness, leading to sudden collapse, as shown in Figure 8.9(a). The use of FRP grids prevented sudden failure, since the FRP grids crossing the crack interfaces could hold the crack, as indicated in Figure 8.9(b). Panels made with UHPC exhibited a ductile behavior due to steel fibers' bridging effect that constrained the propagation and widening of cracks, as depicted in Figure 8.9(c). The UHPC panels reinforced with FRP grids were also ductile due to the combined effect of steel fibers and FRP grids, as shown in Figure 8.9(d). Failure took place after considerable cracking of

the panel and rupture of FRP grids, when FRP grids were used. Only localized concrete crushing was observed at the top of the tested panels.

The experimental results are listed in Table 8.5. The percent values in Table 8.5 are calculated as the ratio of the given response to that of the reference panel (coded as "M" in Tables 8.4 and 8.5).
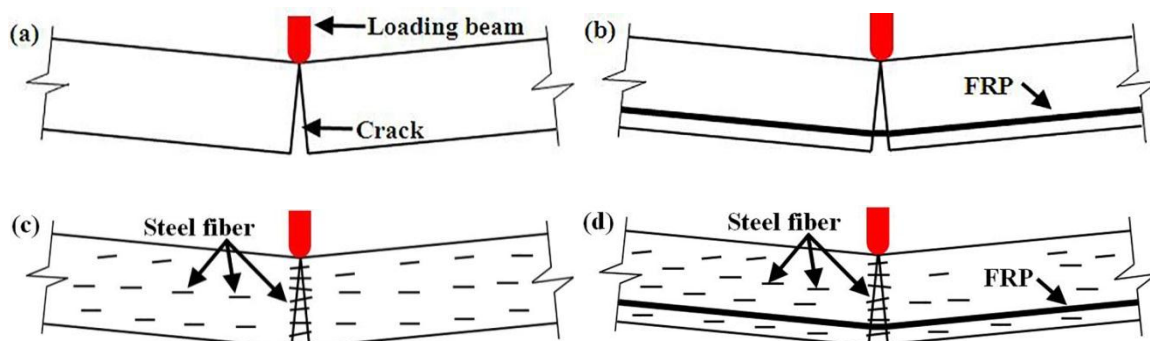
Figure 8.9 Cracking scenarios: (a) Plain HSM panel, (b) HSM panel reinforced with FRP grids, (c) Plain UHPC panel, and (d) UHPC panel reinforced with FRP grids.

Table 8.5 Experimental results of three-point bending tests.

No.	Code	Cracking load		Deflection at cracking load		Peak load		Deflection at peak load		Energy	
		Value (kN)	Percent	Value (mm)	Percent	Value (kN)	Percent	Value (mm)	Percent	Value (J)	Percent
1	M	16.2	0	1.24	0	16.2	0	1.24	0	16	0
2	M1G	15.9	-2%	0.94	-24%	15.9	-2%	0.94	-24%	22	38%
3	M2G	14.7	-9%	0.95	-23%	14.7	-9%	0.95	-23%	32	100%
4	M1C	15.3	-6%	0.94	-24%	15.3	-6%	0.94	-24%	36	125%
5	ST	14.8	-9%	0.41	-67%	18.5	14%	1.0	-17%	186	1055%
6	U1G	13.7	-15%	0.55	-56%	20.2	25%	4.1	242%	209	1198%
7	U2G	13.2	-19%	0.59	-52%	24.2	49%	3.9	215%	296	1739%
8	U1C	14.7	-9%	0.50	-60%	24.9	54%	3.5	182%	336	1987%

The load-deflection relationships of the 24 tested panels are shown in Figures 8.10(a)–8.10(h). The degree of enhancement provided by the steel fibers and FRP grids is evaluated by comparing the flexural performance, in terms of the first cracking load, peak load (load-carrying capacity), deflection at peak load, and energy dissipation, with the responses obtained from the reference panels (coded as "M" in Tables 8.4 and 8.5). The energy is determined as the area under the load-deflection curve, which represents the total work done by external loading. In this study, for comparison purpose, a mid-span

deflection of 8 mm was selected as the upper limit, which corresponding to 2% of the span length. Before cracking occurred, the primary work done by external loading was stored in the form of strain energy. However, after cracking, it was converted into other forms of energy, such as kinetic and acoustic energies, etc.

The HSM panels were brittle in flexure and demonstrated abrupt drop in load-carrying capacity after cracking, as shown in Figures 8.10(a)–8.10(d). The peak load was the same as the initial cracking load. For panels made with HSM and with no FRP, the peak load and its corresponding deflection were 16.2 kN and 1.24 mm, respectively. For the HSM panel with GFRP grids, after the occurrence of crack, the panels continued to resist some load. However, no increase in peak load was observed for the mortar panels reinforced with FRP grids. Instead, the cracking or peak load was reduced up to 9%, as shown in Table 8.5.

Based on the above observations, the main mechanism that causes reduction in cracking load and peak load is discussed. The Young's modulus of the GFRP or CFRP grids is lower than that of the cementitious matrix. For instance, although the glass fiber has a Young's modulus of 72 GPa, which is higher than that of the mortar (49.2 GPa), the epoxy resin has a Young's modulus of 3.5 GPa. Overall, the GFRP demonstrates a Young's modulus of 25 GPa. While the HSM and the GFRP are subjected to the same strain, the mortar can sustain a greater level of stress than the grids until cracking occurs. Thus, to replace some HSM of the panel with GFRP can reduce the cracking load.

Strain-hardening was observed in the UHPC panels containing steel fibers after cracking, as shown in Figure 8.10(e). The peak load was increased by 14%, compared with the HSM panels, as shown in Table 8.5. Since the steel fiber has higher Young's modulus than the HSM, the panel's flexural stiffness was increased. However, the cracking load was reduced by 9%. This reduction might be due to the debonding between the steel fiber and HSM when the strain approached the cracking strain limit of the cementitious matrix. The interfacial behavior is discussed in a latter section. The energy was increased by 1060% compared with the reference panel, implying that the UHPC panel can dissipate over 10 times more energy than the HSM panel without FRP during the flexural testing.
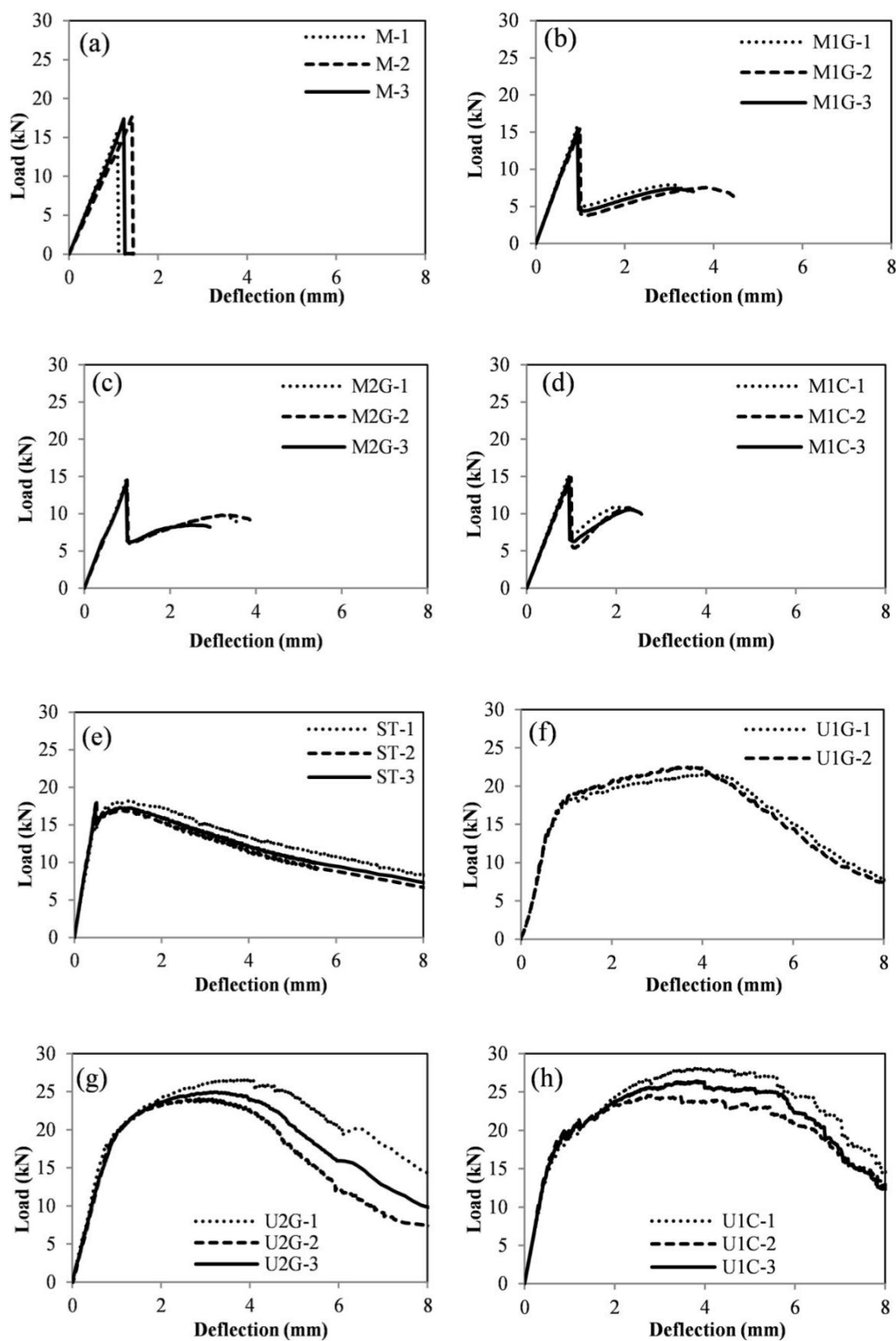
Figure 8.10. Load-deflection curves: (a) HSM panels (reference), (b) HSM panels with single-layer GFRP, (c) HSM panels with dual-layers GFRP, (d) HSM panels with single-layer CFRP, (e) UHPC panels, (f) UHPC panels with single-layer GFRP, (g) UHPC panels with dual-layer GFRP, and (h) UHPC panels with single layer CFRP.

Figures 8.10(f) – 8.10(h) show the results of UHPC panels incorporating a single-layer GFRP, dual-layer GFRP, and single-layer CFRP, respectively. The cracking load was reduced up to 19%, due to the combination of the two reduction effects caused by the use of FRP and steel fibers. Significant enhancement was observed after cracking occurred. Compared with the HSM panels, the peak loads of the UHPC panels were greatly enhanced by the use of GFRP or CFRP grids. Compared with the use of steel fibers that lead to 14% increase in peak load, the levels of increase provided by single-layer and dual-layer GFRP reinforced panels and single-layer CFRP reinforced panels were 25%, 49%, and 54%, respectively.In addition, the energies were increased as well, and the levels of increase corresponding to the single-layer and dual-layer GFRP reinforced panels, and single-layer CFRP reinforced panels were approximately 12, 17, and 20 folds, respectively.The above results clearly indicate that the use of the GFRP or CFRP grids can hardly increase the peak load of the HSM panels, and it can slightly reduce the cracking loads. However, the use of FRP grids can significantly enhance the peak load and energy dissipation when using the UHPC for the panel testing. The use of dual-layer GFRP is shown to provide an enhancement in mechanical performance comparable to that of single-layer CFRP reinforcement.

8.5. MECHANICAL MODEL TO EVALUATE FLEXURAL BEHAVIOR OF COMPOSITE PANELS

A mechanical model to evaluate flexural performance of the investigated panels was elaborated below:

8.5.1. Development of Mechanical Model. A mechanical model is presented to analyze the flexural behavior of simply-supported panels with embedded FRP grids. Given the symmetry and the fact that both the load and the structural element are uniformly in the transverse direction, a unit width can be analyzed instead of the full-width panel, as illustrated in Figure 8.11. Then, the three-dimensional problem can be simplified to two dimensions. Here, it can be assumed that all interfaces have the perfect bond condition. Potential interfacial debonding is discussed in a latter section.

The half panel is subjected to a reaction force, half of the loading force, and a moment, which are denoted by R, F/2, and M, respectively. After the panel cracks, the crack width and the mid-span deflection of the panel are denoted by w and d,

respectively. M is a resultant of the stresses or forces acting at the cut face. F is proportional to M, based on equilibrium conditions; w is proportional to d, based on similarity of triangles, as given in Equation 8.1.

$$F = 4M/L, \; w = 2dt/L \qquad\qquad \text{Equation 8.1}$$
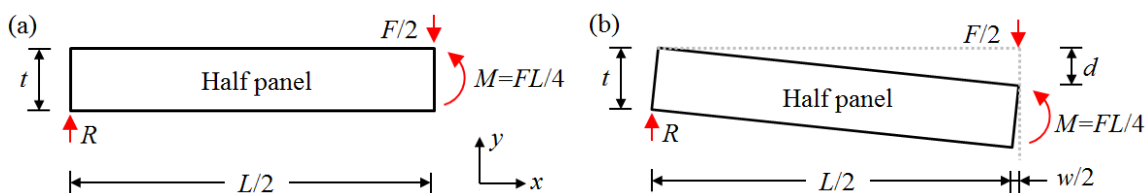
Figure 8.11. Free body diagrams: (a) before crack and (b) after crack.

Table 8.6 shows the analysis of moment at the cut face for the HSM panel (HSM), HSM panel reinforced with FRP grids (HSM+FRP), UHPC panel (UHPC), and UHPC panel reinforced with FRP grids (UHPC+FRP).

Table 8.6 Analysis of bending moments.

Description of sections	Stress or force distribution on cross section	
	Before cracking	After cracking
HSM	$M = \int_0^t \sigma_1(y)\,y\,dy$	$M = 0$
HSM+FRP	$M = M_1 + M_2$ $M_1 = \int_0^t \sigma_1(y)\,y\,dy$ $M_2 = \int_0^t \sigma_2(y)\,y\,dy + Pc$	$M = P(t\text{-}c)$
UHPC	$M = \int_0^t \sigma_1(y)\,y\,dy$	$M = \int_0^t \sigma_1(y)\,y\,dy$
UHPC+FRP	$M = M_1 + M_2$ $M_1 = \int_0^t \sigma_1(y)\,y\,dy$ $M_2 = \int_0^t \sigma_2(y)\,y\,dy + Pc$	$M = M_1 + M_2$ $M_1 = \int_0^t \sigma_1(y)\,y\,dy$ $M_2 = P(t\text{-}c)$

The thicknesses of the panel and cover layer are denoted by t and c, respectively. Since the FRP grids are very thin compared with the panel thickness, the stress can be considered as uniform over the thickness of FRP grids, and, thus, a concentrated tensile force (P) can be used in the calculation of M. Note the magnitudes and the distributions of stresses and forces are not to scale. According to the observations of the three-point bending tests, the concrete crushing was not significant in the compressive zone. Therefore, as a simplification, the mortar and the UHPC can be assumed to be linearly elastic under compression.

Table 8.6 reveals when FRP grids are employed, both the embedded FRP and host materials can contribute to the load-carrying capacity. The use of FRP in the panels adds another term to the expression of load resistance.For a brittle mortar panel, the stress distribution is approximately linear over the entire height of the cross section before panel cracking. The mid-span deflection is given in Equation 8.2.

$$d = FL^3 / 48E_M (t^3 / 12) = FL^3 / 4E_M t^3 \qquad \text{Equation 8.2}$$

where E_M represents the Young's modulus of the mortar. Equation 8.2 explicitly shows that the mid-span deflection is in proportion to the load, which is in good agreement with the experimental results illustrated in Figure 8.10(a). After mortar cracking, the panel collapses with no stress on its crack faces, and thus the moment decreases to zero, as illustrated in Table 8.6. If the crack limit is σ_m, the stress distribution can be expressed as $\sigma_1 (y) = \sigma_m (1-2y/t)$. Then, the corresponding moment and load can be given in Equations 8.3 and 8.4, respectively.

$$M = \int_0^t \sigma_m (1 - 2y/t) y \, dy = \sigma_m t^2 / 6 \qquad \text{Equation 8.3}$$

$$F = 4M / L = 2\sigma_m t^2 / 3L \qquad \text{Equation 8.4}$$

For the HSM panels reinforced with FRP, the composite section consists of mortar and FRP, and, thus, the moment is composed of two parts before panel cracking. The two parts are denoted by M_1 and M_2, respectively, as shown in Table 8.6. M_1 is resisted purely by the HSM, while M_2 is resisted by the FRP and HSM. For each of the

two parts, the forces satisfy equilibrium, and the moment can be calculated by integration as indicated in Equation 8.3.

An "equivalent mortar section" can be used to replace the composite section, as depicted in Figure 8.12. At the A-A cross section, there are longitudinal and transverse FRP strips. The transverse strip passes through the cross section. Since the fibers of the transverse strip are vertical to the longitudinal direction of the simply-supported panel, they have a negligible contribution to carrying loads. The load-carrying capability of the epoxy resin of the transverse strip is also neglectable due to the small Young's modulus of elasticity (3.5 GPa). For simplicity, the load carried by the transverse FRP strip is neglected. As to the loads carried by the longitudinal FRP strips, the cross-sectional area occupied by longitudinal FRP ($A_{L,FRP}$) can be replaced by an equivalent mortar area $A_M = E_{FRP}A_{L,FRP}/E_M$. Then, the second moment of area (I_{eq}) of the equivalent section can be calculated as:

$$I_{eq} = bt^3/12 + (E_{FRP}A_{L,FRP}/E_M - A_{T,FRP})(t/2 - c)^2 \qquad \text{Equation 8.5}$$

where b (= 450 mm) and t (= 40 mm) represent the width and thickness of the panel, respectively. The area occupied by the transverse FRP is denoted by $A_{T, FRP}$. The cover thickness is denoted by c (= 5 mm).
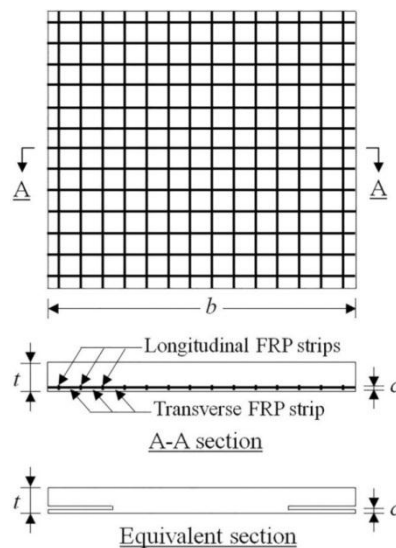
Figure 8.12. Illustration of the equivalent cross section.

The equivalent section has the same flexural stiffness as the original composite section. Thus, Equations 8.3 to 8.5 can be used if a correction factor is introduced to account for the reduction in flexural stiffness due to the presence of FRP grids. The correction factor can be defined as $\alpha = 12I_{eq}/bt^3$. Table 8.7 shows the calculated results.

Table 8.7 Correction factors for composite panels.

Code	$A_{L,FRP}$ (mm^2)	$A_{T,FRP}$ (mm^2)	E_{FRP} (GPa)	E_M (GPa)	I_{eq} ($\times 10^6$ mm^4)	α
M1G	48	900	25	49.2	2.20	0.92
M2G	96	1800	25	49.2	2.01	0.84
M1C	99	1350	40	49.2	2.11	0.88
U1G	48	900	25	50.1	2.20	0.92
U2G	96	1800	25	50.1	2.01	0.84
U1C	99	1350	40	50.1	2.11	0.88

After cracking, the mortar stops contributing to tensile strength and can only resist compression at the upper section, which is in compression. The tensile resistance would then be provided only by the longitudinal FRP strips that are stretched by the two crack faces. The tensile and compressive forces provided by FRP and mortar, respectively, form a force couple with a moment of arm that is approximately (t - c). The tensile force in the FRP can be given in Equation 8.6.

$$P = A_{L,FRP}\sigma_{FRP} = A_{L,FRP}E_{FRP}(1 - c/t)w/2l_d \qquad \text{Equation 8.6}$$

where l_d represents a length of FRP, which averages the length change Δw due to cracking. Since no debonding occurrence is assumed, l_d corresponds to the development length. For simplicity, l_d is considered to be constant. Then, the internal force, P, is proportional to crack width (w). This is in good agreement with the observation that overall the pulling force is in proportion to the deformation in the push-pull tests, proving that the assumptions are acceptable.

Substituting Equations 8.1 and 8.6 into the values of $M = P(t$ - $c)$ in Table 8.3, the relationship between loading force and deflection can be given in Equation 8.7.

$$d = [L/(t - c)]^2 Fl_d / 4E_{FRP}A_{L,FRP} \qquad \text{Equation 8.7}$$

Equation 8.7 shows the load-carrying capacity due to the embedded FRP grids. It demonstrates that d is proportional to F after the panel cracks.

8.5.2. Comparison of Mechanical Model with Experimental Results. For the UHPC panel, before cracking, the stress and force distributions are similar to those of the mortar panel. However, the UHPC panel can carry more loads after it cracks, due to the bridging effect of steel fibers. The relationship of the mid-span deflection and load of the UHPC panel was experimentally determined, as presented in Figure 8.10(e). The load-deflection curve is described using a tri-linear model, as shown in Figure 8.13(a), which also includes the load-carrying models of the HSM panel and FRP grids. Once the load-carrying behavior of each single component is determined, the performance of the composite element can be analyzed as a combination of the single components, as shown in Figure 8.13(b).

Due to the fact that the peaks of cementitious matrix and FRP grids do not correspond to the same deflection value, each of the load-deflection curves of the composite panels have two peaks. One peak corresponds to the peak of the cementitious matrix, and the other peak corresponds to the rupture of FRP grids. Which peak dominates depends on the specific material and dimensions. In this study, according to the experimental results in Figures 8.10(a)–8.10(h), the peak corresponding to the fracture of HSM dominated for HSM panels, while the peak corresponding to the rupture of FRP grids dominated for UHPC panels. This explains the reason why the peak loads of the HSM panels were not increased by the GFRP grids, while the peak loads of the UHPC panels were considerably improved. It is because the mortar panel cracks and loses load resisting capability when the stress in GFRP grids is fully developed. However, for the UHPC panel, although its load resistance decreases after peak load, it can still resist notable load, thus resulting in a higher total load resistance when the GFRP grids are incorporated.

Although the FRP grids effectively enhanced the load-carrying capacity (peak load), the enhancement effectiveness of FRP grids for the UHPC panel was not fully exploited, because when the FRP grids reached their peaks, the load carried by UHPC dropped below the peak. One approach to optimize the effectiveness is to apply pre-tension to FRP grids before casting the UHPC. There are two mechanisms to improve the

flexural capacity. On one hand, the prestressing force applied to FRP can result in compressive stress that can increase the cracking and peak loads of the panel, since the FRP is deployed at the tensile zone, for example, the bottom of UHPC panel, in three-point bending tests. On the other hand, by controlling the prestressing force applied to FRP grids, the FRP can potentially rupture at the same time with the UHPC, thus fully utilizing the tensile strength of FRP grids.

The experimental and mechanical results of the load-deflection behavior of UHPC-FRP panels are compared in Table 8.8. The maximum discrepancy was -9.2%. The discrepancy is because of the complex nature of the cracking mechanism and the employed simplification that the load-deflection curves are taken as linear. Overall, the model provides an adequate prediction for the flexural behaviors of the composite panels.
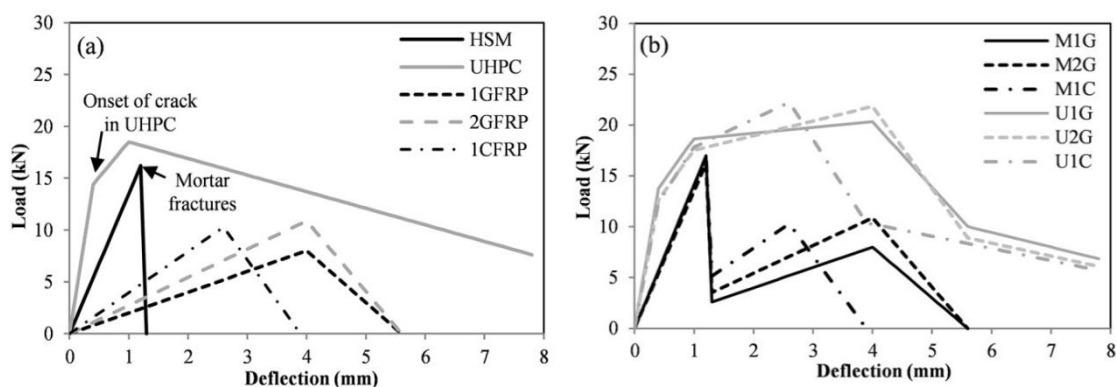
Figure 8.13. Load-deflection relationships derived from mechanical model: (a) individual materials and (b) composite materials and comparison with individual materials.

Table 8.8 Comparison of experimental and mechanical analysis results of peak load values.

Code	Experiment (kN)	Analysis (kN)	Discrepancy (%)
U1G	20.2	20.3	0.6%
U2G	24.2	22.0	-9.1%
U1C	24.9	22.6	-9.2%

8.5.3. Debonding Between FRP Grids and Mortar. In the preceding analysis, the interfaces between the FRP grids and host matrix were considered to be well bonded.

Before cracking occurs, the cementitious matrix is continuous, as illustrated in Figure 8.14(a). An infinitesimal FRP with a length of *dl* is selected. The left and right

faces are marked with "M⁻" and "M⁺", respectively. After the panel cracks with a width of w, the infinitesimal element is stretched to a length of $w+dl$. Therefore, the tensile strain in the infinitesimal element is $(w+dl)/dl$, which is an infinite value and must result in rupture in FRP grids. However, experiments demonstrated that the FRP grids crossing the crack interfaces were not ruptured when cracking was initiated in host matrix. This can be attributed to debonding in the vicinity of the crack faces, as illustrated in Figure 8.14(b). Assume the debonding length is Δl at each side, the tensile strain will be $(w+dl+2\Delta l)/(dl+2\Delta l)$. As dl approaches to zero, $(w+dl+2\Delta l)/(dl+2\Delta l)$ approaches to $(w/2+\Delta l)/\Delta l$, which is finite and does not necessarily rupture FRP when crack appears. Such debonding mechanism explains the experimental phenomenon that sudden rupture of FRP does not occur at the moment when a crack appears in the host matrix.
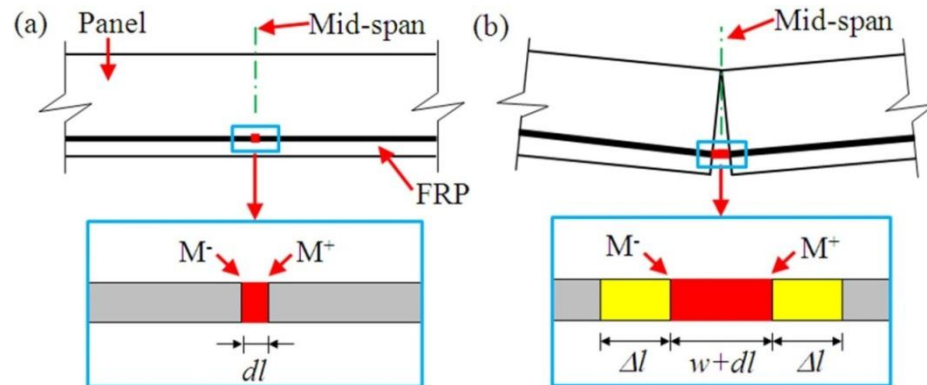
Figure 8.14. Illustration of debonding due to cracking: (a) before cracking and (b) after cracking.

8.6. MICROSTRUCTURE

After the flexural testing, the microstructure of the panel specimens was observed using optical microscope (Figures 8.15(a) and 8.15(b)) and scanning electron microscope (SEM, Figures 8.15(c)–8.15(f)), respectively. Samples shown in Figures 8.15(a) and 8.15(c) were cut from the UHPC panels with GFRP, at a free end that is far away from the mid-span. Samples shown in Figures 8.15(b) and 8.15(d) were cut from the UHPC panels with CFRP, at a free end that is far away from the mid-span, and from the mid-span, respectively. Figures 8.15(a)–8.15(c) show that the fine aggregate (sand) and the

steel fibers were uniformly distributed, and the FRP grids were well embedded in the cementitious matrix. For the samples taken from the free end, no debonding or cracking was observed, as shown in Figures 8.15(a)– 8.15(c).
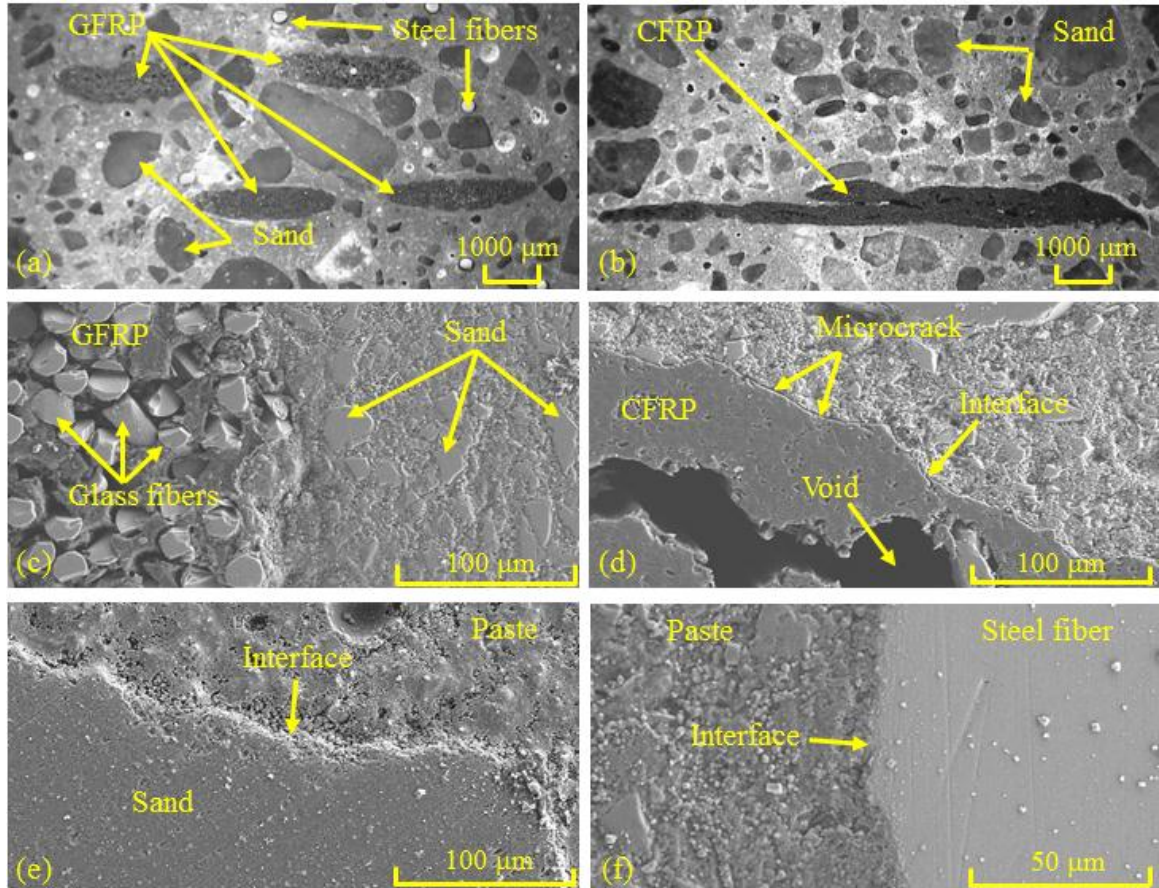
Figure 8.15. Microstructures: (a) optic micrograph of dual-layer GFRP in UHPC, (b) optic micrograph of single-layer CFRP in UHPC, (c) SEM photo of GFRP in UHPC, (d) SEM photo of CFRP in UHPC near the mid-span, (e) SEM photo of sand in UHPC, and (f) SEM photo of steel fiber in UHPC.

However, in the sample taken from the mid-span, microcracks in the mortar and debonding at the interface between the mortar and FRP can be observed, as shown in Figure 8.15(d), which confirms the preceding discussion on debonding. Figures 8.15(e) and 8.15(f) show the interfaces between sand and cement paste, and between steel fiber and paste, respectively. Again, the samples were taken from the free end, and no debonding or cracking was detected. These observations confirm the analysis presented earlier regarding the presence of a debonded zone between the FRP and cement matrix at

the vicinity of cracks. Debonding occurs near the crack faces and does not propagate away from the cracked zone. In addition, adequate bonding was observed at the interface of UHPC embedded FRP grids away from cracked zone.

8.7. NUMERICAL SIMULATIONS

The finite element model was established to simulate the bending behavior of panels elaborated above:

8.7.1. Finite Element Model. A three-dimensional nonlinear finite element model was developed using ABAQUS to investigate the flexural behavior of the UHPC panels with different geometries and reinforcement configurations.

The model was compared to the experimental data in order to validate the model to determine the stress distribution and damage propagation in composite panels. The thin and flexible GFRP grids were modeled using 2-node linear 3-D truss (T3D2) elements. Each T3D2 element has 2 nodes, and each node has 3 degrees of freedom. The UHPC matrix, steel rollers, and rubber pad were modeled using 8-node linear 3-D brick reduced integration (C3D8R) elements. Each C3D8R element has 8 nodes, and each node has 3 degrees of freedom. The contact between GFRP and UHPC was defined using the keyword 'embed,' without considering interfacial debonding. A mesh size convergence study was conducted, and a mesh size of 5 mm was adopted. The nonlinear finite element equations were solved using Newton method (Myer 1998). Surface-to-surface hard contact was defined for the contacting surface pairs using a basic Coulomb friction model, namely penalty friction model. The coefficient of friction was assumed to be constant. It was taken as 0.8 for the contact between steel (rod supports and loading rod) and rubber, and 1.0 for rubber and UHPC (Myer 1998). The steel's Young's modulus and Poisson ratio were taken as 210 GPa and 0.2, respectively. The rubber's Young's modulus and Poisson's ratio were 1 GPa and 0.4, respectively. Figure 8.16 shows the established meshed model.

The concrete damaged plasticity (CDP) model was successfully implemented to characterize UHPC using notch beam specimens (Tao and Chen 2015, Mahmud et al. 2013). Assuming that steel fibers are uniformly distributed in the cementitious matrix, the mechanical properties of the UHPC are considered to be homogeneous (Mahmud et al. 2013). Since no significant concrete crushing was observed in the experiments, the

UHPC was assumed to be elastic under compressive stress. This assumption can be checked in the stress distribution results.

Figures 8.17(a) and 8.17(b) show the constitutive relationships of the strain-stress of the UHPC and the GFRP grids, respectively. The constitutive relationship of the GFRP was tested using a single GFRP strip in tension.
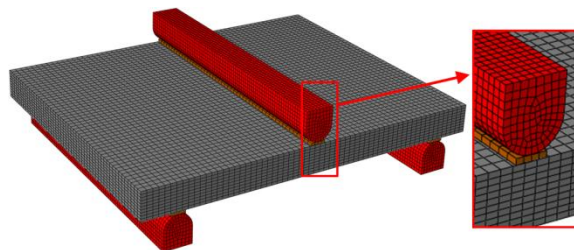
Figure 8.16. Flexural test setup.
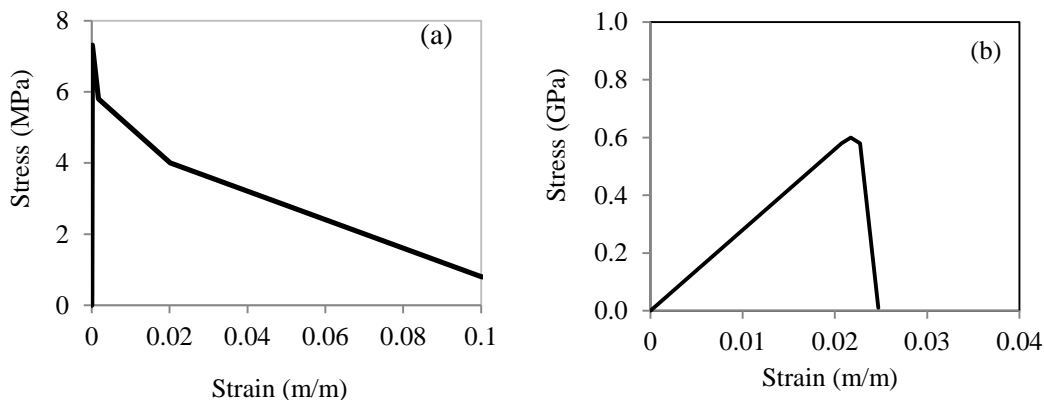
Figure 8.17. Tensile stress-strain relationship for: (a) UHPC and (b) GFRP.

8.7.2. Simulation Results and Discussion. Figures 8.18(a) and 8.18(b) show the distribution of the maximum principle stress in the panel.

The maximum principal stress (MPS) was at the bottom of the panel at the mid-span before cracking occurred. The deflection curve was in a parabolic shape. However, after cracking occurs at the mid-span, the MPS can arise from the bottom to the region near the top. The maximum compressive stress was less than 8 MPa, which was much lower than the UHPC's compressive strength (125 MPa). Hence, the premised assumption that the UHPC was in the elastic stage in compression was validated.

However, the tensile stress/strain went beyond the elastic range. Figures 8.18(c) and 8.18(d) show the development of plastic strain (PS, strain larger than the elastic strain limit) with the increase of the mid-span deflection. The PS first appeared at the center of the panel, and then propagated along the mid-span. The trend was the same as that observed in the experiment test panels.

Figure 8.19 shows the stress distributions in a GFRP strip along the longitudinal direction of the simply-supported panel, at different mid-span deflection levels. When the mid-span deflection reached approximately 70 µm (after cracking occurred), the GFRP's stress at the mid-span increased to a large value. The tensile stress of FRP can increase until it ruptures.
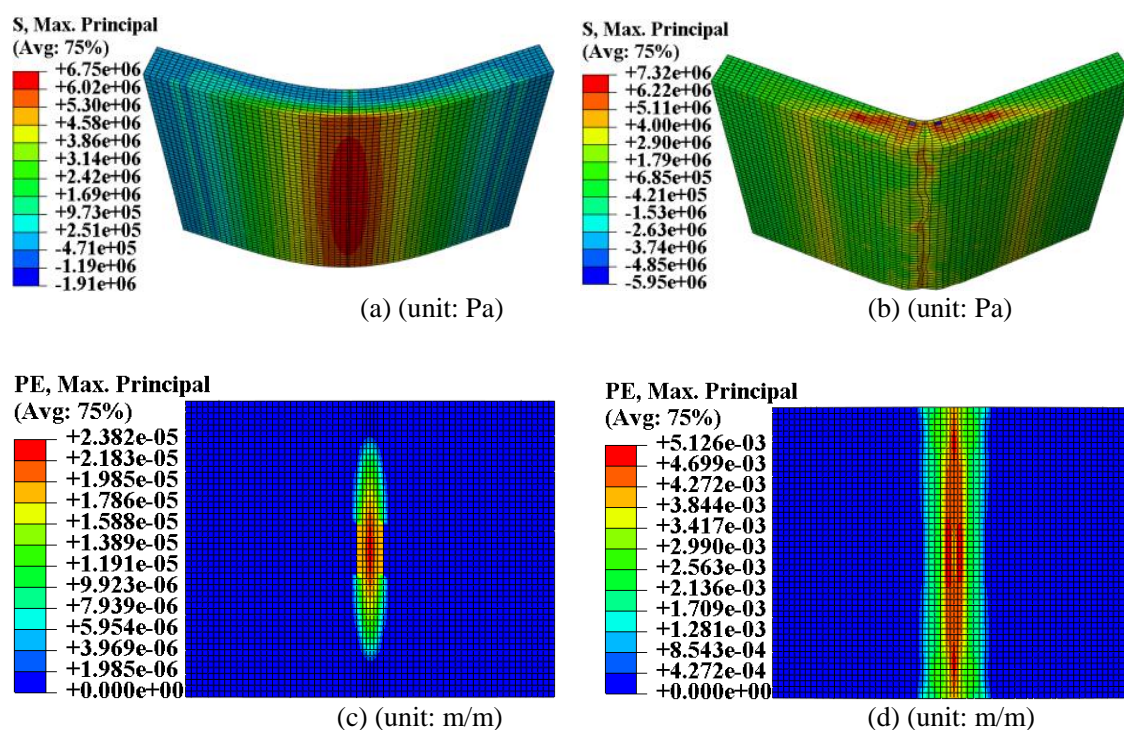
Figure 8.18. Simulation results of stress: (a) distribution of MPS before cracking (scale factor: 500), (b) distribution of MPS after cracking (scale factor: 10), (c) distribution of PS at 0.1-mm mid-span deflection, and (d) distribution of PS at at 0.5-mm mid-span deflection.
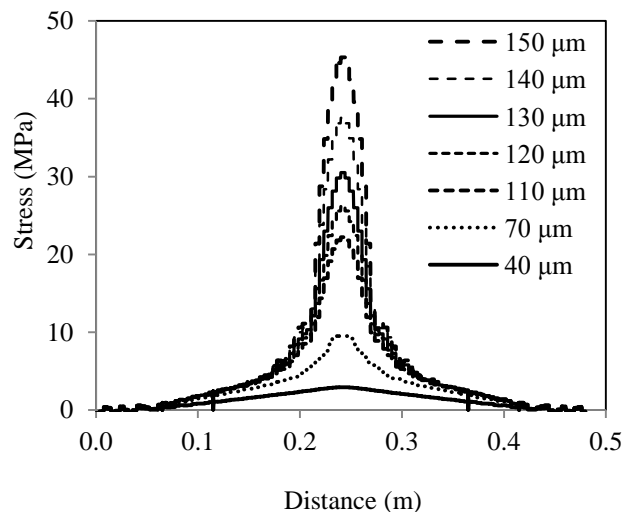
Figure 8.19. Stress distribution in GFRP along longitudinal direction of panel at different mid-span deflections.

Figure 8.20 compares the experimental (Exp_ST, Exp_U1G, and Exp_U2G) and numerical (Sim_ST, Sim_U1G, and Sim_U2G) results. Both results were in satisfactory agreement, thus validating the validity of the numerical model. The experimental and numerical results were in excellent agreement (up to 1% error) for the elastic stage that takes place before cracking occurs.
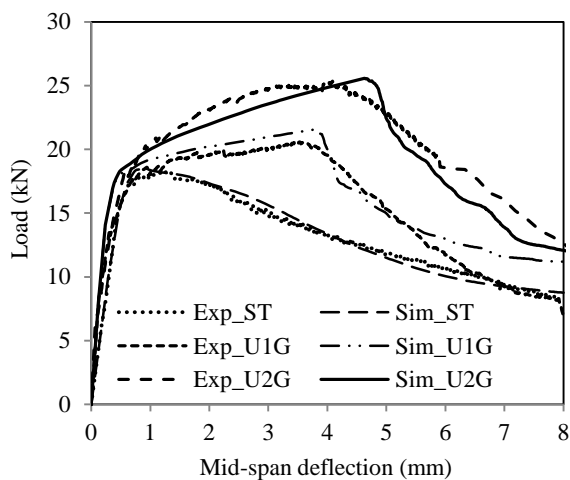
Figure 8.20. Load-deflection relationships of the panels with 40-mm thickness.

A greater error (up to 9.5%) can be observed after cracking occurs. This is because the multiple strips in single or dual-layer FRP grids are assumed to work together

perfectly and rupture at the same time in the numerical simulation. However, the multiple strips can be of different stresses or strains, and they do not necessarily rupture at the same time, as shown in the experimental results, which lead to a reduction in the peak load. Therefore, the numerical model slightly overestimated the peak load. The progressive failure of multiple strips in FRP grids needs to be taken into consideration in order to reduce the error. Therefore, a constitutive relationship for multiple FRP strips should be adopted instead of using a simple stress-strain relationship for a single FRP strip.

8.7.3. Parametric Studies. A parametric study was conducted to investigated the design parameters of the proposed UHPC panels.

8.7.3.1 Load-deflection relationship. Figures 8.21(a)–8.21(c) show the load-deflection relationships of UHPC panels made without any GFRP, those reinforced with a single layer of GFRP grid, and those reinforced with dual layers of GFRP grids.
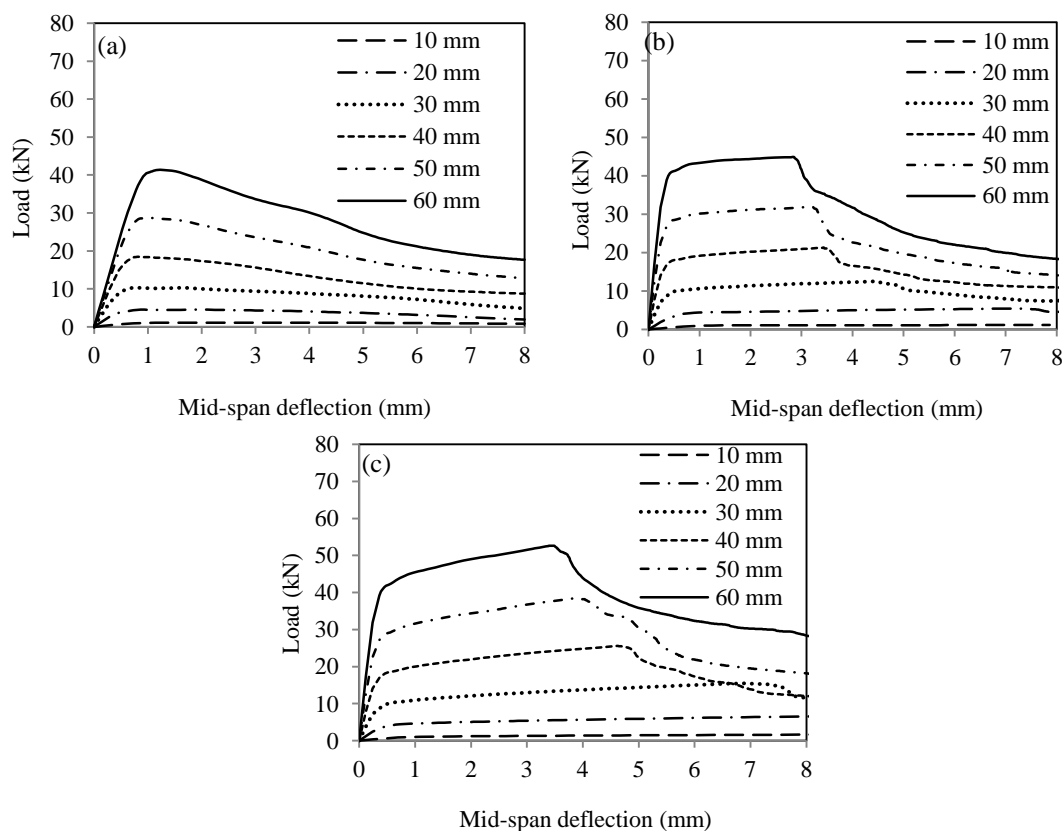
Figure 8.21. Load-deflection relationship as function of panel thickness: (a) ST, (b) U1G, and (c) U2G.

The panel thickness was varied from 10 to 60 mm. The grids were modeled to be at 5 mm from the bottom surface. The parametric study indicated that the first crack and peak loads can increase with the panel thickness. However, no evident difference could be observed for the deflection corresponding to the first crack load and peak load values.

8.7.3.2 Peak load and corresponding deflection. Figures 8.22(a) and 8.22(b) show the peak load (or flexural strength) and the mid-span deflection at peak loads. The peak load increases nonlinearly with the panel thickness. For each panel thickness, the panels reinforced with dual-layer GFRP grids exhibited the largest peak load and the corresponding mid-span deflection, and the UHPC panels without GFRP exhibited the smallest peak load and the corresponding mid-span deflection. Overall the deflection decreased with the panel thickness. However, for the panels without GFRP, the deflection reached its minimum when the thickness was 30 to 40 mm. When the thickness was larger than 30 mm, no evident change was observed between the panels with different configurations.

8.7.4. Energy Dissipation. The integration of the load-deflection curves of Figure 8.22 between deflection values of 0 and 8 mm, allows evaluating the energy dissipation. Energy dissipation of UHPC panels of thickness 10 to 60 mm is given in Figure 8.23.
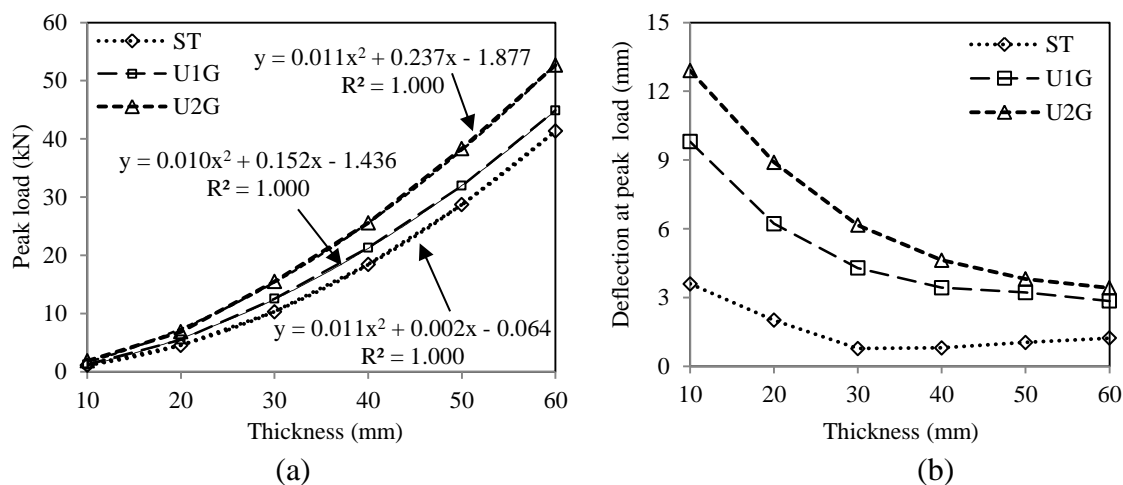
Figure 8.22. Peak load and mid-span deflection at peak load: (a) peak load, and (b) mid-span deflection at peak load.

Regardless of the thickness of the panel, UHPC panels reinforced with the dual-layer GFRP had the highest energy dissipation, followed by single-layer reinforced

panels and panels without GFRP. The spread between two adjacent curves represents the energy dissipation due to the use of one layer of GFRP grids.
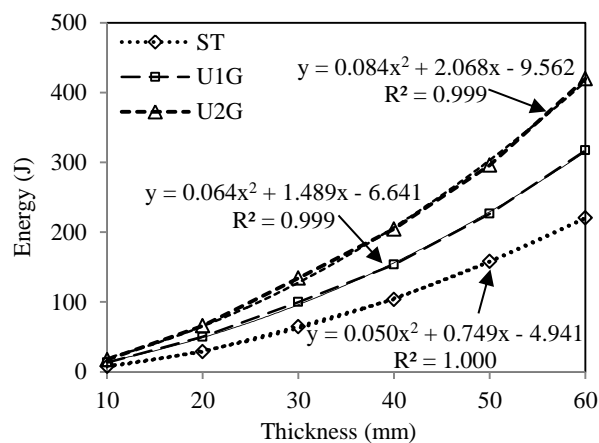
Figure 8.23. Variations of dissipated energy with thickness of various panel configurations.

8.8. SUMMARY

In this study, UHPC panels reinforced with internally-bonded FRP grids were experimentally evaluated and analyzed using a mechanical model. The main findings can be summarized as follows:

(1) The GFRP and CFRP grids tested in uniaxial tension exhibited failure in tension. The average tensile strengths of single strips of GFRP and CFRP were 1.2 and 3.8 kN, respectively. The ultimate strain values at rupture were 0.02 (2%) and 0.01 (1%), respectively.

(2) Bond between FRP grids and UHPC matrix investigated in push-pull tests indicated that an embedment length of 200 mm of the GFRP and CFRP grids in UHPC panels is sufficient to secure adequate bond with UHPC.

(3) HSM panels with different reinforcement configurations investigated in three-point bending tests were brittle in flexure. Their flexural capacities could not increase when using GFRP and CFRP grids. The incorporation of FRP grids prevented sudden collapse but did not increase the load-carrying capacity.

(4) UHPC panels were ductile in flexure and demonstrated 14% higher flexural strength than HSM panels. Flexural capacity of UHPC panels can be further increased by

the use of CFRP or GFRP grids. The use of single- and dual-layer GFRP grids in UHPC panels can result in approximately 25% and 49% increase in flexural capacity, respectively, and the use of a single-layer CFRP can lead to 54% increase. First cracking load can decrease by 15%, 19%, and 9% due to the use of single-layer GFRP, dual-layer GFRP, and single-layer CFRP, respectively.

(5) The enhancement of dual-layer GFRP was comparable with that of the single-layer CFRP. In addition, the energy dissipation capability of panels could be increased by 11 folds when using steel micro fibers. The use of single-layer GFRP, dual-layer GFRP, and single-layer CFRP grids can increase the energy dissipation by 12, 17, and 20 folds, respectively.

(6) A mechanical model was developed to evaluate the flexural behaviors of UHPC panels reinforced with FRP grids. The discrepancy of peak flexural loads between experimental and analytical results was in the range of -9.2% to 0.6%.

(7) Based on the mechanical model, debonding between FRP grids and the host mortar was discussed and was validated by SEM investigations. Such observations showed some debonding between the FRP reinforcement and the UHPC/HSM material at the vicinity of cracks.

(8) The UHPC panels reinforced with embedded GFRP grids were simulated numerically in this study. The developed non-linear finite element model incorporating the CDP model for concrete material allows adequate predictions of the flexural performance of the GFRP reinforced UHPC panels and enables the determination of the stress distribution in the GFRP grids and concrete matrix. Based on the parametric studies using numerical models, the peak load and the energy dissipation are shown to increase with the number of embedded GFRP grids and panel thickness. Such increase can be described in well-established parabolic equations. The mid-span deflection corresponding to peak load decreased with the increase of the overall panel thickness. However, it did not change significantly for the UHPC panel made without any GFRP grids.

9. POTENTIAL APPLICATION OF PREFABRICATED ELEMENT USING UHPC

9.1. BACKGROUND

The high strength of UHPC allows the use of reduced structural sections, which can save materials and enable diverse structural designs. The enhanced durability of UHPC enables UHPC structures to have extended service life, and reduced maintenance cost. In North America, UHPC has been gaining some interest in highway and pedestrian bridge applications in the forms of precast bridge girders (Steinberg 2009; Ghoneim et al. 2010), bridge decks (Aaleti et al. 2011; Saleem et al. 2011), and in-fill bridge deck joints/connection (Perry and Weiss 2009; Graybeal 2010; Aaleti et al. 2011). Bierwagen and Abu-Hawash (2005) reported that the use of UHPC girder increased the spanning capability and enabled use of a single span bridge to replace a two-span bridge. The combination of significantly higher prestressing force and tensile strength of UHPC than those of a comparable normal concrete girder also helped eliminate the transverse reinforcement in the girder. The main advantage of using UHPC in bridge decks is that it prevents early deterioration of deck resulting from cracking that allows penetration of chloride especially during winter months. Naaman and Chandrangsu (2004) developed a UHPC deck with only one layer of steel reinforcing bars at the bottom instead of four (two at the bottom and two at the top). They concluded that approximately 70% of the reinforcement could be eliminated and a significant reduction in crack widths was achieved, by using UHPC rather than conventional concrete.

From the premises, UHPC has been found to be a promising advanced material for various applications. However, the reported applications, especially for prefabricated elements, are very limited. Since UHPC composites are particularly suitable for stay-in-place (SIP) elements (Saleem et al. 2012), in this study, the design of SIP formwork was first explored. SIP formwork is a formwork that is left in place and may become an integral part of the structural element. The use of short fiber and continuously reinforced cementitious panels as SIP panels for formwork has been examined by a number of researchers and organizations (ACI 347-04, 2004). These panels are typically brittle and have poor impact resistance. In order to improve the impact resistance, ductility, and durability, which are the key factors for SIP formwork, UHPC can be employed and they

can also be reinforced with a separate continuous nonmetallic reinforcement system, such as FRP, to further enhance the overall material properties.

Recently, intensive researches have been focused on the use of SIP formwork panels for bridge decks or slabs. Kim et al. (2006; 2008) used glass fiber reinforced concrete (GFRC) for SIP formwork for bridge deck. Leung and Cao (2010) investigated a new approach for the construction of durable concrete bridges. They fabricated bridge deck SIP formworks using pseudo-ductile cementitious composites (PDCC) with a relatively low w/b. With low permeability and high crack resistance, the SIP formwork acts as effective surface cover to prevent corrosion of steel reinforcements. Yu (2014) presented that the bonding between the formwork system and concrete cast within the formwork was improved significantly by modifying the inner surface of the formwork with transverse and longitudinal grooves stiffeners that can be introduced in the formwork. Harris and Roberts-Wollmann (2005) evaluated the punching shear capacity of 12 UHPC panels measuring 1143×1143 mm and with various thicknesses. It was found that a thickness of 25 mm of a UHPC panel can prevent the punching shear failure. However, there is a lack of published work on SIP formwork for vertical elements, such as column elements. Moreover, the flexural capacity of SIP formwork panel reinforced with FRP bars can be increased by nearly four times (Kim et al. 2008). However, compared with FRP bars, FRP grids are more flexible and can provide two-dimensional reinforcement, and thus they can be used to develop thin prefabricated elements (Leung and Cao 2010). The effectiveness of GFRP girds as reinforcement in UHPC panels has been demonstrated (Meng and Khayat 2016).

In the first part of this study, GFRP grids reinforced UHPC prefabricated elements are proposed to produce thin and highly-durable SIP formwork. Using GFRP as reinforcement can provide good cracking resistance, ductility, and enhanced durability. The durability is also assured by using UHPC, which is highly impermeable and resistant to crack. The SIP formwork was developed and evaluated under gravity load and internal pressure due to concrete casting. A three-dimensional finite element model (FEM) incorporating nonlinear material properties experimentally validated as shown in Section 5 is employed to evaluate the designs.

Besides the SIP formwork, a functionally-graded composite (FGC) slab, which is a sandwich composite composed of one UHPC layer and one conventional concrete layer, is presented in this study as prefabricated railway ballastless slab. This concept can also be applied to bridge deck and other kinds of slabs.

The use of UHPC layer may significantly improve the abrasion and crack resistance and flexural properties. The conventional concrete filling provides adequate mechanical properties and helps reduce the cost and improve the sustainability.

9.2. MATERIALS

The investigated materials are detailing below:

9.2.1. Ultra-High Performance Concrete. The UHPC employed in this section is same as presented in Section 8.2.2.

9.2.2. Conventional Concrete. A conventional concrete (CC) was designed with a water-to-cement ratio (w/c) of 0.40. Type III Portland cement and natural concrete sand were used. All test samples were cured for 24 h in molds covered with wet burlap and plastic sheets at room temperature. After demolding, the samples were cured in lime-saturated water at $23 \pm 1°C$ until the age of testing. The average 28-day compressive strength was measured 62 MPa. The 28-day Young's modulus of elasticity and Poisson ratio were measured in compression using cylinder specimen with 100-mm diameter and 200-mm height. Their values were determined 35 GPa and 0.19, respectively.

9.2.3. Steel Bars. The dimension and material properties of the steel bars used in this study is listed in Table 9.1, where d represents the nominal diameter, E denotes the Young's modulus, f_y and f_u represent the yield and ultimate strengths, respectively, and ε_u stands for the ultimate strain. The material properties were experimentally determined.

Table 9.1 Steel bars.

Code	d (mm)	E (GPa)	f_y (MPa)	f_u (MPa)	ε_u (%)
Φ8	8	205	482	685	20.0
Φ10	10	200	1449	1725	9.5
Φ16	16	200	550	609	24.6
Φ20	20	195	554	713	25.3

9.2.4. Fiber-Reinforced Polymers Grids. Two types of FRP grids were considered in this study, which are CFRP and GFRP grids, as presented in Section 8.2.1.

The equivalent force-strain relationship remained linear until shortly before rupture. The slopes of these lines represent the tensile stiffness of the FRP grids. The CFRP specimens demonstrated larger tensile stiffness and tensile strength than the GFRP specimens. However, the GFRP specimens had larger tensile strain limits (or rupture strain) than the CFRP specimens. The average slopes corresponding to the force versus strain were 60 and 480 kN/ε for the GFRP and CFRP samples, respectively. The average tensile peak load was 1.2 and 3.8 kN for the GFRP and CFRP, respectively. The rupture strains were approximately 2×104 and 1×104 μm/m for the GFRP and CFRP materials, respectively.

9.3. STAY-IN-PLACE FORMWORK DESIGN I

The first design of stay-in-place formwork is presented below:

9.3.1. Design of SIP Formwork System. Novel designs of SIP formwork systems are presented and evaluated by numerical simulation in terms of the strain and stress distributions and lateral deformation under gravity load and internal pressure due to concrete casting.

There are some critical considerations for the design of SIP formwork systems: (1) Connection between adjacent members: connection details should be considered to overcome problems of mating precast members to each other and to the existing or cast-in-place structure. (2) Bonding conditions between SIP formwork and post-poured concrete: reliable bonding between formwork and post-poured concrete is essential and can be achieved by: a) special treatment, such as grooving or roughening the form face in contact with the structure concrete; b) use of anchoring devices extending across the interface between form panel and structure concrete; c) a combination of a) and b); and d) use of paint-on or spray-on bonding chemicals. (3) Code requirements: Precast concrete forms used in composite design with cast-in-place concrete in buildings should be designed in accordance with ACI 318. With these considerations, a SIP formwork system is proposed, as depicted in Figure 9.1. A square cross section is considered, which represents a typical column used in building. The outer side length is 500 mm. The wall thickness is denoted by t, which is investigated and the optimum value is discussed in this

study. The total height of each element is 400 mm, of which a 60-mm bottom height is inserted into the adjacent element. Thus, each layer is 340 mm in height. The elements are assembled in site layer by layer (Figure 9.1c).

(a) Vertical cut view

(b) Square shape cross section

(c) Assembly layer by layer
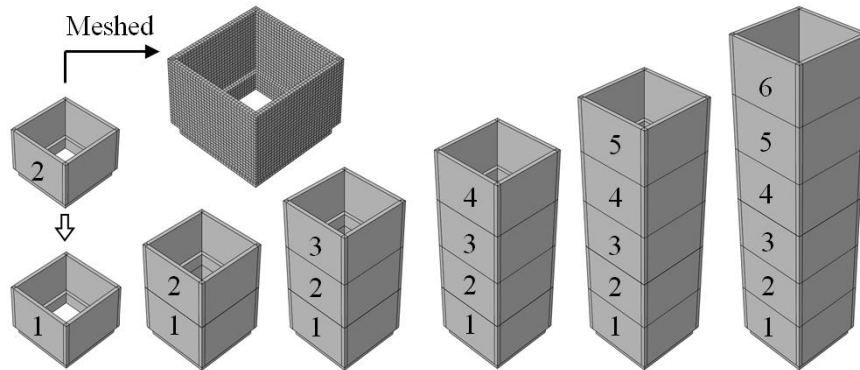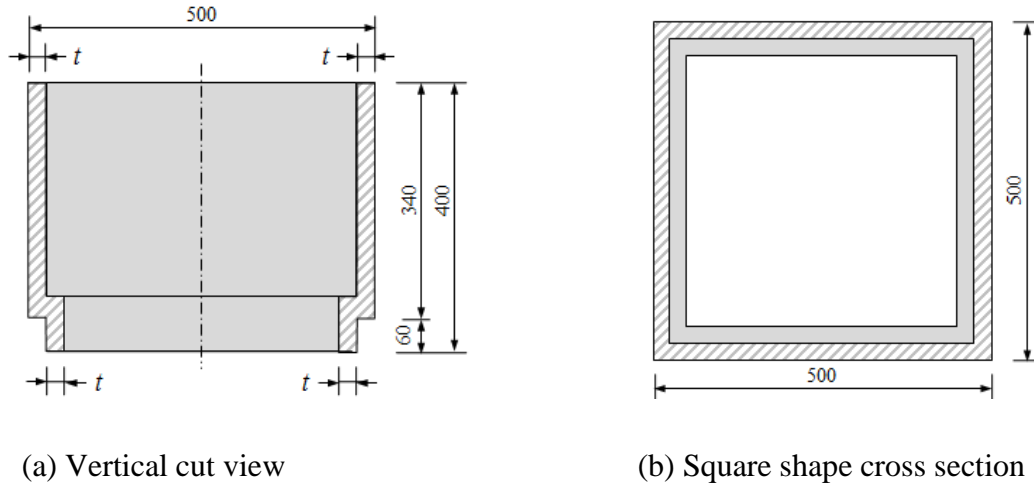
Figure 9.1. Illustration of the Type ISIP formwork system.

9.3.2. Numerical Simulations. Similar as before, the numerical simulations were conducted here.

9.3.2.1 Description of the finite element model. A three-dimensional nonlinear finite element model was developed using ABAQUS to investigate the mechanical performance of the designed formwork.

The thin and flexible GFRP grids were modeled using 2-node linear 3-D truss (T3D2) elements. Each T3D2 element has 2 nodes, and each node has 3 degrees of

freedom. The UHPC matrix was modeled using 8-node linear 3-D brick reduced integration (C3D8R) elements. Each C3D8R element has 8 nodes, and each node has 3 degrees of freedom. The contact between GFRP and UHPC was defined using the keyword 'embed,' without considering interfacial debonding. Surface-to-surface hard contact was defined for the contacting surface pairs using a basic Coulomb friction model, namely penalty friction model. The coefficient of friction was assumed to be constant 0.8 for the contact between UHPC surfaces. The concrete damaged plasticity (CDP) model is employed to consider potential damages in UHPC. Assuming that steel fibers are uniformly distributed in the cementitious matrix, the mechanical properties of the UHPC are considered to be homogeneous. Since no significant concrete crushing was observed in the experiments, the UHPC was assumed to be elastic under compressive stress. This assumption can be checked in the stress distribution results. The formwork pressure due to fresh concrete casting is considered as hydrostatic pressure, which is linearly distributed throughout the height of formwork, as illustrated in Figure 9.2. The density of fresh concrete is assumed to be 2400 kg/m^3. The bottom of formwork is fixed.
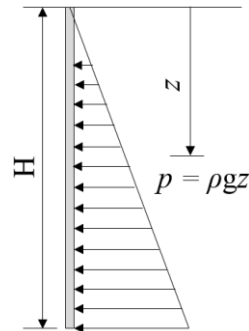
Figure 9.2. Illustration of static hydraulic pressure applied on SIP formwork.

9.3.2.2 Investigated cases. In total, 12 cases were investigated, as listed in Table 9.2.

Four assembly layer numbers are considered, including 3, 4, 5, and 6, respectively. Six layers of element give a total height of 2.04 m for one casting. Three wall thicknesses are considered, which are 15, 20, and 25 mm, respectively. The corresponding volumes are 0.0124, 0.0162, and 0.2 m3, respectively. Given the density

of UHPC, which is 2500 kg/m3, the masses are determined to be 30, 40, and 48 kg, respectively.

Table 9.2 Investigated cases for Type I SIP formwork.

Case	Assembly layer number	Wall thickness (mm)
1-3	3	15, 20, 25
4-6	4	15, 20, 25
7-9	5	15, 20, 25
10-12	6	15, 20, 25

9.3.3. Results and Discussion

The simulation results were addressed below:

9.3.3.1 Strain distribution. Figure 9.3 shows the distribution of maximum principle strain within the six layers of formwork. The maximum principle strain is the largest at the inner surface of corners. The outer surface of wall is also subjected to relatively large tensile strain in the middle. The strain distributions indicate that potential damage may be initiated at the corners. Strengthening the corners by increasing the thickness can reduce the maximum tensile strain. Using round cross section is another possible alternative to reduce the maximum tensile strain. Due to page limit, it is not elaborated in this study.
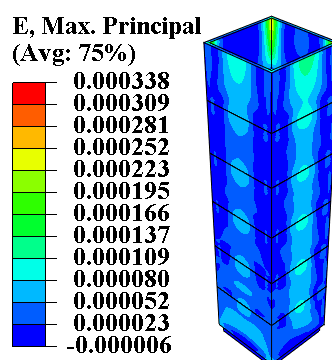
Figure 9.3. Distribution of maximum principle strain.

Figure 9.4 shows the effects of assembly layer number and wall thickness on the maximum principle strain within the formwork elements. The maximum principle strain linearly increases with the assembly layer number, indicating that the assembly height for each cast should be limited. Excessive one-time assembly can potentially lead to damage

in formwork. At the same time, the maximum principle strain decreases with the wall thickness. For a specific UHPC mixture with determined tensile strength, it is essential to select an appropriate wall thickness and one-time assembly height.
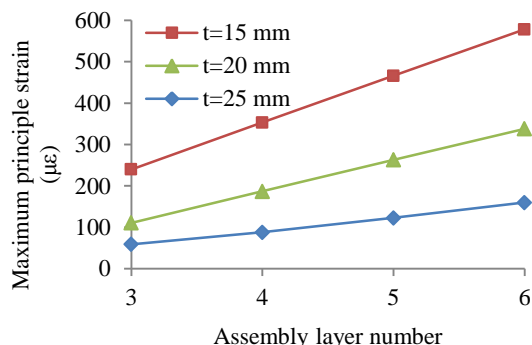
Figure 9.4. Effects of assembly layer number and wall thickness on maximum principle strain.

9.3.3.2 Stress distribution. Figure 9.5 shows the distribution of maximum principle stress within the six layers of formwork. Within the elastic range of UHPC, the strain and stress distributions are alike. The maximum principle stress is the largest at the inner surface of corners. The outer surface of wall is also subjected to relatively large tensile stress in the middle. The strain distributions indicate that potential damage may be initiated at the corners. Strengthening the corners by increasing the thickness can reduce the maximum tensile strain. However, when the strain is large enough to cause inelastic behaviors in UHPC, the strain and stress distributions will be quite different. For the sake of safety, the formwork is designed to operate in elastic range, although it can experience inelastic behaviors in the case of extreme events, such as earthquake, during construction.
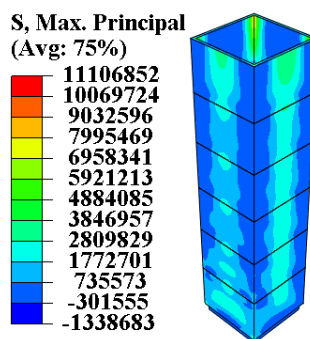
Figure 9.5. Distribution of maximum principle stress.

Figure 9.6 shows the effects of assembly layer number and wall thickness on the maximum principle stress within the formwork elements. The maximum principle stress linearly increases with the assembly layer number. The maximum principle stress decreases with the wall thickness. For the UHPC mixture in this study, which has a crack stress limit of 8 MPa, the assembly layer number can be 3 when t = 15 mm, 4 when t = 20 mm, or higher than 6 when t = 25 mm.
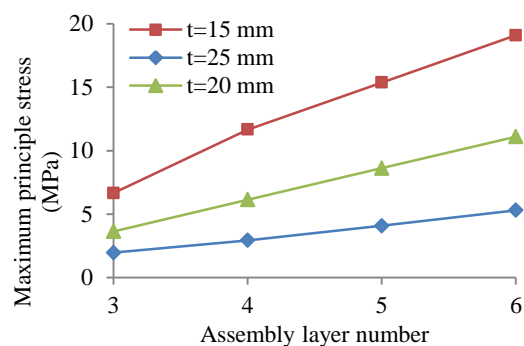
Figure 9.6. Effects of assembly layer number and wall thickness on maximum principle stress.

9.3.3.3 Lateral deformation. Figure 9.7 shows the distribution of lateral deformation of six layers of formwork. The formwork exhibits lateral expansion, which is the largest in the middle of wall at the top where the deformation is subjected to less constraint. The maximum deformation is an indicator of the ability of formwork to retain the designed shape and dimensions during concrete casting. Besides, the distribution of lateral expansion allows the monitoring, control, and assurance of construction quality. Displacement sensors can be deployed at the top of formwork assembly, to monitor the deformation most effectively. Excessively large lateral deformation could indicate damage or dislocation of UHPC elements, or instability of the assembly.

Figure 9.8 shows the effects of assembly layer number and wall thickness on the lateral deformation of formwork. The maximum lateral expansion linearly increases with the assembly layer number, and it decreases with the wall thickness. Overall, the lateral deformation is adequately small. With an assembly consisting of 6 layers of UHPC elements, the maximum lateral deformation is 0.8 mm when t = 15 mm, or less than 0.2 mm when t = 25 mm.
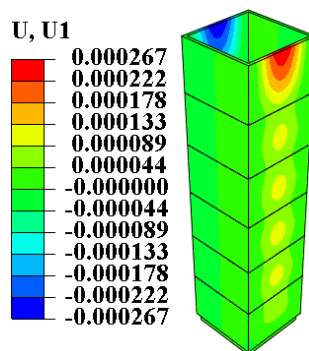
Figure 9.7. Distribution of lateral deformation.
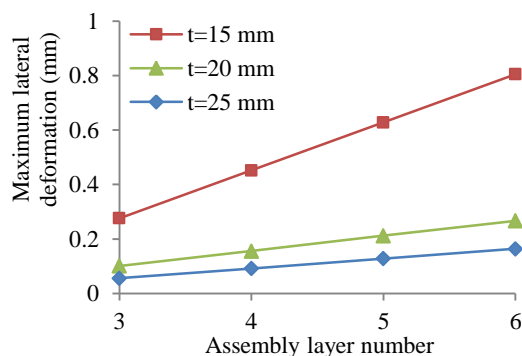
Figure 9.8. Effects of assembly layer number and wall thickness on lateral deformation.

9.4. STAY-IN-PLACE FORMWORK DESIGN II

The second design of SIP formwork is presented as follows:

9.4.1. Design of SIP Formwork System. A design of permanent formwork system consisting of two types of panels is presented, as shown in Figure 9.9 (a).

The straight panel was named 'S' Panel; the semi-circle panel was named 'C' Panel. The popular round-ended columns can be assembled by the two panels. Horizontal stiffeners were considered to the panels to increase the flexural strength and bonding with post-cast concrete. There were two stiffeners in each panel. The mass of the 'S' Panel was about 22 kg; 'C' Panel was about 32 kg.

Each layer of the formwork is assembled by two different panel members, as shown in Figure 9.9(b). A formwork is assembled by three layers of UHPC panels. Since the panel height is 0.5 m, the assembly of three layers is 1.5 m, as shown in Figure 9.9(b). The bottom boundary was fixed to the ground; hard surface-to-surface contacts between

the contacting surfaces were defined. Both gravity loads and hydraulic pressures (Figure 9.2) due to the post-cast concrete were applied on the panels.

(a) Element design (unit: mm)

(b) Assembly of elements
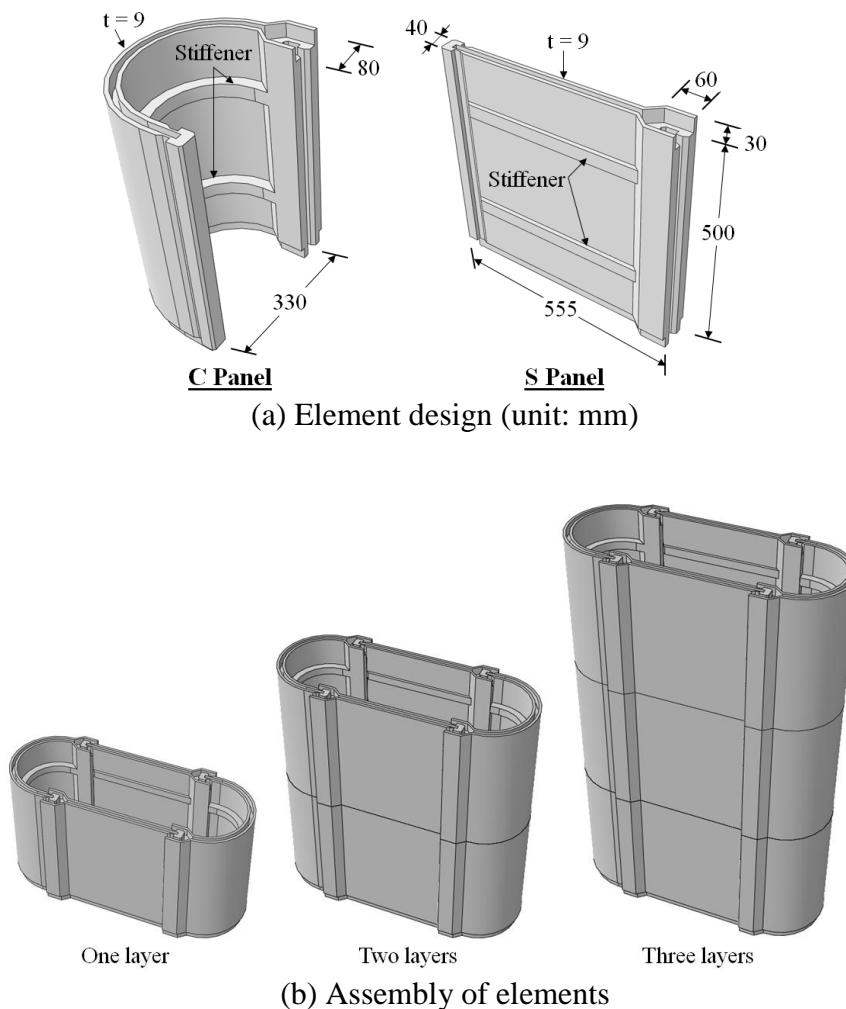
Figure 9.9. Illustration of the Type IISIP formwork system.

9.4.2. Numerical Simulations. The mechanical behaviors of the formwork are investigated through finite element analysis using ABAQUS.

9.4.2.1 Description of the finite element model. The consideration of numerical model is the same as described in Section 9.3.2.1.

9.4.2.2 Investigated cases. In this section, 3 cases of assembly are investigated, as listed in Table 9.3. Different of reinforcements are investigated to reinforce the formwork system.

Table 9.3 Investigated cases for Type II SIP formwork.

Case	No. of FRP layers
1	0
2	2 GFRP layer
3	1 CFRP layer

9.4.3. Results and Discussion. Results for the simulations were detailed as follows:

9.4.3.1 UHPC formwork without GFRP. The simulation results are shown in Figures 9.10(b)-(h). The deformation was 1.3 mm. The maximum stress was 24 MPa, which occurred in the stiffeners. This was because the force arm of the stiffener's inner face was the largest in the formwork. Even though the overall flexural stiffness was increased, a localized larger stress appeared.

(a) A three-layer assembly

(b) Contact stress (unit: Pa)

(c) Top view of deformation (unit: m)

(d) Cut view of deformation(unit: m)

Figure 9.10. Simulation of UHPC formwork with horizontal stiffeners.
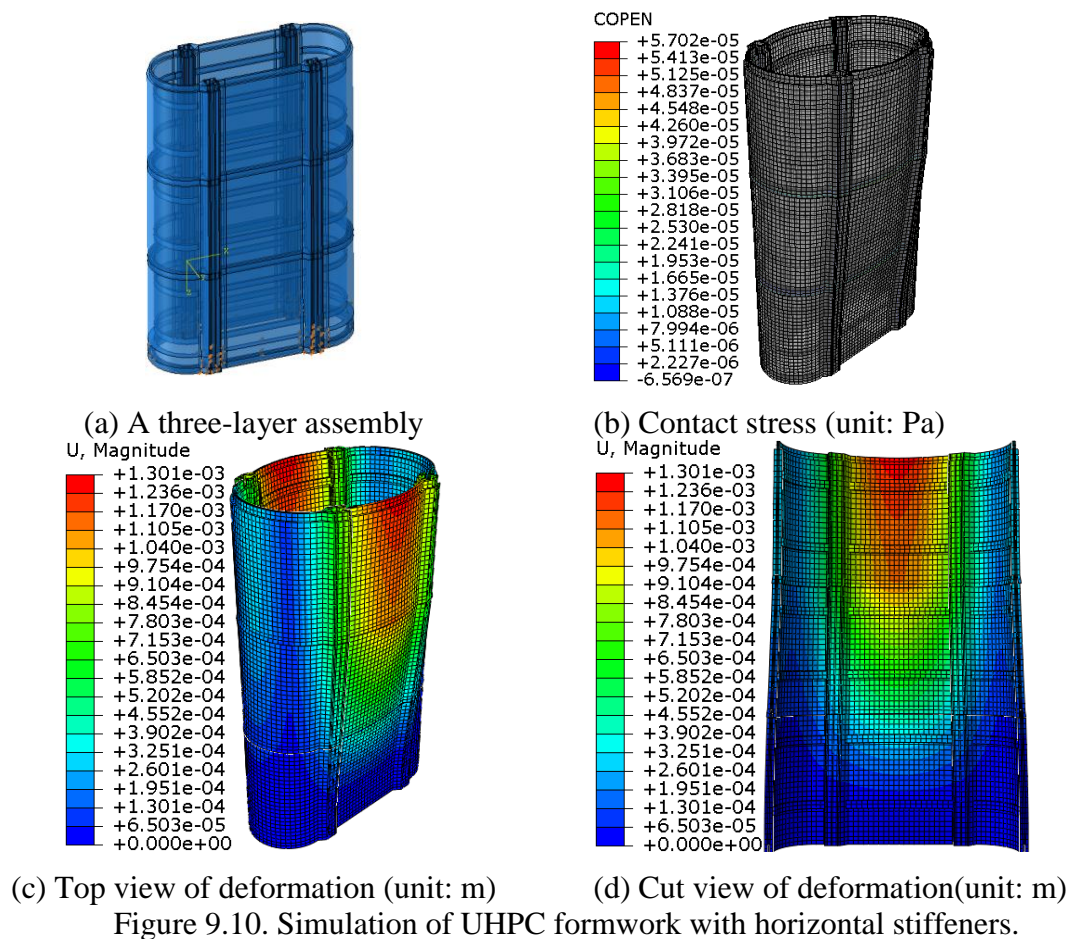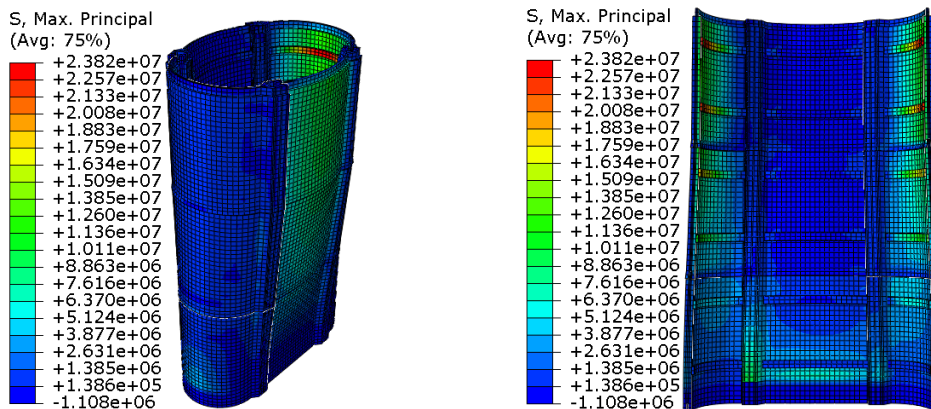
(e) Top view of max. principle stress(unit: Pa)   (f) Cut view of max. (unit: Pa)
Figure 9.10. Simulation of UHPC formwork with horizontal stiffeners. (cont.)

9.4.3.2 UHPC formwork with dual-layers GFRP grid. When two layers of GFRP grids was added to the panels, as shown in Figure 9.11(a), the simulation results are shown in Figure 9.11(b)-(h).

Compared with the formwork without FRP grids, the magnitudes of deformation and maximum principle stress were slightly decreased due to the GFRP grids. However, the changes were not significant. The distributions were not changed. Therefore, the GFRP girds could not appreciably improve the structural performance before the concrete cracked, which was in good agreement with the conclusions from the flexural testing of panels.
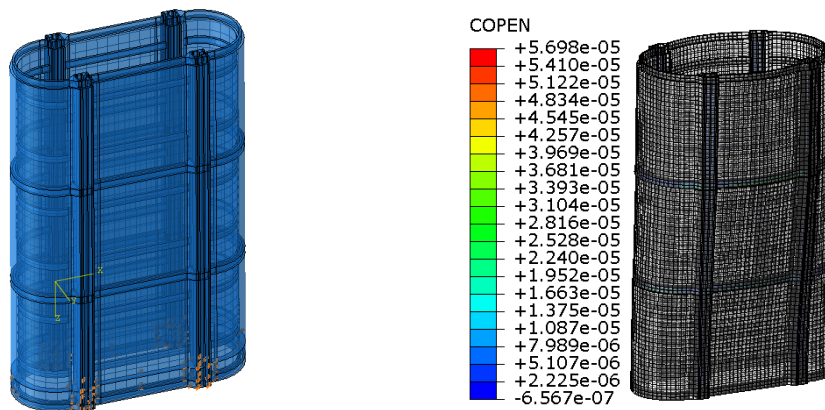
(a) A two-layer assembly   (b) Contact stress (unit: Pa)
Figure 9.11. Simulation of GFRP reinforced UHPC formwork with horizontal stiffeners.

(c) Top view of deformation (unit: m)

(d) Cut view of deformation(unit: m)

(e) Top view of max. principle stress(unit: Pa)

(f) Cut view of max (unit: Pa)

Figure 9.11. Simulation of GFRP reinforced UHPC formwork with horizontal stiffeners. (cont.)
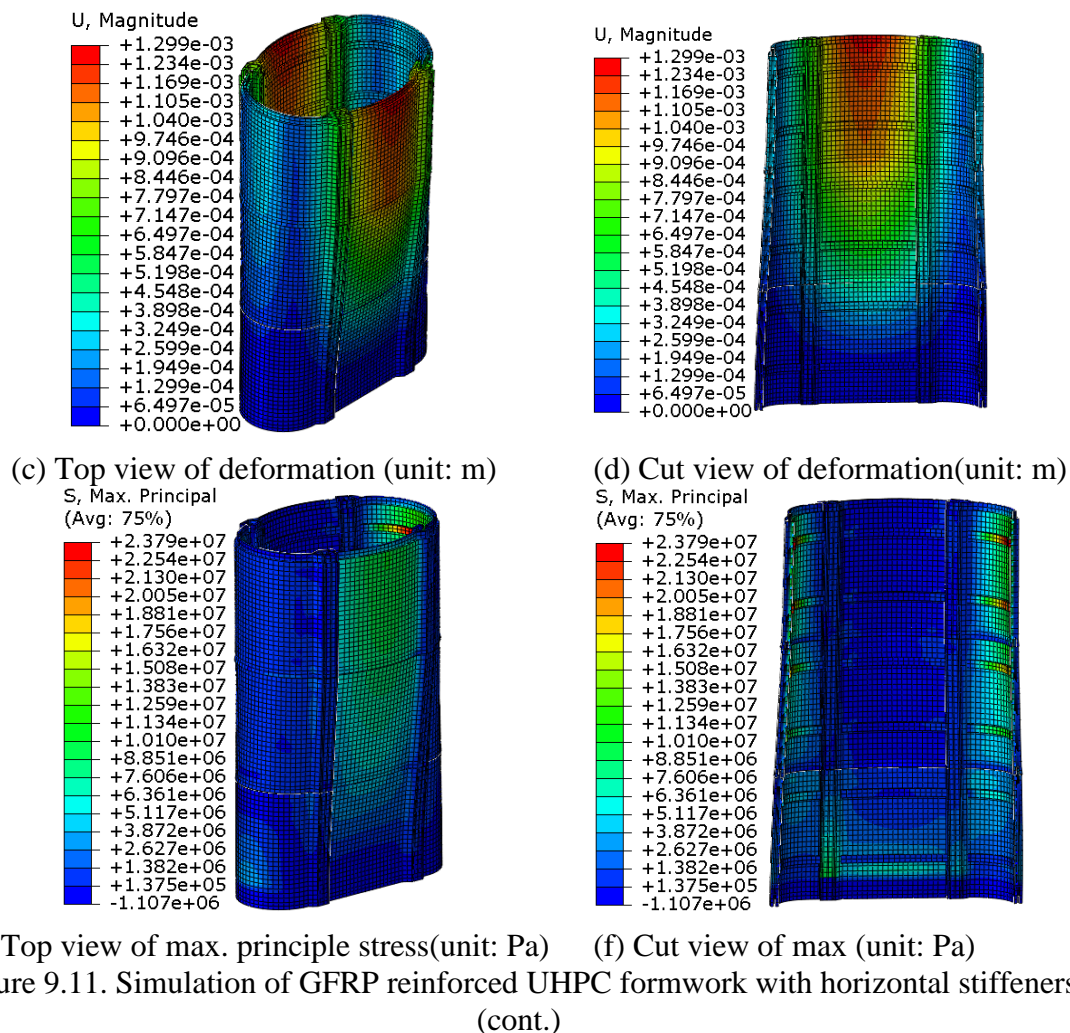
9.4.3.3 UHPC formwork with single-layer CFRP grid. Figure 9.12(a) shows single layers of CFRP grids were added to the panels. As shown in Figure 9.12(b)-(h), compared with the formwork without FRP grids, the magnitudes of deformation and maximum principle stress were slightly decreased due to the CFRP grids. However, the changes were not significant. The distributions were not changed. Therefore, the CFRP girds could not appreciably improve the structural performance before the concrete cracked, which was in good agreement with the conclusions from the flexural testing of panels.

(a) A three-layer assembly

(b) Contact stress (unit: Pa)

(c) Top view of deformation (unit: m)

(d) Cut view of deformation(unit: m)

(e) Top view of max. principle stress(unit: Pa)

(f) Cut view of max. (unit: Pa)
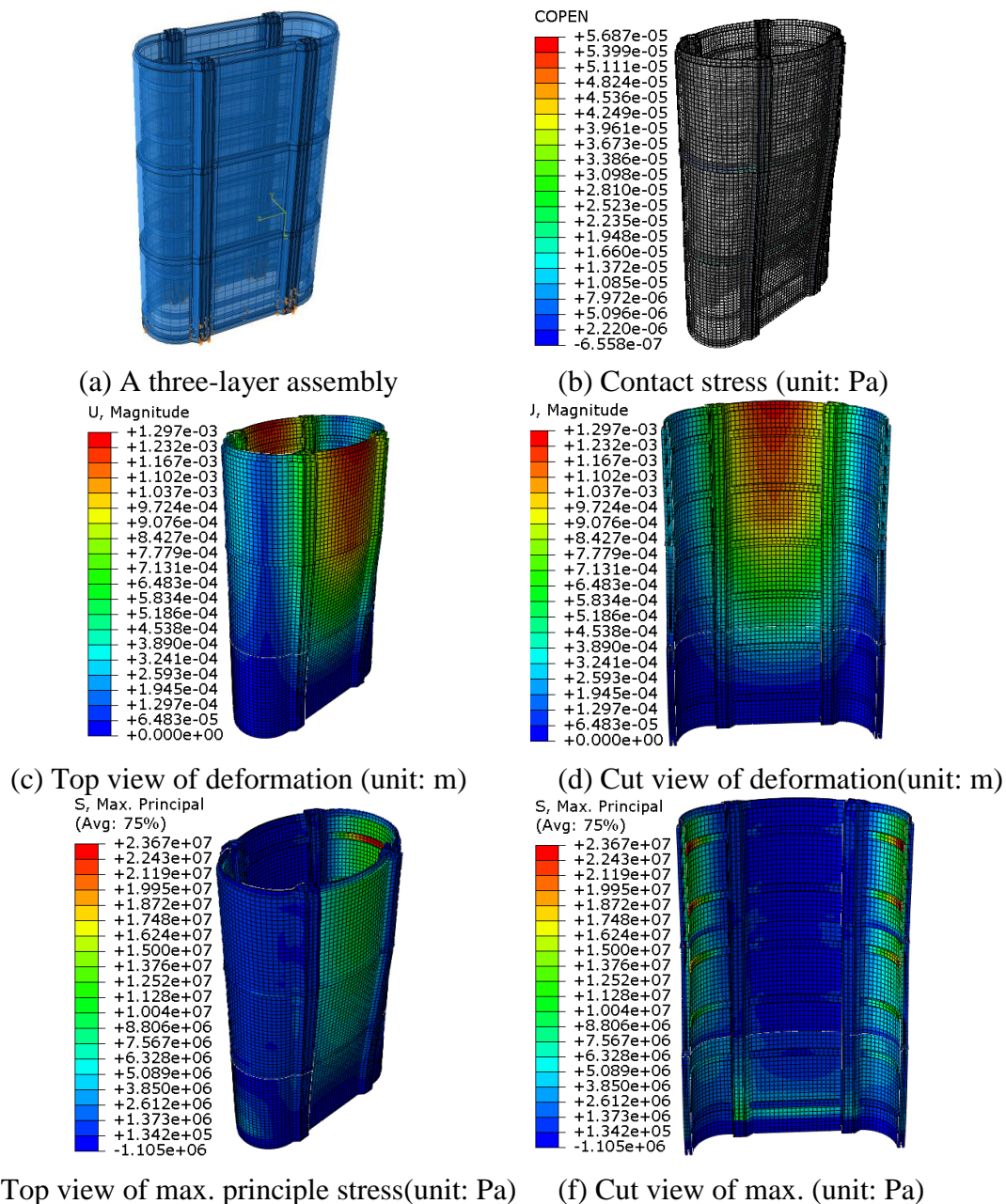
Figure 9.12. Simulation of GFRP reinforced UHPC formwork with horizontal stiffeners.

9.5. FUNCTIONALLY-GRADED SLAB

A ballastless track slab system has various advantages, such as high stability, safety, durability, and low maintenance cost, compared with a ballasted track slab system. Thus, it became increasingly popular in the past decade, and has been extensively used in the construction of high-speed railway network.

205

Due to the absence of any discrete ballast, the deformation of the track system can be greatly reduced, and safety issues caused by flying ballast are eliminated. It is more advantageous with the consideration of the lifetime cost.

Numerous designs have been proposed to improve the performance of the ballastless track slab in terms of mechanical strength, serviceability, durability, and economy. Reinforced concrete slabs have been prevailing in the applications of railway track worldwide (Karthiga et al. 2014; Yang et al. 2015; Madhkhan et al. 2012; Michas 2012). Typically conventional concrete or high strength concrete is used, and the thickness of concrete slab ranges from 0.15 to 0.30 m. The reinforcement ratio typically ranges from 0.8% to 1.5% (Michas 2012). However, cracks can be induced by shrinkage and mechanical loads in concrete, which highly accelerates the degradation and compromises the performance of the track slab.

As tens of thousands of miles of ballastless track are constructed, effective and efficient maintenance for the concrete slabs have become an issue. In this section, UHPC is proposed to fabricate ballastless track slab.

9.5.1. Slab Specimen. A typical CRTS II (Chinese rail transit summit Type-II) plate-type ballastless track slab is investigated. The slab is 6.45 m in length, 2.55 m in width, and 0.20 m in depth (Yang et al. 2015).

Each slab is composed of 10 identical segments, and each segment has a pair of bearing rail stations, as depicted in Figure 9.13. The flexural performance of a representative segment is studied, and its dimension is 2.55 m × 0.645 m × 0.20 m (length × width × depth).
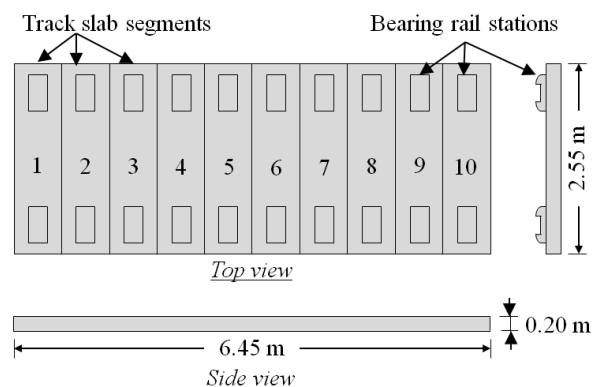
Figure 9.13. CRTS II Track slab.

Three types of track slab were evaluated and compared, including CC, UHPC, and functionally-graded composite (FGC) slabs. The designs of the CC and UHPC slab specimens are shown in Figure 9.14(a) (Yang et al. 2015). The FGC slab is illustrated in Figure 9.14(b). Each FGC slab is composed of two layers: a CC layer at the bottom, and an UHPC layer on the top.

The thickness of the UHPC layer is a half of the total slab thickness in this study, which can be changed in various applications. For the cast of the FGC slab, the CC layer can be cast after finishing pouring UHPC layer, some vibration can be applied to avoid multi-layer casting effect.

Each of the slabs is 0.20 m thickness, and has 50 mm thick cover for the rebar. There are six prestressed steel bars (Φ10) in each slab, and the total prestress force is 409 kN (Yang et al. 2015).
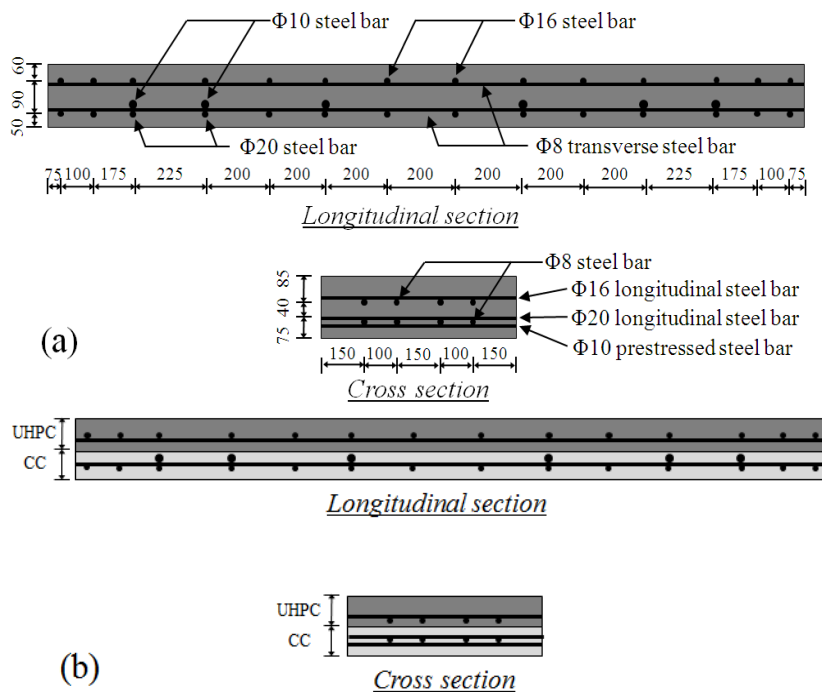
Figure 9.14. Design of specimens (unit: mm): (a) CC and UHPC slabs, and (b) FGC slab.

9.5.2. Finite Element Model. A three-dimensional nonlinear finite element model was developed using ABAQUS for investigating the flexural behavior of the track slabs, as shown in Figure 9.15. The clear span length between the two top rollers is 1.50 m. The structure can be divided into four parts, and each of them can represent the whole structure, due to the symmetry. Therefore, a quarter structure can be analyzed for computational efficiency. In the Cut plane X, the translation along X axis is restrained. In the Cut plane Z, the translation along Z is restrained.

The steel bars were modeled using 2-node linear 3-D truss (T3D2) elements. Each T3D2 element has 2 nodes, and each node has 3 degrees of freedom. The concrete matrixes were modeled using 8-node linear 3-D brick reduced integration (C3D8R) elements. Each C3D8R element has 8 nodes, and each node has 3 degrees of freedom. The interaction between steel rebar and concrete matrix was defined using the keyword 'embed,' without considering any interfacial debonding or sliding. This assumption implies non-conservative prediction of performance, because interfacial debonding and sliding can possibly happen, which is detrimental to the mechanical performance and durability. A mesh size convergence study was conducted, and 10 mm was adopted.
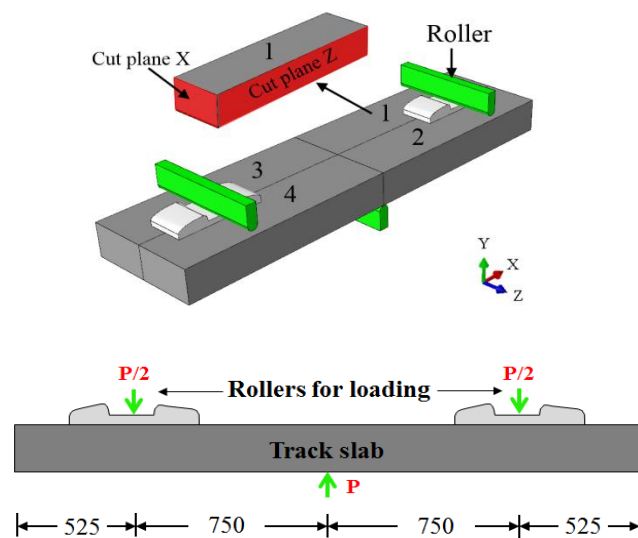
Figure 9.15. Finite element model.

Inelastic behaviors of concrete in tension and compression are respectively represented using a concrete damaged plasticity model. Cracking and post-cracking

behaviors are considered using complete stress-displacement relationships, which are obtained in uniaxial tensile test, as shown in Figure 9.16. Post-cracking behavior is described by the stiffness degradation. In this study, the damage is considered initiated when the peak stress is reached, and the damage parameter d_t is considered changing linearly with the ratio of stress to peak stress. Damage recovery factor in tension is taken as 0, meaning no recovery in tension. Temperature- or rate-dependent behavior is not considered.
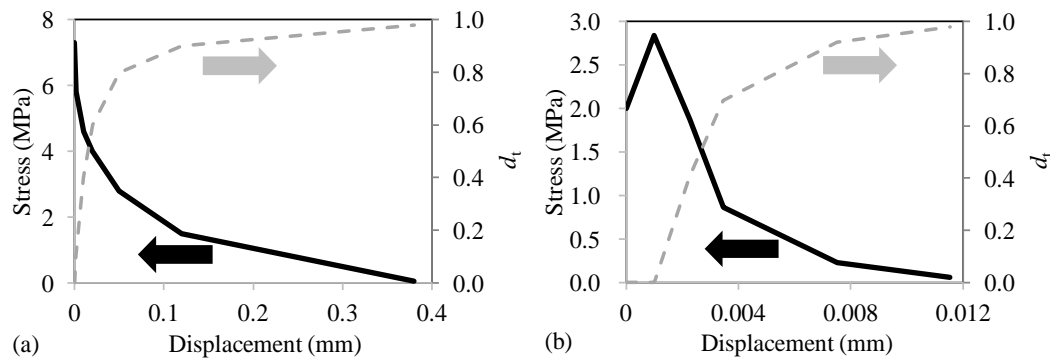
Figure 9.16. Stress-displacement relationships in tension: (a) CC and (b) UHPC.

Unlike the stress-strain relationship depending on the mesh size for modeling localized damage, the stress-displacement relationship is independent on the mesh size, and it can better represent the localized damage behaviors. The CC and UHPC are assumed to be elastic under compressive stress. This assumption can be checked in the plastic strain results.The steel materials are represented using bi-linear models with the consideration of the strain hardening behaviors after yielding. The parameters are listed in Table 9.1.

9.5.3. Simulation Results and Discussion. The detailed simulation results are elaborated below:

9.5.3.1 Damage initiation and propagation. Figure 9.17 shows the modeled damage initiation and propagation within the CC slab. Tension damage (cracking) is shown to initiate at the exterior of the cross section at the mid-span, and then, it propagates along the depth, forming a major crack of which the width increases with the applied displacement at the mid-span. The presence of the crack leads to sudden drop of

the carried load. Because of the rebar that bridges the crack, the crack does not pass all the way through the depth. However, the stiffness (slope) is highly reduced.
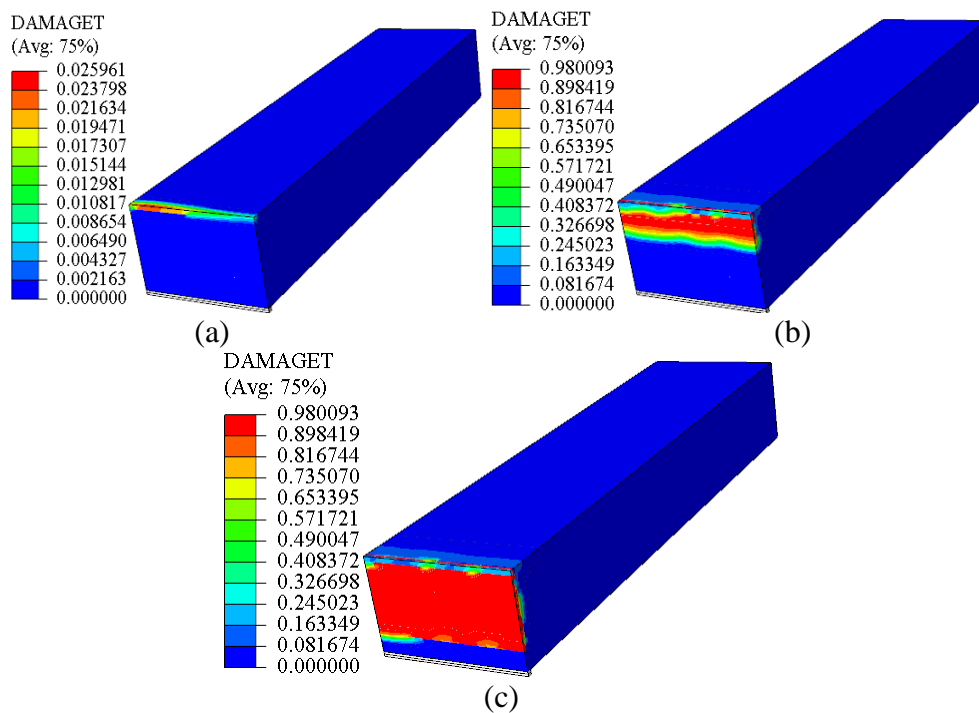
Figure 9.17. Damage evolution in CC slab at different mid-span deflections: (a) 0.27 mm, (b) 0.35 mm, and (c) 0.47 mm.

The development of the plastic strain is shown in Figure 9.18, which quantifies the strain exceeding the elastic strain limit. The plastic strain distribution agrees with the damage distribution. In addition, there is no plastic strain in compression, indicating the compressive strain in concrete is less than the elastic limit.
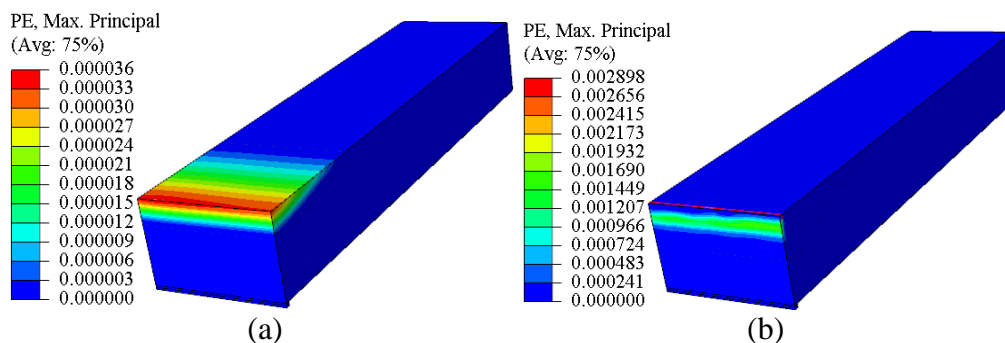
Figure 9.18. Plastic strains in CC slab at different mid-span deflections: (a) 0.26 mm, (b) 0.33 mm, and (c) 0.36 mm.

(c)
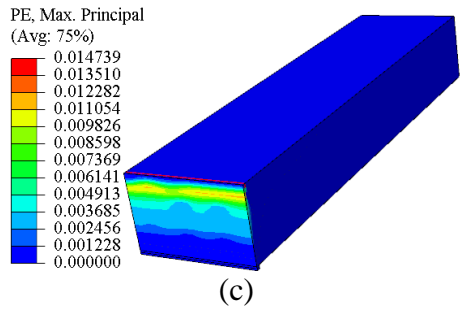
Figure 9.18. Plastic strains in CC slab at different mid-span deflections: (a) 0.26 mm, (b) 0.33 mm, and (c) 0.36 mm. (cont.)

Figure 9.19(a)-(c) show the plastic strain distributions within the CC, UHPC, and UHPC-CC slabs, respectively, when a mid-span deflection of 1 mm is applied. A major crack is present in the CC slab, which corresponds to a plastic strain of 0.0355, as shown in Figure 9.19(a). The major crack would develop at a depth of about 0.16 m, which is 80% of the whole slab thickness.

(a)

(b)

(c)
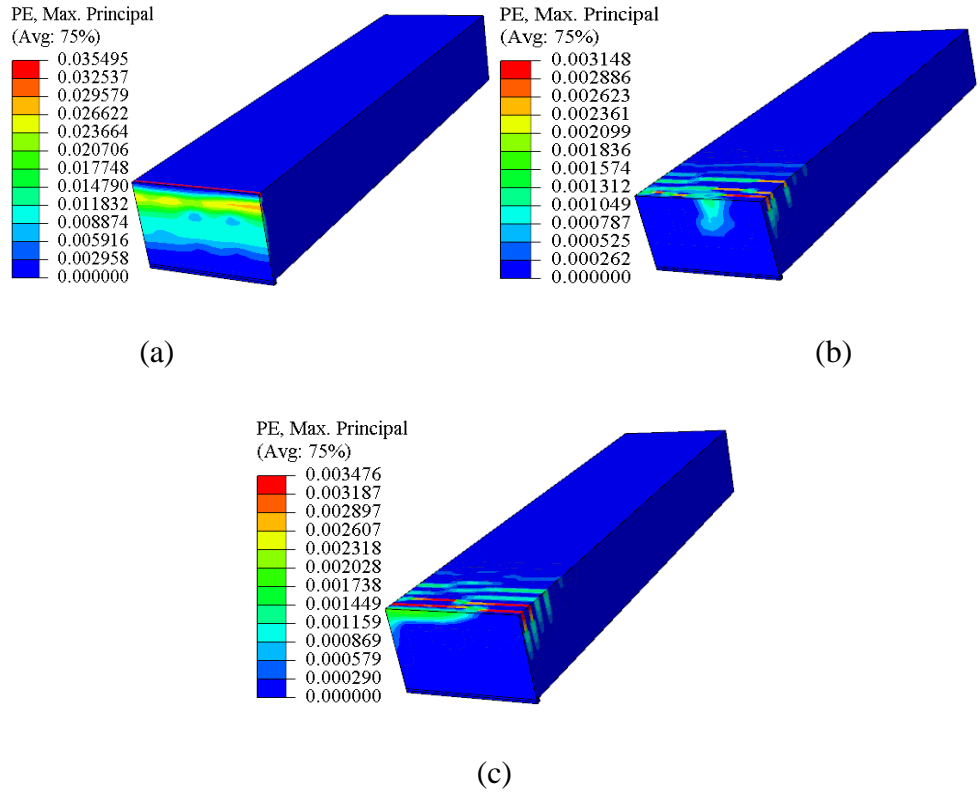
Figure 9.19. Plastic strains at 1 mm mid-span deflection: (a) CC slab, (b) UHPC slab, and (c) UHPC-CC slab.

However, in the UHPC and UHPC-CC slabs, multiple cracks take place, as shown in Figures. 9.19(b) and (c), and the plastic strains were only 0.0031 and 0.0035, respectively, which are less than 10% of that in the CC slab. This indicated that the crack widths would be much smaller than that of the CC slab. Besides, the penetrating depths of the cracks in the UHPC and UHPC-CC slabs would be about 0.02 and 0.10 m, respectively, which are much smaller than that of the CC slab. The reduced crack width and development depth imply enhanced serviceability and durability. With the further increase of mid-span deflection, multiple cracking can eventually happen in the CC slab as well. However, the crack width and crack depth will be highly developed in advance.

9.5.3.2 Load-deflection relationships. The load-deflection curves of the quarter slab are compared in Figure 9.20. For the CC slab, once concrete cracking occurs, the carried load quickly drops from 12 to 6 kN. After that, the load is gradually increased back to about 12 kN, due to the rebar's bridging effect for the crack, and then, it gradually decreases till zero. However, for the UHPC and UHPC-CC slabs, after concrete cracks, the load can be sustained at 39 and 33 kN, respectively, until the cracks are substantially developed. No sudden drop in carried load takes place throughout the loading process. Both the UHPC and the UHPC-CC slabs demonstrate ductile flexural behavior, thus implying better serviceability.
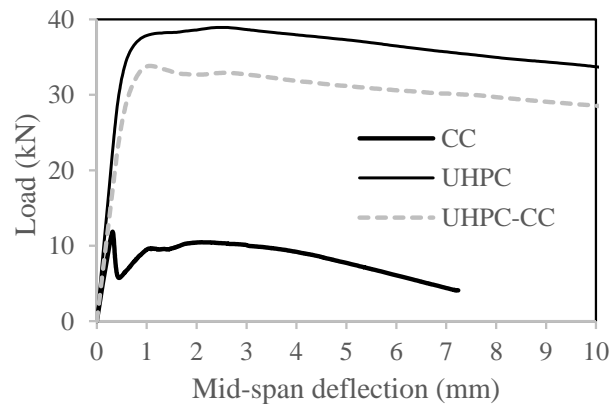
Figure 9.20. Load-deflection relationships.

Based on the load-deflection relationships, the three types of track slabs can be compared in terms of the load capacity, stiffness, and energy dissipation, as shown in Figure 9.21. The UHPC slab can carry about 3.3 times load than the CC slab, and its

stiffness is about 1.8 times of that of the CC slab. The UHPC slab is far more advantageous in terms of the energy dissipation ability. Up to a mid-span deflection of 10 mm, which is 1/150 of the clear span length of three-point bending setup, the energy dissipated by the UHPC slab would be 6 times of that dissipated by the CC slab. The FGC slab demonstrates less yet close load capacity and stiffness, compared with the UHPC slab.
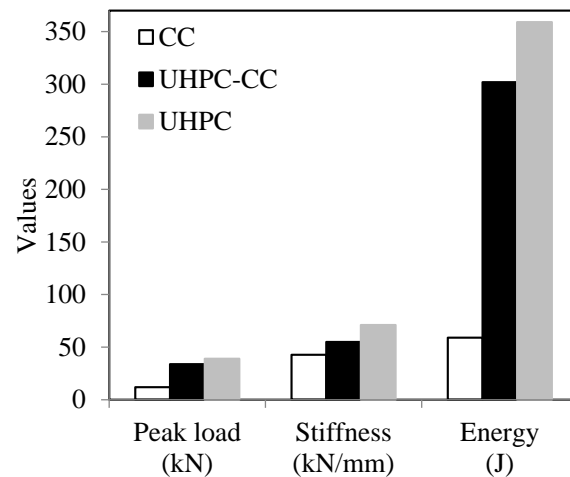
Figure 9.21. Comparison of mechanical performance

9.6. SUMMARY

Based on the above investigations, conclusions can be drawn as follows.

(1) Novel designs of permanent formwork systems for various vertical elements/structures, including round-end columns and rectangular columns were presented and evaluated by numerical simulations. The designs were progressively optimized based on the simulations. The stress and deformation distributions of the formworks were investigated under the gravity load and internal pressure due to post-cast concrete.

(2) Type I SIP UHPC formwork reinforced with embedded GFRP grids is designed for column of buildings with square cross section. The performance of the designed formwork is evaluated using a three-dimensional nonlinear finite element model, in terms of the strain and stress distributions, and the lateral deformation, during concrete casting. Sensitivity studies were conducted for the wall thicknesses of 15, 20, and 25 mm,

at different assembly heights. With the use of the proposed UHPC element reinforced with GFRP grids, the assembly height can be 1 m when the wall thickness is 15 mm, or 2 m when the wall thickness is 25 mm. The largest lateral deformation is less than 1 mm.

(3) Type II SIP UHPC formwork was investigated with different FRP reinforcements. The function and effectiveness of embedded FRP grids were investigated. Before the concrete cracked, the FRP could not significantly reduce the deformation or maximum principle stress in the formwork, which was in good agreement with the flexural testing introduced in Section 5.

(4) The GFRP and CFRP grids demonstrated similar function and effectiveness, but because the CFRP grids are more sensitive to bending and more expensive than GFRP grids, the GFRP grids are preferred and thus can be selected for the implementation of the permanent formwork system.

(5) UHPC is proposed to produce ballastless track slab in this study. Based on the numerical models, the peak load, stiffness, and energy dissipation are shown to increase with the use of UHPC and the thickness of UHPC layer. Such increase appears to be nonlinear with the thickness of the UHPC component. For the FGC slab, with the use of UHPC for half thickness of the slab, the peak load, stiffness, and energy can be increased by 185%, 28%, and 412%, respectively, compared with the CC slab. When the whole slab is made using UHPC, the increase in the peak load, stiffness, and energy can be 228%, 66%, and 508%, respectively. The thickness of UHPC can be further optimized. The structural behavior of UHPC and UHPC-CC track slabs with various configurations is being experimentally investigated. More results will be available and reported in the future.

10. CONCLUSIONS AND FUTURE WORK

10.1. MAIN FINDINGS FROM OVERALL DISSERTATION WORK

In this dissertation, a cost-effective UHPC was optimized and its properties was further enhanced by internal curing, rheology control, and use of different reinforcement, such as hybrid fibers and nanomaterials. Novel design of stay-in-place formwork system and functionally-gradated slab was carried out. Based on the above comprehensive theoretical, experimental, and numerical investigations, several conclusions can be drawn from this study:

(1) A mix design method for UHPC prepared with high-volume supplementary cementitious materials and conventional concrete sand was presented. The method involves the optimization of binder combinations to enhance packing density, compressive strength, and rheological properties. The water-to-cementitious materials ratio is then determined for pastes prepared with the selected binders. The sand gradation is optimized using the modified Andreasen and Andersen packing model to achieve maximum packing density. The binder-to-sand volume ratio is then determined based on the void content, required lubrication paste volume, and compressive strength. The optimum fiber volume is selected based on flowability and flexural performance. The high-range water reducer dosage and w/b are then adjusted according to the targeted mini-slump flow and compressive strength. Finally, the optimized UHPC mix designs are evaluated to determine key properties that are relevant to the intended application. This mix design approach was applied to develop cost-effective UHPC materials. The results indicate that the optimized UHPC can develop 28-d compressive strength of 125 MPa under standard curing condition and 168-178 MPa by heat curing for 1 d. Such mixtures have unit cost per compressive strength at 28 d of 4.1-4.5 $/m^3/MPa under standard curing.

(2) LWS was used as an internal curing agent to enhance mechanical properties and reduce autogenous shrinkage of UHPC. The use of LWS is demonstrated to effectively decelerate and reduce the drop in internal relative humidity and autogenous shrinkage of UHPC. Isothermal calorimetry and thermal gravimetry results showed that the use of LWS promoted cement hydration degree after 28 d of hydration. Mercury

intrusion porosimetry and scanning electron microscope analyses revealed that the porosity was decreased and interface properties between sand and cement matrix is enhanced by use of LWS up to 25%. The optimum replacement ratio of LWS to river sand was found to be 25%, which resulted in the highest compressive strength (168 MPa at 91 d), flexural strength (24 MPa at 28 d), and autogenous shrinkage limited to 365 μm/m at 28 d. In addition, a factorial design approach was employed to evaluate the effects of multiple mix proportioning parameters including LWS content that are important for mixture optimization of UHPC. Statistical models that take into account the coupling effects of mix proportioning parameters were formulated to predict the UHPC properties. The w/b and LWS/NS were the most significant parameters influencing the compressive strength and autogenous shrinkage, respectively. The mixture with w/b of 0.23, LWS/NS of 0.25, and b/s of 1.2 is determined as the optimum UHPC mixture. The material properties of the mixture: the HRWR demand was 0.6%, the 28-d autogenous shrinkage was 260 μm/m, and the 91-d compressive strength was 147 MPa.

(3) Based on the study of rheology control, it was observed that the dispersion and orientation of steel fibers in UHPC are dependent on the rheological properties of the suspending mortar. For UHPC containing 2% of micro steel fibers, the fiber dispersion coefficient increased first and then decreased with the plastic viscosity of the suspending mortar. The optimal plastic viscosity of the suspending mortar that allows for the optimized fiber distribution and flexural performance of UHPC is determined. The plastic viscosity is correlated with the mini V-funnel flow time, which provides a simple alternative to evaluate the plastic viscosity. For a UHPC mixture with 2% micro steel fibers, by volume, the optimal mini V-funnel flow time of suspending mortar was determined to be 46 ± 2 s, which corresponded to the optimal plastic viscosity (53 ± 3 Pa·s) that ensures the greatest fiber dispersion uniformity and flexural performance of UHPC.

(4) The study of effect of using hybrid micro-macro steel and micro steel blended with synthetic fibers and the fiber content on key properties of UHPC indicated that as the plastic viscosity increased with the steel fiber content. At the constant fiber content of 2%, increase the content of PVA or HF also increased the plastic viscosity. Compared with the reference UHPC mixture made with 2% SF, the incorporation of 1% SF and 1%

HF can increase tensile strength, flexural strength, and toughness by about 20%, 25%, and 30%, respectively, and reduce autogenous shrinkage by 25%. The addition of 1.5% SF and 0.5% PVA and can increase flexural strength and toughness by 10% and 15%, respectively, and decrease autogenous shrinkage by 40%. Increasing the SF content from 2% to 5% did not significantly improve the flexural properties, but notably reduced autogenous shrinkage.

(5) Nanomaterials was incorporating in UHPC to enhance its properties. As the content of carbon nanomaterials was increased from 0 to 0.30%, the tensile strength and energy absorption capacity, flexural strength, and T150 can increase up to 55%, 185%, 60%, and 275%, respectively. The isothermal calorimetry test results indicated that the duration of induction period was extend by the use of carbon nanofiber, and shortened by the use of graphite nanoplatelets. The cumulative heat release was increased by increasing the nanomaterials content. As revealed in the single fiber pull-out test, the incorporation of the nanomaterials enhances bond strength and post-debonding performance of the interface between steel fiber and the matrix. In addition, the use of nanomaterials reduced the total porosity of UHPC, as indicated by MIP test. However, the increase of nanomaterials content increased the autogenous shrinkage at all ages.

(6) The unique mechanical characteristics of UHPC with 1% of micro straight steel fibers and 1% of macro hooked-end steel fibers were investigated. Test results indicate that loading rate and notch-to-depth ratio have significant effects on flexural properties of the UHPC notched beams. The flexural strength is shown to increase with the loading rate and the notch-to-depth ratio. The fracture energy increases with the loading rate but decreases with the notch-to-depth ratio. The changes of flexural properties with the loading rate are also dependent on the notch-to-depth ratio. Regression analyses to correlate flexural properties associated with the loading rate and notch-to-depth ratio were conducted to obtain parameters for UHPC structures.

(7) UHPC panels reinforced with internally-bonded FRP grids were experimentally, analytically, and numerically evaluated. Flexural capacity of UHPC panels can be further increased by the use of CFRP or GFRP grids. The use of single- and dual-layer GFRP grids in UHPC panels can result in approximately 25% and 50% increase in flexural capacity, respectively, and the use of a single-layer CFRP can lead to

55% increase. The use of single-layer GFRP, dual-layer GFRP, and single-layer CFRP grids can increase the energy dissipation by 12, 17, and 20 folds, respectively. A mechanical model was developed to evaluate the flexural behaviors of UHPC panels reinforced with FRP grids. In addition, the UHPC panels reinforced with embedded GFRP grids were simulated numerically. The developed model allows adequate predictions of the flexural performance of the GFRP reinforced UHPC panels.

(8) Novel designs of stay-in-place formwork systems for round-end columns and rectangular columns were presented and evaluated by numerical simulations. Type I SIP UHPC formwork was reinforced with embedded GFRP grids. For this design, the assembly height can be 1 m when the wall thickness is 15 mm, or 2 m when the wall thickness is 25 mm. The function and effectiveness of embedded FRP grids for Type II formwork were investigated. In addition, UHPC was proposed to produce functionally-graded slab. Based on the numerical models, the peak load, stiffness, and energy dissipation are shown to increase with the use of UHPC and the thickness of UHPC layer.

10.2. RELATED PUBLICATIONS

For more details, the above main findings can be referred to a number of papers that have been published or submitted for potential publication during the Ph.D. dissertation work. These papers are listed as follows:

10.2.1. Peer-Reviewed Journal Papers. Meng W, Lunkad P, Kumar A, and Khayat KH, Influence of Silica Fume and PCE Dispersant on Hydration Mechanisms of Cement, *Journal of Physical Chemistry C 2016*, Vol 120(47), pp. 26814–26823.

Meng W and Khayat KH Improving Flexural Behavior of Ultra-High Performance Concrete by Rheology Control, *Composites B: Engineering2017*, Vol 117, pp. 26–34.

Meng W and Khayat KH, Mechanical Properties of Ultra-High-Performance Concrete Enhanced with Graphite Nanoplatelets and Carbon Nanofibers, *Composites B: Engineering 2017*, Vol 175, pp. 113–122.

Meng W, Valipour M, and Khayat KH, Optimization and Performance of Cost-Effective Ultra-High Performance Concrete, *Materials and Structures 2016*, Vol 50(1), pp. 29.

Meng W and Khayat KH, Experimental and Numerical Studies on Flexural Behavior of Ultra-High-Performance Concrete Panels Reinforced with Embedded Glass Fiber-Reinforced Polymer Grids, *Transportation Research Record: Journal of the Transportation Research Board 2016*, Vol 2592, pp. 38–44.

Bao Y, **Meng W,** ChenY, Chen G, and Khayat KH, Measuring Mortar Shrinkage and Cracking by Pulse Pre-Pump Brillouin Optical Time Domain Analysis with a Single Optical Fiber, *Materials Letters 2015*, Vol 145, pp. 344–346.

Bao Y, Valipour M, **Meng W,** Khayat KH, and Chen G, Distributed Fiber Optic Sensor-Enhanced Detection and Prediction of Shrinkage-Induced Delamination of Ultra-High-Performance Concrete Bonded over an Existing Concrete Substrate, *Smart Materials and Structures Journal 2017*.

Meng W and Khayat KH, Effects of Saturated Lightweight Sand Content on Key Characteristics of Ultra-High-Performance Concrete, *Cement and Concrete Research*. (Revised version under review)

Meng W, Khayat KH, and Bao Y, Flexural Behavior of Ultra-High-Performance Concrete Panels Reinforced with Embedded Fiber-Reinforced Polymer Grids, *Cement and Concrete Composites*. (Revised version under review)

Meng W, Yao Y, Mobasher B, and Khayat KH, Effects of Loading Rate and Notch-to-Depth Ratio of Notched Beams on Flexural Performance of Ultra-High-Performance Concrete, *Cement and Concrete Composites*. (Revised version under review)

Meng W and Khayat KH, Effect of Graphite Nanoplatelets and Carbon Nanofibers on Rheological Properties, Hydration Kinetics, Shrinkage, and Pore Structure of UHPC, *Cement and Concrete Research*. (Under review)

Meng W, Samaranayake VA, and Khayat KH, Factorial Design and Optimization of Ultra-High-Performance Concrete Using Lightweight Sand for Internal Curing, *ACI Materials Journal* (Under review)

Meng W and Khayat KH, Effect of Hybrid Fibers and Fiber Contents on the Fresh and Hardened Properties of Ultra-High-Performance Concrete, *ASCE Journal of Materials in Civil Engineering*. (Under review)

Meng W, Lunkad P, Kumar A, and Khayat KH, Influence of Silica Fume and PCE Dispersant on Setting, Rheologyical and Mechanical Properties of Cement, (Under preparation)

10.2.2. Peer-Reviewed Conference Papers. Meng W and Khayat KH, Development of Stay-in-Place Formwork Using GFRP Reinforced UHPC Elements, *Proc. 1ˢᵗ Int. Interactive Symposium on UHPC*, Des Moines, Iowa, 2016.

Meng W and Khayat KH, Flexural Performance of Ultra-High Performance Concrete Ballastless Track Slab, *Proc. 2016 Joint Rail Conference,* Columbia, SC, 2016.

10.3. FUTURE WORK

From this study, several aspects of the experiments, numerical simulation, and implementation of UHPC are recommended for further research:

(1) To explore wider application of UHPC, its cost-effectiveness should be further enhanced. For example, polyethylene fibers can be used to replace steel fibers to reduce the cost of the developed UHPC.

(2) Investigation of other mineral admixtures to produce cost-effective sustainable UHPC. Other pozzolans and inert fillers, such as rice husk ash, metakaolin, and lime stone, glass powders could be investigated to replace the cement. The use of these materials reduces the cost of concrete production and increases environmental benefits. Furthermore, the combination of mineral admixtures may also have positive effects on the durability of concrete. It was observed that the addition of GGBS and fly ash can improve the workability of fresh UHPC. This gives rise to the idea that the total cement replacement level can be expected to increase further by using other mineral additives combined with these powder additions. Indeed, it was reported that UHPC can be made with a total cement replacement content up to 75% by a quartery system containing cement, slag, silica fume, and rice husk ash. This can be an important contribution to the sustainable development of cost-effective UHPC.

(3) Mechanism of internal water curing of LWS in UHPC. The use of internal water curing is a very important method to enhance the properties of concrete, especially at low w/b ratio mixes. With decreasing the w/b ratio, the microstructure of mixtures becomes denser and the effective distance of internal curing from 'water reservoirs' to the surroundings is limited. The effective distance of LWS to provide the sufficient

internal curing in UHPC will need to be studied. Furthermore, finer internal curing agent, such as rice husk ash or super absorbent polymers, can be incorporated with LWS to improve the internal curing efficiency.

(4) Modelling of hydration and microstructure development of cement paste containing LWA and nanomaterials. The effects LWS and nanomaterials on the hydration and microstructure development of cement paste should be evaluated. From the hydration process and the built-up microstructure of the blended system, the permeability, the tensile strength, compressive strength, and autogenous shrinkage of concrete will be simulated.

(5) Durability of the developed UHPC will be investigated. It is found that the incorporation of LWS and nanomaterials in UHPC can enhance its mechanical properties. However, there is lack of information on the durability. The chloride penetration, carbonation, alkali silica reactions, structural cracks, damage due to accidents, explosions or earthquakes, etc. should be evaluated.

(6) Large scale testing of UHPC panels and functionally-graded slabs. Further optimizations of slab systems with large or full scale should be carried out. However, it needs to be remembered that particular care should be taken to casting procedure for UHPC elements to align the fibers in the mixture. The thickness of the panels/slabs should be optimized.

(7) It finally has to be considered that thin and light structures as those made possible by UHPC could face could be affected by the risk of local instability. Serviceability limit, such as maximal admissible deformation, problems related to fatigue, should be studied.

(8) More application, such as bridge deck connections of using the developed UHPC can be explored. The experimental validation and implementation of the proposed prefabricated elements should also be carried out.

APPENDIX

Paper No. 1:

CrossMark

ORIGINAL ARTICLE

Optimization and performance of cost-effective ultra-high performance concrete

Weina Meng · Mahdi Valipour ·
Kamal Henri Khayat

Abstract This paper presents a mix design method for ultra-high performance concrete (UHPC) prepared with high-volume supplementary cementitious materials and conventional concrete sand. The method involves the optimization of binder combinations to enhance packing density, compressive strength, and rheological properties. The water-to-cementitious materials ratio is then determined for pastes prepared with the selected binders. The sand gradation is optimized using the modified Andreasen and Andersen packing model to achieve maximum packing density. The binder-to-sand volume ratio is then determined based on the void content, required lubrication paste volume, and compressive strength. The optimum fiber volume is selected based on flowability and flexural performance. The high-range water reducer dosage and w/cm are then adjusted according to the targeted mini-slump flow and compressive strength. Finally, the optimized UHPC mix designs are evaluated to determine key properties that are relevant to the intended application. This mix design approach was applied to develop cost-effective UHPC materials. The results indicate that the optimized UHPC can develop 28-days compressive strength of 125 MPa under standard curing condition and 168 178 MPa by heat curing for 1 days Such mixtures have unit cost per compressive strength at 28 days of 4.1 4.5 \$/m^3/MPa under standard curing.

Keywords Conventional concrete sand ·
Cost-effective · Mix design · Rheological properties ·
Supplementary cementitious materials (SCMs) ·
Ultra-high performance concrete (UHPC)

1 Introduction

With appropriate combination of cementitious materials, adequate sand gradation, and incorporation of fiber reinforcement and high-range water reducer (HRWR), ultra-high performance concrete (UHPC) can be produced to deliver high flowability (self-consolidating), mechanical properties, and durability [1, 2]. However, high material cost is restricting UHPC's wider acceptance worldwide [3 5]. Development of cost-effective UHPC is crucial for greater acceptance of this novel construction material.

High-volume replacement of cement with sustainable supplementary cementitious materials (SCMs), such as fly ash, ground granulated blast furnace slag (GGBS), and silica fume (SF), can be performed to reduce cement content without significantly sacrificing the mechanical strengths [5 8]. Mixtures containing 20 35 % (vol. %) GGBS, 10 30 % Class C fly ash (FAC), and 15 30 % SF have been used in

W. Meng · M. Valipour · K. H. Khayat (✉)
Department of Civil, Architectural, and Environmental
Engineering, Missouri, University of Science and
Technology, 205 ERL 500 W 16th street, Rolla,
MO 65409, USA
e-mail: khayatk@mst.edu

rilem

Paper No2:

Improving flexural performance of ultra-high-performance concrete by rheology control of suspending mortar

CrossMark

Weina Meng, Kamal Henri Khayat[*]

Department of Civil, Architectural, and Environmental Engineering, Missouri University of Science and Technology, 205 ERL 500 W 16th Street, Rolla, MO 65409, USA

ABSTRACT

This study develops a rheology control method to improve steel fiber distribution and flexural performance of ultra-high-performance concrete (UHPC) by adjusting the rheological properties of the suspending mortar of UHPC before steel fibers are added. Correlations among the plastic viscosity of the suspending mortar, the resulting steel fiber distribution, and flexural properties of UHPC are established. This was done by changing the dosage of viscosity modified admixture (VMA) for investigated UHPC mixtures. The optimal plastic viscosity of the suspending mortar that allows for the optimized fiber distribution and flexural performance of UHPC is determined. The plastic viscosity is correlated with the mini V-funnel flow time, which provides a simple alternative to evaluate the plastic viscosity. For a UHPC mixture with 2% micro steel fibers, by volume, the optimal mini V-funnel flow time of suspending motar was determined to be 46 ± 2 s, which corresponded to the optimal plastic viscosity (53 ± 3 Pa s) that ensures the greatest fiber dispersion uniformity and flexural performance of UHPC. However, increasing the VMA dosage retarded the hydration kinetics and reduced the degree of hydration, compressive strength, and the bond properties of the fiber-matrix interface of UHPC.

© 2017 Elsevier Ltd. All rights reserved.

1. Introduction

Ultra-high-performance concrete (UHPC) is a class of cementitious composites that have self-consolidating property, high mechanical strengths, superior durability, and low permeability, due to the low water-to-binder ratio (<0.25) and high packing density [1]. It has been used in highway bridge applications in the forms of precast girders [2] and full-depth deck panels [3]. Steel fibers are commonly employed as reinforcement to enhance the tensile and flexural performance of UHPC. The fibers crossing cracks can restrain the widening and propagation of cracks and allow cracked UHPC to carry sustain load. The tensile and flexural properties of UHPC are closely related to the orientation and spatial dispersion of fibers in UHPC matrix [4–6]. Well-oriented and uniformly-dispersed fibers have greater chance to bridge cracks. Thus, improving the fiber distribution is critical for increasing the tensile and flexural performance of UHPC [7,8].

The fiber orientation in UHPC matrix was associated with the casting scheme [5,6,9]. Due to the high viscosity and fluidity of

UHPC, during the casting, the velocity ingredient of the flow (shear flow) of fresh UHPC mixture drives the fibers orient along with the flow direction [10]. Thus, fresh UHPC that was placed at one end of the mold and flowed to the other end in the longitudinal direction demonstrated more favorable fiber orientation [11]. In the literature, UHPC specimens that were cast in the proper way exhibited more than 60% higher flexural strengths than other UHPC specimens [6,12,13]. However, the casting scheme demonstrated little influence on the dispersion of fibers in UHPC [6,10].

On the other hand, the rheological properties of concrete demonstrated significant effects on the fiber orientation and dispersion [5,10,14]. The mini-slump flow and plastic viscosity of concrete should be controlled at a proper level to ensure the concrete has adequate flowability but no fiber segregation occurs [5,10]. Effects of plastic viscosity on the dispersion of polyvinyl alcohol fibers and the tensile performance of engineered cementitious composites were studied [5,14]. Increasing the plastic viscosity by using viscosity modified admixture (VMA) was found to have two opposite effects on the mechanical properties of engineered cementitious composites. On one hand, increasing the plastic viscosity improved the fiber dispersion and thus increased the tensile properties of engineered cementitious composites [5]. A

223

Paper No.3:

Contents lists available at ScienceDirect

Composites Part B

Mechanical properties of ultra-high-performance concrete enhanced with graphite nanoplatelets and carbon nanofibers

CrossMark

Weina Meng, Kamal H. Khayat[*]

Department of Civil, Architectural, and Environmental Engineering, Missouri University of Science and Technology, 205 ERL, 500 W 16th Street, Rolla, MO 65409, USA

A R T I C L E   I N F O

A B S T R A C T

Effects of graphite nanoplatelets (GNPs) and carbon nanofibers (CNFs) on mechanical properties of ultra-high-performance concrete (UHPC) are investigated. A non-proprietary UHPC mixture composed of 0.5% steel micro fibers, 5% silica fume, and 40% fly ash was used. The content of the nanomaterials ranged from 0 to 0.3% by weight of cementitious materials. The nanomaterials were dispersed using optimized surfactant content and ultra-sonification to ensure uniform dispersion in the UHPC mixture. As the content of nanomaterials is increased from 0 to 0.3%, the tensile strength and energy absorption capacity can be increased by 56% and 187%, respectively; the flexural strength and toughness can be increased by 59% and 276%, respectively. At 0.2% of GNPs, the UHPCs exhibited "strain-hardening" in tension and in flexure.
© 2016 Elsevier Ltd. All rights reserved.

1. Introduction

With appropriate combination of cement and supplementary cementitious materials, adequate sand gradation, low water-to-binder ratio (w/b < 0.25), fiber reinforcement, and high-range water reducer (HRWR), ultra-high-performance concrete (UHPC) can be produced to deliver high flowability, high mechanical, and excellent durability [1,2]. By incorporating steel/polymeric fiber reinforcements, UHPC can exhibit strain hardening behavior in tension and in flexure, exhibiting ductile failure modes. Park et al. [3] found that the strain hardening behavior of UHPC can be observed for tension with multiple cracking, by incorporating micro steel fibers at 1.5% by volume of UHPC. Meng et al. [4,5] reported that under four-point bending, the post-cracking behavior of UHPC exhibited strain hardening when the content of micro steel fibers exceeded 1% by volume of UHPC. However, the micro fibers were found to be ineffective in delaying the initiation and propagation of microcracks, which can be due to the relatively large spacing between fibers [6]. The presence of cracks can make UHPC vulnerable to ingress of moisture and undesired ions, thus resulting in accelerated deterioration. Therefore, to enhance the cracking resistance and the fracture toughness of UHPC is of great importance.

Carbon nanomaterials, such as carbon nanotubes (CNTs), carbon nanofibers (CNFs), and graphite nanoplatelets (GNPs), have been used to enhance mechanical properties of cementitious composites, due to their high elastic modulus and tensile strength [7—9]. For example, Li et al. [10] found an addition of CNT at 0.5% by weight of binder increased the flexural tensile strength, compressive strength, and failure strain of a cementitious composite by 25%, 20%, and 30%, respectively. Gao et al. [11] observed that the compressive strength of a cementitious composite containing 0.16% CNFs was 40% higher than that of the plain cementitious composite. With an addition of 0.13% GNPs, Peyvandi et al. [12] obtained a 70% increase in the flexural tensile strength of a cement paste. The nanoscale spacing and high specific surface areas of the nanomaterials make them effective in suppressing inception and propagation of microcracks [13,14]. On the other hand, carbon nanomaterials were found to be able to enhance the packing density of cementitious materials and accelerate the nucleation and growth of calcium-silicate-hydrate. This can be attributed to the increase in nucleation sites due to the nanomaterials, thus refining the microstructure and improving the mechanical properties [9,15]. However, due to the small size, agglomeration of nanomaterials can potentially compromise their reinforcing performance [16,17]. Ultra-sonification has been used to undermine agglomeration and facilitate their dispersion in aqueous media [18]. Surfactants were incorporated to convert the hydrophobic surface of nanomaterials into hydrophilic surface [19]. Uniformly-dispersed CNTs at

* Corresponding author.
E-mail address: khayatk@mst.edu (K.H. Khayat).

Paper No.4:

Experimental and Numerical Studies on Flexural Behavior of Ultra-High-Performance Concrete Panels Reinforced with Embedded Glass Fiber-Reinforced Polymer Grids

Weina Meng and Kamal H. Khayat

The use of glass fiber-reinforced polymer (GFRP) grids in reinforced concrete construction offers several advantages, such as high tensile strength and excellent corrosion resistance. This paper presents the results of experimental and numerical studies of the flexural performance of ultra-high-performance concrete (UHPC) panels reinforced with GFRP grids. Such panels can be prefabricated and used as permanent formwork elements for bridge columns or walls. The mechanical properties of GFRP grids and UHPC were experimentally evaluated. The flexural performance of panels containing different reinforcement configurations was evaluated in three-point bending tests. The GFRP grids were found to be able to significantly enhance the flexural performance of the UHPC panels. A three-dimensional nonlinear finite element model was established by using ABAQUS, which incorporated the concrete damage plasticity model and can be used to predict the postfracture behaviors. The numerical model was experimentally validated by using the three-point bending test results and was then used for parametric studies. The studied parameters included the panel thickness and the layer number of the GFRP grids reinforcement. The proposed GFRP–UHPC panel system was shown to be promising for the development of lightweight, high-performance permanent formwork. Such formwork can be used in the accelerated construction of critical infrastructures for the enhancement of crack resistance and extension of the service life.

The most notable characteristic of ultra-high-performance concrete (UHPC) is its dense microstructure, which results in superior mechanical properties, durability, and long-term stability (1, 2). UHPC can be reinforced with fibers to enhance its tensile strength and ductility. The high strength of UHPC allows the use of reduced sections, which can save materials and enable diverse design procedures (1). The enhanced durability enables the UHPC structure to have a longer service life and lower maintenance and repair costs (2). In North America, UHPC has been gaining interest in highway and pedestrian bridge applications in the forms of precast girders (3), full-depth deck panels (4), and in-fill deck joints (5). UHPC composites are particularly suitable in thin product applications, such as panels and cladding, for which they may be used as stay-in-place materials (6).

Department of Civil, Architectural, and Environmental Engineering, Missouri University of Science and Technology, 500 West 16th Street, Rolla, MO 65409. Corresponding author: K. H. Khayat, kkhayat@mst.edu.

The effectiveness of fiber-reinforced polymer (FRP) as reinforcement in concrete structures has been demonstrated extensively (7, 8). Compared with conventional steel reinforcement, FRP has higher tensile strength, lower self-weight, and greater resistance to corrosion (9, 10). FRP bars have been extensively implemented as one-dimensional reinforcement in concrete structures, such as bridge girders and decks (8–11). Effective enhancements in flexural strength and ductility have been demonstrated by the combined use of fiber-reinforced concrete and FRP bars in panel construction (12). The flexural capacity of permanent formwork panels reinforced with FRP bars can be increased by nearly four times (13). FRP bars have also been incorporated with UHPC to make bridge decks, which demonstrated good promise to replace conventional open steel grid decks (6). Two-dimensional FRP grids have been used to renovate or strengthen damaged structures (14–16). Compared with FRP bars, FRP grids are more flexible and can provide two-dimensional reinforcement. Thus, they can be used to develop thin prefabricated panels (17, 18).

In this study, UHPC panels incorporating FRP grids, which can be used as permanent formwork, are investigated. Thin and highly durable panel elements can serve as stay-in-place panels for infrastructure construction. The proposed panels can be "Lego-like" in design to facilitate ease and speed of construction. Fibers used as reinforcement can provide good cracking resistance and enhanced durability. Durability is also assured by using UHPC, which is highly impermeable and resistant to cracking. In addition to the improvement in construction efficiency, concrete permanent formwork can result in less waste than wooden formwork (12, 13, 17, 18). However, the design of such panels requires the development of sections that are lightweight, ductile, and durable. Research is needed to fully understand the behavior of UHPC panels reinforced with FRP grids (19–21). This research includes the development of reliable analysis tools capable of predicting failure modes and load capacities of FRP-reinforced UHPC panels in which there is significant flexural-shear cracking (22, 23). The geometrical shape, ductility, modulus of elasticity, and force transfer characteristics of FRP reinforcement are different from those of conventional steel reinforcement. The critical differences between the steel and FRP reinforcements indicate the significance of investigations on concrete members reinforced with FRP grids for the development of design guidelines.

This paper presents the results of experimental and numerical investigations of the flexural behavior of UHPC panels reinforced with GFRP. The flexural performance of the panels was evaluated in three-point bending tests. A three-dimensional (3-D) finite element model incorporating nonlinear material properties was established

Paper No.5:

JRC2016-5814

FLEXTURAL PERFORMANCE OF ULTRA-HIGH PERFORMANCE CONCRETE BALLASTLESS TRACK SLABS

Weina Meng
Department of Civil, Architectural, and
Environmental Engineering,
Missouri University of Science and Technology
Rolla, Missouri, USA

Kamal Henri Khayat
Department of Civil, Architectural, and
Environmental Engineering,
Missouri University of Science and Technology
Rolla, Missouri, USA

ABSTRACT

Ballastless track slab offers excellent stability and durability and has been well accepted in high-speed railways worldwide. Rails are typically laid on precast concrete slabs that are subjected to dynamic load transferred from the rails. Cracks can be induced by shrinkage and mechanical loading in concrete, which accelerates the degradation and affects the performance of the track slab. As tens of thousands of miles of ballastless track are constructed, effective and efficient maintenance for the concrete slabs has become an issue. In this paper, ultra-high performance concrete (UHPC) is proposed to fabricate ballastless track slab. UHPC is a superior fiber-reinforced, cementitioius mortar, which has greatly-improved mechanical strengths and durability. A recently-developed UHPC is evaluated in terms of the flowability, durability, shrinkage, and mechanical properties. A functionally-graded slab design is proposed with the consideration of initial material cost. The slab is cast with two layers: a layer of conventional concrete at the bottom, and a layer of UHPC on the top. A three-dimensional finite element model is developed for ballastless track slab whose flexural performance is investigated and compared with that of slab made with conventional concrete. Concrete damage plasticity model is incorporated to consider the post-cracking behavior. The results indicate that the proposed UHPC is promising for fabricating ballastless track slab with superior performance.

KEYWORD

Ballastless track slab, ultra-high performance concrete (UHPC), functionally-graded composite, finite element model, concrete damage plasticity (CDP) model

INTRODUCTION

A ballastless track slab system has various advantages, such as high stability, safety, durability, and low maintenance cost, compared with a ballasted track slab system. Thus, it became increasingly popular in the past decade, and has been extensively used in the construction of high-speed railway network in China. Due to the absence of any discrete ballast, the deformation of the track system can be greatly reduced, and safety issues caused by flying ballast are eliminated. It is more advantageous with the consideration of the lifetime cost.

Numerous designs have been proposed to improve the performance of the ballastless track slab in terms of mechanical strength, serviceability, durability, and economy. Reinforced concrete slabs have been prevailing in the applications of railway track worldwide [1-5]. Typically conventional concrete or high strength concrete is used, and the thickness of concrete slab ranges from 0.15 to 0.30 m. The reinforcement ratio typically ranges from 0.8% to 1.5% [4, 5]. However, cracks can be induced by shrinkage [6] and mechanical loads in concrete [7], which highly accelerates the degradation and compromises the performance of the track slab. As tens of thousands of miles of ballastless track are constructed, effective and efficient maintenance for the concrete slabs have become an issue.

UHPC is a superior fiber-reinforced, cementitioius mortar, which has good flowability and greatly-improved mechanical strengths and durability due to its dense microstructure [8]. The high strength of UHPC allows the use of reduced sections, which can save materials and enable diverse design procedures. The enhanced durability enables the UHPC structure to have extended service life, and lower maintenance cost. In North America, UHPC has been gaining some interest in highway and pedestrian bridge applications in the forms of precast girders [9], full-depth deck panels [10], and in-fill deck joints [11].

Paper No. 6:

Development of Stay-in-Place Formwork Using GFRP Reinforced UHPC Elements

Weina Meng, Kamal Henri Khayat*
Engineering Research Laboratory, Department of Civil, Environmental, and Architectural Engineering, Missouri University of Science and Technology, 500 W 16th St., Rolla, MO 65409

Abstract:
In this study, stay-in-place (SIP) formwork for structural elements subjected to aggressive environment, such as bridge columns and columns in parking structures subjected to deicing salt are developed by using prefabricated ultra-high performance concrete (UHPC) elements reinforced with embedded glass fiber reinforced polymers (GFRP) grids. Mechanical properties of UHPC and GFRP grids were determined experimentally. Novel designs of SIP formwork systems were presented and evaluated by numerical simulation in terms of strain and stress distributions and lateral deformation under gravity load and internal pressure due to concrete casting. Concrete damage plasticity model is incorporated to consider the post-cracking behavior in using the finite element analysis software ABAQUS. The proposed FRP-UHPC composite is shown to be promising for the development of lightweight, high performance, and cost-effective SIP formwork system for column elements.

Keywords: Ultra-high performance concrete (UHPC), glass fiber reinforced polymer (GFRP) grids, stay-in-place (SIP) formwork, column, accelerated construction

* Corresponding to: Dr. Kamal H. Khayat, email: khayatk@mst.edu

Paper No. 7:

# Influence of Silica Fume and Polycarboxylate Ether Dispersant on Hydration Mechanisms of Cement

Weina Meng,[†] Piyush Lunkad,[†] Aditya Kumar,*[,‡] and Kamal Khayat[†]

[†]Center for Infrastructure Engineering Studies (CIES), Department of Civil, Architectural and Environmental Engineering, Missouri University of Science and Technology (S&T), Rolla, Missouri 65409-0340, United States

[‡]Department of Materials Science and Engineering, Missouri University of Science and Technology (S&T), Rolla, Missouri 65409-0340, United States

S *Supporting Information*

ABSTRACT: Partial replacement of ordinary portland cement by silica fume (SF) accelerates its rate of hydration reactions. This acceleration is attributed to the enhanced heterogeneous nucleation of the main hydration product, i.e., calcium–silicate–hydrate (C–S–H), on the extra surfaces provided by SF. However, such enhancement of C–S–H nucleation is suppressed in the presence of polycarboxylate ether (PCE) dispersant, which is added to regulate the fluidity and rheological properties of fresh paste. A generalized phase boundary nucleation and growth model with time-dependent growth of C–S–H is used to fit the hydration rates of plain and binary (10% to 30% SF) cement pastes prepared with and without PCE. The results show that while SF accelerates cement hydration, increments in hydration rates are significantly smaller in relation to the extra surface area provided by SF. This is because of the agglomeration of SF particles which renders up to 96% of their surface area unavailable for C–S–H nucleation. Furthermore, it is shown that the hydration of cement, in both plain and binary pastes, is suppressed in relation to the PCE dosage. This is because of (a) adsorption of PCE molecules onto cement and SF surfaces resulting in inhibition of sites for product nucleation and (b) interaction of PCE with C–S–H, which suppresses growth of C–S–H throughout the hydration process. It is shown that the effects of nucleation site inhibition by PCE are more pronounced in SF as compared to cement. The outcomes of this study improve our understanding of the mechanisms that drive the hydration of cement in the presence of SF and PCEs.
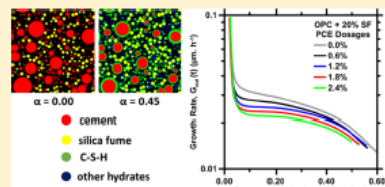
■ INTRODUCTION

The reaction between ordinary portland cement and water, i.e., hydration, involves the dissolution of anhydrous phases concomitant with the precipitation of hydration products. Calcium–silicate–hydrate (C–S–H, as per cement chemistry notation: C = CaO, S = SiO_2, H = H_2O) is the main hydration product[1] composed of SiO_2 tetrahedra and layers of calcium and oxygen atoms interspersed by water within a highly disordered framework.[2,3] C–S–H nucleates and grows heterogeneously on the cement's surface, wherein the strong electrostatic bonding between the nanometer-scale particles binds the paste cohesively.[4–7] In the presence of inorganic mineral additives (e.g., limestone, quartz, rutile), enhanced heterogeneous nucleation of C–S–H on the extra surfaces provided by the minerals results in acceleration of overall hydration kinetics. This acceleratory effect is typically termed the *filler effect*,[4,5,8] wherein the term *filler* signifies the chemically inert nature of the mineral additives.

Silica fume (SF), composed of amorphous silicon dioxide (SiO_2), is typically used to prepare high-performance concrete with enhanced durability and strength. Past studies have shown that SF produces enhancement in cement hydration rates[9–11] at early ages by offering preferential sites for product nucleation, via the filler effect. In addition, in such systems,

SF can dissolve and react chemically with portlandite (i.e., $Ca(OH)_2$: calcium hydroxide) formed during the hydration of cement[12–14] to form pozzolanic C–S–H. The pozzolanic activity of SF, however, is kinetically slow and restricted at early ages[9,13] because of its slow dissolution[15,16] and sparse availability of portlandite in the system, thus limiting the formation of pozzolanic C–S–H. Nevertheless, a minor quantity of pozzolanic C–S–H in the system could still produce profound effects on cement's hydration kinetics. More specifically, Thomas et al.[4] hypothesized that pozzolanic C–S–H acts as an energetically favored template (i.e., a seed) for the nucleation and growth of C–S–H formed due to the hydration of C_3S and C_2S phases present in cement. As C–S–H continues to form and grow in an autocatalytic manner away from the cement particles, the hydration of cement is enhanced. These reactivity enhancements induced by SF at early ages often lead to poor fresh properties (e.g., rapid setting, poor workability) and thus require the use of chemical admixtures to suppress reaction rates as well as to enhance fluidity.

Paper No. 8:

Contents lists available at ScienceDirect

Materials Letters

journal homepage: www.elsevier.com/locate/matlet

materials letters

Measuring mortar shrinkage and cracking by pulse pre-pump Brillouin optical time domain analysis with a single optical fiber

CrossMark

Yi Bao, Weina Meng, Yizheng Chen, Genda Chen *, Kamal Henry Khayat

Department of Civil, Architectural, and Environmental Engineering, Missouri University of Science and Technology, 1401 N. Pine Street, Rolla, MO 65409, USA

A R T I C L E   I N F O

A B S T R A C T

In this study, a new method to measure strain distribution and detect cracking with pulse pre-pump Brillouin optical time domain analysis (PPP-BOTDA) is proposed. A mortar cylinder was cast in a corrugated polyethylene mold with two end plugs and tested according to ASTM C1698 for autogenous shrinkage. It was instrumented with two sensors made of a single optical fiber: one for combined strain and temperature measurement and the other for temperature compensation. The shrinkage-induced compressive strain was non-uniformly distributed over the sensor length. The average of the distributed strain was in excellent agreement with autogenous shrinkage that can be determined from the ASTM test. The location and magnitude of each peak of the distributed strain can be used to detect a corresponding invisible hidden crack.

1. Introduction

Cementitious mortar mixtures proportioned with low water-to-cementitious materials ratio (w/cm) develop not only high strength and stiffness but also significant early-age shrinkage [1]. Shrinkage-induced cracks in reinforced concrete structures [2] can increase the ingress of water and chloride ions that can lead to corrosion of the steel reinforcement, resulting in accelerated structural degradation, particularly in maritime environment [3]. A number of nondestructive testing and evaluation techniques have been developed to investigate early-age shrinkage behavior in cement-based materials [2]. For example, ultrasonic wave (UW) was applied to determine the setting time by relating compressive or shear wave velocity to increasing mortar stiffness [4]. Acoustic emission (AE) was used to determine autogenous shrinkage of cement paste [5] and detect cracking in concrete [6]. Vibrating wire gages were employed to measure shrinkage in concrete [7]. Fiber Bragg gratings sensors were also employed to investigate shrinkage of mortar with low w/cm at multiple points [8].

None of these techniques can monitor both the distribution of shrinkage strain and shrinkage-induced cracking in mortar matrix. In this study, a new method to measure strain induced by early-age shrinkage of mortar is developed and validated with standard ASTM tests. Two distributed sensors made of a single optical fiber are embedded in a mortar specimen and interrogated with pulse

pre-pump Brillouin optical time domain analysis (PPP-BOTDA). The technique enables the localization of cracks induced by shrinkage and the determination of crack opening from the distribution of measured strains.

2. Working principle of PPP-BOTDA

An ultraviolet coated single mode optical fiber consists of 8.2 μm-diameter core, 125 μm-diameter cladding, soft 190 μm-diameter inner coating, and stiff 242 μm-diameter outer coating. Light travels in the fiber core with total internal reflections at the core-cladding interface.

PPP-BOTDA represents the interaction of light wave from a pump laser with the acoustic wave associated with the density non-uniformity of an optical fiber [9], which is stimulated by a probe laser. The pump laser sends a pre-pump long-duration pulse, which is immediately followed by a measurement short-duration pulse at one end of the optical fiber. The probe laser sends a continuous wave at the other end of the optical fiber. The PPP-BOTDA measures the stimulated Brillouin scattering (SBS) spectrum as the pump and probe light waves propagate towards each other from the two ends of an optical fiber; the spectrum reaches its peak when the difference in frequency of the two waves matches with that of the Brillouin frequency of the fiber. With respect to a calibrated Brillouin frequency under strain and temperature references, the shift in the Brillouin frequency due to applied strain and temperature can be measured and linearly related to the applied effects. Given the temperature change

* Corresponding author. Tel.: +1 57 33414462.
  E-mail address: gchen@mst.edu (G. Chen).

Paper No. 9:

Distributed fiber optic sensor-enhanced detection and prediction of shrinkage-induced delamination of ultra-high-performance concrete overlay

Yi Bao, Mahdi Valipour, Weina Meng, Kamal H. Khayat, Genda Chen[*]

Department of Civil, Architectural, and Environmental Engineering, Missouri University of

Science and Technology, Rolla, MO 65401

Abstract: This study develops a delamination detection system for smart ultra-high-performance concrete (UHPC) overlays using a fully-distributed fiber optic sensor. Three 450 mm (length) × 200 mm (width) × 25 mm (thickness) UHPC overlays were cast over an existing 200-mm-thick concrete substrate. The initiation and propagation of delamination due to early-age shrinkage of the UHPC overlay were detected as sudden increases and their extension in spatial distribution of shrinkage-induced strains measured from the sensor based on pulse pre-pump Brillouin optical time domain analysis. The distributed sensor is demonstrated effective in detecting delamination openings from microns to hundreds of microns. A three-dimensional finite element model with experimental material properties is proposed to understand the complete delamination process measured from the distributed sensor. The model is validated using the distributed sensor data. The finite element model with cohesive elements for the overlay-substrate interface can predict the complete delamination process.

Keywords: Delamination; Distributed fiber optic sensor; Early-age shrinkage; Pulse pre-pump Brillouin optical time domain analysis; Ultra-high-performance concrete

---

[*] Corresponding author: Dr. Genda Chen. E-mail address: gchen@mst.edu

BIBLIOGRAPHY

Aaleti S, Sritharan S., Bierwagen D, and Wipf T, Structural Behavior of Waffle Bridge Deck Panels and Connections of Precast Ultra-High-Performance Concrete: Experimental Evaluation, *Transportation Research Record: Journal of the Transportation Research Board* 2001, Vol 2251, pp. 8292.

Aaleti S., Sritharan S, Bierwagen D, and Moore P, Precast UHPC Waffle Deck Panels and Connections for Accelerated Bridge Construction, *PCI & 57th Annual National Bridge Conference*, Salt Lake City, Utah, 2011, pp.2226.

ABAQUS user's manual, Hibbit, Karlsson & Sorensen, Inc., Rhode Island, 1998.

Abrishambaf A, Barros JAO, and Cunha VMCF, Relation between Fibre Distribution and Post-Cracking Behaviour in Steel Fibre Reinforced Self-Compacting Concrete Panels, *Cement and Concrete Research 2013*, Vol 51, pp. 57–66.

Abu Al-Rub RK, Tyson BM, Yazdanbakhsh A, and Grasley Z, Mechanical Properties of Nanocomposite Cement Incorporating Surface-Treated and Untreated Carbon Nanotubes and Carbon Nanofibers, *Journal of Nanomechanical Micromech 2011,* Vol 2(1), pp. 1–6.

ACI 239, Committee in Ultra-High Performance Concrete, Minutes of Committee Meeting October 2012, ACI Annual Conference 2012, Toronto, ON, Canada.

ACI 239 C, Sub Committee on the Structural Design of UHPC, Minutes of Sub-Committee Meeting November 2015, ACI Annual Conference, Denver, CO, USA.

ACI 347-04, Guide to Formwork for Concrete, American Concrete Institute Farmington Hills, MI, 2004.

ACI 440.3R-04 , Guide Test Methods for Fiber Reinforced Polymers (FRP) for Reinforcing or Strengthening Concrete Structures, Detroit, 2004.

Al-Khaiat H, Haque MN, Effect of Initial Curing on Early Strength and Physical Properties of a Lightweight Concrete, *Cement and Concrete Research 1998*, Vol 28(6), pp. 859–866.

Al-Sunna R, Pilakoutas K, Hajirasouliha I, Guadagnini M, Deflection Behaviour of FRP Reinforced Concrete Beams and Slabs: An Experimental Investigation, *Composites Part B: Engineering 2012*,Vol 43(5), pp. 21252134.

Anderson MJ, A New Method for Non-Parametric Multivariate Analysis of Variance, *Austral Ecology* 2001, Vol 26(1), pp. 32–46.

ASTM D3822/D3822M, Standard Test Method for Tensile Properties of Single Textile Fibers, ASTM International, West Conshohocken, Pennsylvania, 2014.

ASTM C230, Standard Specification for Flow Table for Use in Tests of Hydraulic Cement, ASTM International, West Conshohocken, Pennsylvania, 2014.

ASTM C 138/C 138M, Standard Test Method for Density ("Unit Weight"), Yield, and Air Content (Gravimetric) of Concrete, West Conshohocken, 2008.

ASTM C109, Standard Test Method for Compressive Strength of Hydraulic Cement Mortars (Using 50 mm Cube Specimens), ASTM International, West Conshohocken, Pennsylvania, 2013.

ASTM C 231, Standard Test Method for Air Content of Freshly Mixed Concrete by the Pressure Method, ASTM International, West Conshohocken, 2000.

ASTM C469, Standard Test Method for Static Modulus of Elasticity and Poisson's Ratio of Concrete in Compression, ASTM International, West Conshohocken, Pennsylvania, 2014.

ASTM C1609, Standard Test Method for Flexural Performance of Fiber-Reinforced Concrete (Using Beam with Third-Point Loading), ASTM International, West Conshohocken, Pennsylvania, 2006.

ASTM C469, Standard Test Method for Static Modulus of Elasticity and Poisson's Ratio of Concrete in Compression, ASTM International, West Conshohocken, Pennsylvania, 2014.

Aïtcin PC, Cements of Yesterday and Today: Concrete of Tomorrow, *Cement and Concrete Research 2000,* Vol 30(9), pp. 13491359.

Aïtcin PC, High Performance Concrete, *CRC press, 2011*.

Babu KG and Kumar VS, Efficiency of GGBS in Concrete, *Cement and Concrete Research 2000*, Vol 30(7), pp.1031-1036.

Baena M, Torres L, Turon A, and Mias C, Analysis of Cracking Behaviour and Tension Stiffening in FRP Reinforced Concrete Tensile Elements, *Composites Part B: Engineering 2013*, Vol 45, pp.13601367.

Bakhshi M, Barsby C, and Mobasher B, Comparative Evaluation of Early Age Toughness Parameters in Fiber Reinforced Concrete, *Materials and Structures 2014*, Vol 47(5), pp. 853–872.

Bakis CE, Bank LC, Brown VL, Cosenza E, Davalos JF, Lesko JJ, Machida A, Rizkalla SH, and Triantafillou TC, Fiber-Reinforced Polymer Composites for Construction Stateof the Art Review, *Journal of Composites Construction 2002*, Vol 6(2), pp. 7377.

Bank LC, Composites for Construction: Structural Design with FRP Materials, New Jersey: John Wiley & Sons, 2006.

Bao Y, Chen G, Meng W, Tang F, and Chen Y, Kilometer-Long Optical Fiber Sensor for Real-Time Railroad Infrastructure Monitoring to Ensure Safe Train Operation, *Proceeding of Joint Rail Conference 2015*, San Jose, CA, USA.

Bao Y, Meng W, Chen Y, Khayat K, and Chen G, Measuring Mortar Shrinkage and Cracking by Pulse Pre-pump Brillouin Optical Time Domain Analysis with A Single Optical Fiber, *Materials Letter 2015*, Vol 145, pp. 344346.

Barnes HA, Hutton JF, and Walters K, An Introduction to Rheology, Elsevier, 1989.

Behloul M, Bernier G, and Cheyrezy M, Tensile Behavior of Reactive Powder Concrete (RPC), *In Proceedings of the 4th international symposium on utilization of HSC/HPC 1996*, Vol 96, pp. 13751381.

Bentur A, Igarashi S, and Kovler K, Prevention of Autogenous Shrinkage in High-Strength Concrete by Internal Curing Using Wet Lightweight Aggregates, *Cement and Concrete Research 2001*, Vol 31, pp. 15871591.

Bentz D, Lura P, and Roberts J, Mixture Proportioning for Internal Curing, *Concrete Internationa 2005*, Vol 27(2), pp. 3540.

Bentz D, Snyder K, Protected Paste Volume in Concrete: Extension to Internal Curing Using Saturated Lightweight Fine Aggregate, *Cement and Concrete Research 1999*, Vol 29, pp. 1863–1867.

Bentz D and Weiss J, Internal Curing: A 2010 State-of-The-Art Review, NISTIR 7765, U.S.Department of Commerce, 2011.

Benson SD and Karihaloo BL, CARDIFRC®-Development and Mechanical Properties. Part III: Uniaxial Tensile Response and Other Mechanical Properties, *Magazine of Concrete Research 2005*, Vol 57(8), pp. 433–443.

Berry EE, Hemmings RT, and Cornelius BJ, Mechanisms of Hydration Reactions in High Volume FA Pastes and Mortars, *Cement and Concrete Composite 1990*, Vol 12(4), pp. 253–261.

Beushausen H and Gillmer M, The Use of Superabsorbent Polymers to Reduce Cracking of Bonded Mortar Overlays, *Cement and Concrete Composites 2014*, Vol 52, pp. 18.

Bierwagen D and Abu-Hawash A, Ultra High Performance Concrete Highway Bridge, *In Proceeding of the 2005 Mid-Continent Transportation Research Symposium*, Ames, Iowa, 2005, pp. 114.

Bischoff P H, Tension Stiffening and Cracking of Steel Fiber-Reinforced Concrete, *Journal of Materials in Civil Engineering 2003*, Vol 15(2), pp. 174–182.

Björn T and Thomas B, Mineral-Based Bonding of Carbon FRP to Strengthen Concrete Structures, *Journal of Composites Construction 2007*, Vol 11, pp. 120-128.

Bonneau O, Vernet C, Moranville M, and Aïtcin PC, Characterization of the Granular Packing and Percolation Threshold of Reactive Powder Concrete, *Cement and Concrete Research 2000*, Vol 30(12), pp. 1861–1867.

Boulekbache B, Hamrat M, Chemrouk M, and Amziane S, Flowability of Fibre-Reinforced Concrete and Its Effect on the Mechanical Properties of the Material, *Construction and Building Materials 2000*, Vol 24(9), pp. 1664–1671.

Breuer O, Sundararaj U, and Toogood RW, The Design and Performance of a New Miniature Mixer for Specialty Polymer Blends and Nanocomposites, *Polymer Engineering Science 2004*, Vol 44(5), pp. 868–879.

Chanvillard G and Rigaud S, Complete Characterization of Tensile Properties of Ductal$^{®}$ UHPFRC According to the French Recommendations, *In Proceedings of the 4th International RILEM workshop High Performance Fiber Reinforced Cementitious Composites 2003*, pp. 2134.

Cherezy M, Maret V, and Frouin L, Microstructural Analysis of RPC (Reactive Powder Concrete), *Cement and Concrete Research 2005,* Vol 25, pp. 14911500.

De Larrard F and Sedran T, Optimization of Ultra-High-Performance Concrete by the Use of A Packing Model, *Cement and Concrete Research 1994*, Vol 24, pp. 997-1009.

De la Varga I and Graybeal B, Dimensional Stability of Grout-Type Materials Used as Connections Between Prefabricated Concrete Elements, *ASCE Journal of Materials in Civil Engineering 2014*, pp. 19435533. 0001212.

Dhir RK, Hubbard FH, Munday JG, Jones MR, and Duerden SL, Contribution of PFA to Concrete Workability and Strength Development, *Cement and Concrete Research 1988*, Vol 18(2), pp. 277289.

Diamond S, Effects of two Danish Flyashes on Alkali Contents of Pore Solutions of Cement-Flyash Pastes, *Cement and Concrete Research 1981*, Vol 11(3), pp. 383-94

Dils J, Boel V, and De Schutter G, Vacuum Mixing Technology to Improve the Mechanical Properties of Ultra-High Performance Concrete, *Materials and Structures 2015*, Vol 48, pp. 3485-3501.

El-Dieb AS, Mechanical, Durability and Microstructural Characteristics of Ultra-High-Strength Self-Compacting Concrete Incorporating Steel Fibres, *Materials Design 2009*, Vol 30, pp. 42864292.

El-Hacha R and Chen D, Behaviour of Hybrid FRP-UHPC Beams Subjected to Static Flexural Loading, *Composites Part B: Engineering 2002*, Vol 43(2), pp. 582–593.

EFNARC, Specification and Guidelines for Self-Compacting Concrete, European Federation for Specialist Construction Chemicals and Concrete Systems, Norfolk, UK, English ed., 2002.

EN 14651:2005+A1:2007, Test Method for Metallic Fibre Concrete − Measuring the Flexural Tensile Strength (Limit of Proportionality (LOP), Residual), UK: BSI 2007.

Ferrara L, Park YD, and Shah SP, Correlation Among Fresh State Behavior, Fiber Dispersion, and Toughness Properties of SFRCs, *Journal of Materials in Civil Engineering 2008*, Vol 20(7), pp. 493–501.

Ferrara L, Park YD, and Shah SP, A Method for Mix-Design of Fiber-Reinforced Self-Compacting Concrete, *Cement and Concrete Research 2007*, Vol 37(6), pp. 957–971

Ferraris CF, Obla KH, and Hill R, The Influence of Mineral Admixtures on the Rheology of Cement Paste and Concrete, *Cement and Concrete Research 2001*, Vol 31, pp. 245255.

Ferrier E, Michel L, Zuber B, and Chanvillard G, Mechanical Behaviour of Ultra-High-Performance Short-Fibre-Reinforced Concrete Beams with Internal Fibre Reinforced Polymer Bars, *Composites Part B: Engineering 2015*, Vol 68, pp. 246258.

Flatt RJ and Houst YF, A Simplified View on Chemical Effects Perturbing the Action of Superplasticizers, *Cement and Concrete Research 2001*, Vol 31(8), pp. 1169-1176.

Francesca GC, Gabriele M, and Carlo P, Mechanical Properties and Numerical Modeling of Fabric Reinforced Cementitious Matrix (FRCM) Systems for Strengthening of Masonry Structures," *Composites Structures 2014*, Vol 107, pp. 711–725.

Funk JE and Dinger DR, Predictive Process Control of Crowded Particulate Suspension, *Applied to Ceramic Manufacturing 1994*, New York: Kluwer Academic Press.

Gao D, Sturm M, and Mo YL, Electrical Resistance of Carbon-Nanofiber Concrete, *Smart Materials and Structures 2009*, Vol 18(9), pp. 095039.

Gao JM, Qian CX, Liu HF, Wang B, and Li L, ITZ Microstructure of Concrete Containing GGBS, *Cement and Concrete Research 2005*, Vol 35(7), pp. 1299-1304.

Georgios M, Slab Track Systems for High-Speed Railways, Master Thesis, Royal Institute of Technology, Sweden, 2012.

Gesoglu M, Güneyisi E, Muhyaddin GF, and Asaad DS, Strain Hardening Ultra-High Performance Fiber Reinforced Cementitious Composites: Effect of Fiber Type and Concentration, *Composites Part B: Engineering 2016*, Vol 103, pp. 7483.

Ghafari E, Ghahari SA, Costa H, Júlio E, Portugal A, and Durães L, Effect of Supplementary Cementitious Materials on Autogenous Shrinkage of Ultra-High Performance Concrete, *Construction and Building Materials 2016*, Vol 127, pp. 4348.

Ghoneim GAM, Perry VH, and Carson G, Ultra-High Performance Fiber Reinforced Concrete in Footbridges, *Proceeding 8th International Conference on Short & Medium Span Bridges*, Niagara Falls, Ontario, Canada, 2011, Vol 346, pp. 111.

Graybeal B, Material Property Characterization of Ultra-High Performance Concrete, *Report No. FHWA-HRT-06-103*, FHWA, U.S. Department of Transportation, 2006.

Graybeal B, Behavior of Field-Cast Ultra-High Performance Concrete Bridge Deck Connections under Cyclic and Static Structural Loading, *Report No. FHWA-HRT-11-023*, FHWA, U.S. Department of Transportation, 2010.

Graybeal B, Ultra-High Performance Concrete, *Report No. FHWA-HRT-11-038*, FHWA, U.S. Department of Transportation, 2011.

Graybeal B and Stone B, Compression Response of a Rapid-Strengthening Ultra-High Performance Concrete Formulation, *Report No. FHWA-HRT-12-065*, FHWA, U.S. Department of Transportation, National Technical Information Service Accession No. PB2012-112545, 2012.

Grünewald S, Performance-Based Design of Self-Compacting Fibre Reinforced Concrete, PhD thesis, Delft University of Technology, Department of Structural and Building Engineering, Delft University Press, 2004.

Habeeb GA and Fayyadh MM, Rice Husk Ash Concrete: the Effect of RHA Average Particle Size on Mechanical Properties and Drying Shrinkage, *Australian Journal of Basic and Applied Sciences 2009*, Vol 3(3), pp. 1616–1622.

Habel K, Viviani M, Denarie E, and Bruehwiler E, Development of the Mechanical Properties of an Ultra-High Performance Fiber Reinforced Concrete (UHPFRC), *Cement and Concrete Research 2006*, Vol 36(7), pp. 1362–1370.

Habert G, Denarié E, Šajna A, and Rossi P, Lowering the Global Warming Impact of Bridge Rehabilitations by Using Ultra High Performance Fibre Reinforced Concretes, *Cement and Concrete Composites 2013*, Vol 38, pp. 111.

Han B, Sun S, Ding S, Zhang L, Yu X, and Ou J, Review of Nanocarbon-Engineered Multifunctional Cementitious Composites, *Composites Part A: Applied Science Manufacture 2015*, Vol 70, pp. 69–81.

Hassan AMT, Jones S, and Mahmud GH, Experimental Test Methods to Determine the Uniaxial Tensile and Compressive Behaviour of Ultra-High Performance Fibre Reinforced Concrete (UHPFRC), *Construction Building Materials 2012*, Vol. 37, pp. 874882.

Hannawi K, Bian H, Prince-Agbodjan W, and Raghavan B, Effect of Different Types of Fibers on the Microstructure and the Mechanical Behavior of Ultra-High Performance Fiber-Reinforced Concretes, *Composites Part B: Engineering 2016*, Vol 86, pp. 214–220.

He J, Barry ES, and Della MR, Hydration of FA-Portland Cements, *Cement and Concrete Research 1984*, Vol 14(4), pp.505–512.

Henkensiefken R, Internal Curing in Cementitious Systems Made Using Saturated Lightweight Aggregate, PhD dissertation, Purdue University, 2008.

Huang S, Multifunctional Graphite Nanoplatelets (GNP) Reinforced Cementitious Composites, Master Thesis, National University of Singapore, Singapore, 2012

Hwang S, Khayat KH, and Youssef D, Effect of Moist Curing and Use of Lightweight Sand on Characteristics of High-Performance Concrete, *ACI Material Journal 2012*, Vol 46, pp. 3546.

Iveson SM, Litster JD, Hapgood K, and Ennis BJ, Nucleation, Growth and Breakage Phenomena in Agitated Wet Granulation Processes: A Review, *Powder Technology 2001*, Vol 117, pp. 3–39.

Jawed I and Skalny J, Alkalies in Cement: A Review: II. Effects of Alkalies on Hydration and Performance of Portland Cement, *Cement and Concrete Research 1978*, Vol 8(1), pp. 3751.

Jensen OM and Hansen PF, Water-Entrained Cement-Based Materials: I. Principles and Theoretical Background, *Cement and Concrete Research 2001*, Vol 31(4), pp. 647–654

John AN, On the Use of Shear-Lag Methods for Analysis of Stress Transfer in Unidirectional Composites, *Mechanical Materials 1997*, Vol 26(2), pp. 63–80.

Jonkers HM, Thijssen A, Muyzer G, Copuroglu O, and Schlangen E, Application of Bacteria as Self-Healing Agent for the Development of Sustainable Concrete, *Ecological Engineering 2010*, Vol 36(2), pp. 230–235.

Juenger MC and Siddique R, Recent Advances in Understanding the Role of Supplementary Cementitious Materials in Concrete, *Cement and Concrete Research 2015,* Vol 78, pp. 7180.

Justs J, Wyrzykoski M, Winnefeld F, Bajare D, and Lura P, Influence of Superabsorbent Polymers on Hydration of Cement Pastes with Low Water-to-Binder Ratio, *Journal Thermal Analytical Calorimetry 2014*, Vol 115, pp. 425–432.

Justs J, Wyrzykoski M, Bajare D, and Lura P, Internal Curing by Superabsorbent Polymers in Ultra-High Performance Concrete, *Cement and Concrete Research 2016*, Vol 76, pp. 82–90.

Kang ST, Choi JI, Koh KT, Lee KS, and Lee BY, Hybrid Effects of Steel Fiber and Microfiber on the Tensile Behavior of Ultra-High Performance Concrete, *Composite Structures 2016*, Vol 145, pp. 37–42.

Kang ST and Kim JK, The Relation Between Fiber Orientation and Tensile Behavior in an Ultra High Performance Fiber Reinforced Cementitious Composites (UHPFRC), *Cement and Concrete Research 2011*, Vol 41, pp. 1001–1014.

Kang ST and Kim JK, Numerical Simulation of the Variation of Fiber Orientation Distribution During Flow Molding of Ultra High Performance Cementitious Composites (UHPCC), *Cement and Concrete Composites 2012*, Vol 34(2), pp. 208–217.

Kang ST, Lee BY, Kim JK, and Kim YY, The Effect of Fibre Distribution Characteristics on the Flexural Strength of Steel Fibre-Reinforced Ultra High Strength Concrete, *Construction and Building Materials 2011*, Vol 25(5), pp. 2450–2457.

Karthiga P, Selija K, Javali PN, and Elavenil S, Analysis and Design of Ballastless Track Slab," *International Journal of Emerging Technology and Advanced Engineering 2014*, Vol 4(4), pp. 6976.

Khayat KH, Workability, Testing, and Performance of Self-Consolidating Concrete," *ACI Materials Journal 1999*, Vol. 96, pp.346–353.

Khayat KH, Kassimi F, and Ghoddousi P, Mixture Design and Testing of Fiber-Reinforced Self-Consolidating Concrete, *ACI Materials Journal 2014*, Vol 111, pp. 143152.

Kobayashi K, Fiber Reinforced Concrete, Ohm-sha, Tokyo, 1981.

Konsta-Gdoutos MS, Metaxa ZS, and Shah SP, Multi-Scale Mechanical and Fracture Characteristics and Early-Age Strain Capacity of High Performance Carbon Nanotube/Cement Nanocomposites, *Cement and Concrete Composites 2010*, Vol 32(2), pp. 110–115.

Konsta-Gdoutos MS, Metaxa ZS, and Shah SP, Highly Dispersed Carbon Nanotube Reinforced Cement Based Materials, *Cement and Concrete Research 2010*, Vol 40(7), pp.1052–1059.

Kim DJ, Naaman AE, and El-Tawil S, Correlation between Tensile and Bending Behavior of FRC Composites with Scale Effect, *Proceeding of 7th International Conference for Fracture Mechanics of Concrete and Concrete Structures*, Jeju Island, South Korea, 2010.

Kim GB, Development of Thin FRP GFRC Permanent Formwork Systems, PhD dissertation, University of Sheffield, 2006.

Kim GB, Pilakouta K, and Waldron P, Development of Thin FRP Reinforced GFRC Permanent Formwork Systems, *Construction and Building Materials 2008*, Vol 22, pp. 22502259.

Kim GB, Pilakoutas K, and Waldron P, Finite Element Analysis of Thin GFRC Panels Reinforced with FRP, *Construction and Building Materials 2009,* Vol 23(2), pp. 936942.

Kirgiz MS, Advance Treatment by Nanographite for Portland Pulverised Fly Ash Cement (the Class F) Systems, *Composites Part B: Engineering 2015*, Vol 82, pp. 5971.

Kwon S, Nishiwaki T, Kikuta T, and Mihashi H, Development of Ultra-High-Performance Hybrid Fiber-Reinforced Cement-Based Composites, *ACI Materials Journal 2014*, Vol 111(3), pp. 309–318.

Lawler JS, Zampini D, Shah SP, Microfiber and Macrofiber Hybrid Fiber-Reinforced Concrete, *Journal of Materials in Civil Engineering 2009*, Vol 17(5):595604.

Le JL, Du H, and Dai PS, Use of 2D Graphene Nanoplatelets (GNP) in Cement Composites for Structural Health Evaluation, *Composites Part B: Engineering 2014*, Vol 67, pp. 555–563.

Le HT, Müller M, Siewert K, and Ludwig HM, The Mix Design for Self-Compacting High Performance Concrete Containing Various Mineral Admixtures, *Materials Design 2015*, Vol 72, pp. 51–62.

Lee BY, Fiber Distribution Evaluation Using Digital Image Processing and Its Effect on Tensile Behavior of Fiber Reinforced Cement Composites, Korea Advanced Institute of Science and Technology. Ph.D. Dissertation, 2009.

Lee BY, Kim JK, Kim JS, and Kim YY, Quantitative Evaluation Technique of Polyvinyl Alcohol (PVA) Fiber Dispersion in Engineered Cementitious Composites, *Cement and Concrete Composites 2009*, Vol 31(6), pp. 408–417.

Lee BY, Kang ST, Yun HB, and Kim YY, Improved Sectional Image Analysis Technique for Evaluating Fiber Orientations in Fiber-Reinforced Cement-Based Materials, *Materials 2016*, Vol 9(1), pp. 42.

Lee HK, Lee KM, and Kim BG, Autogenous Shrinkage of High-Performance Concrete Containing Fly Ash, *Magazine of Concrete Research 2003*, Vol 55(6), pp. 507-515.

Leung KY and Cao Q, Development of Pseudo-Ductile Permanent Formwork for Durable Concrete Structures, *Materials and Structures 2010*, Vol 43, pp. 993–1007.

Li LG and Kwan AKH, Mortar Design Based on Water Film Thickness, *Construction and Building Materials 2011*, Vol 25, pp. 23812390.

Li LG and Kwan AKH, Packing Density of Concrete Mix Under Dry and Wet Conditions, *Powder Technology 2014*, Vol 253, pp. 514521.

Li G, Wang P, and Zhao X, Mechanical Behavior and Microstructure of Cement Composites Incorporating Surface-Treated Multi-Walled Carbon Nanotubes, *Carbon 2005*, Vol 43(6), pp. 1239–1245.

Li M and Li VC, Rheology, Fiber Dispersion, and Robust Properties of Engineered Cementitious Composites, *Materials and Structures 2013*, Vol 46, pp. 405–420.

Li X, Wang J, Bao Y, and Chen G, Cyclic Behavior of Damaged Reinforced Concrete Columns Repaired with Environment-Friendly Fiber-Reinforced Cementitious Composites, *Engineering Structures 2017*, Vol 136, pp. 26–35.

Li Z, Drying Shrinkage Prediction of Paste Containing Meta-Kaolin and Ultrafine Fly Ash for Developing Ultra-High Performance Concrete, *Materials Today Communications 2016*, Vol 6, pp.7480.

Liang JZ, Du Q, Tsui GC, and Tang CY, Tensile Properties of Graphene Nano-Platelets Reinforced Polypropylene Composites, *Composites Part B: Engineering 2016*, Vol 95, pp. 166171.

Loukili A, Khelidj A, and Richard P, Hydration Kinetics, Change of Relative Humidity, and Autogenous Shrinkage of Ultra-High-Strength Concrete, *Cement and Concrete Research 1999*, Vol 29(4), pp. 577584.

Lu C, Lu Z, Li Z, and Leung CK, Effect of Graphene Oxide on the Mechanical Behavior of Strain Hardening Cementitious Composites, *Construction and Building Materials 2016*, Vol 120, pp. 457–464.

Luo J, Duan Z, and Li H, The Influence of Surfactants on the Processing of Multiwalled Carbon Nanotubes in Reinforced Cement Matrix Composites, *Physical Status Solidi A 2009*, Vol 206(12), pp. 2783–2790.

Lura P and Bisschop J, On the Origin of Eigenstresses in Lightweight Aggregate Concrete, *Cement and Concrete Composites 2004*, Vol 26(5), pp. 445–452.

Madhkhan M, Entezam M, and Torki ME, Mechanical Properties of Precast Reinforced Concrete Slab Tracks on Non-Ballasted Foundations, *Scientia Iranica A 2012*, Vol 19 (1), pp. 2026.

Ma J and Dietz J, Ultra High Performance Self Compacting Concrete, *LACER No. 7*, 33-42, 2012.

Ma J, Orgass M, Dehn F, Schmidt D, and Tue NV, Comparative Investigations on Ultra-High Performance Concrete with and without Coarse Aggregates," *In Proceedings of International Symposium on Ultra High Performance Concrete*, Germany,2004, pp. 205212.

Mahmud GH, Yang Z, and Hassan AMT, Experimental and Numerical Studies of Size eEffects of Ultra High Performance Steel Fibre Reinforced Concrete (UHPFRC) Beams, *Construction and Building Materials 2013*, Vol 48, pp. 1027–1034.

Makar JM and Chan GW, Growth of Cement Hydration Products on Single-Walled Carbon Nanotubes, *Journal of American Ceramic Society 2009*, Vol 92(6), pp. 1303–1310.

Matte V and Moranville M, Durability of Reactive Powder Composites: Influence of Silica Fume on the Leaching Properties of Very Low Water/Binder Pastes, *Cement and Concrete Composites 1999*, 21(1):pp. 19.

Mechtcherine V, Dudziak L, and Hempel S, Internal Curing to Reduce Cracking Potential of Ultra High Performance Concrete by Means of Super Absorbent Polymers, *Proceedings of 2nd International RILEM Workshop on Concrete Durability and Service Life Planning 2009*, pp. 3138.

Mehdipour I and Khayat HK, Coupled Effect of SRA or LWS on Efficacy of Calcium Sulfoaluminate Cement to Mitigate Shrinkage: Hydration and Expansion Characterization," *Cement and Concrete Composit 2017*, In press.

Meng W, Valipour M, and Khayat KH Optimization and Performance of Cost-Effective Ultra-High Performance Concrete, *Materials and Structures 2017*, Vol 50(1), pp. 29.

Meng W and Khayat KH, Mechanical Properties of Ultra-High-Performance Concrete Enhanced with Graphite Nanoplatelets and Carbon Nanofibers, *Composites Part B: Engineering 2017a*, Vol 1751, pp. 113–122.

Meng W and Khayat KH, Experimental and Numerical Studies on Flexural Behavior of Ultra-High-Performance Concrete Panels Reinforced with Embedded Glass Fiber-Reinforced Polymer Grids, *Transportation Research Record: Journal of Transportion Research Board 2016*, Vol 2592, pp. 38–44.

Meng W and Khayat KH, Improving Flexural Performance of Ultra-High-Performance Concrete by Rheology Control of Suspending Mortar, *Composites Part B: Engineering 2017b,* Vol 117, pp. 26–34.

Meng W, Lunkad P, Kumar A, and Khayat KH, Influence of Silica Fume and PCE Dispersant on Hydration Mechanisms of Cement," *Journal of Physical Chemistry C 2016*, Vol 120(47), pp. 26814–26823.

Metaxa ZS, Konsta-Gdoutos M, and Shah SP, Carbon Nanofiber-Reinforced Cement-Based Materials, *Transportation Research Record: Journal of Transportion Research Board 2010, Vol* 2142, pp. 114–118.

Metaxa ZS, Seo JW, Konsta-Gdoutos MS, Hersam MC, and Shah SP, Highly Concentrated Carbon Nanotube Admixture for Nano-Fiber Reinforced Cementitious Materials, *Cement and Concrete Composites 2012*, Vol 34(5), pp. 612–617.

Mehta PK, Greening of the Concrete Industry for Sustainable Development, *Concrete International 2002*, pp. 23.

Mias C, Torres L, Turon A, and Sharaky IA, Effect of Material Properties on Long-Term Deflections of GFRP Reinforced Concrete Beams, *Construction and Building Materials 2013*, Vol 41, pp. 99108.

Mihashi H and Kohno Y, Toughening Mechanism of Hybrid Fiber Reinforced Cement Composites," *Fracture Mechanic of Concrete and Concrete Structures–High Performance Concrete*, Brick Masonry and Environmental Aspects, 2007, Vol 3 pp. 1329–1339.

Milani G, Kinematic FE Limit Analysis Homogenization Model for Masonry Walls Reinforced with Continuous FRP Grids" *International Journal of Solids Structure 2011*, Vol 48(2), pp. 326345.

Mobasher B, Dey V, Cohen Z, and Peled A, Correlation of Constitutive Response of Hybrid Textile Reinforced Concrete from Tensile and Flexural Tests, *Cement and Concrete Composites 2014,* Vol 53, pp. 148–161.

Mobasher B, Bakhshi M, and Barsby C, Back Calculation of Residual Tensile Strength of Regular and High Performance Fiber Reinforced Concrete from Flexural Tests, *Construction and Building Materials 2014, Vol* 70, pp. 243–253.

Monai B and Schnabl H, Practice of UHPC in Austria. In: Second international Symposium on Ultra High Performance Concrete, Kassel, 2008, pp. 839–846.

Multon S, Cyr M, Sellier A, Leklou N, and Petit L, Coupled Effects of Aggregate Size and Alkali Content on ASR Expansion, *Cement and Concrete Research 2008*, Vol 38(3), pp. 350359.

Musso S, Tulliani JM, Ferro G, and Tagliaferro A, Influence of Carbon Nanotubes Structure on the Mechanical Behavior of Cement Composites, *Composites Science Technology 2009*, Vol 69(11), pp. 1985–1990.

Myer K, Mechanical Engineers Handbook, 2nd Edition, John Wiley&Sons, Inc., New York, 1998.

Naaman AE and Chandrangsu K, Innovative Bridge Deck System Using High-Performance Fiber-Reinforced Cement Composites, *Structural Journal 2004,* Vol 101(1), pp. 5764.

Naaman AE, Prestressed Concrete Analysis and Design: Fundamentals, 3rd Edition. Techno Press 3000, Ann Arbor, MI, USA, 1982.

Nanni A, Fiber-Reinforced-Plastic for Concrete Structures: Properties and Applications, Elsevier Science, Amsterdam, 1993.

Nehdi M, Mindess S, and Aïtcin PC, Rheology of High-Performance Concrete: Effect of Ultrafine Particles, *Cement and Concrete Research 1998*, Vol 28(5), pp. 687697.

Nguyen VT, Rice Husk Ash as a Mineral Admixture for Ultra High Performance Concrete, Ph.D. Dissertation, Netherlands, Delft University, 2011.

Nguyen DL, Ryu GS, Koh KT, and Kim DJ, Size and Geometry Dependent Tensile Behavior of Ultra-High-Performance Fiber-Reinforced Concrete, *Composites Part B: Engineering 2014*, Vol 58, pp. 279292.

Nguyen DL, Kim DJ, Ryu GS, and Koh KT, Size Effect on Flexural Behavior of Ultra-High-Performance Hybrid Fiber-Reinforced Concrete, *Composites Part B: Engineering 2013,* Vol 45(1), pp. 1104–1116.

Nochaiya T and Chaipanich A, Behavior of Multi-Walled Carbon Nanotubes on the Porosity and Microstructure of Cement-Based Materials, *Applied Surface Science 1945*, Vol 257(6), pp. 1941–1945.

Ooi E and Yang Z, Efficient Prediction of Deterministic Size Effects Using the Scaled Boundary Finite Element Method, *Engineering Fracture Mechanics 2010*, Vol 77, pp. 985-1000.

Park SH, Kim DJ, Ryu GS, and Koh KT, Tensile behavior of Ultra High Performance Hybrid Fiber Reinforced Concrete, *Cement and Concrete Composites 2012,* Vol 34(2), pp. 172–184.

Passuello A, Moriconi G, and Shah SP, Cracking Behavior of Concrete with Shrinkage Reducing Admixtures and PVA Fibers, *Cement and Concrete Composites 2009,* Vol 31(10), pp. 699–704.

Perry VH and Seibert PJ, The Use of UHPFRC for Bridges in North America: the Technology, Applications and Challenges Facing Commercialization, *Proceeding 2nd International Symposium on UHPC*, Kassel, Germany, 2008, pp. 815822.

Perry VH and Weiss G, Innovative Field Cast UHPC Joints for Precast Bridge Decks – Design Prototype Testing and Projects AFGC – Designing and Building with UHPFRC: State of the Art & Development, Marseille, France, 2009, pp. 1719.

Peyvandi A, Sbia LA, Soroushian P, and Sobolev K, Effect of The Cementitious Paste Density on the Performance Efficiency of Carbon Nanofiber in Concrete Nanocomposite, *Construction and Building Materials 2013*, Vol 48, pp. 265–269.

Peyvandi A, Soroushian P, Abdol N, and Balachandra AM, Surface-Modified Graphite Nanomaterials for Improved Reinforcement Efficiency in Cementitious Paste, *Carbon* 2013, Vol 63, pp. 175–186.

Piggott MR, Short Fibre Polymer Composites: A Fracture-Based Theory of Fibre Reinforcement, *Journal of Composite Materials 1994*, Vol 28(7), pp. 588–606.

Plank J, Schroefl C, Gruber M, Lesti M, and Sieber R, Effectiveness of Polycarboxylate Superplasticizers in Ultra-High Strength Concrete: the Importance of PCE Compatibility with Silica Fume, *Journal of Advanced Concrete Technology 2009*, Vol 7(1), pp. 512.

Polat R, Demirboğa R, and Khushefati WH, Effects of Nano and Micro Size of CaO and MgO, Nano-Clay and Expanded Perlite Aggregate on the Autogenous Shrinkage of Mortar, *Construction and Building Materials 2015,Vol* 81, pp. 268–275.

Pyo S, Wille K, El-Tawil S, and Naaman AE, Strain Rate Dependent Properties of Ultra High Performance Fiber-Reinforced Concrete (UHP-FRC) Under Tension, *Cement and Concrete Composites 2015,*Vol 56, pp. 15–24.

Ranade R, Li VC, and Heard WF, Tensile Rate Effects in High Strength-High Ductility Concrete, *Cement and Concrete Research 2015,* Vol 68, pp. 94–104.

Regourd M, Thomassin JH, Baillif P, and Touray JC, Blast-Furnace GGBS Hydration Surface Analysis, *Cement and Concrete Research 1983*, Vol 13, pp. 549–556.

Reineck KH and Frettlöhr B, Tests on Scale Effect of UHPFRC Under Bending and Axial Forces, *Proceeding of 3rd Fiber International Congress 2010*, Washington D.C., pp. 14.

Richard P and Cheyrezy M, Reactive Powder Concretes with High Ductility and 200-800 MPa Compressive Strength, *ACI Materials Journal 1994*, Vol 144, pp. 507518

Richard P and Cheyrezy M, Composition of Reactive Powder Concretes, *Cement and Concrete Research 1995,* Vol 25, pp. 15011511

RILEM TC 162-TDF, Test and Design Methods for Steel Fiber Reinforced Concrete-Bending Test, *Materials and Structures 2002*, Vol 35, pp. 579–582.

Rueden C, Dietz C, Horn M, Schindelin J, Northan B, Berthold M, and Eliceiri K, ImageJ Ops [Software]. (http://imagej.net/Ops accessed on July 16, 2016).

Saleem MA, Mirmiran A, and Xia J, Ultra High Performance Concrete Bridge Decks Reinforced with High-Strength Steel or Fiber Reinforced Polymers" *ACI Structure Journal 2011*, Vol 108(5), pp. 601609.

Sanchez F and Sobolev K, Nanotechnology in Concrete – A Review, *Construction and Building Materials 2010,* Vol 24(11), pp. 2060–2071.

Sbia LA, Peyvandi A, Soroushian P, Lu J, and Balachandra AM, Enhancement of Ultrahigh Performance Concrete Material Properties with Carbon Nanofiber, *Advanced Civil Engineering 2014*, pp. 10.

Scrivener KL, Crumbie AK, and Laugesen P, The Interfacial Transition Zone (ITZ) Between Cement Paste and Aggregate in Concrete, *Interface Science 2004*, Vol 12(4), pp.411421.

Seibert P, Perry VH, Ghomeim GAM, Carson G, El-Hacha R, Cariaga I, and Zakariasen D, The First Architectural UHPC Facade Application in North America. Ultra-High Performance Concrete and Nanotechnology in Construction, *Proceeding Hipermat 2012. 3rd International Symposium on UHPC and Nanotechnology for High Performance Construction Materials*, Kassel, 2012, pp. 9971004.

Sharbatdar MK, Saatcioglu M, and Benmokrane B, Seismic Flexural Behavior of Concrete Connections Reinforced with CFRP Bars and Grids, *Composite Structures 2011*, Vol 93, pp. 24392449.

Singh AP, Gupta BK, Mishra M, Chandra A, Mathur RB, and Dhawan SK, Multiwalled Carbon Nanotube/Cement Composites with Exceptional Electromagnetic Interference Shielding Properties, *Carbon 2013*, Vol 56, pp. 86–96.

Sonobe Y, Fukuyama H, Okamoto T, Kani N, Kimura K, and Kobayashi K, Design Guidelines of FRP Reinforced Concrete Building Structures, *Journal of Composite Construction 1997*, Vol 1(3), pp. 90-115.

Soranakom C and Mobasher B, Correlation of Tensile and Flexural Responses of Strain Softening and Strain Hardening Cement Composites, *Cement and Concrete Composites 2008*, Vol 30(6), pp. 465–477.

Spasojevic A, Redaelli D, Fernández Ruiz M, and Muttoni A, Influence of Tensile Properties of UHPFRC on Size Effect in Bending" *Proceeding of 2nd International Symposium Ultra High Performance Concrete*, No. EPFL-CONF-121520,2008, pp. 303–310.

Standard JC, Method of Test for Fracture Energy of Concrete by Use of Notched Beam, *JCI-S-001-2003*, Japan Concrete Institute, 2003.

Steinberg E, Structural Reliability of Prestressed UHPC Flexure Models for Bridge Girders, *Journal of Bridge Engineering 2009*, Vol 15(1), pp. 6572.

Sun G, Liang R, Lu Z, Zhang J, and Li Z, Mechanism of Cement/Carbon Nanotube Composites with Enhanced Mechanical Properties Achieved by Interfacial Strengthening, *Construction and Building Materials 2016*, Vol 115, pp. 87–92.

Sun W, Chen H, Luo X, Qian H, The Effect of Hybrid Fibers and Expansive Agent on the Shrinkage and Permeability of High-Performance Concrete, *Cement and Concrete Research 2001*, Vol 31(4), pp. 595–601.

Suzuki K, Nishikawa T, Ikenaga H, and Ito S, Effect of NaCl or NaOH on the Formation of C- S- H, *Cement and Concrete Research 1986*, Vol 16(3), pp. 333340.

Swamy RN and Mangatm PS, Influence of Fibre-Aggregate Interaction on Some Properties of Steel Fibre Reinforced Concrete, *Materials and Structures 1974*, Vol 7(5), pp. 307–314.

Tang F, Bao Y, Chen Y, Tang Y, and Chen G, Impact and Corrosion Resistances of Duplex Epoxy/Enamel Coated Plates, *Construction and Building Materials 2016*, Vol 112(1), pp. 7–18.

Tao Y and JF Chen, Concrete Damage Plasticity Model for Modeling FRP-to-Concrete Bond Behavior, *Journal of Composites for Construction 2015*, Vol 19, pp. 04014026.

Tattersall GH and Banfill PFG, The Rheology of Fresh Concrete, London, Pitman, 1983.

Taylor HFW, Famy C, and Scrivener KL, Delayed Ettringite Formation, *Cement and Concrete Research 2001*, Vol 31(5), pp. 683693

Thomassin JH, Goni J, Baillif P, Touray JC, and Jaurand NC, An XPS Study of the Dissolution Kinetics of Chrysotile in 0.1n Oxalic Acid at Different Temperatures, *Physics and Chemistry of Minerals 1977*, Vol 1(4), pp. 385–398.

Tomas J, Fundamentals of Cohesive Powder Consolidation and Flow, *Granular Matter 2004*, Vol 6, pp. 7586.

Tosun-Felekoğlu K, Felekoğlu B, Ranade R, Lee BY, and Li VC, The Role of Flaw Size and Fiber Distribution on Tensile Ductility of PVA-ECC, *Composites Part B: Engineering 2014,* Vol 56, pp. 536–545.

Tran NT, Tran TK, Jeon JK, Park JK, and Kim DJ, Fracture Energy of Ultra-High-Performance Fiber-Reinforced Concrete at High Strain Rates, *Cement and Concrete Research 2016*, Vol 79, pp. 169184.

Tyson BM, Abu Al-Rub RK, Yazdanbakhsh A, and Grasley Z, Carbon Nanotubes and Carbon Nanofibers for Enhancing the Mechanical Properties of Nanocomposite Cementitious Materials, *Journal of Materials in Civil Engineering 2011*, Vol 23(7), pp. 1028–1035.

Van VTA, Rößler C, Bui DD, and Ludwig HM, Rice Husk Ash as Both Pozzolanic Admixture and Internal Curing Agent in Ultra-High Performance Concrete, *Cement and Concrete Composites 2014*, Vol 53, pp. 270–278.

Vydra V, Trtík K, and Vodák F, Size Independent Fracture Energy of Concrete, *Construction and Building Materials 2012*, Vol 26(1), pp. 357–361.

Wang W, Liu J, Agostini F, Davy CA, Skoczylas F, and Corvez D, Durability of an Ultra High Performance Fiber Reinforced Concrete (UHPFRC) under Progressive Aging, *Cement and Concrete Research 2014*, Vol 55, pp. 113.

Wang C, Yang C, Liu F, Wan C., and Pu X, Preparation of Ultra-High Performance Concrete with Common Technology and Materials," *Cement and Concrete Composites 2012*, Vol 34, pp. 538544.

Wee TH, Babu DS, Tamilselvan T, and Lim HS, Air-Void System of Foamed Concrete and Its Effect on Mechanical Properties, *ACI Materials Journal 2006*, Vol 103(1), pp. 45–52.

Wei F, Michael WG, and Della MR, The Retarding Effects of FA Upon the Hydration of Cement Pastes: the First 24 Hours, *Cement and Concrete Research 1985*, Vol 15(1), pp. 174–184.

Weiss J, Bentz D, Schindler A, and Lura P, Internal Curing, *Structure A Joint Publication of NCSEA*, CASE, SEI, 2012.

Wille K and Boisvert-Cotulio C, Development of Non-Proprietary Ultra-High Performance Concrete for Use in the Highway Bridge Sector, *Report No. PB2013-110587*, National Technical Information Service, Springfield, VA, 2013.

Wille K and Naaman AE, Effect of Ultra-High Performance Concrete on Pullout Behavior of High-Strength Brass-Coated Straight Fibers, *ACI Materials Journal 2013*, Vol 4, pp. 451–462.

Wille K, Kim DJ, and Naaman AE, Strain-Hardening UHP-FRC with Low Fiber Contents, *Materials and Structures 2011*, Vol 44(3), pp. 583–598.

Wille K and Loh K, Nanoengineering Ultra-High-Performance Concrete with Multiwalled Carbon Nanotubes, *Transportation Research Record: Journal of Transportion Research Board* 2010, Vol 2142, pp. 119–126.

Wille K, Naaman AE, and El-Tawil S, Optimizing Ultra-High-Performance Fiber-Reinforced Concrete, *Concrete International 2011*, Vol 33, pp. 3541.

Wille K, Naaman AE, and Parra-Montesinos GJ, Ultra-High Performance Concrete with Compressive Strength Exceeding 150 MPa (22 ksi): A Simpler Way, *ACI Materials Journal 2011*, Vol 108(1).

Wu X, Roy DM, and Langton CA, Early Stage Hydration of GGBS-Cement, *Cement and Concrete Research 1983*, Vol 13(2), pp.277–286.

Xia M, Hamada H, Maekawa Z, Flexural Stiffness of Injection Molded Glass Fiber Reinforced Thermoplastics, *International Polymer Processing 1995*, Vol 10(1), pp. 74–81.

Xu M, Hallinan B, and Wille K, Effect of Loading Rates on Pullout Behavior of High Strength Steel Fibers Embedded in Ultra-High Performance Concrete, *Cement and Concrete Composite 2016*, Vol 70, pp. 98–109.

Xu M and Wille K, Fracture Energy of UHP-FRC under Direct Tensile Loading Applied at Low Strain Rates, *Composites Part B: Engineering 2015*, Vol 80, pp. 116–125.

Yang SL, Millard SG, Soutsos MN, Barnett SJ, and Le TT, Influence of Aggregate and Curing Regime on the Mechanical Properties of Ultra-High Performance Fibre Reinforced Concrete (UHPFRC), *Construction and Building Materials 2009*, Vol 2, pp. 2291–2298.

Yang Y, Wu G, Wu Z, Jiang J, and Wang X, Structural Performance of Ballastless Track Slabs Reinforced with BFRP and SFCB, *Composites Part B: Engineering 2015*, Vol 71, pp. 103112.

Yoo DY, Banthia N, and Yoon YS, Predicting the Flexural Behavior of Ultra-High-Performance Fiber-Reinforced Concrete, *Cement and Concrete Composite 2016*, Vol 74, pp. 71–87.

Yoo DY, Banthia N, Kang ST, and Yoon YS, Effect of Fiber Orientation on the Rate-Dependent Flexural Behavior of Ultra-High-Performance Fiber-Reinforced Concrete, *Composite Structures 2016*, Vol 157, pp. 62–70.

Yoo DY, Banthia N, Kang ST, and Yoon YS, Size Effect in Ultra-High-Performance Concrete Beams, *Engineering Fracture Mechanics 2016, Vol* 157, pp. 86–106.

Yoo DY, Park JJ, Kim SW, and Yoon YS, Early Age Setting, Shrinkage and Tensile Characteristics of Ultra High Performance Fiber Reinforced Concrete, *Construction and Building Materials 2013,* Vol 41, pp. 427–438.

Yost JR, Goodspeed CH, and Schmeckpeper ER, Flexural Performance of Concrete Beams Reinforced with FRP Grids, *Journal of Composites Construction 2001*, Vol 5(1), pp. 18–25.

Yu C, The Study of Reinforced Pseudo-Ductile Cementitious Composite Permanent formwork, Ph. D Thesis, *Hong Kong University of Science and Technology, 2014*.

Yu R, Spiesz P, and Brouwers HJH, Mix Design and Properties Assessment of Ultra-High Performance Fibre Reinforced Concrete (UHPFRC), *Cement and Concrete Research 2014*, Vol 56, pp. 2939.

Yu R, Spiesz P, and Brouwers HJH, Development of An Eco-Friendly Ultra-High Performance Concrete (UHPC) with Efficient Cement and Mineral Admixtures Uses, *Cement and Concrete Composite 2015*,Vol 55, pp. 383394.

Zhang XX, Abd Elazim AM, Ruiz G, and Yu RC, Fracture Behavior of Steel Fibre-Reinforced Concrete at a Wide Range of Loading Rates, *International Journal Impact Engineering 2014*, Vol 71, pp. 89–96.

Zdeb T and Śliwiński J, The Influence of Steel Fibre Content and Curing Conditions on Mechanical Properties and Deformability of Reactive Powder Concrete at Bending, *Proceeding of 9th International Symposium of Brittle Matrix Composites 2009*, pp. 33–42.

Zhutovsky S and Kovler K, Effect of Internal Curing on Durability-Related Properties of High Performance Concrete, *Cement and Concrete Research 2012*, Vol 42, pp. 20–26.

Zhang MH, Lastra R, and Malhotra VM, Rice-Husk Ash Paste and Concrete: Some Aspects of Hydration and the Microstructure of the Interfacial Zone between the Aggregate and Paste, *Cement and Concrete Research 1996*, Vol 26(6), pp. 963-977.

Zhang T, Yu Q, Wei J, Gao P, and Zhang P, Study on Optimization of Hydration Process of Blended Cement, *Journal of Thermal Analytical Calorimetry 2012*, Vol 107, pp. 489–498.

Zingg A, Winnefeld F, Holzer L, Pakusch J, Becker S, Figi R, and Gauckler L, Interaction of Polycarboxylate-Based Superplasticizers with Cements Containing Different C3A amounts, *Cement and Concrete Composites 2009*, Vol 31(3), pp. 153162.

VITA

Weina Meng was awarded the degrees of Bachelor and Master from the Department of Civil Engineering at Southwest Jiaotong University, China in 2009 and 2012, respectively. She was a Research Assistant at Southwest Jiaotong University from 2009 to 2012. She joined the Missouri University of Science and Technology in 2013, and became a Research Assistant since then. She worked as a teaching assistant in between August 2016 to May 2017. In July 2017, she received her Ph.D. degree in Civil Engineering from Missouri University of Science and Technology, Rolla, Missouri.